Stony Brook University

The Fluid Dynamics of Mercury Target Delivery and Exhaust for A Muon Collider Particle Production System

A Dissertation Presented

by

Yan Zhan

to

The Graduate School

in Partial Fulfillment of the

Requirements

for the Degree of

Doctor of Philosophy

in

Mechanical Engineering

Stony Brook University

December 2014

Stony Brook University

The Graduate School

Yan Zhan

We, the dissertation committee for the above candidate for the
Doctor of Philosophy degree, hereby recommend
acceptance of this dissertation.

Foluso Ladeinde, Dissertation Advisor

Associate Professor, Dept. of Mechanical Engineering

Thomas Cubaud, Chairperson of Defense

Associate Professor, Dept. of Mechanical Engineering

Harold G. Kirk, Co-Advisor

Senior Scientist, Dept. of Physics, Brookhaven National Laboratory

Kirk T. McDonald, Outside Member

Professor, Dept. of Physics, Princeton University

This dissertation is accepted by the Graduate School

Charles Taber

Dean of the Graduate School

Abstract of the Dissertation

The Fluid Dynamics of Mercury Target Delivery and Exhaust for A Muon Collider Particle Production System

by

Yan Zhan

Doctor of Philosophy

in

Mechanical Engineering

Stony Brook University

2014

Liquid mercury has been investigated as a potential high-Z target for the production of Muon particles for the Muon Collider project. This thesis investigates the dynamics of mercury flow in a design of the target delivery system, with the objective of determining pipe configurations that yield weak turbulence intensity at the exit of the pipe. Curved circular pipes with various half-bend angles, with/without nozzles in the exit region, and with/without welds on the pipe inner surface are studied. Theoretical analysis is carried out for steady laminar incompressible flow, whereby the terms representing curvature effects are examined. Subsequent simulations of the turbulent flow regime in the pipes are based on a realizable $k - \varepsilon$ Reynolds-averaged Navier-Stokes (RANS) equations approach. The simulations in this thesis have been based on the FLUENT commercial computational fluid dynamics (CFD) codes. The effects of turning angles, presence of a nozzle, and presence of a weld (on the inner surface of the pipes) on momentum thickness and turbulence intensity at the exit of the curved pipe are discussed, as are the implications for the target delivery pipe designs. It was found that the pressure loss from inlet to outlet is nearly the same for all pipes. A nozzle reduces the turbulence intensity of the flow while a weld increases it.

In order to locate the free surface of the mercury jet exhausting from the pipe into air, a coupled level set (LS) and volume of fluid (VOF) method (CLSVOF) has been applied. When we started this project, FLUENT did not support this approach. Therefore we developed, validated, and employed a coupled VOF and LS method that uses high-order weighted essentially non-oscillatory (WENO) schemes for the re-initialization equation in the LS method. Several successful validations of the developed CLSVOF code are presented in this dissertation. However, the "production runs" for the jet flow were carried out using the CLSVOF method that was eventually implemented in FLUENT by the vendor of the software. The flow conditions obtained at the pipe outlet have been used as the inlet conditions for the free-jet simulations. The dynamics of mercury jet flow are determined by the combined effects of turning angles and weld.

Contents

List of Figures

List of Tables

List of Abbreviations

LS	Level Set
VOF	Volume of Fluid
MAC	Marker and Cell
CLSVOF	Coupled Level Set Volume of Fluid
RANS	Reynolds-Averaged Navier-Stokes
RSM	Reynolds Stress Model
SA	Spalart-Allmaras
SKE	Standard $k - \varepsilon$
RKE	Realizable $k - \varepsilon$
SIMPLE	Semi Implicit Method for Pressure Linked Equations
CSF	Continuum Surface Force
UDS	User Defined Scalar
UDM	User Defined Memory
MUSCL	Monotone Upstream-Centered Scheme for Conservation Laws
TVD	Total Variation Diminishing
WENO	Weighted Essentially Non-Oscillatory
RK	Runge-Kutta
RHS	Right Hand Side
CV	Convex Side
CC	Concave Side

LES	Large Eddy Simulation
ILES	Implicit Large Eddy Simulation
DNS	Direct Numerical Simulation
NSE	Navier-Stokes Equations

List of Symbols

a	pipe radius (m)
R	curvature radius (m)
De	Dean number
Re	Reynolds number
δ	curvature ratio $(\delta \equiv a/R)$
u_τ	mean friction velocity (m/s)
Re_τ	Reynolds number based on u_τ
φ	half-bend angle of the target delivery pipe $(^\circ)$
r	radial direction (m)
θ	azimuthal angle $(^\circ)$
z	axial coordinate (m)
$\widetilde{z}$	flow direction tangential to the pipe center-line (m)
I	turbulence intensity $(\%)$
k	turbulence kinetic energy per unit mass (m^2/s^2)
k^*	non-dimensional k
$\overline{k}$	mean turbulence kinetic energy per unit mass (m^2/s^2)
ε	turbulence kinetic energy per unit mass dissipation rate (m^2/s^3)
ε^*	non-dimensional ε
u	instantaneous velocity in the r-direction (m/s)

v	instantaneous velocity in the θ- direction (m/s)
w	instantaneous velocity in the z- direction (m/s)
u^*	non-dimensional u
v^*	non-dimensional v
w^*	non-dimensional w
r^*	normalized r
θ^*	normalized θ
z^*	normalized z
ρ	mass density (kg/m^3)
U_b	bulk velocity (m/s)
∇^{*2}	non-dimensional Laplacian operator
∇_n^*	non-dimensional normal gradient
t	time (s)
p	instantaneous/reduced pressure $(N/m^2,\ Pa)$
p^*	non-dimensional instantaneous pressure
P^*	non-dimensional mean pressure
$(\acute{p})^*$	non-dimensional fluctuating pressure
$\mathbf{u}^*$	non-dimensional instantaneous velocity vector
$\mathbf{U}^*$	non-dimensional mean velocity vector
$(\acute{\mathbf{u}})^*$	non-dimensional fluctuating velocity vector
τ^*	non-dimensional shear stress tensor
μ^*	non-dimensional dynamic viscosity
μ_t^*	non-dimensional eddy viscosity
C_μ	eddy viscosity coefficient
$\overline{S}_{ij}^*$	symmetric part of the deformation tensor
$\overline{\Omega}_{ij}^*$	antisymmetric part of the deformation tensor
A_0	RKE model constant, 4.04

A_s	RKE model constant
σ_k	turbulent Prandtl number for κ
σ_ε	turbulent Prandtl number for ε
G_t	production of turbulence kinetic energy (m^2/s^3)
l^*	non-dimensional turbulent characteristic length
D_h^*	non-dimensional hydraulic diameter
ϕ	level set function (m)
Φ	mean level set function (m)
ϕ'	fluctuating level set function (m)
ϕ_0	initial value of ϕ (m)
F_{st}	surface tension term (N/m)
D	rate of deformation tensor $(1/s)$
ϵ	half of the interface thickness (m)
H_ϵ	smoothed Heaviside function
σ	surface tension coefficient (N/m)
δ_ϵ	smoothed delta function
$\mathbf{n}$	normal vector of the interface
κ	mean curvature of the interface $(1/m)$
D_T	turbulent diffusivity (m^2/s)
c_1	constant for turbulent diffusivity equation
$S(\phi)$	sign function
d	distance from the local point to the interface (m)
Δ	filter width (m)
J	Jacobian of transformation
F	liquid volume fraction
$\Delta\mathbf{s}$	displacement vector
$\mathbf{A}$	face area vector (m^2)

V	cell volume (m^3)
$\mathbf{r}$	direction vector from cell center to face center
C_{cfl}	CFL number
L_c	continuity equation for flow in a curved pipe
L_{M_1}	r-momentum equation for flow in a curved pipe
L_{M_2}	θ-momentum equation for flow in a curved pipe
L_{M_3}	z-momentum equation for flow in a curved pipe
$\widetilde{L}_c$	continuity equation for flow in a straight pipe
$\widetilde{L}_{M_1}$	r-momentum equation for flow in a straight pipe
$\widetilde{L}_{M_2}$	θ-momentum equation for flow in a straight pipe
$\widetilde{L}_{M3}$	z-momentum equation for flow in a straight pipe
D_c^*	curvature term of continuity equation
D_r^*	curvature term of r-momentum equation
D_θ^*	curvature term of θ- momentum equation
$D_{\widetilde{z}}^*$	curvature term of $\widetilde{z}$-momentum equation
s	pseudo location coordinate direction
φ	pseudo bend angle coordinate direction
y^+	non-dimensional wall distance
δ_θ	momentum thickness (m)
$u_{rms}^{'}$	root-mean-squared fluctuating velocity (m/s)
C_p	static pressure coefficient
We	Weber number
Oh	Ohnesorge number
ϱ	ellipticity

List of Superscripts

*	non-dimensional parameter
(1)	first time step of RK
(2)	second time step of RK
n	time step of n
$n+1$	time step of n+1

List of Subscripts

l	liquid phase
g	gas phase
i	i index
j	j index
k	k index
ξ	curvilinear coordinates ξ
η	curvilinear coordinates η
ζ	curvilinear coordinates ξ
CD	central differencing
SOU	second-order up winding
f	value on the face
0	cell 0
1	cell 1
c	continuity equation
M_1	r-momentum equation
M_2	θ-momentum equation
M_3	z-momentum equation

Acknowledgements

The completion of this dissertation depends largely on the encouragement and guidelines of many others. I take this opportunity to express my sincere gratitude to the accelerator group staff at Brookhaven National Laboratory (BNL) for the discussions on this interesting project. I would like to express my greatest appreciation to my supervisors Dr. Foluso Ladeinde (Stony Brook University), Dr. Harold Kirk (BNL), and Dr. Kirk McDonald (Princeton University). Without their constant guidance, support and help, this project would not have materialized. I feel motivated and encouraged every time I attend the target meeting with accelerator colleagues. Special thank you to Van Graves (ORNL) for the important experimental information needed for my numerical simulation. I also would like to express my appreciation to Dr. Roman Samulyak, for his valuable suggestions. I am grateful to all my colleagues at the Advanced Fluid Dynamics Lab (AFDL) at Stony Brook University. They willingly helped me during my pregnancy. Finally, I am forever indebted to my parents, my husband, Shuai, and my son, Bryce, for their understanding, endless patience and encouragement. I also would like to acknowledge the financial sponsorship for this work by the United States Department of Energy (DOE) via the Brookhaven National Laboratory, High Energy Physics Department, Upton, New York.

Chapter 1

Introduction

In this chapter, we present the background of the study, motivations, review of flow in curved pipes, and the objectives of the thesis work.

1.1 Mercury Target Issues in the Muon Collider Project

The MERIT experiment at CERN [1, 2] is a proof-of-principle test for a target system that converts a 4-MW proton beam into a high-intensity muon beam for either a neutrino factory complex or a Muon Collider (Fig. 1.1). The mercury jet issues from the nozzle at the end of a delivery pipe to form a target that intercepts an intense proton beam inside a 15-T solenoid magnet. The use of liquid targets overcomes problematic effects of solid targets, such as melting/vaporization of components, damage by beam-induced pressure waves for pulsed beams, and extensive radiation damage. Also, liquid target systems offer the advantage of continuous regeneration of the target volume. However, the design of the mercury delivery pipe introduces new challenges.

The MERIT experiment uses a 180° bend, which has half-bend angles of 90° in the shape of a "U", for the delivery of the mercury. This geometry complicates the flow relative to that in a straight pipe, and affects the quality of the jet. Since the quality of the jet greatly influences the production of muon particles, it is pertinent to investigate the dynamics of

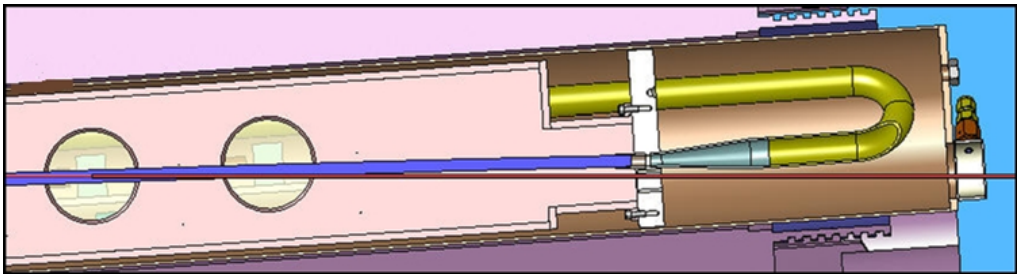

Figure 1.1: Sectional view of the target supple pipe of the MERIT experiment. The mercury jet generated at the end of the nozzle is on top of the nominal beam trajectory (both mercury jet and proton beam move from right to left)

the flow of mercury in the 180° bend, with a focus on exit-flow properties. Furthermore, for optimum muon particles production, the mercury jet flow should be laminar or weakly turbulent.

1.2 Motivations of the Study

In the MERIT experiment, the coupling between pipe geometry, magnetic field and energy deposition results in very complex flow conditions. In this thesis, an investigation of mercury internal flow and jet flow is carried out without a magnetic field or high energy deposition. This clarifies the pure geometry effects of delivery pipe on the dynamics of mercury flow and it is the baseline for understanding the effects of magnetic field and high energy deposition.

Due to the difficulties of using experimental investigations to optimize the target delivery pipe, computational fluid dynamics (CFD) comes in handy as a valuable analytical tool. The commercial code ANSYS FLUENT is a general-purpose CFD code, which is very stable in simulating incompressible low-speed flows. Also FLUENT has a VOF method for modeling two phase flows. A CLSVOF method developed in this thesis couples the LS method and VOF methods via UDFs in FLUENT to achieve a better free interface capturing capability. This thesis investigates mercury flow inside curved pipes and mercury flow in the jet plume by using the UDFs in the FLUENT code.

1.3 Review of Flow in Curved Pipes

Eustice [3, 4] is among the first to demonstrate the existence of a secondary flow in a curved pipe, an observation he made from injecting ink into water flowing through a pipe. Dean [5, 6] introduced a parameter which bears his name (Dean number, $De \equiv Re\delta^{1/2}$, where Re is the Reynolds number based on the area-averaged mean velocity through a pipe of diameter of $2a$, and δ is curvature radio ($\delta \equiv a/R$, where R is radius of curvature and a is the pipe radius)) to characterize the magnitude and shape of the secondary motions inside a loosely coiled pipe ($\delta << 1$). Subsequent works by others have investigated curved pipes with different values of R. Adler [7] presents experimental results of laminar and turbulent flows in three pipes with different R values. Rowe [8] investigates turbulent water flows for a curvature ratio of $\delta = 1/24$ in a circular 180° bend. Total pressure and yaw angle relative to the bend axis are measured for a Reynolds number of $Re = 236,000$. Enayat *et al.* [9] reports on the axial components of the mean and fluctuating velocities for the turbulent water flow in a circular 90° bend for a δ value of 1/5.6 and a wide range of Reynolds numbers. Azzola *et al.* [10] compute and measure the developed turbulent flows in a 180° bend for $\delta = 1/6.75$ and Reynolds number values of $57,400$ and $110,000$. The standard $k - \varepsilon$ model is used. Answer *et al.* [11] measure the Reynolds stresses and mean velocity components in vertical and horizontal planes containing the pipe axis, for air flow in a 180° bend, with $\delta = 1/13$ and $Re = 50,000$. Sudo *et al.* [12] report on the measurements of turbulent flow through a circular 90° bend for $\delta = 1/4$. Sudo and his co-workers [13] also measure turbulent air flow in a 180° circular bend for the same δ value, but with $Re = 60,000$. The axial, radial, and circumferential components of the mean velocity and the corresponding components of the Reynolds stress tensor are reported. Hüttl *et al.* [14] investigate the influence of curvature and torsion on turbulent flow in helically-coiled pipes for a Reynolds number $Re_\tau = 230$, where Re_τ is based on the friction velocity, u_τ. The pipe curvature was found to induce a secondary flow, which has a strong effect on the dynamics. Rudolf *et al.* [15] study the flow characteristics in several curved ducts: single elbow to coupled elbows in shapes of "U," "S,"

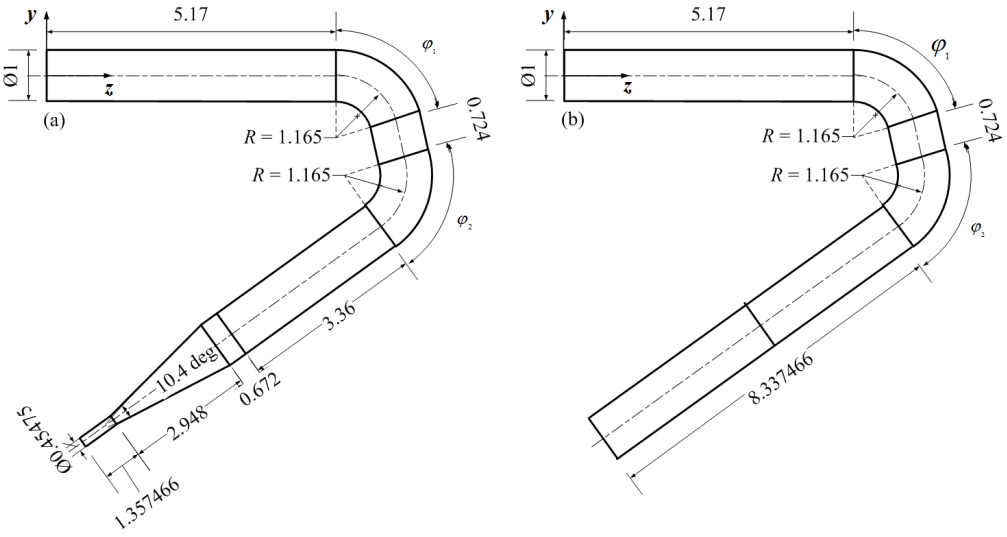

Figure 1.2: Coordinates along a curved pipe

and non-coplanar right angle, for a fixed value of $\delta = 1/4$ and $Re = 60,000$.

The uniqueness of the present study can be found in the effects of the half-bend angle, φ (as shown in Figure 1.2), and that of the presence of a nozzle in the exit region of eight pipe configurations on the momentum thickness and turbulence intensity at the pipe exit. The curvature ratios match those of the pipes that are tested in the MERIT experiment. The pipe geometries investigated are shown in Figure 1.3.

1.4 Review of Turbulent Flows Through Pipes with Rough Inner Surfaces

Turbulent flows in pipes have always been a major source of inspiring practical problems in the study of fluid dynamics. Among the numerous investigations in the field, noticeable efforts have been devoted to the cases in which the pipe had inner-surface roughness, e.g., grooves, fins, and other constrictions. These types of problems attracted special attentions for their wide applications in the fields of heat transfer [17, 18, 19], cardiac-vascular blood flow studies [20, 21, 22], and the design of unsteady flow meters [23, 24].

Two categories of roughness on the inner surfaces of pipes are usually considered in the

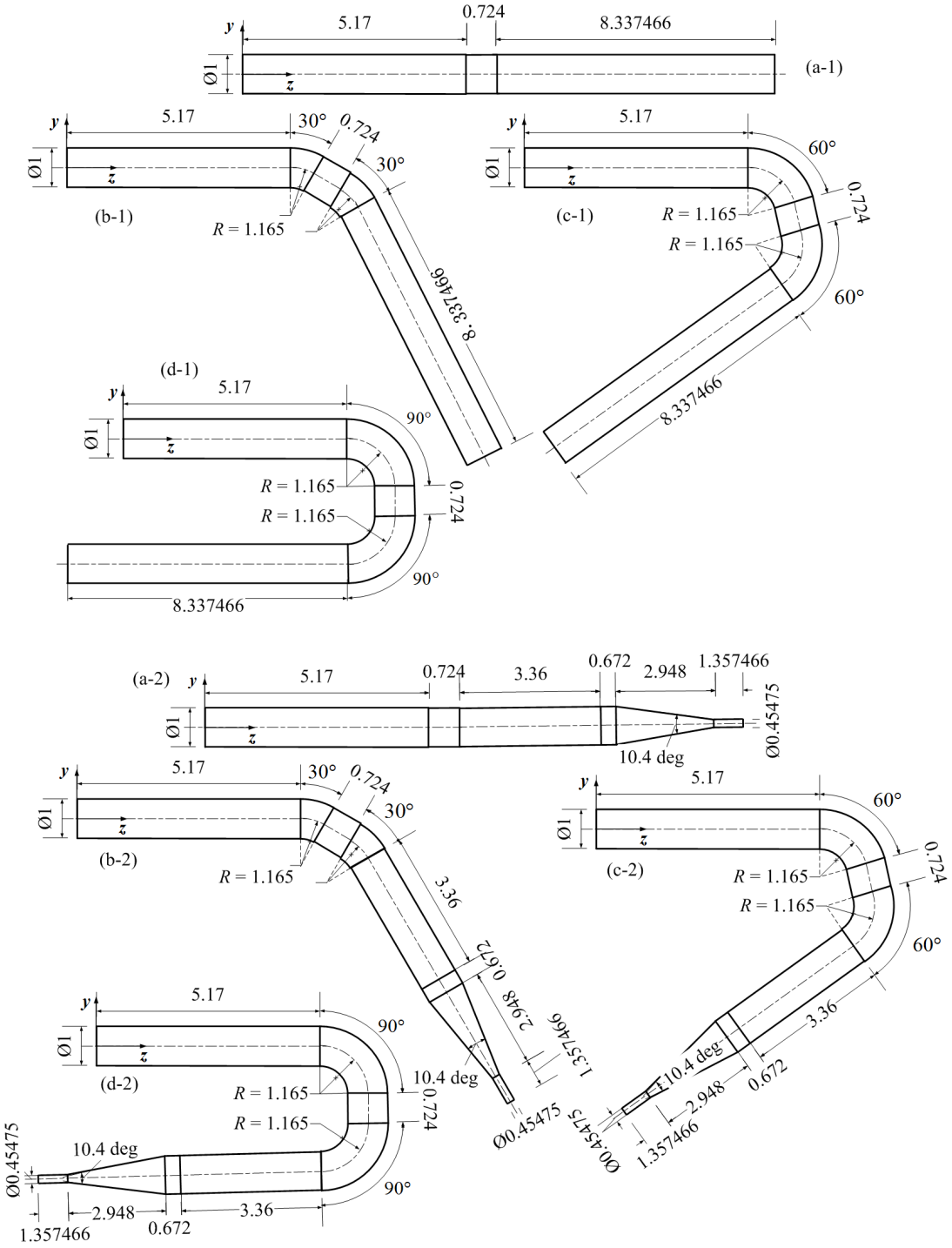

Figure 1.3: Configurations of the pipes investigated(normalized by the pipe diameter): without nozzles for φ_1/φ_2 of (a-1) 0°/0° (b-1) 30°/30° (c-1) 60°/60° (d-1) 90°/90°; with nozzles for φ_1/φ_2 of (a-2) 0°/0° (b-2) 30°/30° (c-3) 60°/60° (d-2) 90°/90°

literature. The first category includes corrugations and grooves, in which case the main research interests lie in the interactions between vorticity occupying cavities and core flows along the axial direction of pipes [25, 26, 28, 29]. The other category is related to various types of constrictions, such as valves in blood vessels [30, 31], welded pipe-flange joints [32, 33], and turbulators in heat exchangers [16, 19]. For both categories, several physical quantities are used to describe the properties of the flows, including pressure gradient, pressure loss, vorticity, maximum velocity, shear stress, turbulence kinetic energy, and turbulence viscosity. In the following sections, we will review the effects of the two types of inner-surface roughness on turbulent pipe flows in detail.

1.4.1 Turbulent Flows Through Pipes with Corrugations

Corrugations are discrete grooves placed at periodic intervals along the inner surfaces of pipes. A lot of efforts have been devoted to the investigation of the interactions between recirculating fluid inside the grooves and the main flows in the pipe. Previous works in this filed are focused on the momentum transfer phenomenon between the main flow and recirculating flows, and the resulting increase in pressure jump and friction forces.

One of the earliest contributions to the study of the effects of corrugations on turbulent flows through pipes was carried out by Perry and collaborators [25]. In their work, the "d-type" and "k-type" corrugations were introduced, based on their different effects on the interactions between flows in grooves and main flows along the axial direction of pipes. Cavities with a length-to-height ratio less than 4 are referred to as "d-type" corrugations, which are able to largely isolate the recirculating flows in the grooves from the main flow. In this case, the equivalent surface roughness length scale depends only on the boundary layer thickness. On the other hand, the "k-type" corrugations are those with length-to-height ratios larger than four. This kind of corrugation allows large momentum transfers between cavity flows and the main flow.

Later experimental studies by Djenidi *et al.* [26, 27] illustrate that the isolation of the

recirculating fluid in cavities from outer flows is not a general property of all the d-type corrugations. They reported significant increase in the turbulent intensities in the vicinity of downstream corners of the cavities. The existence of interactions between main and groove flows in pipes with "d-type" corrugations is furthered supported by the numerical study of Chang and his collaborators [34]. It is shown that both normal and shear stresses increase noticeably at the opening of the cavities. They also observe that the most significant enhancement occurred near the downstream corners of the cavities, which is consistent with the aforementioned results from Djenidi *et al.* [27].

Sutardi *et al.* [35] perform experiments on the turbulent flows through pipes with three different types of transverse grooves and for two different Reynolds numbers. For all the six tests, the friction factors measured are all larger than those from smooth inner-surface pipe flows. The drag force in a square groove is 50% higher than that in the semi-circular and triangular grooves. It is found that the square cavity sustains the existence of two smaller eddies above the main vortex, which results in more fluid ejections and momentum transfers from the groove into the core flow.

Increased friction factors in pipes with corrugations compared with those having smooth inner-surfaces is reported by Eiamsa-ard *et al.* [28] through simulations. Turbulent forced convection through channels with "k-type", "d-type", and intermediate cavities are simulated. Their main conclusion is consistent with that by Sutardi's group [35]: grooved channels provide considerable increase in the friction factor over smooth channels. This kind of increase in drag force is also reported by Luo *et al.* [36] in their simulations of a horizontal parallel-plate channel with periodic transverse ribs. Recirculating flow patterns are formed in the cavity between two adjacent ribs, and their interaction with the core flow is inferred to be the cause of the increase in the friction factor. The interaction between vortex flows in grooves and the main flow in the axial direction is further corroborated by Yang[37], Vijiapurapu and Cui [38], and experiments by Promvonge and Thianpong [39] and Dong *et al.* [40].

1.4.2 Turbulent Flows in Pipes with Constrictions

Turbulent flows through constrictions have attracted much attention recently for their increasing relevance in many engineering applications. Both experimental studies and numerical simulations have revealed the ability of constrictions to cause significant resistance to flow and pressure loss [41, 42, 43]. Independent studies [44, 45] showed that vortical structures occurred in the vicinity of the constrictions when the main flow is in the deceleration phase. Besides, several authors reported that the increases in shear stress and loss of pressure resulting from the existence of restrictions are larger in the deceleration phase than in the acceleration phase [46, 47, 48]. Most of the these applications are in the physiological sciences and bioengineering. In this dissertation, we study the turbulent flows in pipes with constriction/weld in the field of mechanical engineering, which has not been stated by other people as we know.

1.5 Review of Multiphase Models

There are generally two approaches for modelling two-phase flow: one-fluid model and two-fluid model. The main difference between these two models is the number of conservation equations solved. The one-fluid model solves one set of conservation equations for the mixture and is more widely used than the two-fluid model for two-phase flow. In the one-fluid model, the interfacial motion can be computed using Lagrangian tracking methods or Eulerian capturing methods. Lagrangian tracking techniques [49] are very accurate and efficient for flexible moving boundaries with small deformations. Examples include the MAC (marker and cell) methods [50], arbitrary Lagrangian-Eulerian methods, [51, 53, 54], and the front tracking methods. [55, 56] However, the tracking techniques are difficult to use in the cases where the interface breaks up or coalesces with another interface. Also, additional remeshing is required when a large deformation of the interface occurs. Eulerian capturing methods use an auxiliary function for the motion of the interface and have a wide range of applicability.

The Level Set (LS) and Volume of Fluid (VOF) methods are two examples of one-fluid model using the Eulerian capturing methods. They are robust but require a higher mesh resolution. In this work, both of these methods are used.

The LS method [57, 58, 59, 60] uses a zero contour of a continuous signed distance function, known as the level set function, to represent the interface. The distance function is positive on one side of the interface and negative on the other. The motion of interface is governed by the level set transport equation and a re-initialization equation is applied to make the level set function a signed distance function. The LS method has better accuracy in computing curvature and the normal to the interface. However, it is not conservative, leading to a significant, physically incorrect loss/gain of mass for incompressible two-phase flow.

The VOF method [61, 62, 63, 71] describes the interface with a volume of fluid function, F, which is defined as the volume fraction of one of the fluids in each cell. F is zero or unity in cells with a pure fluid, but has a value of $0 < F < 1$ in cells containing more than one fluid. The interface is explicitly described in each "multi-fluid" cell based on F. The distribution of F is solved through an advection equation using the reconstructed interface and the underlying velocity field. In an incompressible continuity equation, the conservation of mass equals to the conservation of volume. Therefore, the volume-of-fluid advection to advance an interface conserves the volume. The conservation of volume of each fluid is an important property of the VOF method. However, the VOF method lacks an accurate method for calculating surface tension in problems with high density ratios. Moreover, a higher-order of accuracy is difficult to achieve for VOF method because of the discontinuity in the volume fraction.

In order to obtain a better performance in capturing an interface, a combination of LS and VOF, abbreviated as CLSVOF, has been used by many researchers [72, 73, 74, 75, 76, 77, 78]. The CLSVOF method retains the advantages of each method: LS, to compute curvature and normal to the interface, and VOF, to capture the interface. Normally, the CLSVOF method

is superior to the individual LS and VOF methods [72, 79, 80].

1.6 Objectives of the Thesis Research

This thesis work has the following objectives: (i) Analysis of the secondary flow in a curved pipe; (ii) Numerical simulations of turbulent mercury flow in a curved pipe with/without a weld, with the purpose of studying the effects of pipe geometry and weld on turbulence intensity at the pipe exit; (iii) Numerical simulation of mercury jet flow using the exit conditions of pipe flow as the inlet conditions.

Rather than proposing a new numerical code, this study works with the user-defined functions (UDFs) in commercial code FLUENT to carry out the various simulations in this study.

In this dissertation, we describe mathematical models, numerical algorithms, numerical verification and validation, numerical simulations for the internal flow and jet flow. In chapter 2, the governing equations for internal laminar and turbulent flow, LS method, VOF method, the coupling between LS and VOF, and the continuum surface model are presented. In chapter 3, the numerical procedure of solving the governing equations are described. In chapter 4, verification and validations of the simulations are given. The results of mercury pipe flow and mercury jet flow are presented in chapter 5. The dissertation concludes with future work in chapter 6.

Chapter 2

Governing Equations and Boundary Conditions

2.1 Governing Equations for Laminar Flow in Curved Pipes

To better understand the global resulting flow in the target delivery pipe, a first study, which is restricted to the modeling of laminar flow through standard bends, without magnetic field or energy deposition is carried out.

The motion of a fluid particle in a pipe segment, assuming isothermal conditions, is governed by the conservation of mass and momentum of the flow. The cylindrical polar coordinate system (r, θ, z) is used for the baseline straight pipe of circular cross-section, where r is the radial distance, θ is the azimuthal angle, and z is the axial coordinate direction. The vector (u,v,w), in dimensional form, denotes the components of the instantaneous velocity in the r, θ, and z coordinate directions, respectively. Steady state and incompressible flow conditions are assumed. The non-dimensional continuity equation in the straight pipe can be written as

$$L_c(u^*, v^*, w^*) = 0, \tag{2.1}$$

where (u^*, v^*, w^*) are the non-dimensional components of the instantaneous velocity.

The non-dimensional momentum equations in the normalized r^*, θ^*, and z^* coordinate directions of the straight circular pipe can be written as

$$L_{M_i}(u^*, v^*, w^*) = 0, \tag{2.2}$$

where $i = 1$, 2, and 3 refer to the r^*, θ^*, and z^* components, respectively. Thus, [84]

$$L_c(u^*, v^*, w^*) \equiv \frac{\partial u^*}{\partial r^*} + \frac{u^*}{r^*} + \frac{1}{r^*}\frac{\partial v^*}{\partial \theta^*} + \frac{\partial w^*}{\partial z^*}, \tag{2.3}$$

$$\begin{aligned} L_{M_1}(u^*, v^*, w^*) \equiv \frac{\partial u^*}{\partial t^*} + u^*\frac{\partial u^*}{\partial r^*} + \frac{v^*}{r^*}\frac{\partial u^*}{\partial \theta^*} + w^*\frac{\partial u^*}{\partial z^*} - \frac{v^{*2}}{r^*} + \frac{\partial p^*}{\partial r^*} \\ -\frac{1}{Re}(\nabla^{*2}u^* - \frac{u^*}{r^{*2}} - \frac{2}{r^{*2}}\frac{\partial v^*}{\partial \theta^*}), \end{aligned} \tag{2.4}$$

$$\begin{aligned} L_{M_2}(u^*, v^*, w^*) \equiv \frac{\partial v^*}{\partial t^*} + u^*\frac{\partial v^*}{\partial r^*} + \frac{v^*}{r^*}\frac{\partial v^*}{\partial \theta^*} + w^*\frac{\partial v^*}{\partial z^*} + \frac{u^*v^*}{r^*} + \frac{1}{r^*}\frac{\partial p^*}{\partial \theta^*} \\ -\frac{1}{Re}(\nabla^{*2}v^* + \frac{2}{r^{*2}}\frac{\partial u^*}{\partial \theta^*} - \frac{v^*}{r^{*2}}), \end{aligned} \tag{2.5}$$

$$L_{M_3}(u^*, v^*, w^*) \equiv \frac{\partial w^*}{\partial t^*} + u^*\frac{\partial w^*}{\partial r^*} + \frac{v^*}{r^*}\frac{\partial w^*}{\partial \theta^*} + w^*\frac{\partial w^*}{\partial z^*} + \frac{\partial p^*}{\partial z^*} - \frac{1}{Re}\nabla^{*2}w^*. \tag{2.6}$$

The scales for dimensionalization are as follows:

$$\begin{aligned} u^* = u/U_b, v^* = v/U_b, w^* = w/U_b, r^* = r/2a, z^* = z/2a, \\ p^* = p/\rho U_b^2, Re \equiv \frac{2aU_b\rho}{\mu}, \end{aligned} \tag{2.7}$$

where p is the reduced pressure, ρ is the mass density of fluid, a is the radius of the circular pipe, and U_b is the bulk velocity:

$$U_b = \frac{\int u(r,\theta) r dr d\theta}{\int r dr d\theta}, \tag{2.8}$$

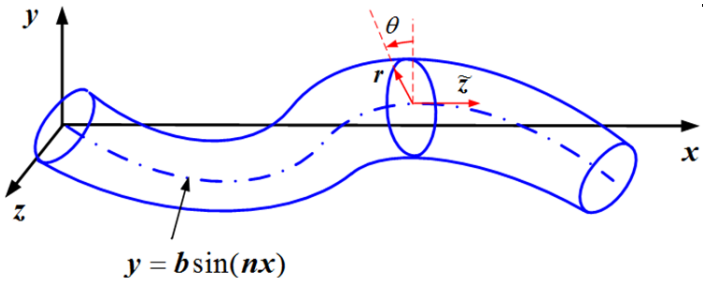

Figure 2.1: Curvilinear coordinates for the periodically-curved pipe $y = b\sin(nx)$

where $u(r, \theta)$ is the instantaneous axial velocity component.

The Laplacian operator, ∇^{*2}, is

$$\nabla^{*2} \equiv \frac{1}{r^*}\frac{\partial}{\partial r^*}(r^*\frac{\partial}{\partial r^*}) + \frac{1}{r^{*2}}\frac{\partial^2}{\partial \theta^{*2}} + \frac{\partial^2}{\partial z^{*2}}. \tag{2.9}$$

The motion of a fluid in a curved pipe whose center-line varies locally in a two-dimensional plane will be described in the curvilinear coordinates $(r, \theta, \tilde{z})$, as shown in Fig. 2.1.

The coordinates r and θ are the same as those defined for a straight pipe, while $\tilde{z}$ is a coordinate direction which is positive along the flow direction and is locally tangential to the pipe center-line. The coordinates $(r, \theta, \tilde{z})$ are a right-handed system and are always mutually orthogonal when the pipe center-line is a two-dimensional curve [85]. The vector (u,v,w) represents the instantaneous velocity components in the r, θ, and $\tilde{z}$ coordinate directions, respectively.

Murata [85] has analyzed the steady laminar motion of a fluid through pipes of circular cross-section, assuming small center-line curvature. We will use his model as the starting point for identifying the sources of secondary flows and compare the velocity distributions associated with such sources to one obtained from a CFD analysis of the same physical problem. For this purpose, we consider a pipe profile of the form $y = b\sin(nx)$ (Figure 2.1), where $b = 0.1, \cdots, 1, 2, 3, \cdots$ and $n = 0.05, 0.1, \cdots, 1, \cdots$. We illustrate with the results for $b = 3.0$ and $n = 0.1$. The results will be examined at the arbitrary point $x = 60$, where the

flow is already fully-developed. The following relations are defined:

$$x = \widetilde{z} - \frac{nbr\cos\theta}{L}\cos(nx), y = b\sin(nx) + \frac{r\cos\theta}{L}, z = r\sin\theta,$$
$$\Gamma^1_{33} = -L\kappa_c\sqrt{g_{33}}\cos\theta, \Gamma^2_{33} = \frac{L}{r}\kappa_c\sqrt{g_{33}}\sin\theta, \Gamma^3_{13} = \Gamma^3_{31} = \frac{L}{\sqrt{g_{33}}}\kappa_c\cos\theta,$$
$$\Gamma^3_{23} = \Gamma^3_{32} = -\frac{L}{\sqrt{g_{33}}}\kappa_c r\sin\theta, \Gamma^3_{33} = \frac{1}{\sqrt{g_{33}}}\frac{\partial}{\partial\widetilde{z}}\sqrt{g_{33}}, \tag{2.10}$$

where

$$L = [1 + n^2b^2\cos^2(nx)]^{1/2}, \tag{2.11}$$
$$\sqrt{g_{33}} = L(1 + r\kappa_c\cos\theta), \tag{2.12}$$
$$\kappa_c = \frac{n^2b\sin(nx)}{L^3}. \tag{2.13}$$

Compared to Eqn. (2.3) through (2.6), the additional terms can be non-dimensionalized using the following scales:

$$g^*_{33} = g_{33},\ \Gamma^{1*}_{33} = a\Gamma^1_{33}, \Gamma^{2*}_{33} = \Gamma^2_{33}a^2,\ \Gamma^{3*}_{13} = a\Gamma^3_{13},\ \Gamma^{3*}_{31} = a\Gamma^3_{31},\ \Gamma^{3*}_{23} = \Gamma^3_{23},$$
$$\Gamma^{3*}_{32} = \Gamma^3_{32},\ \Gamma^{3*}_{33} = a\Gamma^3_{33}. \tag{2.14}$$

The non-dimensional continuity and momentum equations can then be written as follows:

Continuity:

$$\widetilde{L}_c(u^*, v^*, w^*) = 0, \tag{2.15}$$

where

$$\widetilde{L}_c(u^*, v^*, w^*) = \frac{1}{r^*}\frac{\partial(r^*u^*)}{\partial r^*} + \frac{1}{r^*}\frac{\partial v^*}{\partial\theta} + \frac{1}{\sqrt{g_{33}}}\frac{\partial w^*}{\partial\widetilde{z}^*} + \Gamma^{3^*}_{31}u^* + \Gamma^{3^*}_{32}\frac{v^*}{r^*}. \tag{2.16}$$

Momentum:

$$\widetilde{L}_{M_i}(u^*, v^*, w^*) = 0, \tag{2.17}$$

where

$$\begin{aligned}
\widetilde{L}_{M_1}(u,v,w) &= u^*\frac{\partial u^*}{\partial r^*}+\frac{v^*}{r^*}\frac{\partial u^*}{\partial \theta^*}-\frac{v^{*2}}{r^*}+\frac{w^*}{\sqrt{g_{33}}}\frac{\partial u^*}{\partial \widetilde{z}^*}+\Gamma_{33}^{1*}\frac{w^{*2}}{g_{33}}+\frac{\partial p^*}{\partial r^*}\\
&-\frac{1}{Re}[\frac{\partial^2 u^*}{\partial r^{*2}}+\frac{1}{r^*}\frac{\partial u^*}{\partial r^*}-\frac{u^*}{r^{*2}}+\frac{1}{r^{*2}}\frac{\partial^2 u^*}{\partial \theta^{*2}}+\frac{1}{g_{33}}\frac{\partial^2 u^*}{\partial \widetilde{z}^{*2}}\\
&-\frac{2}{r^{*2}}\frac{\partial v^*}{\partial \theta^*}+\frac{\Gamma_{33}^{1^*}}{g_{33}}(\Gamma_{13}^{3*}u^*+\Gamma_{23}^{3*}\frac{v^*}{r^*}-\frac{\partial u^*}{\partial r^*})+\frac{\Gamma_{33}^{2*}}{g_{33}}(v^*-\frac{\partial u^*}{\partial \theta^*})\\
&+\frac{\Gamma_{33}^{3*}}{g_{33}}\frac{\partial u^*}{\partial \widetilde{z}^*}+\frac{1}{g_{33}}\{\frac{w^*}{\sqrt{g_{33}}}\frac{\partial}{\partial \widetilde{z}^*}(\Gamma_{33}^{1*})+2\Gamma_{33}^{1*}\frac{\partial}{\partial \widetilde{z}^*}(\frac{w^*}{\sqrt{g_{33}}})\}], \qquad (2.18)
\end{aligned}$$

$$\begin{aligned}
\widetilde{L}_{M_2}(u^*,v^*,w^*) &= u^*\frac{\partial v^*}{\partial r^*}+\frac{v^*}{r^*}\frac{\partial v^*}{\partial \theta^*}+\frac{u^*v^*}{r^*}+\frac{w^*}{\sqrt{g_{33}}}\frac{\partial v^*}{\partial \widetilde{z}^*}+\Gamma_{33}^{2*}\frac{r^*w^{*2}}{g_{33}}\\
&+\frac{1}{r^*}\frac{\partial p^*}{\partial \theta^*}-\frac{1}{Re}[\frac{\partial^2 v^*}{\partial r^{*2}}+\frac{1}{r^*}\frac{\partial v^*}{\partial r^*}-\frac{v^*}{r^{*2}}+\frac{1}{r^{*2}}\frac{\partial^2 v^*}{\partial \theta^{*2}}\\
&+\frac{1}{g_{33}}\frac{\partial^2 v^*}{\partial \widetilde{z}^{*2}}+\frac{2}{r^{*2}}\frac{\partial u^*}{\partial \theta^*}+\frac{\Gamma_{33}^{2*}}{g_{33}}(\Gamma_{13}^{3*}r^*u^*-u^*+\Gamma_{23}^{3*}v^*-\frac{\partial v^*}{\partial \theta^*})\\
&-\frac{\Gamma_{33}^{1*}}{g_{33}}\frac{\partial v^*}{\partial r^*}-\frac{\Gamma_{33}^{3*}}{g_{33}}\frac{\partial v^*}{\partial \widetilde{z}^*}+\frac{r^*}{g_{33}}\{\frac{w^*}{\sqrt{g_{33}}}\frac{\partial}{\partial \widetilde{z}^*}(\Gamma_{33}^{2*})\\
&+2\Gamma_{33}^{2*}\frac{\partial}{\partial \widetilde{z}^*}(\frac{w^*}{\sqrt{g_{33}}})\}], \qquad (2.19)
\end{aligned}$$

$$\begin{aligned}
\widetilde{L}_{M_3}(u^*,v^*,w^*) &= u^*\frac{\partial}{\partial r^*}(\frac{w^*}{\sqrt{g_{33}}})+\frac{v^*}{r^*}\frac{\partial}{\partial \theta^*}(\frac{w^*}{\sqrt{g_{33}}})+\frac{w^*}{g_{33}}\frac{\partial w^*}{\partial \widetilde{z}^*}\\
&+\frac{2w^*}{\sqrt{g_{33}}}(\Gamma_{31}^{3*}u^*+\Gamma_{32}^{3*}\frac{v^*}{r^*})+\frac{1}{g_{33}}\frac{\partial p^*}{\partial \widetilde{z}^*}\\
&-\frac{1}{Re}[\frac{\partial^2}{\partial r^{*2}}(\frac{w^*}{\sqrt{g_{33}}})+\frac{1}{r^*}\frac{\partial}{\partial r^*}(\frac{w^*}{\sqrt{g_{33}}})+\frac{1}{r^{*2}}\frac{\partial^2}{\partial \theta^2}(\frac{w^*}{\sqrt{g_{33}}})\\
&+\frac{1}{g_{33}}\frac{\partial}{\partial \widetilde{z}^*}(\frac{1}{\sqrt{g_{33}}}\frac{\partial w^*}{\partial \widetilde{z}^*})+\frac{1}{g_{33}}\{u^*\frac{\partial}{\partial \widetilde{z}^*}(\Gamma_{13}^{3*})+\frac{v^*}{r^*}\frac{\partial}{\partial \widetilde{z}^*}(\Gamma_{23}^{3*})\}\\
&+\frac{w^*}{\sqrt{g_{33}}}\{\frac{\partial}{\partial r^*}(\Gamma_{13}^{3*})+\frac{1}{r^{*2}}\frac{\partial}{\partial \theta}(\Gamma_{23}^{3*})\}\\
&+\Gamma_{13}^{3*}\{\frac{2}{g_{33}}\frac{\partial u^*}{\partial \widetilde{z}^*}+2\frac{\partial}{\partial r^*}(\frac{w^*}{\sqrt{g_{33}}})+\frac{1}{r^*}\frac{w^*}{\sqrt{g_{33}}}\}\\
&+\frac{2\Gamma_{23}^{3*}}{r^{*2}}\{\frac{r^*}{g_{33}}\frac{\partial v^*}{\partial \widetilde{z}^*}+\frac{\partial}{\partial \theta^*}(\frac{w^*}{\sqrt{g_{33}}})\}+\frac{w^*}{\sqrt{g_{33}}}\{(\Gamma_{13}^{3*})^2+(\frac{\Gamma_{32}^{3*}}{r^*})^2\}
\end{aligned}$$

$$-\frac{1}{g_{33}}\{\Gamma_{33}^{1*}\frac{\partial}{\partial r^*}(\frac{w^*}{\sqrt{g_{33}}})+\Gamma_{33}^{2*}\frac{\partial}{\partial \theta^*}(\frac{w^*}{\sqrt{g_{33}}})\}]. \tag{2.20}$$

2.2 Governing Equations for Turbulent Flow

2.2.1 Continuity and Momentum Equations

As stated earlier, the mean flow $(\mathbf{U}^*, P^*)$ is calculated with RANS, where the mean flow is related to the instantaneous $(\mathbf{u}^*, p^*)$ and fluctuating $(\mathbf{u}')^*, (p')^*)$ components as follows:

$$\mathbf{u}^* = \mathbf{U}^* + (\mathbf{u}')^* \tag{2.21}$$

$$p^* = P^* + (p')^*. \tag{2.22}$$

The governing equations for the mean flow can be expressed in terms of mass conservation (continuity):

$$\frac{\partial \mathbf{U}^*}{\partial t} + \nabla^* \cdot \mathbf{U}^* = 0, \tag{2.23}$$

and the momentum conservation:

$$\frac{\partial \mathbf{U}^*}{\partial t} + \mathbf{U}^* \cdot \nabla^* \mathbf{U}^* = -\frac{1}{\rho^*}\nabla^* P^* + \frac{1}{Re}\nabla^* \cdot \tau^* + \mathbf{F}. \tag{2.24}$$

The internal mercury pipe flow is assumed to be steady state without the gravity force. Thus, the continuity and momentum equations can be simplified to be

$$\nabla^* \cdot \mathbf{U}^* = 0, \tag{2.25}$$

and,

$$\mathbf{U}^* \cdot \nabla^* \mathbf{U}^* = -\frac{1}{\rho^*}\nabla^* P^* + \frac{1}{Re}\nabla^* \cdot \tau^*. \tag{2.26}$$

The shear stress tensor, τ^*, is modeled as

$$\tau_{ij}^* = (\mu^* + \mu_t^*)(\frac{\partial U_i^*}{\partial x_j^*} + \frac{\partial U_j^*}{\partial x_i^*}) \tag{2.27}$$

and the eddy viscosity is computed from

$$\mu_t^* = \rho^* C_\mu \frac{k^{*2}}{\varepsilon^*}, \tag{2.28}$$

where k^* is the kinetic energy of turbulence, $k^* \equiv \frac{1}{2}(\overline{(u')^*}^2 + \overline{(v')^*}^2 + \overline{(w')^*}^2)$, and ε^* is its dissipation rate. C_μ is modeled as [89]

$$C_\mu = \frac{1}{A_0 + A_s \frac{k^* U^{(*)}}{\varepsilon^*}}, \tag{2.29}$$

where

$$U^{(*)} \equiv \sqrt{S_{ij}^* S_{ij}^* + \overline{\Omega}_{ij}^* \overline{\Omega}_{ij}^*}, \tag{2.30}$$

$$S_{ij}^* = \frac{1}{2}(U_{i,j}^* + U_{j,i}^*), \tag{2.31}$$

$$\overline{\Omega}_{ij}^* = \frac{1}{2}(U_{i,j}^* - U_{j,i}^*). \tag{2.32}$$

S_{ij}^* is the symmetric part of the rate-of-strain (deformation) tensor, with $\overline{\Omega}_{ij}^*$ the antisymmetric part.

The model constants A_0 and A_s are given as [89]

$$A_0 = 4.04, A_s = \sqrt{6}\cos\phi, \tag{2.33}$$

where

$$\phi = \frac{1}{3}\cos^{-1}(\sqrt{6}W), W = \frac{S_{ij}^* S_{jk}^* S_{ki}^*}{\widetilde{S}^{*3}}, \widetilde{S}^* = \sqrt{S_{ij}^* S_{ij}^*}. \tag{2.34}$$

2.2.2 Realizable $k-\varepsilon$ model

A Reynolds-averaged Navier-Stokes (RANS) equation approach will suffice for the current problem in which the fluid is bounded by a circular, no-slip wall, and the interest is mainly on the mean flow. The Reynolds stress model (RSM) [86] has been judged to be the most accurate RANS model for turbulent flow in curved pipes, as it includes memory effects and the effects of streamline curvature. However, RSM is a six-equation model that is computationally expensive for practical engineering problems. Several options exist for the simpler one- or two-equation RANS approaches, including the Spalart-Allmaras (SA) [87], Standard $k-\varepsilon$ (SKE) [88], and Realizable $k-\varepsilon$ (RKE) [89] models. In this work, the RKE model is selected for the simulation of the curved-pipe internal flow problem.

The $k-\varepsilon$ turbulent model is a useful engineering approach for predicting the mean velocity profiles of turbulent flows. In general, the stand $k-\varepsilon$ model qualitatively predicts most turbulent flows, while it fails to give consistent prediction for the plane jet and round jet problems [90, 91]. The RKE model is also used for the turbulent jet flow simulation.

The non-dimensional equations for RKE model can be written as [89]

$$\frac{\partial k^*}{\partial t} + \mathbf{U}^* \cdot \nabla^* k^* = \nabla^* \cdot [(\frac{1}{Re} + \frac{1}{\sigma_k Re_t})\nabla^* k^*] + G_t^* - \varepsilon^*, \tag{2.35}$$

$$\frac{\partial \varepsilon^*}{\partial t} + \mathbf{U}^* \cdot \nabla^* \varepsilon^* = \nabla^* \cdot [(\frac{1}{Re} + \frac{1}{\sigma_\varepsilon Re_t})\nabla^* \varepsilon^*] + C_1 \overline{S}^* \varepsilon^* - C_2 \frac{1}{a} \frac{\varepsilon^{*2}}{k^* + \sqrt{\nu^* \varepsilon^*}}, \tag{2.36}$$

where σ_k and σ_ε are the turbulent Prandtl numbers for k and ε, respectively. Re_t is the Reynolds number based on the eddy viscosity (Eqn. (2.28)).

The production of turbulence kinetic energy, G_t^*, is evaluated in a manner consistent with the Boussinesq hypothesis:

$$G_t^* = (2\frac{1}{Re_t}\overline{S}_{ij}^* - \frac{2}{3}k^* \delta_{ij}) U_{i,j}^*. \tag{2.37}$$

The constants for the RKE model are

$$\sigma_k = 1.0, \sigma_\varepsilon = 1.2, C_1 = \max[0.43, \frac{\Gamma}{\Gamma + 5}], C_2 = 1.9, \tag{2.38}$$

where

$$\Gamma = \overline{S}\frac{k}{\varepsilon}, \overline{S} = \sqrt{2\overline{S}_{ij}\overline{S}_{ij}}. \tag{2.39}$$

2.2.3 Boundary Conditions

The inlet velocity for all pipes is that of a fully developed flow for a straight pipe aligned with the x-direction:

$$U^* = V^* = 0, W^* = W^*(r^*). \tag{2.40}$$

The discrete form of $W^*(r^*)$ is taken as the solution at the exit of a straight pipe obtained from an auxiliary simulation, with the axial velocity profile shown in Fig. 2.2. At the inlet, the mean pressure is $P = 30$ bar (or $P^* = 30$), while the turbulence conditions are

$$k^* = \frac{3}{2}(U^* I)^2, \varepsilon^* = \frac{C_\mu^{3/4} k^{*3/2}}{l^*}, \tag{2.41}$$

where I is the turbulence intensity, $I = 0.16 Re^{-1/8}$. The values of C_μ and l^* are:

$$C_\mu = 0.09, l^* = 0.07 D_h^*, \tag{2.42}$$

and $D_h^* = 2$. No-slip conditions are specified at the wall,

$$U^* = V^* = W^* = 0, \tag{2.43}$$

while zero-gradient conditions are assumed at the pipe exit:

$$\nabla_n^* U^* = \nabla_n^* V^* = \nabla_n^* W^* = \nabla_n^* P^* = \cdots = 0, \tag{2.44}$$

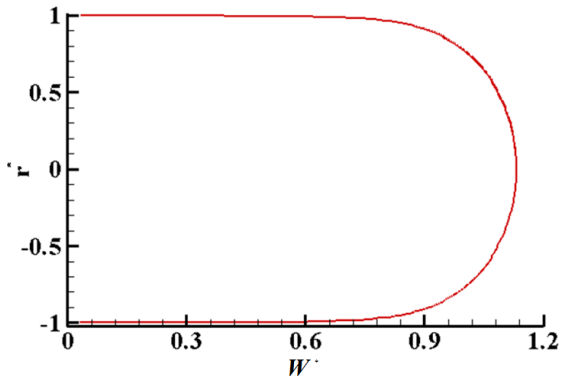

Figure 2.2: Fully developed normalized velocity profile $W^*(r^*)$ at pipe inlet

where $\nabla_n^* \equiv \partial^*/\partial n^*$ and "n^*" is the outward-pointing normal at the outlet.

2.3 The Level Set Method

In the level set (LS) [57, 60, 92, 93, 94], the level set function, ϕ, is used to represent and propagate the free surface. The interface, where the points have the ϕ value of 0, divides the liquid region ($\phi > 0$) from the gas region ($\phi < 0$). The interface is transported by the level set equation:

$$\phi_t + \mathbf{u} \cdot \nabla\phi = 0. \tag{2.45}$$

Note that the dimensional form of the equations are presented and used for the description of the two-phase problem.

2.3.1 Reynolds-Averaged Level Set Equation

In an incompressible flow, $\nabla \cdot \mathbf{u} = 0$, and the LS equation is mathematically equivalent to the conservation law:

$$\phi_t + \nabla \cdot (\mathbf{u}\phi) = 0. \tag{2.46}$$

In a turbulent flow field, ϕ and $\mathbf{u}$ may be decomposed into mean and fluctuating compo-

nents:

$$\phi = \Phi + \phi', \tag{2.47}$$

$$\mathbf{u} = \mathbf{U} + \mathbf{u}'. \tag{2.48}$$

Applying Reynolds-averaging to the instantaneous Φ equation yields

$$\overline{\phi}_t + \nabla \cdot (\mathbf{U}\overline{\phi} + \overline{\mathbf{u}'\phi'}) = 0. \tag{2.49}$$

The scalar flux term is modeled via the gradient-flux approximation [96]:

$$-\overline{\mathbf{u}'\phi'} = D_T \nabla \overline{\phi}, \tag{2.50}$$

where the turbulent diffusivity is

$$D_T = c_1 \overline{k}^2/\varepsilon \tag{2.51}$$

and c_1 is a constant. Nilsson and Bai used $c_1 = 0.129$ [97], a value that will also be used in this thesis. Thus, the averaged equation, omitting the averaging symbols, can be written as

$$\phi_t + \nabla \cdot (\mathbf{U}\phi - D_T \nabla \phi) = 0. \tag{2.52}$$

In the LS method, the density and the dynamic viscosity are described as

$$\rho(\mathbf{x},t) = \rho_l[1 - H_\epsilon(\phi(\mathbf{x},t))] + \rho_g H_\epsilon(\phi(\mathbf{x},t)), \mu(\mathbf{x},t) = \mu_l[1 - H_\epsilon(\phi(\mathbf{x},t))] + \mu_g H_\epsilon(\phi(\mathbf{x},t)), \tag{2.53}$$

where the subscripts l and g denote liquid and gas phase, respectively[98]. H_ϵ is the smoothed

Heaviside function[58]

$$H_\epsilon(\phi) = \begin{cases} 0 & if\ \phi < -\epsilon, \\ (\phi + \epsilon)/2\epsilon + \sin(\pi\phi/\epsilon)/2\pi & if\ |\phi| < \epsilon, \\ 1 & if\ \phi > \epsilon, \end{cases} \tag{2.54}$$

where ϵ is a parameter whose value ranges from one to two times the local mesh size close to the interface. Physically, ϵ represents half of the interface thickness.

2.3.2 Re-initialization Equation

In order to make ϕ the signed normal distance and interface as the zero level set function, a re-initialization equation is required [58]:

$$\phi_\tau + S(\phi^0)(|\nabla\phi| - 1) = 0, \tag{2.55}$$

where ϕ^0 is the initial condition of ϕ and S is the sign function, which can be defined as

$$S(\phi_0) = \frac{\phi_0}{\sqrt{\phi_0^2 + \delta_\epsilon}}, \tag{2.56}$$

where the parameter, $\delta_\epsilon = 10^{-16}$, which is introduced in order to avoid division by zero.

Equation (2.55) is written in the form

$$\phi_\tau + \mathbf{w} \cdot \nabla\phi = S(\phi^0), \tag{2.57}$$

for the purpose of spatial discretization, where $\mathbf{w}$ is the unit velocity vector pointing away from the interface $\phi^0 = 0$. ϕ^0 is the initial condition for Eqn. (2.57) and

$$\mathbf{w} = S(\phi_0)\frac{\nabla\phi}{|\nabla\phi|}, \tag{2.58}$$

2.4 The Volume of Fluid Method

The volume of fluid (VOF) method uses the volume fraction of one of the fluids within each cell to determine the interface. The volume fraction is one if the cell is filled with the liquid phase, zero if the cell is filled with the gas phase, and between zero and one in cells containing an interface. The liquid volume fraction, F, is advected with the velocity field:

$$\frac{\partial F}{\partial t} + \mathbf{u} \cdot \nabla F = 0. \tag{2.59}$$

Given the fixed grid, the velocity field $\mathbf{u}$, and the field F at the previous time step, the liquid volume fraction field F can be updated. The 2D interface is considered to be a continuous, piecewise smooth curve. In order to reconstruct the interface, first we need to determine which cells contain the interface, and then decide the location in these cell by considering the volume fraction, F, in the cells bounding the interface. The simplest reconstruction method for the interface is the Simple Line Interface Calculation (SLIC) [100], which is first-order accurate. More accurate VOF techniques attempt to fit the interface through piecewise linear segments, like the Piecewise Linear Interface Calculation (PLIC) [63] method. Figure 2.3 (a) shows the exact value of the volume of fraction for a smooth circular arc over a square grid. An interface that has been reconstructed using SLIC method is shown in Fig. 2.3(b), while the one reconstructed by the PLIC method is given in Fig. 2.3(c).

In the VOF method, the density and the dynamic viscosity are approximated by the following formulas:

$$\rho(x,t) = \rho_l F + \rho_g(1-F), \mu(x,t) = \mu_l F + (\mu_g(1-F), \tag{2.60}$$

where l and g denote "liquid" and "gas" phases, respectively, and F is the liquid volume fraction.

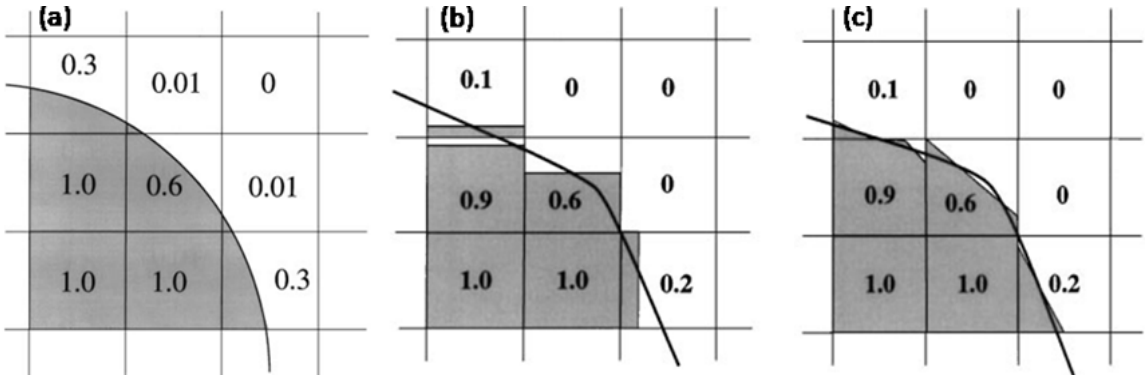

Figure 2.3: (a) The exact interface for a circular arc over a square grid; Interface reconstructed by the scheme of: (b) Simple Line Interface Calculation (SLIC) (c) Piecewise Linear Interface Calculation (PLIC)

2.5 Coupling Level Set and Volume of Fluid

The LS method tends to lose/gain mass [79]. The VOF method encounters numerical difficulties at the interface and it is difficult to calculate the interface curvature. CLSVOF method overcomes these problems by mitigating the disadvantages of these two methods.

To couple the VOF method and the LS method, the volume fraction F, in a given cell of the domain, at time t, is defined as a function of the level set ϕ[64]:

$$F(\Omega, t) = \frac{1}{|\Omega|} \int_{\Omega} H_{\epsilon}(\phi(x, y, t)) dxdy, \tag{2.61}$$

where H_{ϵ} is the smoothed Heaviside function defined in Eqn. (2.54) and $dxdy$ is the element area.

When the present project was started, FLUENT did not support the CLSVOF method, only implementing the VOF method. Therefore we only needed to solve the LS method and couple it to the VOF method inside FLUENT. In Nichita's Ph.D. thesis [49] , a detailed algorithm for his CLSVOF method through FLUENT is presented (Fig. 2.4), which is also used in this thesis.

However, Nichita's code was implemented only for structured (Cartesian) grids and for laminar flows. Based on Nichita's CLSVOF algorithm, this work develops a CLSVOF mod-

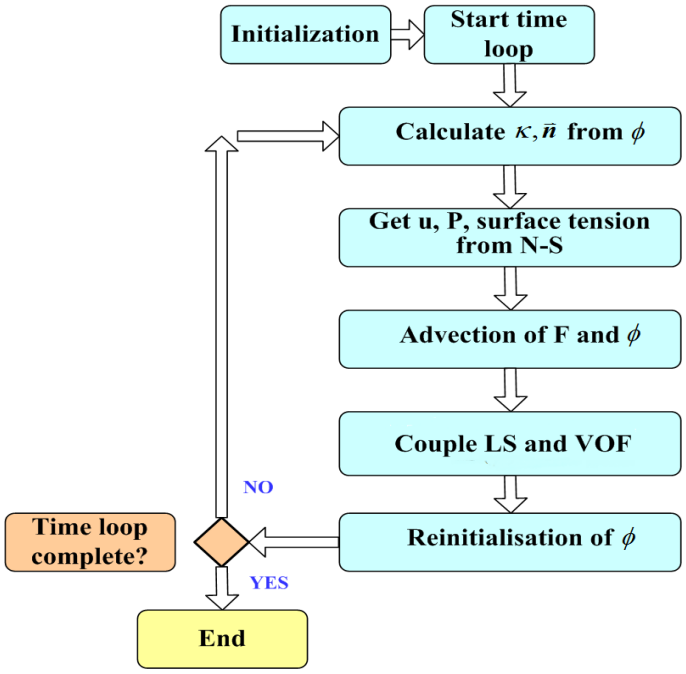

Figure 2.4: Algorithm of CLSVOF method used in this thesis

ule that is applicable to unstructured meshes, by solving the level set and re-initialization equations in a transformed coordinate system.

2.6 The Continuum Surface Model

For multiphase flow, the surface tension force is considered in the momentum equations. The CSF (Continuum Surface Force) model of Brackbill *et al.* [67], is used to approximate the surface tension force:

$$\mathbf{F}_{st} = \sigma\kappa(\phi)\mathbf{n}\delta_\epsilon(\phi), \tag{2.62}$$

where σ is the surface tension coefficient. For mercury-air, its value is 0.4855 N/m at room temperature. $\delta_\epsilon(\phi)$ is the smoothed delta function, which is defined as the derivative of the smoothed Heaviside function, $H_\epsilon(\phi)$, with respect to ϕ:

$$\delta_\epsilon(\phi) = \begin{cases} 0 & if \ \ |\phi| > \epsilon, \\ 1/2\epsilon + \cos(\pi\phi/\epsilon)/2\epsilon & if \ \ |\phi| < \epsilon. \end{cases} \tag{2.63}$$

κ is the mean curvature of the interface, and $\mathbf{n}$ is the normal vector of the interface. In the LS method, they are defined as

$$\mathbf{n} = \frac{\nabla\phi}{|\nabla\phi|}, \quad \kappa = \nabla \cdot \frac{\nabla\phi}{|\nabla\phi|}. \tag{2.64}$$

Chapter 3

Numerical Procedure

3.1 Discretization of The Continuity Equation

Control-volume-based technique is used in the commercial FLUENT code, which requires integrating the governing equations about each control volume. Eqn. (2.23) is a non-dimensional continuity equation in differential equation form. The integral form of a dimensional continuity equation for an arbitrary control volume Ω assuming incompressible flow can be written as

$$\frac{\partial}{\partial t}\int_{\Omega}\mathbf{U}d\Omega + \int_{S}(\mathbf{U}\cdot\mathbf{n}_S)dS = 0, \tag{3.1}$$

where $\mathbf{n}_S$ is the local, outward-pointing unit normal to the S.

Equation (3.1) can be discretized on a given control volume in the computational domain to yield the discretized equation

$$\frac{\partial \mathbf{U}}{\partial t}\triangle V + \sum_{f}^{N_{faces}}\mathbf{U}_f\mathbf{A}_f = 0 \tag{3.2}$$

where N_{faces} is the number of faces enclosing the control volume, U_f is the velocity normal to the face f, and A_f is the area of face f.

3.1.1 Temporal Discretization

The first-order explicit discretization is used for temporal term:

$$\frac{\mathbf{U}^{n+1} - \mathbf{U}^{n}}{\Delta t}\Delta V = \Gamma(\mathbf{U}^{n}), \tag{3.3}$$

where Γ incorporates any spatial discretization.

3.1.2 Spatial Discretization

The spatial discretization in Eq. (3.2) in the integral form is

$$\Gamma(\mathbf{U}) = \int_{S}(\mathbf{U}\cdot\mathbf{n}_{S})dS. \tag{3.4}$$

And its discretized form can be written as

$$\Gamma(\mathbf{U}) = -\sum_{f}^{N_{faces}}\mathbf{U}_{f}\mathbf{A}_{f}. \tag{3.5}$$

The FLUENT saves all fluid information at the cell centers. Taking the 2D control volume shown in Fig. 3.1 (uniform Δx and Δy) as an example, the discretized form of the continuity equation is

$$\Gamma(\mathbf{U}) = -(U_{i+1/2,j} - U_{i-1/2,j}) \triangle y - (V_{i,j+1/2} - V_{i,j-1/2}) \triangle x, \tag{3.6}$$

where $U_{i+1/2,j}, U_{i-1/2,j}, V_{i,j+1/2}$, and $V_{i,j-1/2}$ are the velocities on the faces surrounding the control volume (i, j).

The values of the velocities at the cell surfaces $(U_{i+1/2,j}, U_{i-1/2,j}, V_{i,j+1/2}, V_{i,j-1/2})$, can be calculated from the values of velocity at the cell centers. Linear interpolation of cell-centered velocities to the face results in unphysical checker-boarding of pressure [68]. Instead, a procedure similar to that by Rhie and Chow [69] is used to prevent checkerboarding. The

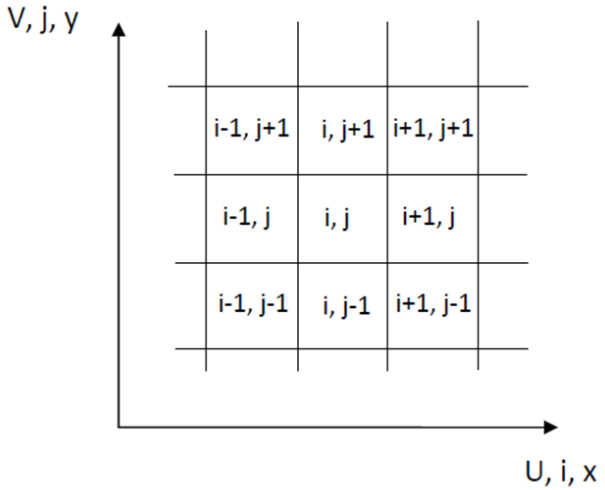

Figure 3.1: Two dimensional control volume for continuity equation

values of the velocities at the cell surfaces are momentum-weighted averages instead of linear averages:

$$\begin{aligned} U_f &= \frac{U_{c_0}/a_{p,c_0} + U_{c_1}/a_{p,c1}}{1/a_{p,c_0} + 1/a_{p,c1}} + \frac{d_f}{\rho_f}[(P_{c_0} + (\nabla P)_{c_0} \cdot \mathbf{r}_0) - (P_{c_1} + (\nabla P)_{c_1} \cdot \mathbf{r}_1)] \\ &= \widehat{J}_f + \frac{d_f}{\rho_f}(P_{c_0} - P_{c_1}), \end{aligned} \tag{3.7}$$

where U_{c_0}, U_{c1} and P_{c_0}, P_{c_1} are the normal velocities and pressures within the two cells on either side of the face f , a_{p,c_0} and $a_{p,c1}$ are the under-relaxation factors for velocity. The under-relaxation factors are used in the pressure-based solver in FLUENT to stabilize the convergence behavior of the outer nonlinear iterations [68]. $\widehat{J}_f$ contains the influence of velocities in these cells. The term d_f is a function of $\overline{a}_P$, the average of the momentum equation coefficients a_P for the cells on either side of face f [68]. ρ_f is value of density at the cell surfaces.

This procedure works well as long as the velocity variation between cell centers is smooth. However, when there are jumps or large gradients of velocity, the face velocities cannot be interpolated using this momentum-weighted averaging [68]. Instead, other alternate interpolation methods should be used:

(1) The linear scheme computes the face velocities as the average of the cell-center velocities of the adjacent cells:

$$U_f = \frac{U_{c_0} + U_{c_1}}{2}. \tag{3.8}$$

(2) The second-order upwind scheme:

$$U_f = U + \nabla U \cdot \mathbf{r}, \tag{3.9}$$

where U and ∇U are the cell-centered value and its gradient in the upstream cell, and $\mathbf{r}$ is the displacement vector from the upstream cell centroid to the face centroid. The determination of ∇U is required in this scheme, which can be computed by Green-Gauss cell-based method or least-squares cell-based method. When a polyhedral mesh is used, the cell-based least square gradients are recommended for use over the Green-Gauss cell-based method. The details of the evaluation of gradients can also be found in the FLUENT theory guide [68]. It is illustrated in the FLUENT theory guide that the second-order scheme is not applicable to the VOF model [68].

(3) The central-differencing scheme

The central-differencing scheme provides improved accuracy for LES (Large Eddy Simulation) calculations [68].

$$U_f = \frac{1}{2}(U_{c_0} + U_{c_1}) + \frac{1}{2}(\nabla U_{c_0} \cdot \mathbf{r}_{c_0} + \nabla U_{c_1} \cdot \mathbf{r}_{c_1}), \tag{3.10}$$

where ∇U_{c_0} and ∇U_{c1} are the normal velocities within the two cells on either side of the face f respectively, and $\mathbf{r}$ is the vector directed from the cell centroid toward the face centroid.

3.2 Discretization of The Momentum Equation

The non-dimensional differential equation form of the momentum equations is given in Eq. (2.24). The dimensional integral form of the momentum equations is

$$\rho[\frac{\partial}{\partial t}\int_{\Omega}\mathbf{U}d\Omega+\int_{S}(\mathbf{U}\mathbf{U}\cdot\mathbf{n}_{S})dS]=-\int_{S}P\mathbf{n}_{S}dS+\int_{S}(\tau\cdot\mathbf{n}_{S})dS+\int_{\Omega}\mathbf{F}d\Omega. \tag{3.11}$$

The discretization of the above equations on a given control volume, or cell yields

$$\rho\frac{\partial\mathbf{U}}{\partial t}\Delta V+\rho\sum_{f}^{N_{faces}}(\mathbf{U}_{f}\mathbf{U}_{f}\cdot\mathbf{A}_{f})=-\sum_{f}^{N_{faces}}P\mathbf{A}_{f}+\sum_{f}^{N_{faces}}\tau\cdot\mathbf{A}_{f}+\mathbf{F}\Delta V, \tag{3.12}$$

where N_{faces} is the number of faces enclosing the control volume, $\mathbf{U}_f$ is the velocity vector normal to the face f, $\mathbf{U}_f\cdot\mathbf{A}_f$ is the volume flux through the face, $\mathbf{A}_f$ is the face area vector, ΔV is the volume of the cell.

3.2.1 Temporal Discretization

The generic expression for the above equation is given by

$$\rho\frac{d}{dt}\int_{\Omega}\mathbf{U}d\Omega=\Gamma(\mathbf{U}), \tag{3.13}$$

where Γ incorporates any spatial discretization. The first-order explicit discretization is

$$\rho\frac{\mathbf{U}^{n+1}-\mathbf{U}^{n}}{\Delta t}\Delta V=\Gamma(\mathbf{U}^{n}). \tag{3.14}$$

3.2.2 Spatial Discretization

The spatial discretization, $\Gamma(\mathbf{U})$, defined as

$$\Gamma(\mathbf{U})=-\int_{S}(\mathbf{U}\mathbf{U}\cdot\mathbf{n}_{S})dS-\int_{S}P\mathbf{n}_{S}dS+\int_{S}(\tau\cdot\mathbf{n}_{S})dS+\int_{\Omega}\mathbf{F}d\Omega \tag{3.15}$$

can be written as

$$\Gamma(\mathbf{U}) = -\rho \sum_{f}^{N_{faces}} (\mathbf{U}_f \mathbf{U}_f \cdot \mathbf{A}_f) - \sum_{f}^{N_{faces}} P\mathbf{A}_f + \sum_{f}^{N_{faces}} \overline{\overline{\tau}} \cdot \mathbf{A}_f + \mathbf{F}\Delta V. \tag{3.16}$$

Applied to the same 2D control volume shown in Fig. 3.1,the corresponding discretizations are as follows:

$$\begin{aligned}
\Gamma(U) &= -(E^{(1)}_{i+1/2,j} - E^{(1)}_{i-1/2,j}) \triangle y - (K^{(1)}_{i,j+1/2} - K^{(1)}_{i,j-1/2}) \triangle x \\
&\quad -(P_{i+1,j} - P_{i,j})\Delta y + F^{(1)}_{i,j}\Delta x \Delta y \qquad (3.17) \\
\Gamma(V) &= -(E^{(2)}_{i+1/2,j} - E^{(2)}_{i-1/2,j}) \triangle y - (K^{(2)}_{i,j+1/2} - K^{(2)}_{i,j-1/2}) \triangle x \\
&\quad -(P_{i,j+1} - P_{i,j})\Delta x + F^{(2)}_{i,j}\Delta x \Delta y, \qquad (3.18)
\end{aligned}$$

where $E^{(1)}$, $E^{(2)}$, $K^{(1)}$, and $K^{(2)}$ are defined as follows

$$\begin{aligned}
E^{(1)} &= \rho U^2 - (\mu + \mu_t)\frac{\partial U}{\partial x}, \qquad (3.19) \\
E^{(2)} &= \rho UV - (\mu + \mu_t)\frac{\partial V}{\partial x}, \qquad (3.20) \\
K^{(1)} &= \rho UV - (\mu + \mu_t)\frac{\partial U}{\partial y}, \qquad (3.21) \\
K^{(2)} &= \rho V^2 - (\mu + \mu_t)\frac{\partial V}{\partial y}. \qquad (3.22)
\end{aligned}$$

Thus

$$\begin{aligned}
E^{(1)}_{i+1/2,j} &= \rho U^2_{i+1/2,j} - (\mu + \mu_t)\left.\frac{\partial U}{\partial x}\right|_{i+1/2,j}, \qquad (3.23) \\
E^{(1)}_{i-1/2,j} &= \rho U^2_{i-1/2,j} - (\mu + \mu_t)\left.\frac{\partial U}{\partial x}\right|_{i-1/2,j}, \qquad (3.24) \\
E^{(2)}_{i+1/2,j} &= \rho (UV)_{i+1/2,j} - (\mu + \mu_t)\left.\frac{\partial V}{\partial x}\right|_{i+1/2,j}, \qquad (3.25) \\
E^{(2)}_{i-1/2,j} &= \rho (UV)_{i-1/2,j} - (\mu + \mu_t)\left.\frac{\partial V}{\partial x}\right|_{i-1/2,j}, \qquad (3.26)
\end{aligned}$$

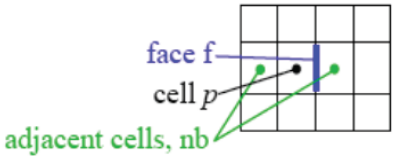

Figure 3.2: Cell p and its adjacent cells nb, neighboring the cell p

$$K^{(1)}_{i,j+1/2} = \rho(UV)_{i,j+1/2} - (\mu+\mu_t)\left.\frac{\partial U}{\partial y}\right|_{i,j+1/2}, \tag{3.27}$$

$$K^{(1)}_{i,j-1/2} = \rho(UV)_{i,j-1/2} - (\mu+\mu_t)\left.\frac{\partial U}{\partial y}\right|_{i,j-1/2}, \tag{3.28}$$

$$K^{(2)}_{i,j+1/2} = \rho V^2{}_{i,j+1/2} - (\mu+\mu_t)\left.\frac{\partial V}{\partial y}\right|_{i,j+1/2}, \tag{3.29}$$

$$K^{(2)}_{i,j-1/2} = \rho V^2{}_{i,j-1/2} - (\mu+\mu_t)\left.\frac{\partial V}{\partial y}\right|_{i,j-1/2}. \tag{3.30}$$

The face velocities and face gradients can be interpolated through the values at the cell centers by the schemes described for the continuity equation. Consequently, Eqns. (3.17) and (3.18) can be written as

$$\Gamma(U) = -a_{i,j}U_{i,j} - \sum_{nb} a_{nb}U_{nb} - \Delta y(P_{i+1,j} - P_{i,j}) - F^1_{i,j}\Delta x\Delta y, \tag{3.31}$$

$$\Gamma(V) = -b_{i,j}V_{i,j} - \sum_{nb} b_{nb}V_{nb} - \Delta x(P_{i,j+1} - P_{i,j}) - F^2_{i,j}\Delta x\Delta y, \tag{3.32}$$

where a, a_{nb} b, and b_{nb} are linearized coefficients for U, U_{nb}, V, and V_{nb} respectively. $\sum_{nb} a_{nb}U_{nb}$ and $\sum_{nb} b_{nb}V_{nb}$ represent all the convective and diffusive contributions from the neighboring nodes. The subscript nb refers to the neighboring cells, as the locations between the cell center p and the adjacent cells nb shown in Fig. 3.2.

3.2.3 Pressure-Velocity Coupling SIMPLE (Semi Implicit Method for Pressure Linked Equations) Scheme

The SIMPLE algorithm uses the relationship between velocity and pressure correction to enforce mass conservation and to obtain the pressure field [68]. First, we guess a pressure

P^*. Then a velocity U_f^* can be computed by P^* through Eqn.(3.7)

$$U_f^* = \widehat{J}_f^* + \frac{d_f}{\rho_f}(P_{c_0}^* - P_{c_1}^*). \tag{3.33}$$

However, U_f^* does not satisfy the continuity equation. A correction is introduced:

$$U_f = U_f^* + U_f', \tag{3.34}$$

which satisfies the continuity equation. The SIMPLE scheme postulates that U_f' be written as

$$U_f' = \frac{d_f}{\rho_f}(P_{c_0}' - P_{c_1}'), \tag{3.35}$$

where P' is the cell pressure correction.

Substitute the correction equations (3.34) and (3.35) into the discrete continuity equation (3.2) to obtain a discrete equation for the pressure correction P' in the cell:

$$a_P P' = \sum_{nb} a_{nb} P_{nb}' + c, \tag{3.36}$$

where the source term c is the net flow rate into the cell:

$$c = \sum_{f}^{N_{faces}} U_f^* A_f. \tag{3.37}$$

Once a solution for Eqn. (3.36) has been obtained, the cell pressure and face velocity are corrected by

$$P = P^* + a_P P', \tag{3.38}$$

$$U_f = J_f^* + \frac{d_f}{\rho_f}(P_{c_0}' - P_{c_1}'), \tag{3.39}$$

where a_p is the under-relaxation factor for pressure. The corrected U_f satisfies the discrete

continuity equation identically during each iteration.

3.3 Discretization of the k and ε Equations

The integral form of the k and ε equations are

$$\rho[\frac{\partial}{\partial t}\int_\Omega k d\Omega + \int_S (k\mathbf{U}\cdot\mathbf{n}_S)dS] = \int_S[(\mu+\frac{\mu_t}{\sigma_k})\nabla k\cdot\mathbf{n}_S]dS + \int_\Omega (G_k-\rho\varepsilon)d\Omega, \quad (3.40)$$

$$\rho[\frac{\partial}{\partial t}\int_\Omega \varepsilon d\Omega + \int_S (\varepsilon\mathbf{U}\cdot\mathbf{n}_S)dS] = \int_S[(\mu+\frac{\mu_t}{\sigma_\varepsilon})\nabla\varepsilon\cdot\mathbf{n}_S]dS + \int_\Omega(\rho C_1\overline{S}\varepsilon - \rho C_2\frac{\varepsilon^2}{k+\sqrt{\nu\varepsilon}})d\Omega. \quad (3.41)$$

Appling the above equations to each control volume, or cell, in the computational domain, yields the discretized k and ε equations on a given cell:

$$\rho\frac{\partial k}{\partial t}\Delta V + \rho\sum_f^{N_{faces}} k_f\mathbf{U}_f\cdot\mathbf{A}_f = \sum_f^{N_{faces}}(\mu+\frac{\mu_t}{\sigma_k})\nabla k_f\cdot\mathbf{A}_f + (G_k-\rho\varepsilon)\Delta V, \quad (3.42)$$

$$\rho\frac{\partial \varepsilon}{\partial t}\Delta V + \rho\sum_f^{N_{faces}} \varepsilon_f\mathbf{U}_f\cdot\mathbf{A}_f = \sum_f^{N_{faces}}(\mu+\frac{\mu_t}{\sigma_\varepsilon})\nabla k_f\cdot\mathbf{A}_f + (\rho C_1\overline{S}\varepsilon - \rho C_2\frac{\varepsilon^2}{k+\sqrt{\nu\varepsilon}})\Delta V. \quad (3.43)$$

3.3.1 Temporal Distretization

The temporal discretization uses the first-order explicit integration as the temporal discretization of the continuity and momentum equations:

$$\frac{k^{n+1}-k^n}{\Delta t}\Delta V = \Gamma(k^n), \quad (3.44)$$

$$\frac{\varepsilon^{n+1}-\varepsilon^n}{\Delta t}\Delta V = \Gamma(\varepsilon^n), \quad (3.45)$$

where Γ equation incorporates the spatial discretization of the k or ε equation.

3.3.2 Spatial Discretization

The spatial discretization in k and ε equations in integral form are

$$\begin{aligned}
\Gamma(k) &= -\int_S (k\mathbf{U}\cdot\mathbf{n}_S)dS] + \int_S [(\mu + \frac{\mu_t}{\sigma_k})\nabla k \cdot \mathbf{n}_S]dS + \int_\Omega (G_k - \rho\varepsilon)d\Omega, \qquad (3.46)\\
\Gamma(\varepsilon) &= -\int_S (\varepsilon\mathbf{U}\cdot\mathbf{n}_S)dS] + \int_S [(\mu + \frac{\mu_t}{\sigma_\varepsilon})\nabla \varepsilon \cdot \mathbf{n}_S]dS \\
&\quad + \int_\Omega (\rho C_1 \overline{S}\varepsilon - \rho C_2 \frac{\varepsilon^2}{k + \sqrt{\nu\varepsilon}})d\Omega. \qquad (3.47)
\end{aligned}$$

Their corresponding discretized equations can be written as

$$\begin{aligned}
\Gamma(k) &= -\rho \sum_f^{N_{faces}} k_f \mathbf{U}_f\cdot\mathbf{A}_f + \sum_f^{N_{faces}} (\mu + \frac{\mu_t}{\sigma_k})\nabla k_f \cdot \mathbf{A}_f + (G_k - \rho\varepsilon)\Delta V, \qquad (3.48)\\
\Gamma(\varepsilon) &= -\rho \sum_f^{N_{faces}} \varepsilon_f \mathbf{U}_f\cdot\mathbf{A}_f + \sum_f^{N_{faces}} (\mu + \frac{\mu_t}{\sigma_\varepsilon})\nabla k_f \cdot \mathbf{A}_f \\
&\quad + (\rho C_1 \overline{S}\varepsilon - \rho C_2 \frac{\varepsilon^2}{k + \sqrt{\nu\varepsilon}})\Delta V. \qquad (3.49)
\end{aligned}$$

Applied to the same 2D control volume shown in Fig. 3.1, the corresponding discretizations are as follows:

$$\begin{aligned}
\Gamma(k) &= -(M^{(1)}_{i+1/2,j} - M^{(1)}_{i-1/2,j}) \triangle y - (N^{(1)}_{i,j+1/2} - N^{(1)}_{i,j-1/2}) \triangle x \\
&\quad + (G_k - \rho\varepsilon)_{i,j}\Delta x\Delta y \qquad (3.50)\\
\Gamma(\varepsilon) &= -(M^{(2)}_{i+1/2,j} - M^{(2)}_{i-1/2,j}) \triangle y - (N^{(2)}_{i,j+1/2} - N^{(2)}_{i,j-1/2}) \triangle x \\
&\quad + (\rho C_1 \overline{S}\varepsilon - \rho C_2 \frac{\varepsilon^2}{k + \sqrt{\nu\varepsilon}})_{i,j}\Delta x\Delta y, \qquad (3.51)
\end{aligned}$$

where $M^{(1)}$, $M^{(2)}$, $N^{(1)}$, and $N^{(2)}$ are defined as follows

$$\begin{aligned}
M^{(1)} &= \rho k U - (\mu + \frac{\mu_t}{\sigma_k})\frac{\partial k}{\partial x}, \qquad (3.52)\\
M^{(2)} &= \rho \varepsilon U - (\mu + \frac{\mu_t}{\sigma_\varepsilon})\frac{\partial \varepsilon}{\partial x}, \qquad (3.53)
\end{aligned}$$

$$N^{(1)} = \rho k V - (\mu + \frac{\mu_t}{\sigma_k})\frac{\partial k}{\partial y}, \tag{3.54}$$

$$N^{(2)} = \rho \varepsilon V - (\mu + \frac{\mu_t}{\sigma_\varepsilon})\frac{\partial \varepsilon}{\partial y}. \tag{3.55}$$

Thus

$$M^{(1)}_{i+1/2,j} = \rho(kU)_{i+1/2,j} - (\mu + \frac{\mu_t}{\sigma_k})\left.\frac{\partial k}{\partial x}\right|_{i+1/2,j}, \tag{3.56}$$

$$M^{(1)}_{i-1/2,j} = \rho(kU)_{i-1/2,j} - (\mu + \frac{\mu_t}{\sigma_k})\left.\frac{\partial k}{\partial x}\right|_{i-1/2,j}, \tag{3.57}$$

$$M^{(2)}_{i+1/2,j} = \rho(\varepsilon U)_{i+1/2,j} - (\mu + \frac{\mu_t}{\sigma_\varepsilon})\left.\frac{\partial \varepsilon}{\partial x}\right|_{i+1/2,j}, \tag{3.58}$$

$$M^{(2)}_{i-1/2,j} = \rho(\varepsilon U)_{i-1/2,j} - (\mu + \frac{\mu_t}{\sigma_\varepsilon})\left.\frac{\partial \varepsilon}{\partial x}\right|_{i-1/2,j}, \tag{3.59}$$

$$N^{(1)}_{i,j+1/2} = \rho(kV)_{i,j+1/2} - (\mu + \frac{\mu_t}{\sigma_k})\left.\frac{\partial k}{\partial y}\right|_{i,j+1/2}, \tag{3.60}$$

$$N^{(1)}_{i,j-1/2} = \rho(kV)_{i,j-1/2} - (\mu + \frac{\mu_t}{\sigma_k})\left.\frac{\partial k}{\partial y}\right|_{i,j-1/2}, \tag{3.61}$$

$$N^{(2)}_{i,j+1/2} = \rho(\varepsilon V)_{i,j+1/2} - (\mu + \frac{\mu_t}{\sigma_\varepsilon})\left.\frac{\partial \varepsilon}{\partial y}\right|_{i,j+1/2}, \tag{3.62}$$

$$N^{(2)}_{i,j-1/2} = \rho(\varepsilon V)_{i,j-1/2} - (\mu + \frac{\mu_t}{\sigma_\varepsilon})\left.\frac{\partial \varepsilon}{\partial y}\right|_{i,j-1/2}. \tag{3.63}$$

The values of k and ε at the cell surfaces ($k_{i+1/2,j}$, $k_{i,j+1/2}$, $k_{i-1/2,j}$, $k_{i,j-1/2}$, $\varepsilon_{i+1/2,j}$, $\varepsilon_{i,j+1/2}$, $\varepsilon_{i-1/2,j}$, $\varepsilon_{i,j-1/2}$) is accomplished using upwind schemes and the diffusion terms in k and ε equations always use second-order central-differenced schemes. The first-order upwind and second-order upwind schemes are described in the context of discretization of continuity equation. The third-order MUSCL (Monotone Upstream-centered Scheme for Conservation Laws) scheme is used for the discretization of the k and ε equations when a high order scheme is required. The third-order MUSCL scheme blends a central differencing scheme and second-order upwind scheme as [68]

$$\gamma_f = \theta\gamma_{f,CD} + (1-\theta)\gamma_{f,SOU}, \tag{3.64}$$

where γ represents a general scalar, $\gamma_{f,CD}$ is a face value obtained with a central differencing scheme and $\gamma_{f,SOU}$ is a face value obtained with a second-order upwind scheme. The first term is written as follows:

$$\gamma_{f,CD} = \frac{1}{2}(\gamma_0 + \gamma_1) + \frac{1}{2}(\nabla\gamma_0 \cdot \mathbf{n}_0 + \nabla\gamma_1 \cdot \mathbf{n}_1), \tag{3.65}$$

where γ_0 and γ_1 are the values at the centroids of two neighboring control volumes sharing the same face, $\nabla\gamma_0$ and $\nabla\gamma_1$ are the gradients of the scalar computed at cell centroids and $\mathbf{n}_0$ and $\mathbf{n}_1$ are the direction vectors pointing from cell centroid to the face centroid.

The second term, $\gamma_{f,SOU}$, is computed as

$$\gamma_{f,SOU} = \gamma + \nabla\gamma \cdot \triangle\mathbf{s}, \tag{3.66}$$

where γ and $\nabla\gamma$ are the value at the cell center and its gradients in the upstream cell, respectively. $\triangle\mathbf{s}$ is the displacement vector from the upstream cell centroid to the face centroid. The gradient $\nabla\gamma$ is computed using the divergence theorem,

$$\nabla\gamma = \frac{1}{\Delta V} \sum_{f}^{N_{face}} \tilde{\gamma}_f \mathbf{A}_f. \tag{3.67}$$

Here, the face values $\tilde{\gamma}_f$ are computed by averaging γ from the two cells adjacent to the face.

3.4 Numerical Procedure for the Level Set Method

3.4.1 UDFs in ANSYS FLUENT

Figure 3.4 illustrates the solution process for the pressure-based solvers, used in this study. It begins with a two-step initialization sequence that is executed outside the solution iteration loop. This sequence begins by initializing equations to user-specified (or default)

values taken from the ANSY FLUENT user interface. Next, PROFILE UDFs are called, followed by a call to INIT UDFs. Initialization UDFs overwrite initialization values that were previously set. The solution iteration loop begins with the execution of ADJUST UDFs. Next, ANSYS FLUENT solves the governing equations of continuity and momentum sequentially or in a coupled fashion. Subsequently, the energy and species equations are solved, followed by turbulence and other scalar transport equations, as required. Note that PROFILE and SOURCE UDFs are called by each "Solve" routine for the variable currently under consideration (e.g., species, velocity).

Properties are updated after solving the conservation equations, using PROPERTY UDFs. For the CLSVOF method, the re-initialization and coupling between LS and VOF method are carried out at the end of each iteration. A check for either convergence or additional requested iterations is done, and the loop either continues or stops.

Since FLUENT already contains a VOF method, only the LS method needs to be implemented in our code via UDFs. The level set equation is solved by enabling the User Defined Scalar (UDS) equation in FLUENT. The use of macros DEFINE_UDS_UNSTEADY, DEFINE_UDS_FLUX, and DEFINE_DIFFUSIVITY set up the scalar equation for level set function in FLUENT. The unsteady and advection terms are added to FLUENT in the User-Defined Scalars panel. The scalar diffusivity is assigned in the Materials panel. The boundary condition for the scalar equation is assigned in the Boundary Condition panel. Especially note that the boundary condition for the LS function at inlet must be fixed to zero, due to that hyperbolic nature of Eq. (2.55). The characteristics propagate outward from the zero level set, $\phi = 0$.

3.4.2 UDF's for the Unsteady Term in Level Set Equation

The unsteady term of the level set function Eq.(2.52) is moved to the right hand side and discretized as follows:

$$\begin{aligned} unsteady\,term &= -\int_{\Omega}\frac{\partial\phi}{\partial t}d\Omega = -[\frac{\phi^{n+1}-\phi^{n}}{\Delta t}]\cdot\Delta V \\ &= -\frac{\triangle V}{\triangle t}\phi^{n+1}+\frac{\triangle V}{\triangle t}\phi^{n}. \end{aligned} \tag{3.68}$$

The macro DEFINE_UDS_UNSTEADY is used for the user-defined scalar time derivatives. The temporal discretization uses the first-order explicit time integration as

$$\frac{\phi^{n+1}-\phi^{n}}{\Delta t} = \Gamma(\phi^{n}). \tag{3.69}$$

3.4.3 UDF's for the Flux Term in Level Set Equation

The advection terms in the level set equation have the following form:

$$flux\ term = \nabla\cdot(\mathbf{U}\phi). \tag{3.70}$$

The integral and discretization of the flux terms on a given cell are

$$flux\ term\ in\ the\ integral\ form = \int_{S}(\phi\mathbf{U}\cdot\mathbf{n}_{S})dS \tag{3.71}$$

$$flux\ term\ in\ the\ disrectized\ form = \sum_{f}^{N_{faces}}(\phi_{f}\mathbf{U_{f}}\cdot\mathbf{A}_{f}). \tag{3.72}$$

The third-order MUSCL scheme is used to calculate the face value ϕ_f,

$$\phi_{f} = \theta\phi_{f,CD}+(1-\theta)\phi_{f,SOU}, \tag{3.73}$$

where the factor θ is set to 0.125 for the problem being studied, and,

$$\phi_{f,CD} = \frac{1}{2}(\phi_0 + \phi_1) + \frac{1}{2}(\nabla\phi_0 \cdot \mathbf{r}_0 + \nabla\phi_1 \cdot \mathbf{r}_1), \tag{3.74}$$

$$\phi_{f,SOU} = \phi + \nabla\phi \cdot \triangle\mathbf{s}, \tag{3.75}$$

where ϕ_0 and ϕ_1 are the cell centroid values of the two neighboring control volumes sharing the same face, $\nabla\phi_0$ and $\nabla\phi_1$ are the gradients of the scalar computed at cell centroids and $\mathbf{r}_0$ and $\mathbf{r}_1$ are the direction vectors pointing from cell centroid to the face centroid, ϕ and $\nabla\phi$ are the cell-centered value and its gradients in the upstream cell, and $\triangle\mathbf{s}$ is the displacement vector from the upstream cell centroid to the face centroid. The gradient is computed using the divergence theorem,

$$\nabla\phi = \frac{1}{\Delta V}\sum_{f}^{N_{face}} \widetilde{\phi}_f \mathbf{A}_f. \tag{3.76}$$

Here, the face value $\widetilde{\phi}_f$ are computed by averaging ϕ from the two cells adjacent to the face.

The macro DEFINE_UDS_FLUX is used for the flux term and it needs to return the scalar value $\mathbf{U} \cdot \mathbf{A}$ to FLUENT, where $\mathbf{A}$ is the face normal vector. Since Eqn. (3.70) is without the fluid density, it's just simple to include "return F_FLUX(f,t)/ρ" in the DEFINE_UDS_FLUX UDF. The denominator ρ can be determined by averaging the adjacent cells' density values C_R (F_C0(f,t), THREAD_T0(t)) and C_R (F_C1(f,t), THREAD_T1(t)), where C_R is the flow variable macro in UDF for density, t is a pointer to the thread on which the user-defined scalar flux is to be applied, and f is an index that identifies a face within the given thread. F_C0, F_C1, THREAD_T0 and THREAD_T1 are neighboring cells of the face f, and their corresponding threads [68].

3.4.4 UDF's for the Diffusion Terms in Level Set Equation

The diffusion terms in the Reynolds-averaged LS equation are

$$diffusion\,term = -\nabla \cdot (D_T \nabla \phi). \tag{3.77}$$

The integral and discretized forms of the diffusion term are

$$flux\,term\,in\,the\,integral\,form = -\int_S (D_T \nabla \phi \cdot \mathbf{n}_S) dS, \tag{3.78}$$

$$flux\,term\,in\,the\,discretized\,form = -\sum_f^{N_{faces}} (D_T \nabla \phi_f \cdot \mathbf{A}_f). \tag{3.79}$$

The face value ϕ_f uses the same MUSCL scheme as described in Eq.(3.73), and the gradient of ϕ on the face is computed using the divergence theorem,

$$\nabla \phi_f = \frac{1}{\Delta V} \sum_f^{N_{face}} \phi_f \mathbf{A}_f. \tag{3.80}$$

The diffusion coefficient, D_T, used in the macro "DEFINE_DIFFUSIVITY " is defined as

$$D_T = c_1 k^2 / \varepsilon, \tag{3.81}$$

and $c_1 = 0.129$ is a constant.

3.4.5 Discretization of Re-initialization Equation

The re-initialization equation is implemented and solved at every time step and a DEFINE_EXECUTE_AT_END UDF is used. The temporal term is discretized by means of TVD Runge-Kutta (RK) methods. The third-order time integration schemes can be written as

$$\phi^{(1)} = \phi^n + \Delta t \cdot L(\phi^n), \tag{3.82}$$

$$\phi^{(2)} = \frac{1}{4}[3\phi^n + \phi^{(1)} + \Delta t \cdot L(\phi^{(1)})], \tag{3.83}$$

$$\phi^{n+1} = \frac{1}{3}[\phi^n + 2\phi^{(2)} + 2\Delta t \cdot L(\phi^{(2)})], \tag{3.84}$$

where $L(\phi)$ is (Eqn.(2.57))

$$L(\phi) = S(\phi_0) - \mathbf{w} \cdot \nabla\phi. \tag{3.85}$$

Flux evaluation must be carried out during each stage of the Runge-Kutta method. The explicit scheme considered above requires the computation of a time step Δt to be used in Eqn. (3.84), such that the stability of the numerical method is ensured. One way of choosing Δt is

$$\Delta t = \frac{C_{cfl}}{U_0} \times \min(\Delta x, \Delta y, \Delta z), \tag{3.86}$$

where U_0 is initial bulk velocity, C_{cfl} is the CFL number and is chosen as

$$0 < C_{cfl} \leq 1/3. \tag{3.87}$$

in three space dimensions.

The convection term in Eqn. (2.57) can be expanded as

$$\mathbf{w} \cdot \nabla\phi = W_\xi \phi_\xi + W_\eta \phi_\eta + W_\zeta \phi_\zeta, \tag{3.88}$$

where W_i are the contravariant velocities, defined by

$$W_\xi = w_x\xi_x + w_y\xi_y + w_z\xi_z, \tag{3.89}$$

$$W_\eta = w_x\eta_x + w_y\eta_y + w_z\eta_z, \tag{3.90}$$

$$W_\zeta = w_x\zeta_x + w_y\zeta_y + w_z\zeta_z, \tag{3.91}$$

where

$$w_x = S(\phi_0)\frac{\phi_x}{|\nabla\phi|}, \tag{3.92}$$

$$w_y = S(\phi_0)\frac{\phi_y}{|\nabla\phi|}, \tag{3.93}$$

$$w_z = S(\phi_0)\frac{\phi_z}{|\nabla\phi|}. \tag{3.94}$$

Two schemes have been used to evaluate the partial derivatives $\phi_x, \phi_y, \phi_z, \phi_\xi, \phi_\eta$, and ϕ_ζ in the spatial discretization using two different finite different methods. The partial derivatives of ϕ in the coordinate system (x, y, z) is computed as

$$\frac{\partial\phi}{\partial x} = J[(\frac{\xi_x}{J}\phi)_\xi + (\frac{\eta_x}{J}\phi)_\eta + (\frac{\zeta_x}{J}\phi)_\zeta], \tag{3.95}$$

$$\frac{\partial\phi}{\partial y} = J[(\frac{\xi_y}{J}\phi)_\xi + (\frac{\eta_y}{J}\phi)_\eta + (\frac{\zeta_y}{J}\phi)_\zeta], \tag{3.96}$$

$$\frac{\partial\phi}{\partial z} = J[(\frac{\xi_z}{J}\phi)_{)\xi} + (\frac{\eta_z}{J}\phi)_\eta + (\frac{\zeta_z}{J}\phi)_\zeta], \tag{3.97}$$

where $\xi_x, \eta_x, \zeta_x, \xi_y, \eta_y, \zeta_y, \xi_z, \eta_z$, and ζ_z are metrics. The two schemes are described below.

(1) Second-order finite difference scheme

For the derivatives of ϕ with respect to (x, y, z), the central finite difference is used as described in Eqn. (3.98). Here, illustrations are given for the term $(\frac{\xi_x}{J}\phi)_\xi$ and the other components $()_\eta$ and $()_\zeta$. The central second-order finite differences are evaluated as

$$(\frac{\xi_x}{J}\phi)_\xi = \frac{1}{2}[(\frac{\xi_x}{J}\phi)_{i+1,j,k} - (\frac{\xi_x}{J}\phi)_{i-1,j,k}], \tag{3.98}$$

when both of the cells $(i-1, j, k)$ and $(i+1, j, k)$ are available. Otherwise, one-sided second-order finite differences are used. The form of right-sided second-order finite differences is

$$(\frac{\xi_x}{J}\phi)_\xi = \frac{1}{2}[-3 * (\frac{\xi_x}{J}\phi)_{i,j,k} + 4 * (\frac{\xi_x}{J}\phi)_{i+1,j,k} - (\frac{\xi_x}{J}\phi)_{i+2,j,k}], \tag{3.99}$$

and the left-sided second-order finite difference is

$$(\frac{\xi_x}{J}\phi)_\xi = \frac{1}{2}[3 * (\frac{\xi_x}{J}\phi)_{i,j,k} - 4 * (\frac{\xi_x}{J}\phi)_{i-1,j,k} + (\frac{\xi_x}{J}\phi)_{i-2,j,k}]. \tag{3.100}$$

For the calculation of ϕ_ξ,ϕ_η, and ϕ_ζ in Eqn. (3.88), a first-order upwind scheme is used and the values of the contravariant velocities are used to decide the upwind stencil:

$$\phi_\xi = \phi_{i+1/2,j,k} - \phi_{i-1/2,j,k}, \tag{3.101}$$

$$\phi_\eta = \phi_{i,j+1/2,k} - \phi_{i,j-1/2,k}, \tag{3.102}$$

$$\phi_\zeta = \phi_{i,j,k+1/2} - \phi_{i,j,k-1/2}. \tag{3.103}$$

The mid-point values are calculated using the first-order upwind scheme:

$$\phi_{i+1/2,j,k} = \begin{cases} \phi_i & W_\xi \le 0 \\ \phi_{i+1} & W_\xi < 0 \end{cases}, \tag{3.104}$$

$$\phi_{i-1/2,j,k} = \begin{cases} \phi_{i-1} & W_\xi \le 0 \\ \phi_i & W_\xi < 0 \end{cases}. \tag{3.105}$$

Similarly for $\phi_{i,j\pm1/2,k}$ and $\phi_{i,j,k\pm1/2}$.

(2) Fifth-order Hamilton-Jacobi WENO scheme

To evaluate the gradient terms using a fifth-order WENO scheme, a point (i, j, k) needs three points behind and three points after it in every direction. This poses no difficulties for a point inside the domain, but when the point is within 3 nodes from the boundary, the scheme doesn't work anymore due to the lack of points. The stencil structure for the fifth-order WENO scheme is shown in Fig. 3.3.

The definitions of ϕ_x, ϕ_y, and ϕ_z are given in Eqns.(3.95), (3.96), and (3.97). The partial derivative terms $(\frac{\xi_x}{J}\phi)_\xi$, $(\frac{\eta_x}{J}\phi)_\eta$, $(\frac{\zeta_x}{J}\phi)_\zeta$, $(\frac{\xi_y}{J}\phi)_\xi$, $(\frac{\eta_y}{J}\phi)_\eta$, $(\frac{\zeta_y}{J}\phi)_\zeta$, $(\frac{\xi_z}{J}\phi)_\xi$, $(\frac{\eta_z}{J}\phi)_\eta$, and $(\frac{\zeta_z}{J}\phi)_\zeta$ are evaluated using WENO scheme, as are ϕ_ξ, ϕ_η, and ϕ_ζ. Here, the details are only given for

the partial derivatives of ϕ with respect to (ξ, η, ζ).

To solve ϕ_ξ, ϕ_η, and ϕ_ζ using Sussman's method [64], the following equations are introduced:

$$a = \phi_\xi^-,\ b = \phi_\xi^+,\ c = \phi_\eta^-,\ d = \phi_\eta^+,\ e = \phi_\zeta^-,\ f = \phi_\zeta^+, \tag{3.106}$$

where a, b, c, d, e, and f are computed with a fifth-order Hamilton-Jacobi WENO approximation. First, the derivative of ϕ in 1D is described and then the formulations in 3D are given. To approximate ϕ_ξ on a left-biased stencil $\{i-3, i-2, i-1, i, i+1, i+2\}$, we introduce $\phi_i = \phi(i)$, $\Delta^+\phi_i = \phi_{i+1} - \phi_i$, and $\Delta^-\phi_i = \phi_i - \phi_{i-1}$. The WENO approximation of ϕ_ξ is a combination of the weighted average of ϕ_ξ, computed by ENO schemes. The 3rd order accurate ENO scheme will choose one from the following

$$\phi_{\xi,i}^{-,0} = \frac{1}{3}\Delta^+\phi_{i-3} - \frac{7}{6}\Delta^+\phi_{i-2} + \frac{11}{6}\Delta^+\phi_{i-1} \tag{3.107}$$

$$\phi_{\xi,i}^{-,1} = -\frac{1}{6}\Delta^+\phi_{i-2} + \frac{5}{6}\Delta^+\phi_{i-1} + \frac{1}{3}\Delta^+\phi_i \tag{3.108}$$

$$\phi_{\xi,i}^{-,2} = \frac{1}{3}\Delta^+\phi_{i-1} + \frac{5}{6}\Delta^+\phi_i - \frac{1}{6}\Delta^+\phi_{i+1}, \tag{3.109}$$

where $\phi_{\xi,i}^{-,s}$ is the third-order approximation to ϕ_ξ based on the sth substencil $\{i+s-3, i+s-2, i+s-1, i+s\}$ for $s = 0, 1, 2$.

The WENO approximation of ϕ_ξ is a weighted average of $\phi_{\xi,i}^{-,s}$ $(s = 0, 1, 2)$:

$$\phi_{\xi,i}^- = \omega_0\phi_{\xi,i}^{-,0} + \omega_1\phi_{\xi,i}^{-,1} + \omega_2\phi_{\xi,i}^{-,2}. \tag{3.110}$$

Here, ω_s is the weight associated with the sth sub-stencil and the weights satisfy the consistency equality: $\omega_0 + \omega_1 + \omega_2 = 1$. The definitions of the weights will be given shortly. Substituting $\phi_{\xi,i}^{-,s}$ into $\phi_{\xi,i}^-$, we obtain

$$\begin{aligned}\phi_{\xi,i}^- = {} & \frac{1}{12}(-\Delta^+\phi_{i-2} + 7\Delta^+\phi_{i-1} + 7\Delta^+\phi_i - \Delta^+\phi_{i+1}) \\ & -\phi^{WENO}(\Delta^-\Delta^+\phi_{i-2}, \Delta^-\Delta^+\phi_{i-1}, \Delta^-\Delta^+\phi_i, \Delta^-\Delta^+\phi_{i+1}),\end{aligned} \tag{3.111}$$

where[49]

$$\phi^{WENO}(a,b,c,d) = \frac{1}{3}\omega_0(a-2b+c) + \frac{1}{6}(\omega_2 - \frac{1}{2})(b-2c+d) \tag{3.112}$$

and the weights ω_0 and ω_2 are defined as

$$\omega_0 = \frac{\alpha_0}{\alpha_0+\alpha_1+\alpha_2}, \tag{3.113}$$

$$\omega_2 = \frac{\alpha_2}{\alpha_0+\alpha_1+\alpha_2}, \tag{3.114}$$

where

$$\begin{aligned}
\alpha_0 &= \frac{1}{(\delta_\epsilon + IS_0)^2}, \\
\alpha_1 &= \frac{6}{(\delta_\epsilon + IS_1)^2}, \alpha_2 = \frac{3}{(\delta_\epsilon + IS_2)^2}, \\
IS_0 &= 13(a-b)^2 + 3(a-3b)^2, \\
IS_1 &= 13(b-c)^2 + 3(b+c)^2, \\
IS_2 &= 13(c-d)^2 + 3(3c-d)^2.
\end{aligned} \tag{3.115}$$

Here, δ_ϵ is used to prevent the denominators from becoming zero. We set $\delta_\epsilon = 10^{-16}$.

By symmetry, the fifth-order WENO for $\phi^+_{\xi,i}$ on the right-biased stencil $\{i+s-2, i+s-1, i+s, i+s+1\}$ for $s = 0, 1$, and 2, can be written as

$$\begin{aligned}
\phi^+_{\xi,i} &= \frac{1}{12}(-\Delta^+\phi_{i-2} + 7\Delta^+\phi_{i-1} + 7\Delta^+\phi_i - \Delta^+\phi_{i+1}) \\
&\quad + \phi^{WENO}(\Delta^-\Delta^+\phi_{i+2}, \Delta^-\Delta^+\phi_{i+1}, \Delta^-\Delta^+\phi_i, \Delta^-\Delta^+\phi_{i-1}).
\end{aligned} \tag{3.116}$$

For the general 3D case, the fifth-order Hamilton-Jacobi WENO approximations for the first derivative of ϕ with respect to ξ, η, and ζ are:

$$\begin{aligned}
\phi^\pm_{\xi,i,j,k} &= \frac{1}{12}(-\Delta^+_\xi\phi_{i-2,j,k} + 7\Delta^+_\xi\phi_{i-1,j,k} + 7\Delta^+_\xi\phi_{i,j,k} - \Delta^+_\xi\phi_{i+1,j,k}) \\
&\quad \pm \phi^{WENO}(\Delta^-_\xi\Delta^+_\xi\phi_{i\pm2,j,k}, \Delta^-_\xi\Delta^+_\xi\phi_{i\pm1,j,k}, \Delta^-_\xi\Delta^+_\xi\phi_{i,j,k}, \Delta^-_\xi\Delta^+_\xi\phi_{i\mp1,j,k}),
\end{aligned} \tag{3.117}$$

$$\phi^{\pm}_{\eta,i,j,k} = \frac{1}{12}(-\Delta^+_\eta\phi_{i,j-2,k} + 7\Delta^+_\eta\phi_{i,j-1,k} + 7\Delta^+_\eta\phi_{i,j,k} - \Delta^+_\eta\phi_{i,j+1,k}) \\ \pm\phi^{WENO}(\Delta^-_\eta\Delta^+_\eta\phi_{i\pm2,j,k}, \Delta^-_\eta\Delta^+_\eta\phi_{i\pm1,j,k}, \Delta^-_\eta\Delta^+_\eta\phi_{i,j,k}, \Delta^-_\eta\Delta^+_\eta\phi_{i\mp1,j,k}), \quad (3.118)$$

$$\phi^{\pm}_{\zeta,i,j,k} = \frac{1}{12}(-\Delta^+_\zeta\phi_{i,j,k-2} + 7\Delta^+_\zeta\phi_{i,j,k-1} + 7\Delta^+_\zeta\phi_{i,j,k} - \Delta^+_\zeta\phi_{i,j,k+1}) \\ \pm\phi^{WENO}(\Delta^-_\zeta\Delta^+_\zeta\phi_{i,j,k\pm2}, \Delta^-_\zeta\Delta^+_\zeta\phi_{i,j,k\pm1}, \Delta^-_\zeta\Delta^+_\zeta\phi_{i,j,k}, \Delta^-_\zeta\Delta^+_\zeta\phi_{i,j,k\mp1}). \quad (3.119)$$

If we define a^+, b^-, c^+, d^-, e^+, and f^+ as follows:

$$\begin{aligned} a^+ &\equiv \max(a,0),\ b^- \equiv \min(b,0), \\ c^+ &\equiv \max(c,0),\ d^- \equiv \min(d,0), \\ e^+ &\equiv \max(e,0),\ f^- \equiv \min(f,0), \end{aligned} \quad (3.120)$$

then ϕ_ξ , ϕ_η , and ϕ_ζ can be calculated as follows:

$$\begin{aligned} \phi_\xi &\equiv f_s(a^+,b^-)\sqrt{\max[(a^+)^2,(b^-)^2]}, \\ \phi_\eta &\equiv f_s(c^+,d^-)\sqrt{\max[(c^+)^2,(d^-)^2]}, \\ \phi_\zeta &\equiv f_s(e^+,f^-)\sqrt{\max[(e^+)^2,(f^-)^2]}, \end{aligned} \quad (3.121)$$

where f_s is given by

$$f_s(a^+,b^-) = \begin{cases} sign(a) & if\ \ \max[(a^+)^2,(b^-)^2 = (a^+)^2, \\ sign(b) & if\ \ \max[(a^+)^2,(b^-)^2 = (b^-)^2. \end{cases} \quad (3.122)$$

For points that don't have a complete WENO stencil, second-order schemes are used to obtain the gradient of ϕ: one-sided second-order scheme for points on the boundary and central second-order scheme for the rest. The formulations are shown in Eqns. (3.98), (3.99), and (3.100).

3.5 Discretization of Volume of Fluid Equation

The integral form for the volume of fluid equation is

$$\int_{\Omega} \frac{\partial F}{\partial t} d\Omega + \int F \mathbf{u} \cdot \mathbf{n}_S dA = 0. \tag{3.123}$$

Its discretization on a given cell volume ΔV is

$$\frac{\partial F}{\partial t} \Delta V + \sum_{f}^{N_{faces}} F_f \mathbf{u}_f \cdot \mathbf{A}_f = 0. \tag{3.124}$$

The first-order explicit temporal discretization is used,

$$\frac{F^{n+1} - F^n}{\Delta t} \Delta V + \sum_{f}^{N_{faces}} F_f^n \mathbf{u}_f^n \cdot \mathbf{A}_f = 0. \tag{3.125}$$

The face value of F is obtained by the second-order upwind scheme.

$$F_f = F + \nabla F \cdot \mathbf{r}, \tag{3.126}$$

where F and ∇F are the cell-centered value and its gradient in the upstream cell, and $\mathbf{r}$ is the displacement vector from the centroid of the upstream cell to that of the face.

3.6 Coupling Method

3.6.1 Reconstruction of Level Set Values with Planes in Partial Cells

After solving the convection equations of the level set function ϕ and the volume fraction value F, we need to use F to correct ϕ before solving the reinitialization equation for ϕ. This is exactly where the coupling between LS and VOF methods happens, which is necessary

to overcome the volume loss problem of the original LS method. To make this correction feasible, we first need to define the interface in the cell Ω_{ijk} as a plane (a straight line in 2D). As in Sussman and Puckett [64] , the following reconstructed level set ϕ^R_{ijk} is defined:

$$\phi^R_{ijk}(x,y,z) = a_{ijk}(x-x_i) + b_{ijk}(y-y_j) + c_{ijk}(z-z_k) + d_{ijk}. \tag{3.127}$$

When the equation is normalized such that $a^2_{ijk}+b^2_{ijk}+c^2_{ijk}=1$, as pointed out by Menard et al [65], the unit vector $\mathbf{n}_{ijk} = (a_{ijk}, b_{ijk}, c_{ijk})$ represents the normal to the interface. Correspondingly, d_{ijk} denotes the normal distance from the cell center (x_i, y_j, z_k) to the interface.

To make ϕ^R_{ijk} an accurate approximation to the original level set function ϕ, as in Sussman and Puckett [64], we minimize the following L_2 error:

$$E_{ijk} = \int_{x_{i-1/2}}^{x_{i+1/2}} \int_{y_{j-1/2}}^{y_{j+1/2}} \int_{z_{k-1/2}}^{z_{k+1/2}} \delta_\epsilon(\phi) \left(\phi - \phi^R_{ijk}(x,y,z)\right)^2 \mathrm{dxdydz}. \tag{3.128}$$

We choose a 27-point stencil and the discrete form of the above error function reads [65]:

$$E_{ijk} = \sum_{i'=i-1}^{i'=i+1} \sum_{j'=j-1}^{j'=j+1} \sum_{k'=k-1}^{k'=k+1} w_{i'-i,j'-j,k'-k} \delta_\epsilon(\phi_{i'j'k'}) \left(\phi_{i'j'k'} - \phi^R_{ijk}(x,y,z)\right)^2, \tag{3.129}$$

where $\delta_\epsilon(\phi)$ is the smoothed Dirac function with the thickness $\epsilon = \sqrt{2} min(dx, dy, dz)$, where dx, dy, and dz are space step size. $w_{l,m,n}$ are weights that are larger on the central cell (i,j,k) and smaller on the surrounding cells (i',j',k'). In particular, we choose a ratio of 16 between central cell weight and those of the surrounding cells as in Menard *et al.*[65]:

$$w_{l,m,n} = \begin{cases} 16 & (l,m,n) = (0,0,0) \\ 1 & (l,m,n) \neq (0,0,0) \end{cases}. \tag{3.130}$$

To minimize E_{ijk}, its first order derivatives with respect to a_{ijk}, b_{iijk}, c_{ijk}, and d_{ijk} should

all vanish:

$$\frac{\partial E_{ijk}}{\partial a_{ijk}} = \frac{\partial E_{ijk}}{\partial b_{ijk}} = \frac{\partial E_{ijk}}{\partial c_{ijk}} = \frac{\partial E_{ijk}}{\partial d_{ijk}} = 0, \tag{3.131}$$

which leads to the following linear system:

$$\begin{bmatrix} \sum\sum\sum whX^2 & \sum\sum\sum whXY & \sum\sum\sum whXZ & \sum\sum\sum whX \\ \sum\sum\sum whXY & \sum\sum\sum whY^2 & \sum\sum\sum whYZ & \sum\sum\sum whY \\ \sum\sum\sum whXZ & \sum\sum\sum whYZ & \sum\sum\sum whZ^2 & \sum\sum\sum whZ \\ \sum\sum\sum whX & \sum\sum\sum whY & \sum\sum\sum whZ & \sum\sum\sum wh \end{bmatrix} \cdot \begin{bmatrix} a_{ijk} \\ b_{ijk} \\ c_{ijk} \\ d_{ijk} \end{bmatrix} = \begin{bmatrix} \sum\sum\sum whX\phi \\ \sum\sum\sum whY\phi \\ \sum\sum\sum whZ\phi \\ \sum\sum\sum wh\phi \end{bmatrix}, \tag{3.132}$$

where the following abbreviations are adopted:

$$\begin{aligned} \sum\sum\sum = \sum_{i'=i-1}^{i'=i+1} \sum_{j'=j-1}^{j'=j+1} \sum_{k'=k-1}^{k'=k+1}, \; wh = w_{i'-i,j'-j,k'-k} \delta_\epsilon \left(\phi_{i'j'k'}\right), \\ X = \left(x_{i'} - x_i\right), \; Y = \left(y_{j'} - y_j\right), \; Z = \left(z_{k'} - z_k\right), \; \phi = \phi_{i'j'k'}. \end{aligned} \tag{3.133}$$

To solve the above linear system, we use the Gaussian elimination method with pivoting as illustrated in Press *et al.* [66].

3.6.2 Correction of the Level Set Values with Volume Fractions

With the plane reconstruction of level set values, we are ready to correct them with the knowledge of volume fractions, in order to avoid mass loss. The essence of this correction is based on the idea that the volume of liquid in a given partial cell must be the same, no matter what method is used to calculate it. More specifically, the liquid volumes calculated from the level set plane and from the result of the convection equation of the liquid volume fraction should agree with each other. If we use F_{ijk} to denote the volume fraction of liquid, we obtain [65]:

$$\frac{1}{\text{dxdydz}} \int_{z_{k-1/2}}^{z_{k+1/2}} \int_{y_{j-1/2}}^{y_{j+1/2}} \int_{x_{i-1/2}}^{x_{i+1/2}} H_\epsilon \left(\phi_{ijk}^R \left(x, y, z\right)\right) \text{dxdydz} = F_{ijk}. \tag{3.134}$$

The above equality will not be satisfied after we solve the advection equations of ϕ_{ijk} and F_{ijk} by using FLUENT. As a result, the Newton iterative method is adopted to modify the parameter d_{ijk} until a given precision is satisfied for the above equation:

$$d_{ijk}^{\text{new}} = d_{ijk} - \frac{\frac{1}{\text{dxdydz}} \int_{z_{k-1/2}}^{z_{k+1/2}} \int_{y_{j-1/2}}^{y_{j+1/2}} \int_{x_{i-1/2}}^{x_{i+1/2}} H_\epsilon \left(\phi_{ijk}^R(x,y,z)\right) \text{dxdydz} - F_{ijk}}{\frac{1}{\text{dxdydz}} \int_{z_{k-1/2}}^{z_{k+1/2}} \int_{y_{j-1/2}}^{y_{j+1/2}} \int_{x_{i-1/2}}^{x_{i+1/2}} \delta_\epsilon \left(\phi_{ijk}^R(x,y,z)\right) \text{dxdydz}}. \tag{3.135}$$

It is important to note that the Newton iterations are only performed for the cells around the interface between air and liquid.

3.7 Surface Tension Force for Multiphase Flow

The momentum equations in two-phase flow contain the surface tension terms. The surface tension terms are approximated using the CSF (Continuum Surface Force) model, as in Eqn. (2.62). The DEFINE_SOURCE UDF specifies custom source term for momentum equations in FLUENT,

$$source \;\; term = \sigma\kappa(\phi)\mathbf{n}\delta_\epsilon(\phi). \tag{3.136}$$

We need to determine the interface curvature, κ, and the normal to the interface, $\mathbf{n}$. Utilizing level set function, ϕ, curvature and normal to the interface are computed through DEFINE_ADJUST function and are then stored in the User Defined Memory (UDM) for each cell center.

By definition of the normal vector to a level surface, the unit normal $\overrightarrow{n}$ is achieved by normalizing $\nabla\phi$ with $|\nabla\phi|$:

$$n_x = \frac{\partial\phi}{\partial x}/[(\frac{\partial\phi}{\partial x})^2 + (\frac{\partial\phi}{\partial y})^2 + (\frac{\partial\phi}{\partial z})^2]^{1/2}, \tag{3.137}$$

$$n_y = \frac{\partial\phi}{\partial y}/[(\frac{\partial\phi}{\partial x})^2 + (\frac{\partial\phi}{\partial y})^2 + (\frac{\partial\phi}{\partial z})^2]^{1/2}, \tag{3.138}$$

$$n_z = \frac{\partial\phi}{\partial z}/[(\frac{\partial\phi}{\partial x})^2 + (\frac{\partial\phi}{\partial y})^2 + (\frac{\partial\phi}{\partial z})^2]^{1/2}. \tag{3.139}$$

The mean surface curvature is computed by taking the partial derivatives of the unit normal components in the manner consistent with the partial derivatives of ϕ:

$$\begin{aligned}
\frac{\partial n_x}{\partial x} &= J[(\frac{\xi_x}{J}n_x)_\xi + (\frac{\eta_x}{J}n_x)_\eta + (\frac{\zeta_x}{J}n_x)_\zeta)], && (3.140)\\
\frac{\partial n_y}{\partial y} &= J[(\frac{\xi_y}{J}n_y)_\xi + (\frac{\eta_y}{J}n_y)_\eta + (\frac{\zeta_y}{J}n_y)_\zeta)], && (3.141)\\
\frac{\partial n_z}{\partial z} &= J[(\frac{\xi_z}{J}n_z)_\xi + (\frac{\eta_z}{J}n_z)_\eta + (\frac{\zeta_z}{J}n_z)_\zeta], && (3.142)\\
\Longrightarrow\ & \kappa \equiv \nabla\cdot\nabla\phi/|\nabla\phi| = \frac{\partial n_x}{\partial x} + \frac{\partial n_y}{\partial y} + \frac{\partial n_z}{\partial z}. && (3.143)
\end{aligned}$$

Each component of the partial derivatives is evaluated using second-order finite differences as in Eqs. (3.98), (3.99), and (3.100).

We now discuss the computation of the metrics. The metrics are solved numerically through the expressions by x_ξ, x_η, x_z, etc., which can be computed by finite difference approximations. To obtain the relations, the differential expressions are considered:

$$\begin{aligned}
dx &= \frac{\partial x}{\partial \xi}d\xi + \frac{\partial x}{\partial \eta}d\eta + \frac{\partial x}{\partial \zeta}d\zeta,\\
dy &= \frac{\partial y}{\partial \xi}d\xi + \frac{\partial y}{\partial \eta}d\eta + \frac{\partial y}{\partial \zeta}d\zeta,\\
dz &= \frac{\partial z}{\partial \xi}d\xi + \frac{\partial z}{\partial \eta}d\eta + \frac{\partial z}{\partial \zeta}d\zeta. && (3.144)
\end{aligned}$$

The above equations can be cast in a matrix form:

$$\begin{bmatrix} dx \\ dy \\ dz \end{bmatrix} = \begin{bmatrix} x_\xi & x_\eta & x_\zeta \\ y_\xi & y_\eta & y_\zeta \\ y_\xi & y_\eta & y_\zeta \end{bmatrix} \begin{bmatrix} d\xi \\ d\eta \\ d\zeta. \end{bmatrix} \qquad (3.145)$$

Inverting, we have

$$d\xi = \frac{\partial \xi}{\partial x}dx + \frac{\partial \eta}{\partial y}dy + \frac{\partial \zeta}{\partial z}dz,$$

$$
\begin{aligned}
d\eta &= \frac{\partial \eta}{\partial x}dx + \frac{\partial \eta}{\partial y}dy + \frac{\partial \eta}{\partial z}dz, \\
d\zeta &= \frac{\partial \zeta}{\partial x}dx + \frac{\partial \zeta}{\partial y}dy + \frac{\partial \zeta}{\partial z}dz,
\end{aligned} \tag{3.146}
$$

or

$$
\begin{bmatrix} d\xi \\ d\eta \\ d\zeta \end{bmatrix} = \begin{bmatrix} \xi_x & \xi_y & \xi_z \\ \eta_x & \eta_y & \eta_z \\ \zeta_x & \zeta_y & \zeta_z \end{bmatrix} \begin{bmatrix} dx \\ dy \\ dz. \end{bmatrix} \tag{3.147}
$$

Comparing the two matrices, we see that

$$
\begin{bmatrix} \xi_x & \xi_y & \xi_z \\ \eta_x & \eta_y & \eta_z \\ \zeta_x & \zeta_y & \zeta_z \end{bmatrix} = \begin{bmatrix} x_\xi & x_\eta & x_\zeta \\ y_\xi & y_\eta & y_\zeta \\ y_\xi & y_\eta & y_\zeta \end{bmatrix}^{-1}, \tag{3.148}
$$

from which

$$
\xi_x = J(y_\eta z_\zeta - y_\zeta z_\eta), \xi_y = J(x_\zeta z_\eta - x_\eta z_\zeta), \xi_z = J(x_\eta y_\zeta - x_\zeta y_\eta), \tag{3.149}
$$

$$
\eta_x = J(y_\zeta z_\xi - y_\xi z_\zeta), \eta_y = J(x_\xi z_\zeta - x_\zeta z_\xi), \eta_z = J(x_\zeta y_\xi - x_\xi y_\zeta), \tag{3.150}
$$

$$
\zeta_x = J(y_\xi z_\eta - y_\eta z_\xi), \zeta_y = J(x_\eta z_\xi - x_\xi z_\eta), \zeta_z = J(x_\xi y_\eta - x_\eta y_\xi), \tag{3.151}
$$

where J is the Jacobian of transformation, defined by

$$
J = \frac{\partial(\xi, \eta, \zeta)}{\partial(x, y, z)} = \frac{1}{x_\xi(y_\eta z_\zeta - y_\zeta z_\eta) + x_\eta(y_\zeta z_\xi - y_\xi z_\zeta) + x_\zeta(y_\xi z_\eta - y_\eta z_\xi)}. \tag{3.152}
$$

In 2D, the expression for J is

$$
J = [\frac{\partial(x, y)}{\partial(\xi, \eta)}]^{-1} = (x_\xi y_\eta - x_\eta y_\xi)^{-1}, \tag{3.153}
$$

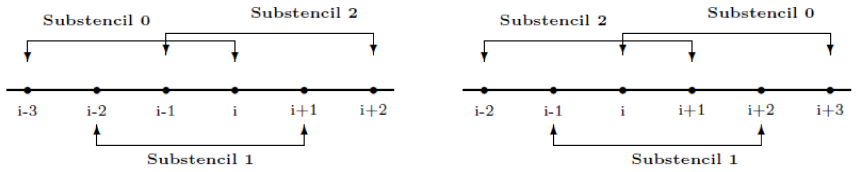

Figure 3.3: The three sub-stencils: (a) the left-biased stencil; (b) the right-biased stencil

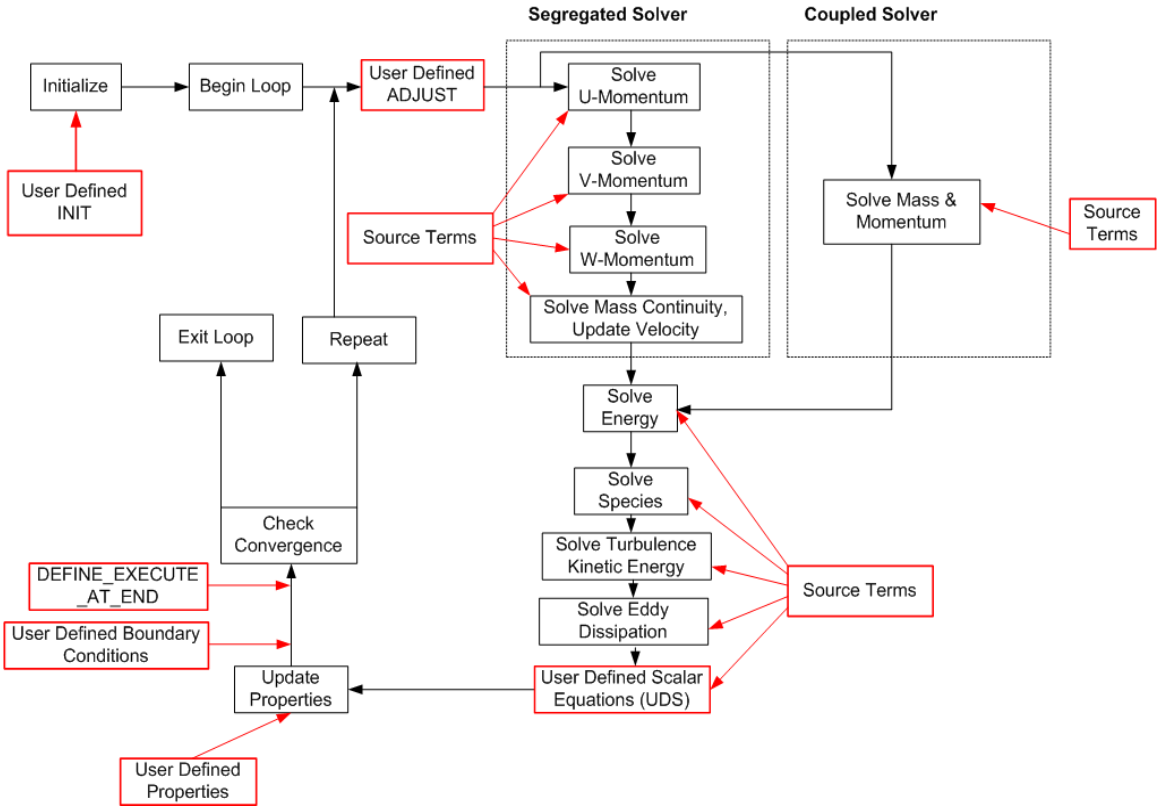

Figure 3.4: Solution procedure for the pressure-based segregated/coupled solver

so that

$$\xi_x = J * y_\eta,\ \xi_y = -J * x_\eta,\ \eta_x = -J * y_\xi,\ \eta_y = J * x_\xi. \tag{3.154}$$

Second-order finite differences are used to discretize the derivatives $x_\xi, x_\eta, x_\zeta, y_\xi, y_\eta, y_\zeta, z_\xi, z_\eta$, and z_ζ. The procedure is the same as those shown in Eqs. (3.98), (3.99), and (3.100).

Chapter 4

Numerical Verification and Validation

4.1 Understanding the Secondary Flows in Curved Pipes

For better understanding of the secondary flows in a curved pipe, we compare the governing equations for a curved pipe with those for a straight pipe and study the terms that represent the differences between two sets of equations. We decompose the equations for a curved pipe as follows:

$$\widetilde{L}_c(u^*, v^*, w^*) = L_c(u^*, v^*, w^*) + D_c^*, \tag{4.1}$$

$$\widetilde{L}_{M_1}(u^*, v^*, w^*) = L_{M_1}(u^*, v^*, w^*) + D_r^*, \tag{4.2}$$

$$\widetilde{L}_{M_2}(u^*, v^*, w^*) = L_{M_2}(u^*, v^*, w^*) + D_\theta^*, \tag{4.3}$$

$$\widetilde{L}_{M_3}(u^*, v^*, w^*) = L_{M_3}(u^*, v^*, w^*) + D_{\widetilde{z}}^*, \tag{4.4}$$

where the first terms on the right-hand side of the equations represent the contribution of a straight pipe and the remaining terms are due to curvature. The latter can easily be written as follows:

$$D_c^* \equiv \frac{\partial w^*}{\partial \widetilde{z}^*}\left(\frac{1}{\sqrt{g_{33}}} - 1\right) + \Gamma_{31}^{3*} u^* + \Gamma_{32}^{3*} \frac{v^*}{r^*}, \tag{4.5}$$

$$
\begin{aligned}
D_r^* \equiv\ & w^*\frac{\partial u^*}{\partial \widetilde{z}^*}\left(\frac{1}{\sqrt{g_{33}}}-1\right)+\Gamma_{33}^{1*}\frac{w^{*2}}{g_{33}}-\frac{1}{Re}\Big[\frac{\partial^2 u^*}{\partial \widetilde{z}^{*2}}\left(\frac{1}{g_{33}}-1\right)+\frac{\Gamma_{33}^{1*}}{g_{33}}\left(\Gamma_{13}^{3*}u^*+\Gamma_{23}^{3*}\frac{v^*}{r^*}-\frac{\partial u^*}{\partial r^*}\right)\\
&+\frac{\Gamma_{33}^{2*}}{g_{33}}\left(v^*-\frac{\partial u^*}{\partial \theta^*}\right)-\frac{\Gamma_{33}^{3*}}{g_{33}}\frac{\partial u^*}{\partial \widetilde{z}^*}+\frac{1}{g_{33}}\Big\{\frac{w^*}{\sqrt{g_{33}}}\frac{\partial}{\partial \widetilde{z}^*}\left(\Gamma_{33}^{1*}\right)+2\Gamma_{33}^{1*}\frac{\partial}{\partial \widetilde{z}^*}\left(\frac{w^*}{\sqrt{g_{33}}}\right)\Big\}\Big], \qquad (4.6)\\
D_\theta^* \equiv\ & w^*\frac{\partial v^*}{\partial \widetilde{z}^*}\left(\frac{1}{\sqrt{g_{33}}}-1\right)+\Gamma_{33}^{2*}\frac{r^*w^{*2}}{g_{33}}-\frac{1}{Re}\Big[\frac{\partial^2 v^*}{\partial \widetilde{z}^{*2}}\left(\frac{1}{g_{33}}-1\right)+\frac{\Gamma_{33}^{2*}}{g_{33}}\left(\Gamma_{13}^{3*}r^*u^*-u^*+\Gamma_{23}^{3*}v^*\right.\\
&\left.-\frac{\partial v^*}{\partial \theta^*}\right)-\frac{\Gamma_{33}^{1*}}{g_{33}}\frac{\partial v^*}{\partial r^*}-\frac{\Gamma_{33}^{3*}}{g_{33}}\frac{\partial v^*}{\partial \widetilde{z}^*}+\frac{r^*}{g_{33}}\Big\{\frac{w^*}{\sqrt{g_{33}}}\frac{\partial}{\partial \widetilde{z}^*}\left(\Gamma_{33}^{2*}\right)+2\Gamma_{33}^{2*}\frac{\partial}{\partial \widetilde{z}^*}\left(\frac{w^*}{\sqrt{g_{33}}}\right)\Big\}\Big], \qquad (4.7)\\
D_{\widetilde{z}}^* \equiv\ & \left(u^*\frac{\partial w^*}{\partial r^*}+\frac{v^*}{r^*}\frac{\partial w^*}{\partial \theta^*}\right)\left(\frac{1}{\sqrt{g_{33}}}-1\right)-\frac{w^*}{g_{33}}\left(u^*\frac{\partial \sqrt{g_{33}}}{\partial r^*}-\frac{v^*}{r^*}\frac{\partial \sqrt{g_{33}}}{\partial \theta^*}\right)\\
&+\left(w^*\frac{\partial w^*}{\partial \widetilde{z}^*}+\frac{\partial p^*}{\partial \widetilde{z}^*}\right)\left(\frac{1}{g_{33}}-1\right)+\frac{2w^*}{\sqrt{g_{33}}}\left(\Gamma_{31}^{3*}u^*+\Gamma_{32}^{3*}\frac{v^*}{r^*}\right)\\
&-\frac{1}{Re}\Big[\left(\frac{1}{\sqrt{g_{33}}}-1\right)\left(\frac{\partial^2 w^*}{\partial r^{*2}}+\frac{1}{r^*}\frac{\partial w^*}{\partial r^*}+\frac{1}{r^{*2}}\frac{\partial^2 w^*}{\partial \theta^{*2}}\right)+\left(\frac{1}{(\sqrt{g_{33}})^3}-1\right)\frac{\partial^2 w^*}{\partial \widetilde{z}^{*2}}\\
&-\left(\frac{2}{g_{33}}\frac{\partial w^*}{\partial r^*}-\frac{w^*}{g_{33}^2}\frac{\partial g_{33}}{\partial r^*}+\frac{w^*}{r^*g_{33}}\right)\frac{\partial \sqrt{g_{33}}}{\partial r^*}-\left(\frac{2}{g_{33}}\frac{\partial w^*}{\partial \theta^*}-\frac{w^*}{g_{33}^2}\frac{\partial g_{33}}{\partial \theta^*}\right)\frac{1}{r^{*2}}\frac{\partial \sqrt{g_{33}}}{\partial \theta^*}\\
&-\frac{1}{g_{33}^2}\frac{\partial w^*}{\partial \widetilde{z}^*}\frac{\partial \sqrt{g_{33}}}{\partial \widetilde{z}^*}-\frac{w^*}{g_{33}}\left(\frac{\partial^2 \sqrt{g_{33}}}{\partial r^{*2}}+\frac{1}{r^{*2}}\frac{\partial^2 g_{33}}{\partial \theta^{*2}}\right)+\frac{w^*}{\sqrt{g_{33}}}\Big\{\frac{\partial}{\partial r^*}\left(\Gamma_{13}^{2*}\right)+\frac{1}{r^{*2}}\frac{\partial}{\partial \theta^*}\left(\Gamma_{23}^{3*}\right)\Big\}\\
&+\frac{1}{g_{33}}\Big\{u^*\frac{\partial}{\partial \widetilde{z}^*}\left(\Gamma_{13}^{3*}\right)+\frac{v^*}{r^*}\frac{\partial}{\partial \widetilde{z}^*}\left(\Gamma_{23}^{3*}\right)\Big\}+\Gamma_{13}^{3*}\Big\{\frac{2}{g_{33}}\frac{\partial u^*}{\partial \widetilde{z}^*}+2\frac{\partial}{\partial r^*}\left(\frac{w^*}{\sqrt{g_{33}}}\right)+\frac{1}{r^*}\frac{w^*}{\sqrt{g_{33}}}\Big\}\\
&+\frac{w^*}{\sqrt{g_{33}}}\Big\{\left(\Gamma_{12}^{3*}\right)^2+\left(\frac{\Gamma_{33}^{3*}}{r^*}\right)^2\Big\}+\frac{\Gamma_{23}^{3*}}{r^{*2}}\Big\{\frac{2r^*}{g_{33}}\frac{\partial v^*}{\partial \widetilde{z}^*}+2\frac{\partial}{\partial \theta^*}\left(\frac{w^*}{\sqrt{g_{33}}}\right)\Big\}\\
&-\frac{1}{g_{33}}\Big\{\Gamma_{33}^{1*}\frac{\partial}{\partial r^*}\left(\frac{w^*}{\sqrt{g_{33}}}\right)+\Gamma_{33}^{2*}\frac{\partial}{\partial \theta^*}\left(\frac{w^*}{\sqrt{g_{33}}}\right)\Big\}\Big]. \qquad (4.8)
\end{aligned}
$$

For fully-developed laminar flow in a straight pipe, $D_c^* = D_r^* = D_\theta^* = D_{\widetilde{z}}^* = 0$ when $g_{33} = 0$, $\kappa_c = 0$, $L = 0$, $\Gamma_{ij}^{k*} = 0$, $u^* = v^* = 0$, and $w^* = w^*(r^*)$. For fully-developed laminar flow in the sinusoidal pipe configuration, Eqs. (2.10) to (2.13), and the conditions $u^* = u^*(r^*, \theta^*)$, $v^* = v^*(r^*, \theta^*)$, and $w^* = w^*(r^*, \theta^*)$ lead to the following simplification of the curvature terms:

$$
D_c^*(u^*, v^*, w^*) \equiv \Gamma_{31}^{3*}u^* + \Gamma_{32}^{3*}\frac{v^*}{r^*} = \frac{\kappa_c \cos\theta^*}{1 + r^*\kappa_c \cos\theta^*}u^* - \frac{\kappa_c \sin\theta^*}{1 + r^*\kappa_c \cos\theta^*}v^*, \qquad (4.9)
$$

$$
D_r^*(u^*, v^*, w^*) \equiv \Gamma_{33}^{1*}\frac{w^{*2}}{g_{33}} = -\frac{w^{*2}\kappa_c \cos\theta^*}{1 + r^*\kappa_c \cos\theta^*}, \qquad (4.10)
$$

$$
D_\theta^*(u^*, v^*, w^*) \equiv \Gamma_{33}^{2*}\frac{r^*w^{*2}}{g_{33}} = \frac{w^{*2}\kappa_c \sin\theta^*}{1 + r^*\kappa_c \cos\theta^*}, \qquad (4.11)
$$

$$
\begin{aligned}
&D_{\tilde{z}}^{*}(u^{*},v^{*},w^{*}) \equiv (u^{*}\frac{\partial w^{*}}{\partial r^{*}}+\frac{v^{*}}{r^{*}}\frac{\partial w^{*}}{\partial \theta^{*}})(\frac{1}{\sqrt{g_{33}}}-1)-\frac{w^{*}}{g_{33}}(u^{*}\frac{\partial \sqrt{g_{33}}}{\partial r^{*}}-\frac{v^{*}}{r^{*}}\frac{\partial \sqrt{g_{33}}}{\partial \theta^{*}})\\
&+\frac{\partial p^{*}}{\partial \tilde{z}^{*}}(\frac{1}{g_{33}}-1)+\frac{2w^{*}}{\sqrt{g_{33}}}(\Gamma_{31}^{3*}u^{*}+\Gamma_{32}^{3*}\frac{v^{*}}{r^{*}})\\
&=(u^{*}\frac{\partial w^{*}}{\partial r^{*}}+\frac{v^{*}}{r^{*}}\frac{\partial w^{*}}{\partial \theta^{*}})[\frac{1}{L(1+r\kappa_{c}\cos\theta^{*})}-1]-\frac{w^{*}}{g_{33}}(u^{*}\frac{\partial \sqrt{g_{33}}}{\partial r^{*}}\\
&-\frac{v^{*}}{r^{*}}\frac{\partial \sqrt{g_{33}}}{\partial \theta^{*}})+\frac{\partial p^{*}}{\partial \tilde{z}^{*}}(\frac{1}{L^{2}(1+r\kappa_{c}\cos\theta^{*})^{2}}-1)\\
&+\frac{2w^{*}}{\sqrt{g_{33}}}\kappa_{c}\frac{\cos\theta^{*}u^{*}-\sin\theta^{*}v^{*}}{1+r^{*}\kappa_{c}\cos\theta^{*}}.
\end{aligned}
\tag{4.12}
$$

We propose that Eqns. (4.10) and (4.11) describe the secondary flows in a curved pipe. To test this hypothesis, we evaluate these terms (D_r^* and D_θ^*) using velocities obtained from a straight pipe, and compare the results to the velocities (u^* and v^*) obtained directly from a numerical simulation of the flow in a curved pipe. Physically, D_r^* and D_θ^* represent inertial forces caused by the presence of the curvature, with units in Newtons when expressed in dimensional form. The profiles of u^* and v^* are plotted in Fig. 4.1(a) and Fig. 4.1(b), respectively. The iso-contours of D_r^* and D_θ^* are obtained by substituting the straight-pipe velocity solutions into the expression for these terms. The results are shown in Fig. 4.1(c) and Fig. 4.1(d). The qualitative similarity between Fig. 4.1(a) (Fig. 4.1(b)) and Fig. 4.1 (c) (Fig. 4.1(d)) support the suggestion that the inertial terms identified above contribute to the secondary flow in curved pipes. The inertial terms identified in this paper are consistent with the centrifugal force terms discussed in Berger *et al.* [106]. It is also important to note that D_r^* and D_θ^* do not include the terms v^{*2}/r^* and u^*v^*/r^*, respectively. Although these other terms were referred to as centrifugal force terms in Webster and Humphrey [107], it seems as if their significance is found in their ability to promote instability, even in a straight pipe.

The author acknowledges that the procedure just described for identifying the secondary flow terms in the equations is ad hoc. A more rigorous approach could try to isolate explicit, physically-meaningful terms in the momentum equations, in the same manner that the Navier-Stokes equations in a rotating frame of reference involve the additional terms

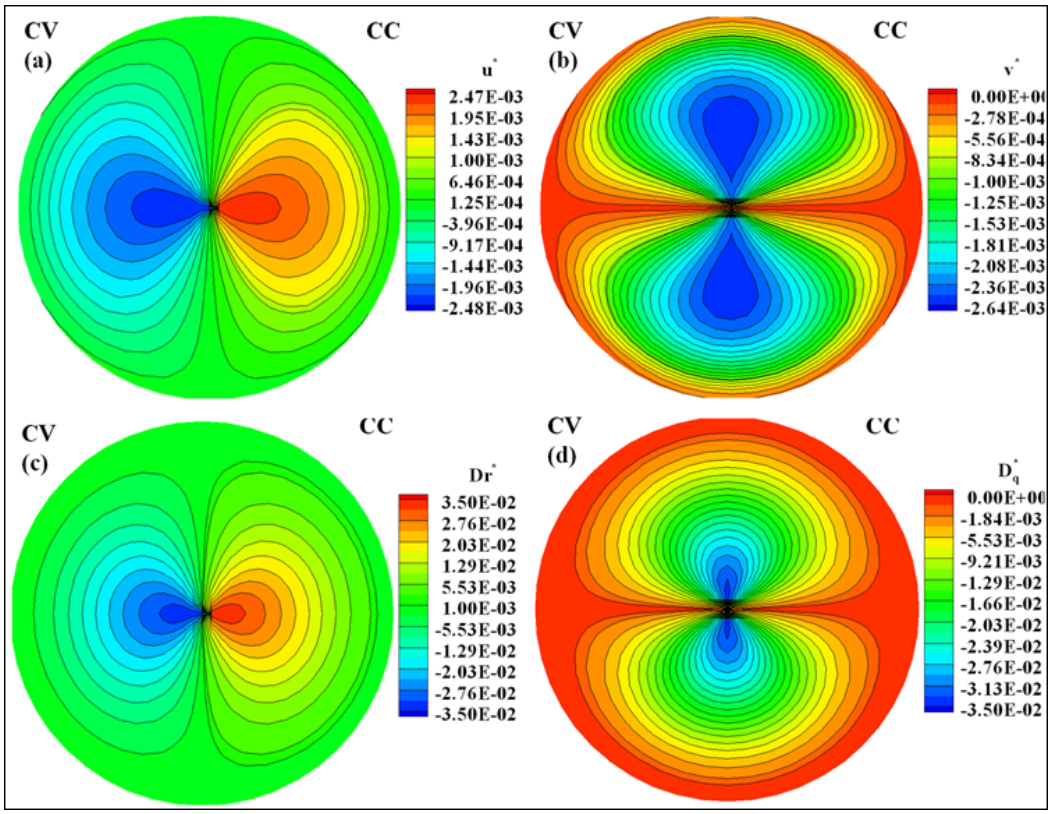

Figure 4.1: Contour plots of (a) u^*, (b) v^*, (c) D_r^*, and (d) D_θ^* at $x = 60$ of the periodically-curved pipe ($Re = 1000$)

$\rho[\mathbf{\Omega} \times \mathbf{\Omega} \times \mathbf{r}+2\mathbf{\Omega} \times \mathbf{u}]$ [108], which, respectively, consist of the centrifugal and Coriolis force fields. ($\mathbf{\Omega}$, $\mathbf{r}$ and $\mathbf{u}$ are the vectors of angular velocity, position, and instantaneous rotating frame velocity, respectively.) The present problem appears to be more complicated and the foregoing analysis has been carried out only for insight.

4.2 Realizable $k - \varepsilon$ Model For Flow in Curved Pipes

SA, SKE, and RKE models are applied to simulate turbulence flow in a 90° bend curved pipe. The results show that RKE model has better performance than the other two. The test conditions are taken from Sudo [12] and consist of a 90° bend (Fig. 4.2) with $\delta = 1/4$. The pipe has a 100-diameter upstream tangent section and a 40-diameter downstream tangent section. The results are compared in Fig. 4.3 for the static pressure coefficient, C_p, at 17.6 diameters upstream of the bend. The variable s is a pseudo coordinate direction, introduced in this section for the purpose of describing the locations on the straight (tangent) portions of the pipe. This consists of the upstream tangent ($-1 \leq s \leq 0^-$) and the region after the bend ($0^+ \leq s \leq 5$). Note that $\theta = -90°$ is the convex side of the bend, while $\theta = 90°$ is the concave side, which is consistent with the use in Sudo's experiment. Fairly close agreement between the methods is apparent. However, the RKE results match the experimental data better than the results from SA and SKE for the three locations plotted in Figure 4.3. Thus, the RKE model is used for subsequent pipe calculations in this paper.

4.3 Numerical Validations of the Developed CLSVOF Model

Numerical tests are presented in this section to verify and validate the accuracy and stability of the CLSVOF method. The ϵ in Eq. (2.54) is set to $1.5\Delta x$, where Δx is the mesh size in the x direction. The CLSVOF method is validated with two forms of convection velocities: constant velocity and vortex velocity. Pure movements of interface are expected without any deformation under constant velocity with the goal of establishing that the CLSVOF code

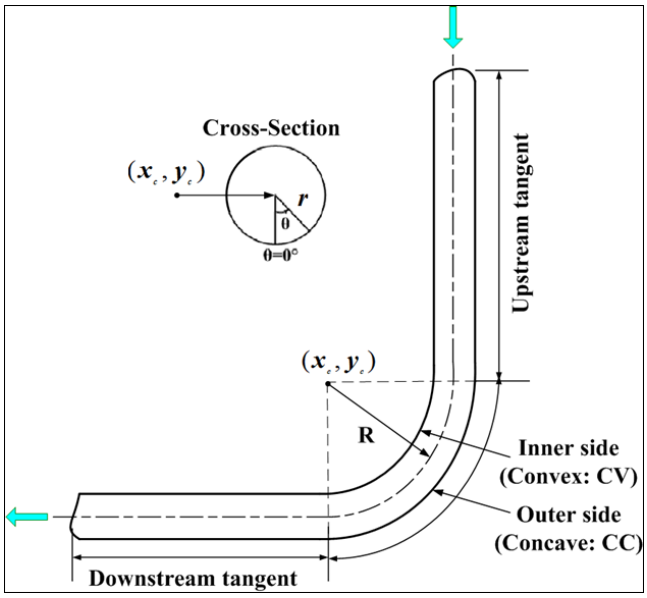

Figure 4.2: The sketch of a curved pipe with a 90° bend. CV implies "convex (inner) side", CC is "concave (outer) side", (x_c, y_c) denotes the curvature center and R is the radius of curvature

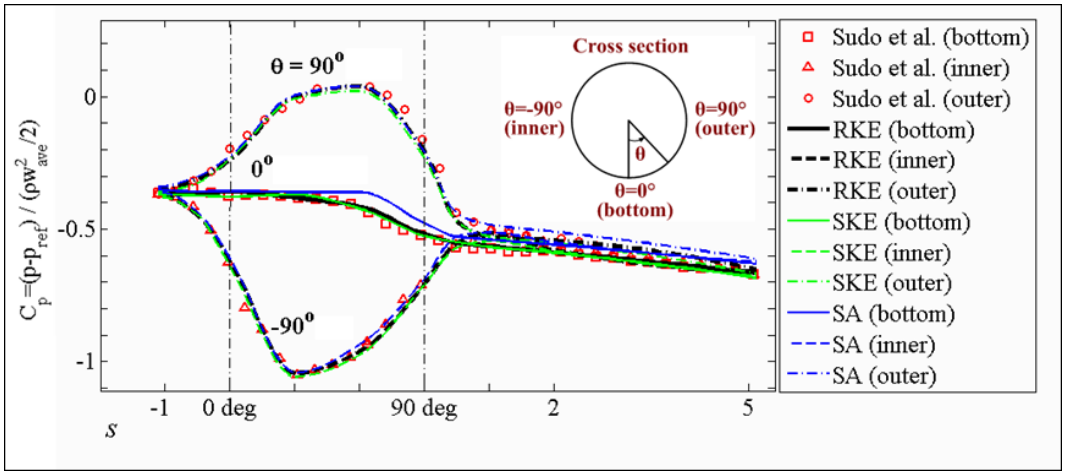

Figure 4.3: Longitudinal distribution of static pressure at the convex ($\theta = -90°$), concave ($\theta = 90°$) and bottom ($\theta = 0°$) sides of the 90° bend ($Re = 60,000$)

doesn't have any artificial velocities for the momentum equations. The deformation of interface happens under the vortex velocity. The results of the CLSVOF method developed in this paper is compared with the CLSVOF method built in ANSYS FLUENT as well as with some results in the literature.

4.3.1 Droplet Movement Due to A Constant Velocity Field

Initially, we have a blob of fluid (assuming 2D), which is being considered by another fluid. The radius of the blob is 0.15 mm and it is initially centered at $(-0.25, 0.25)$ in a unit square domain. Wall boundary condition is used at all sides. Convection by three different constant velocity vectors is tested: $(U = 1, V = 0)$, $(U = 0, V = -1)$, and $(U = 1, V = -1)$. The results are shown in Figs. 4.4, 4.5, and 4.6. No deformation of droplet but only pure movement is observed in all cases, which illustrates that there is no artificial movement when the driving velocity field is constant.

4.3.2 Droplet Deformation Due to A Vortex Velocity Field

Using the same conditions as in Rider [52], the simulation of the time reversed single vortex flow is presented. A droplet of fluid with a radius of 0.15 mm, initially centered at (0.5, 0.75) in a unit square domain, is deformed by a vortex velocity field defined by the following stream function:

$$\psi(x, y) = \frac{1}{\pi} \sin^2[\pi x] \sin^2[\pi y] \cos(\pi t/T), \tag{4.13}$$

where T is the period and the velocity components are defined by

$$U = -\frac{\partial \psi}{\partial y}, \quad V = \frac{\partial \psi}{\partial x}. \tag{4.14}$$

The droplet is water and air surrounds it. A surface tension coefficient of $0.1 N/m$ is

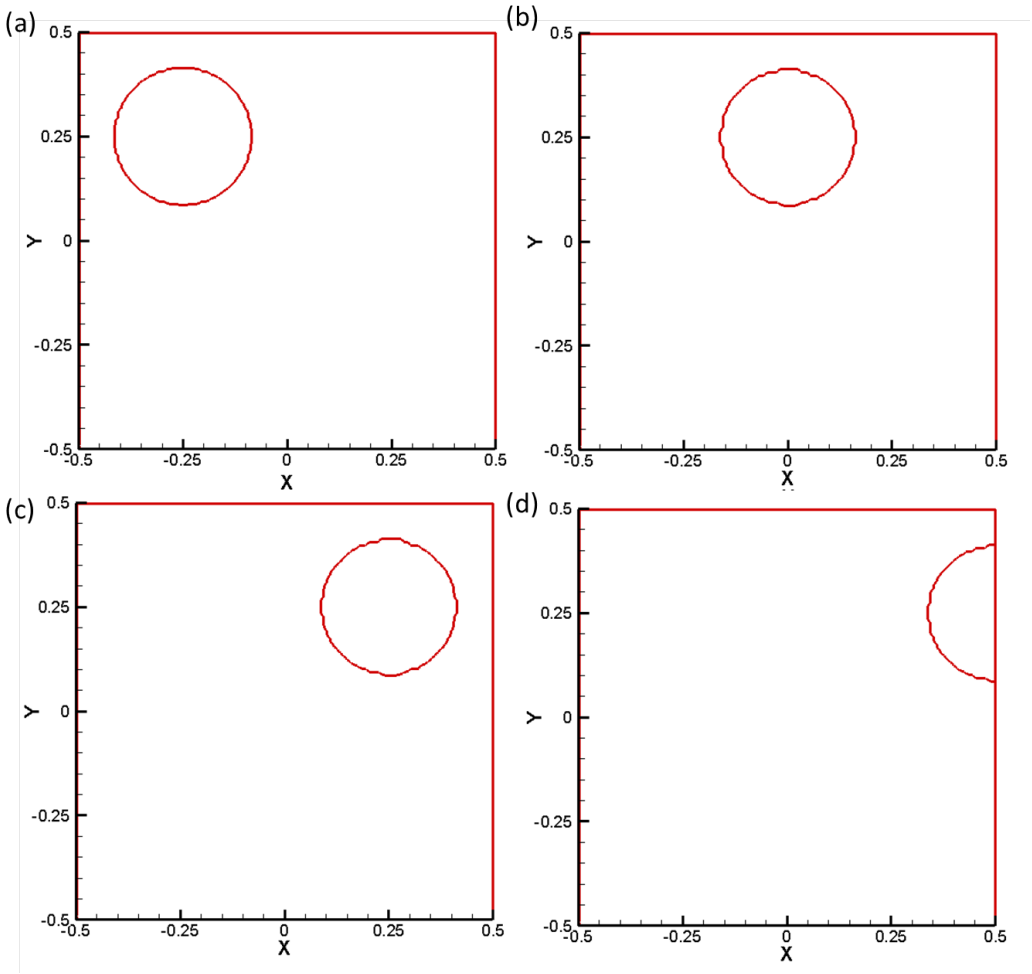

Figure 4.4: Convection of a blob of fluid under the velocity ($U = 1$,$V = 0$) in the developed CLSVOF method and a grid of 128×128 at (a) $t = 0s$, (b) $t = 0.25s$, (c) $t = 0.5s$, and (d)$t = 0.75s$

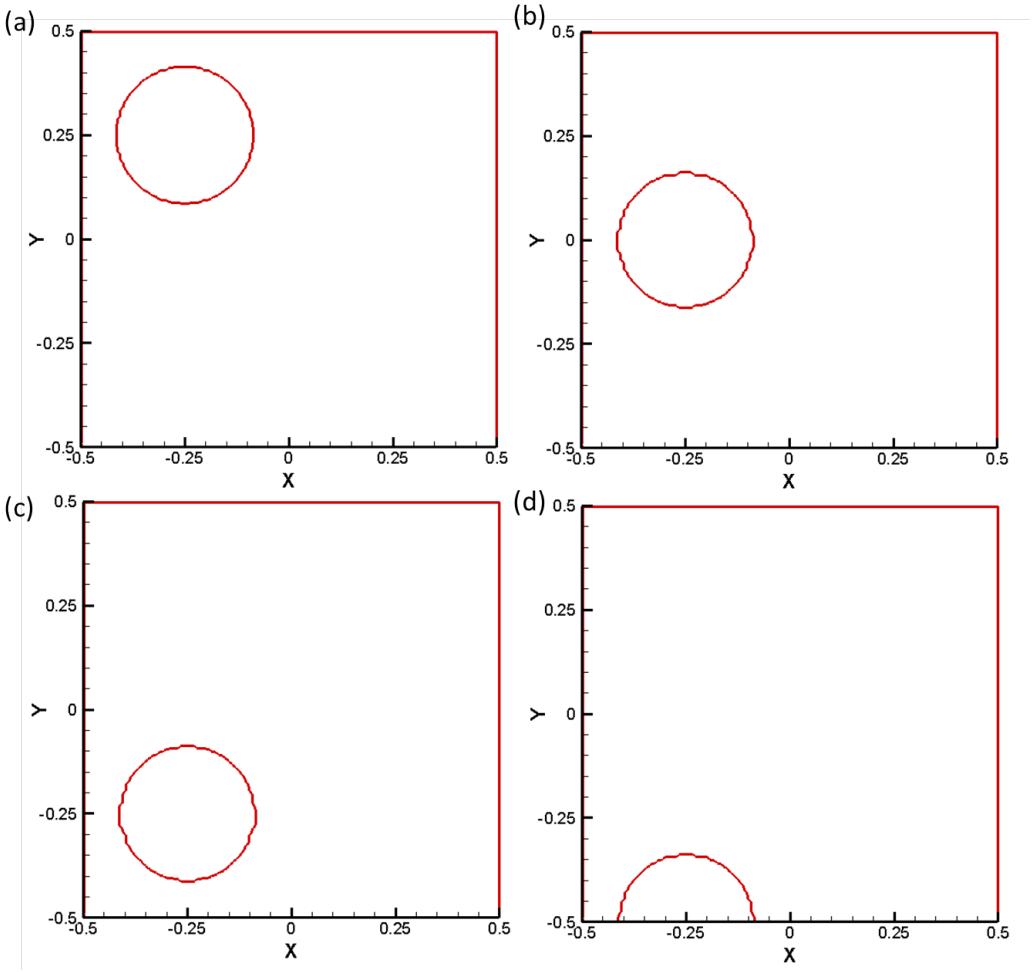

Figure 4.5: Convection of a blob of fluid under the velocity ($U = 0$,$V = -1$) in the developed CLSVOF method and a grid of 128×128 at (a) $t = 0s$, (b) $t = 0.25s$, (c) $t = 0.5s$, and (d)$t = 0.75s$

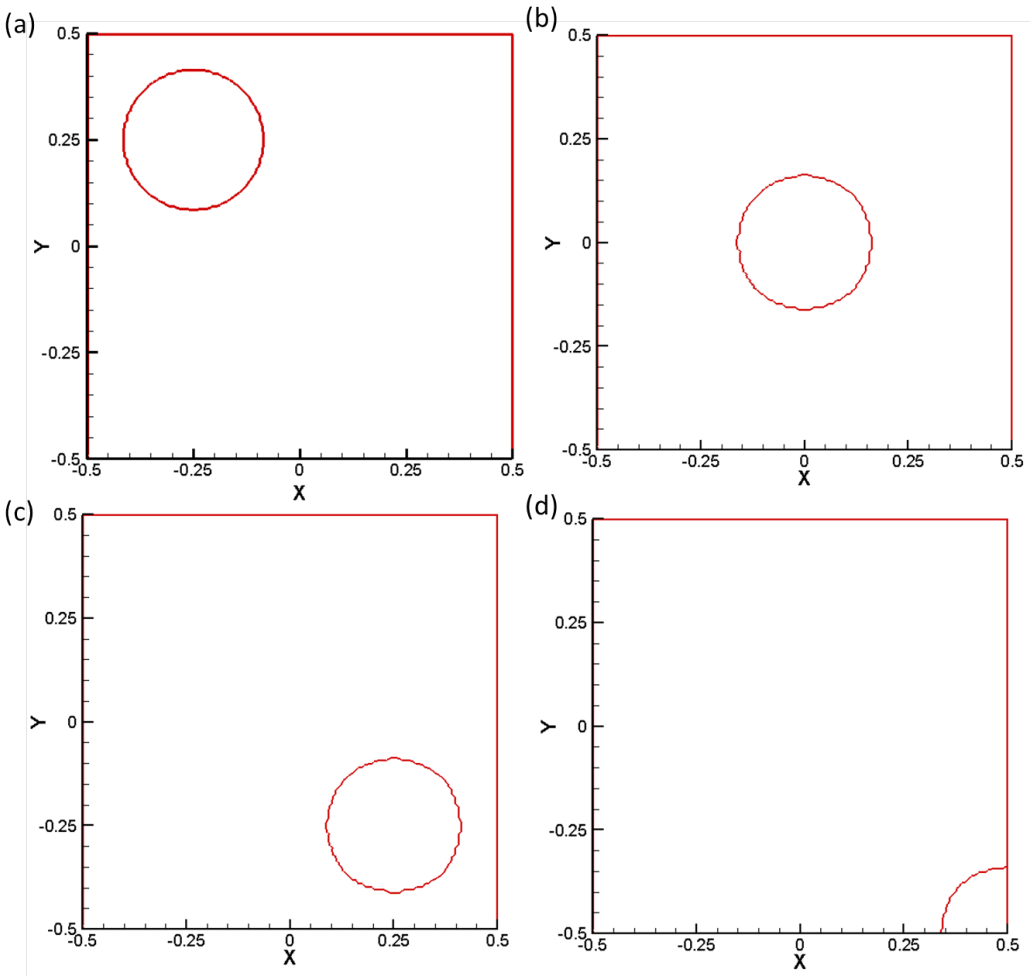

Figure 4.6: Convection of a blob of fluid under the velocity ($U = 1$,$V = -1$) in the developed CLSVOF method and a grid of 128×128 at (a) $t = 0s$, (b) $t = 0.25s$, (c) $t = 0.5s$, and (d)$t = 0.75s$

used for air-water. A no-slip wall boundary condition is used for all boundaries. Under the formation of the time periodic vortex velocity field, the largest deformation of the droplet of fluid happens at $t = T/2$ and it goes back to its initial shape at $t = T$. This test can be used to access the code's ability to resolve the thin fluid filaments formed by interface stretching. The deformation reaches different levels for different time periods. Three different time periods were tested for the developed CLSVOF method: $T = 2.0s$, $T = 6.0$, and $T = 12.0s$, using three different mesh densities: 128×128, 256×256, and 512×512. Since detail simulation results of $T = 6.0s$ is available in Nichita's developed CLSVOF method [49], here we compare the results of $T = 6.0$ obtained from the developed CLSVOF method in this paper to the CLSVOF results from FLUENT and the available data in Nichita's paper [49].

Figs. (4.7), (4.8), and (4.9) show the interface deformations with a time period of $T = 2$ on a grid of 128×128, and 256×256, and 512×512 mesh points, respectively. Figs. (4.10) and (4.12) show the interface deformation with a time period of $T = 6$ on a grid of 128×128, and 256×256, and 512×512 mesh points, respectively. Figs. (4.19) and (4.21) show the interface deformation with a time period of $T = 12$ on a grid of 128×128, and 256×256, and 512×512 mesh points, respectively. All the results show that the deformation of the droplet increases as the time period increases and breakup happens at large time periods, e.g. $T = 12$. When refining the mesh, the tip of the filament becomes sharper and the difference between (a) and (c) is smaller. When the mesh is 512×512, the droplet returns perfectly to its initial shape. Also, for the simulations with a time period of $T = 6$, the results of FLUENT are shown in Fig. (4.13) on a grid of 128×128 mesh points, and the results from Nichita's simulations [49] are shown in Figs. (4.16), (4.17), and (4.18). We can see that the results of the developed CLSVOF method agree with those by FLUENT and Nichita.

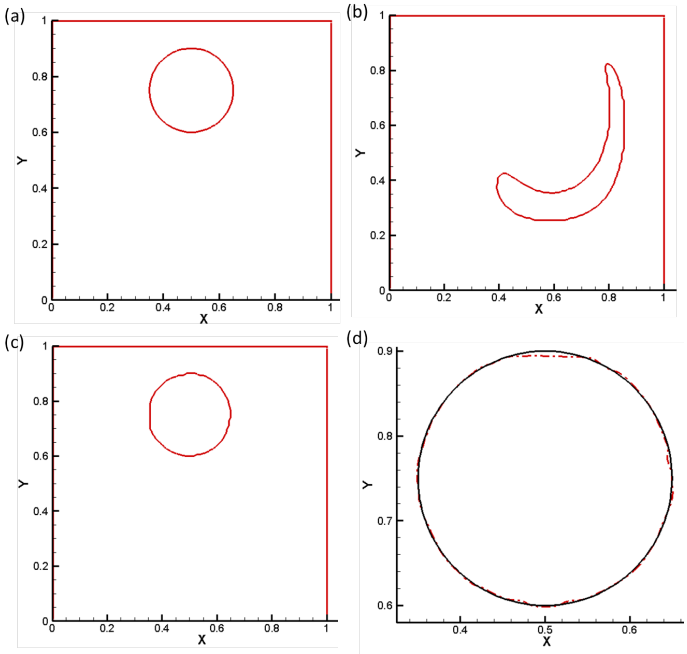

Figure 4.7: Deformation of a droplet of fluid convected by a vortex field of $\psi(x,y)=\frac{1}{\pi}\sin^2[\pi x]\sin^2[\pi y]\cos(\pi t/2)$ in the developed CLSVOF method and a grid of 128×128 at (a) $t = 0s$ (b) $t = 1s$ (c) $t = 2s$ (d) enlarged comparison between (a) and (c)

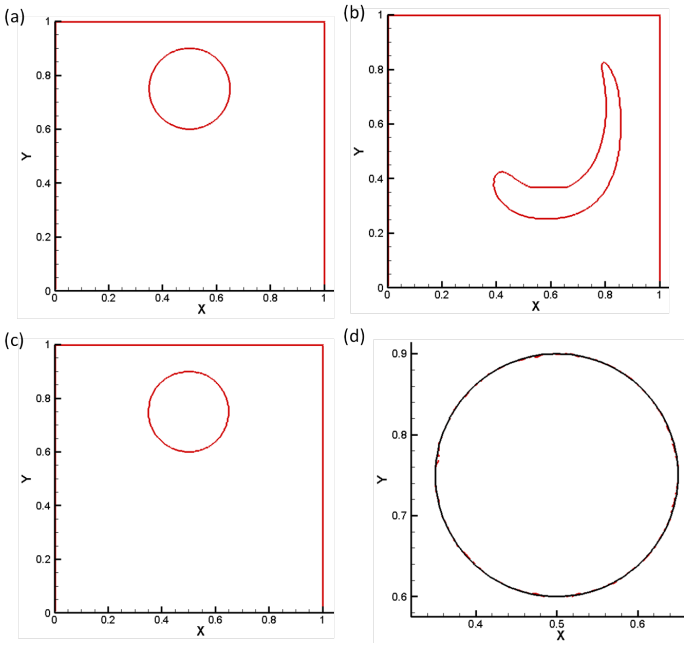

Figure 4.8: Deformation of a droplet of fluid convected by a vortex field of $\psi(x,y)=\frac{1}{\pi}\sin^2[\pi x]\sin^2[\pi y]\cos(\pi t/2)$ in the developed CLSVOF method and a grid of 256×256 at (a) $t = 0s$ (b) $t = 1s$ (c) $t = 2s$ (d) enlarged comparison between (a) and (c)

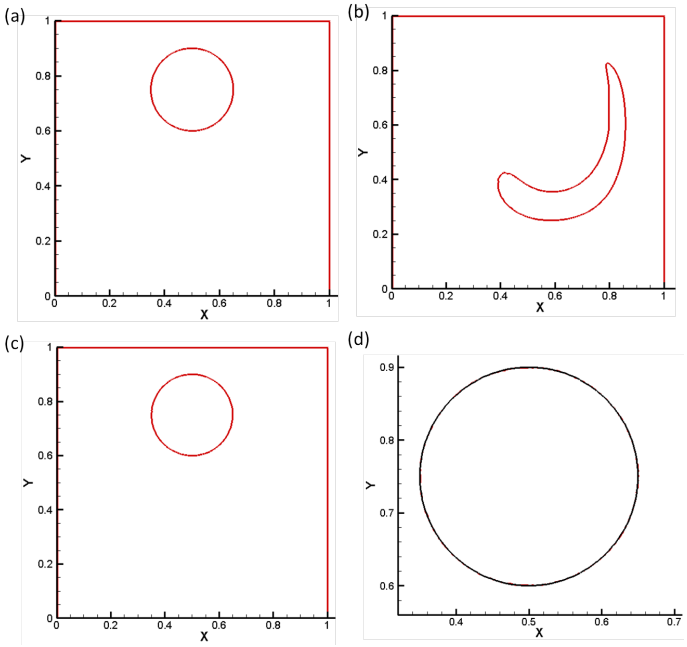

Figure 4.9: Deformation of a droplet of fluid convected by a vortex field of ψ(x,y)=$\frac{1}{\pi}$ $\sin^2[\pi x]\sin^2[\pi y]\cos(\pi t/2)$ in the developed CLSVOF method and a grid of 512×512 at (a) $t = 0s$ (b) $t = 1s$ (c) $t = 2s$ (d) enlarged comparison between (a) and (c)

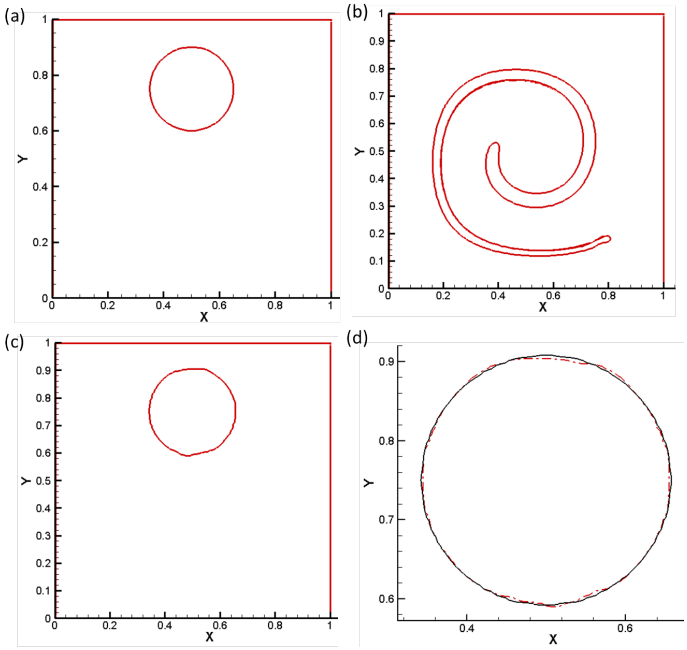

Figure 4.10: Deformation of a droplet of fluid convected by a vortex field of ψ(x,y)=$\frac{1}{\pi}$ $\sin^2[\pi x]\sin^2[\pi y]\cos(\pi t/6)$ in the developed CLSVOF method and a grid of 128×128 at (a) $t = 0s$ (b) $t = 3s$ (c) $t = 6s$ (d) enlarged comparison between (a) and (c)

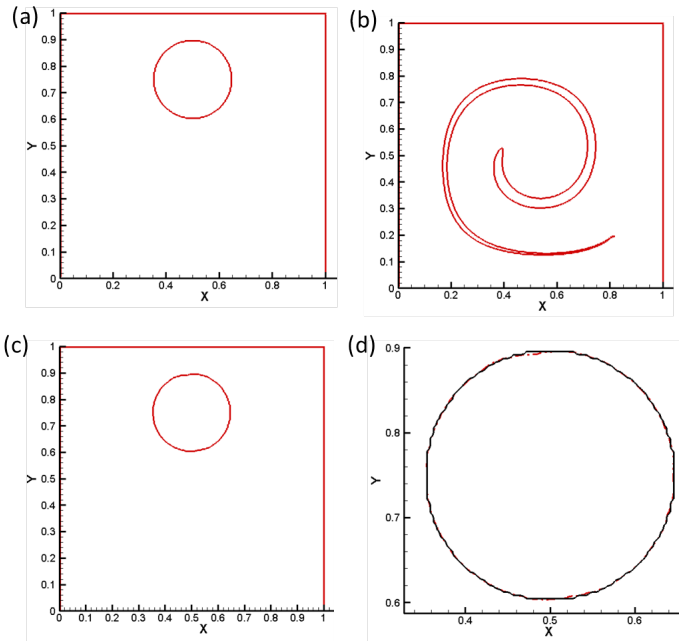

Figure 4.11: Deformation of a droplet of fluid convected by a vortex field of ψ(x,y)=$\frac{1}{\pi}$ $\sin^2[\pi x]\sin^2[\pi y]\cos(\pi t/6)$ in the developed CLSVOF method and a grid of 256×256 at (a) $t = 0s$ (b) $t = 3s$ (c) $t = 6s$ (d) enlarged comparison between (a) and (c)

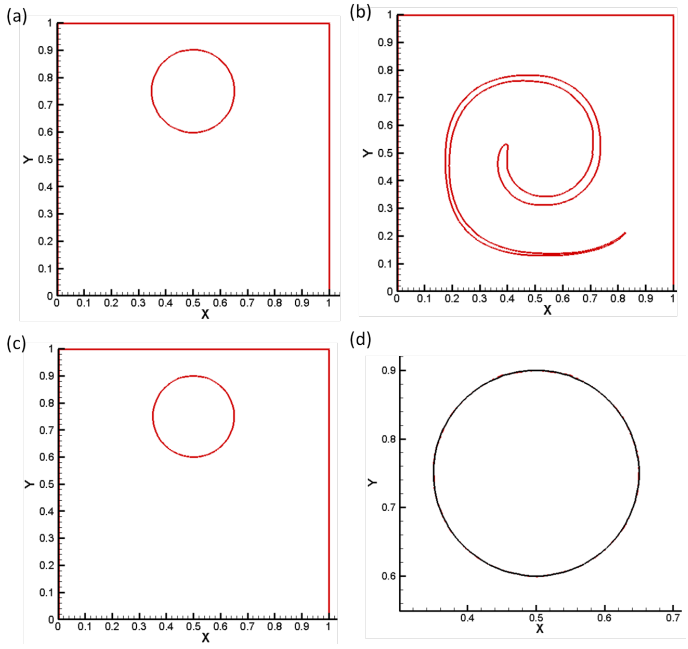

Figure 4.12: Deformation of a droplet of fluid convected by a vortex field of ψ(x,y)=$\frac{1}{\pi}$ $\sin^2[\pi x]\sin^2[\pi y]\cos(\pi t/6)$ in the developed CLSVOF method and a grid of 512×512 at (a) $t = 0s$ (b) $t = 3s$ (c) $t = 6s$ (d) enlarged comparison between (a) and (c)

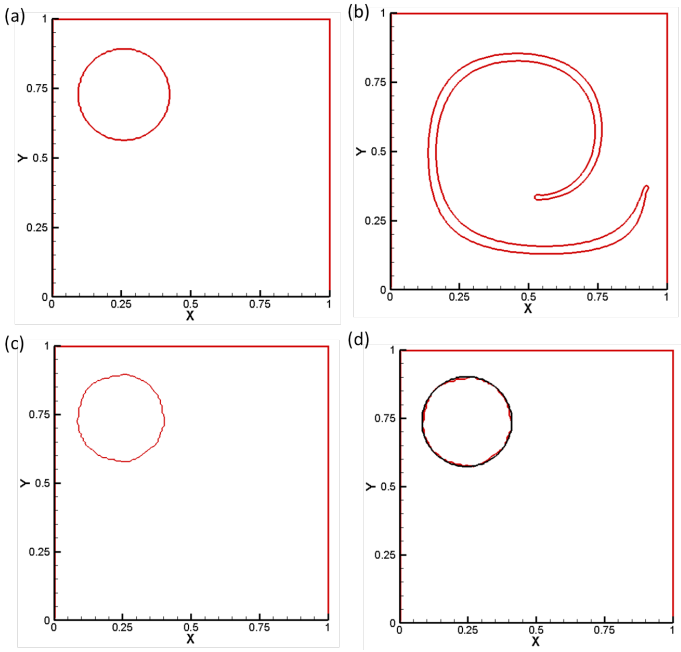

Figure 4.13: Deformation of a droplet of fluid convected by a vortex field of $\psi(x,y)=\frac{1}{\pi}\sin^2[\pi x]\sin^2[\pi y]\cos(\pi t/6)$ in the CLSVOF method in ANSYS FLUENT and a grid of 128×128 at (a) $t = 0s$ (b) $t = 3s$ (c) $t = 6s$ (d) enlarged comparison between (a) and (c)

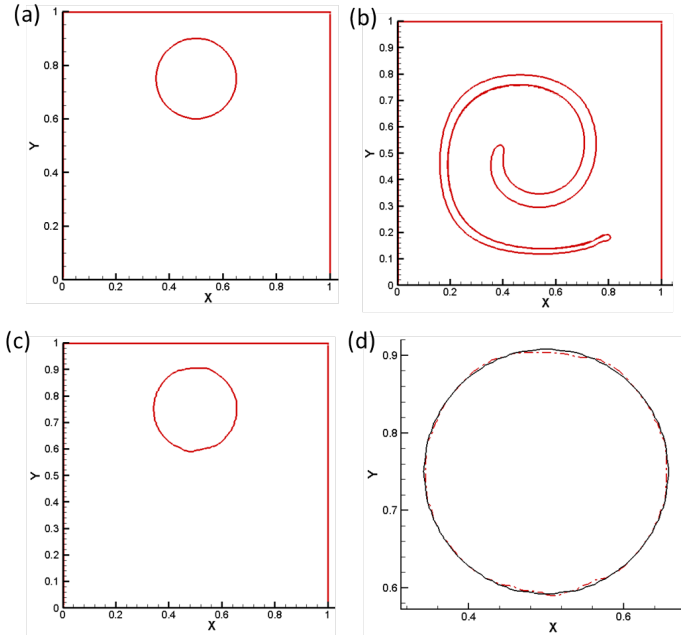

Figure 4.14: Deformation of a droplet of fluid convected by a vortex field of $\psi(x,y)=\frac{1}{\pi}\sin^2[\pi x]\sin^2[\pi y]\cos(\pi t/6)$ in the CLSVOF method in ANSYS FLUENT and a grid of 256×256 at (a) $t = 0s$ (b) $t = 3s$ (c) $t = 6s$ (d) enlarged comparison between (a) and (c)

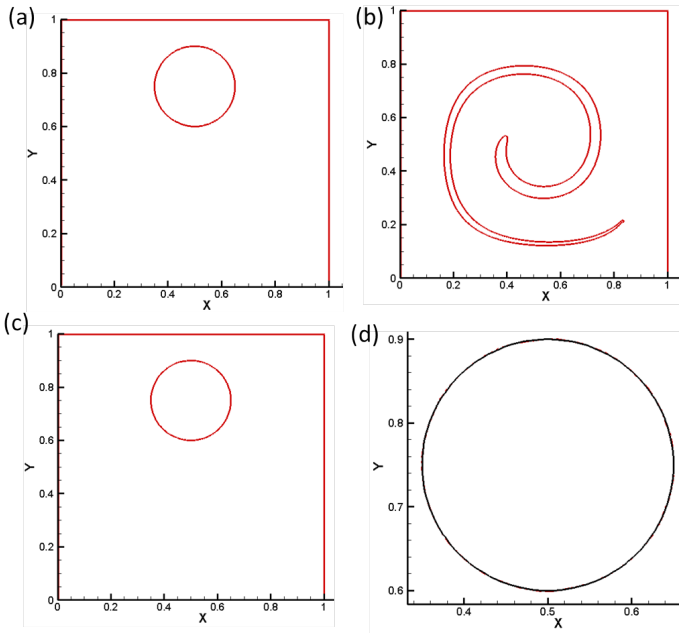

Figure 4.15: Deformation of a droplet of fluid convected by a vortex field of ψ(x,y)=$\frac{1}{\pi}\sin^2[\pi x]\sin^2[\pi y]\cos(\pi t/6)$ in the CLSVOF method in ANSYS FLUENT and a grid of 512×512 at (a) $t = 0s$ (b) $t = 3s$ (c) $t = 6s$ (d) enlarged comparison between (a) and (c)

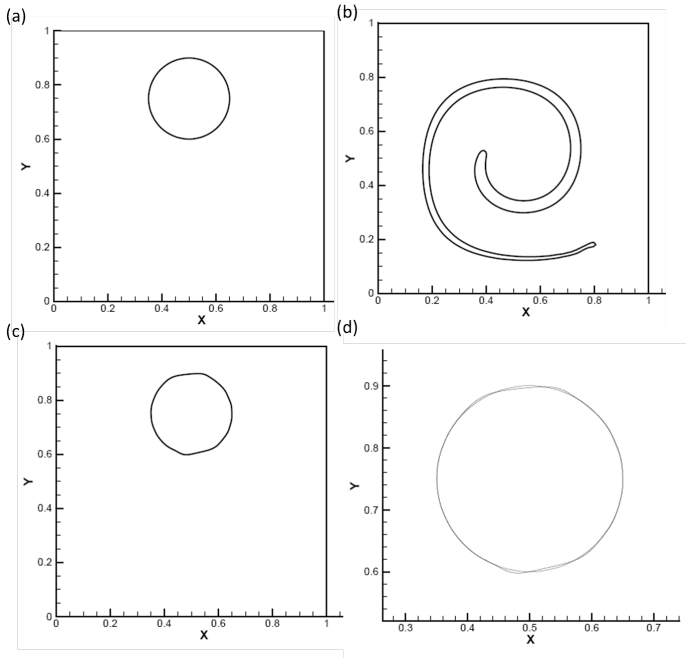

Figure 4.16: Deformation of a droplet of fluid convected by a vortex field of ψ(x,y)=$\frac{1}{\pi}\sin^2[\pi x]\sin^2[\pi y]\cos(\pi t/6)$ from the Nichita's simulation and a grid of 128×128 at (a) $t = 0s$ (b) $t = 3s$ (c) $t = 6s$ (d) enlarged comparison between (a) and (c)

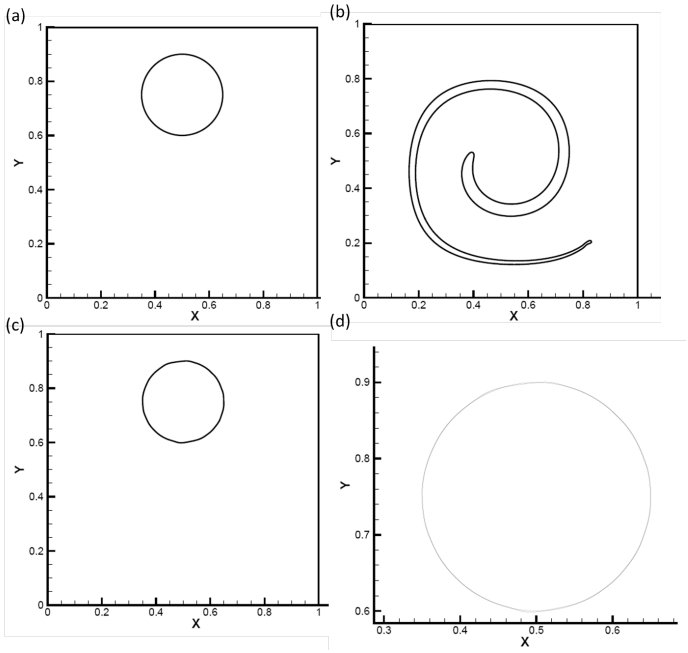

Figure 4.17: Deformation of a droplet of fluid convected by a vortex field of ψ(x,y)=$\frac{1}{\pi}\sin^2[\pi x]\sin^2[\pi y]\cos(\pi t/6)$ from the Nichita's simulation and a grid of 256×256 at (a) $t = 0s$ (b) $t = 3s$ (c) $t = 6s$ (d) enlarged comparison between (a) and (c)

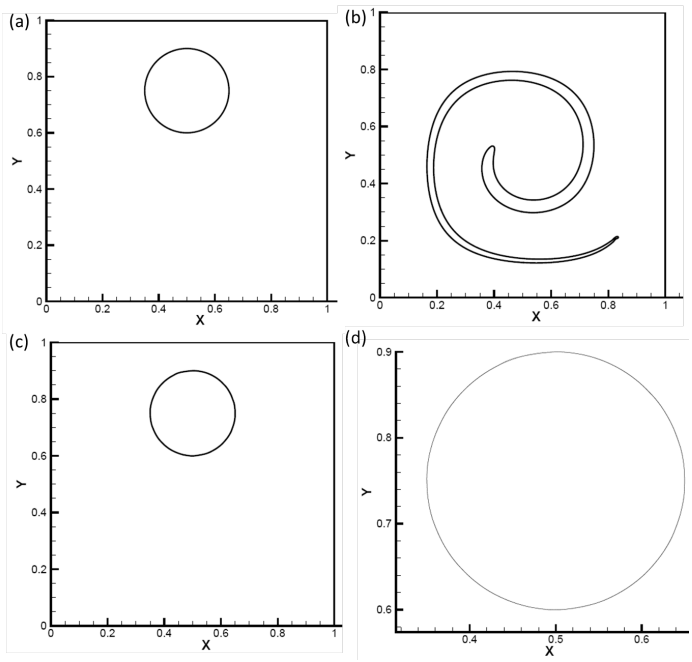

Figure 4.18: Deformation of a droplet of fluid convected by a vortex field of ψ(x,y)=$\frac{1}{\pi}\sin^2[\pi x]\sin^2[\pi y]\cos(\pi t/6)$ from the Nichita's simulation and a grid of 512×512 at (a) $t = 0s$ (b) $t = 3s$ (c) $t = 6s$ (d) enlarged comparison between (a) and (c)

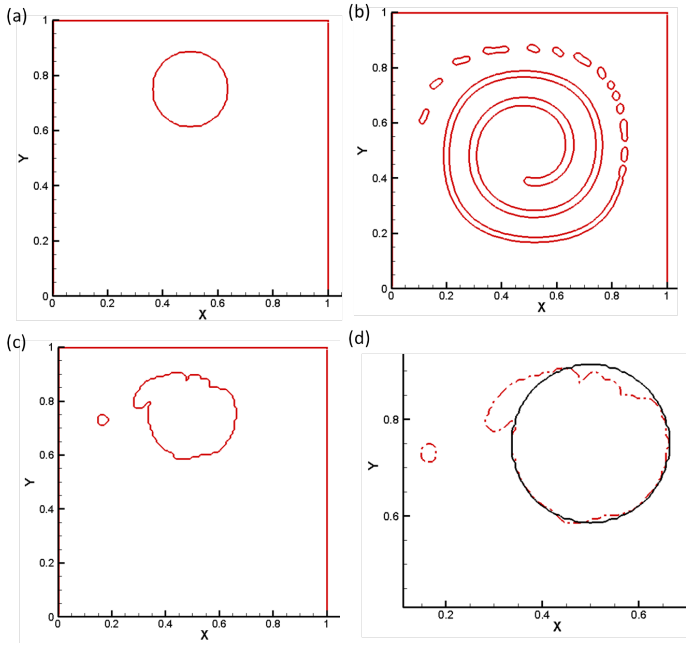

Figure 4.19: Deformation of a droplet of fluid convected by a vortex field of $\psi(x,y)=\frac{1}{\pi}\sin^2[\pi x]\sin^2[\pi y]\cos(\pi t/12)$ in the developed CLSVOF method and a grid of 128×128 at (a) $t = 0s$ (b) $t = 6s$ (c) $t = 12s$ (d) enlarged comparison between (a) and (c)

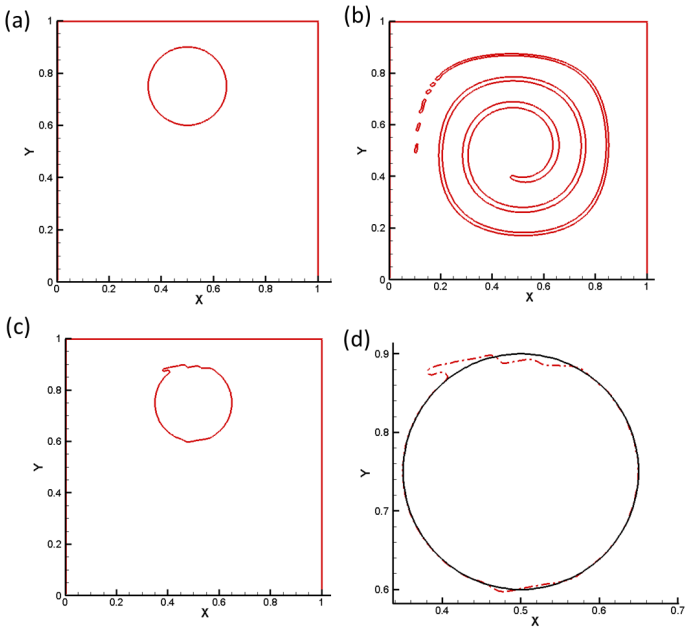

Figure 4.20: Deformation of a droplet of fluid convected by a vortex field of $\psi(x,y)=\frac{1}{\pi}\sin^2[\pi x]\sin^2[\pi y]\cos(\pi t/12)$ in the developed CLSVOF method and a grid of 256×256 at (a) $t = 0s$ (b) $t = 6s$ (c) $t = 12s$ (d) enlarged comparison between (a) and (c)

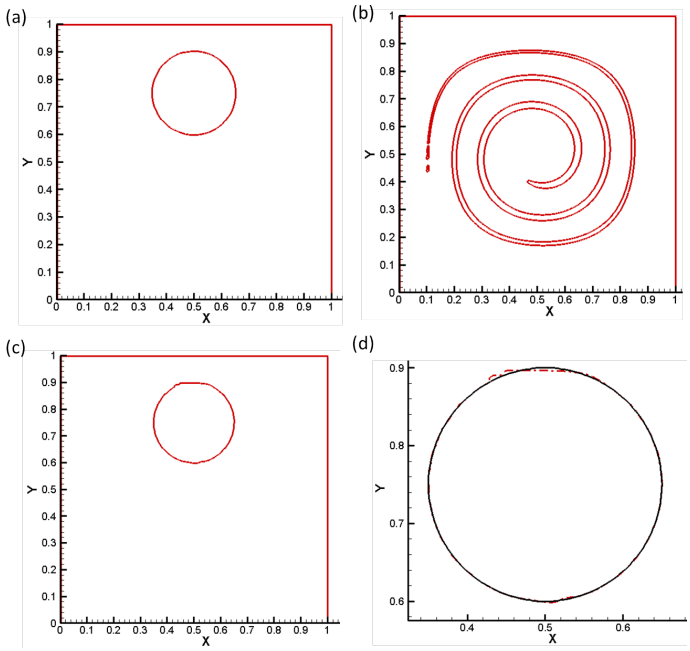

Figure 4.21: Deformation of a droplet of fluid convected by a vortex field of ψ(x,y)=$\frac{1}{\pi}\sin^2[\pi x]\sin^2[\pi y]\cos(\pi t/12)$ in the developed CLSVOF method and a grid of 512×512 at (a) $t = 0s$ (b) $t = 6s$ (c) $t = 12s$ (d) enlarged comparison between (a) and (c)

4.4 Two Dimensional Jet Simulations Based on FLUENT Code

Before starting the simulation of mercury jet for the Muon Collider project, two dimensional jet is simulated first to verify the FLUENT code.

4.4.1 Two Dimensional Laminar Round Jet Flow

The two dimensional jet simulation studied in this case is a laminar round jet with the advantage of analytical solution given by Schlichting[109]. The problem is shown in Fig. 4.22. Air emerges into still air issuing from a circular orifice at $x = 0$. At any cross section, the momentum flux is assumed constant. Air jet spreads at a constant pressure of 1 bar. Temperature is constant at 300 K. The Reynolds number based on the inlet velocity (0.64 m/s) is 400. The density of air is $1.16kg/m^3$ and kinematic viscosity is $1.610 - 5m^2/s$.

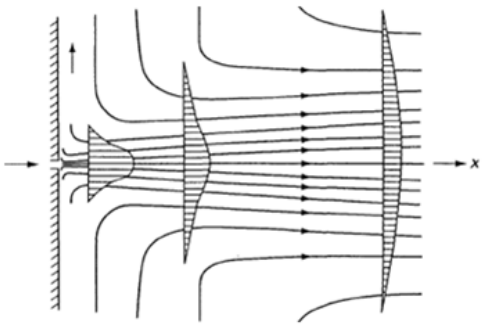

Figure 4.22: Typical 2D laminar round jet streamline pattern

The governing equations for the 2D laminar round jet flow are

$$\frac{\partial \overline{u}}{\partial x} + \frac{1}{r}\frac{\partial (r\overline{v})}{\partial r} = 0 \tag{4.15}$$

$$\overline{u}\frac{\partial \overline{u}}{\partial x} + \overline{v}\frac{\partial \overline{u}}{\partial r}\frac{1}{r}\frac{\partial (r\overline{v})}{\partial r} \approx \frac{\nu}{r}\frac{\partial}{\partial r}(r\frac{\partial \overline{u}}{\partial r}) \tag{4.16}$$

The analytical solution is

$$\overline{u} = \frac{3J}{8\pi\mu x}(1 + \frac{C^2\eta^2}{4})^{-2}, \tag{4.17}$$

where $C \equiv (\frac{3J}{16\pi\rho\nu^2})^{1/2}$, $J = \rho\int_{-\infty}^{\infty} u^2 2\pi r dr$, and $\eta = \frac{r}{x}$.

The boundary conditions for the 2D laminar round jet are shown in Fig. 4.23. Constant axial velocity is assumed at the velocity inlet. The edges at the inlet side ate set as a non-slip wall boundary condition. Considering the round jet, axis boundary condition is used for the center line and only halved model for the simulation. The results of the 2D laminar round jet simulation are analyzed as below. Figure 4.24 shows the center line velocity ($\overline{u}_c$) distribution with the distance (x) away from the jet nozzle. $\overline{u}_c$ drops as x increases, roughly following the order of $1/x$. The radial distribution of mean velocity ($\overline{u}$) at locations $x = 10d$,$x = 30d$, $x = 50d$, $x = 70d$, and $x = 90d$ are shown in Fig. 4.25. The numerical $\overline{u}$ is very close to the theoretical $\overline{u}$ at $x = 30d$, but the difference becomes bigger at downstream locations. Jet half-width is defined as the radial distance from the axis to the position at the which the absolute value of the axial velocity drops to half its value on the axis. The relationship between jet half-width and distance from the jet nozzle is mostly linear, which can be seen

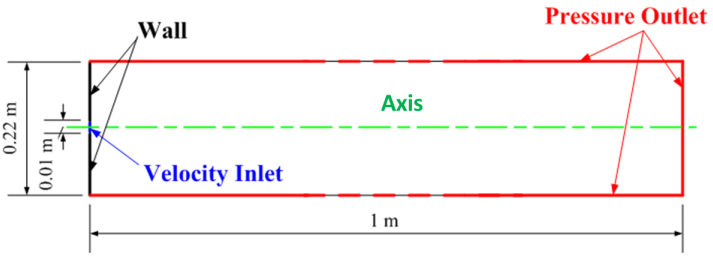

Figure 4.23: The boundary conditions for 2D laminar round jet

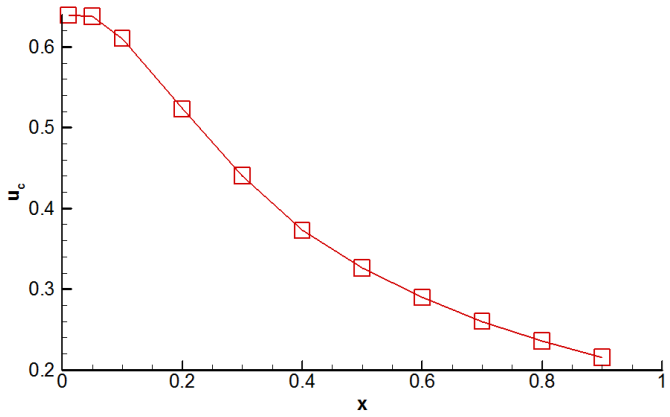

Figure 4.24: The distribution of the center line velocity of the 2D round jet with axial distance

in Fig. 4.26. Self-similarity distribution can be observed in Fig.4.27. Fig. 4.28 shows the changes in the momentum thickness at different locations downstream of the jet. It can be seen that the rate of change of the momentum thickness reduces downstream of the jet.

4.4.2 Two Dimensional Laminar Plane Jet Flow

Schlichting [109] reported the analytical solutions for a 2D laminar plane jet. The problem is shown in Fig. 4.29. Air emerges into a still air from a 2D slot at $x = 0$. At any cross section, the momentum flux is constant. Air jet spreads at a constant pressure of 1 bar. Temperature is constant at 300 K. The Reynolds number based on the inlet velocity (0.64 m/s) is 400. The density of air is 1.225 kg/m^3 and kinematic viscosity is 1.4607310^{-5} m^2/s.

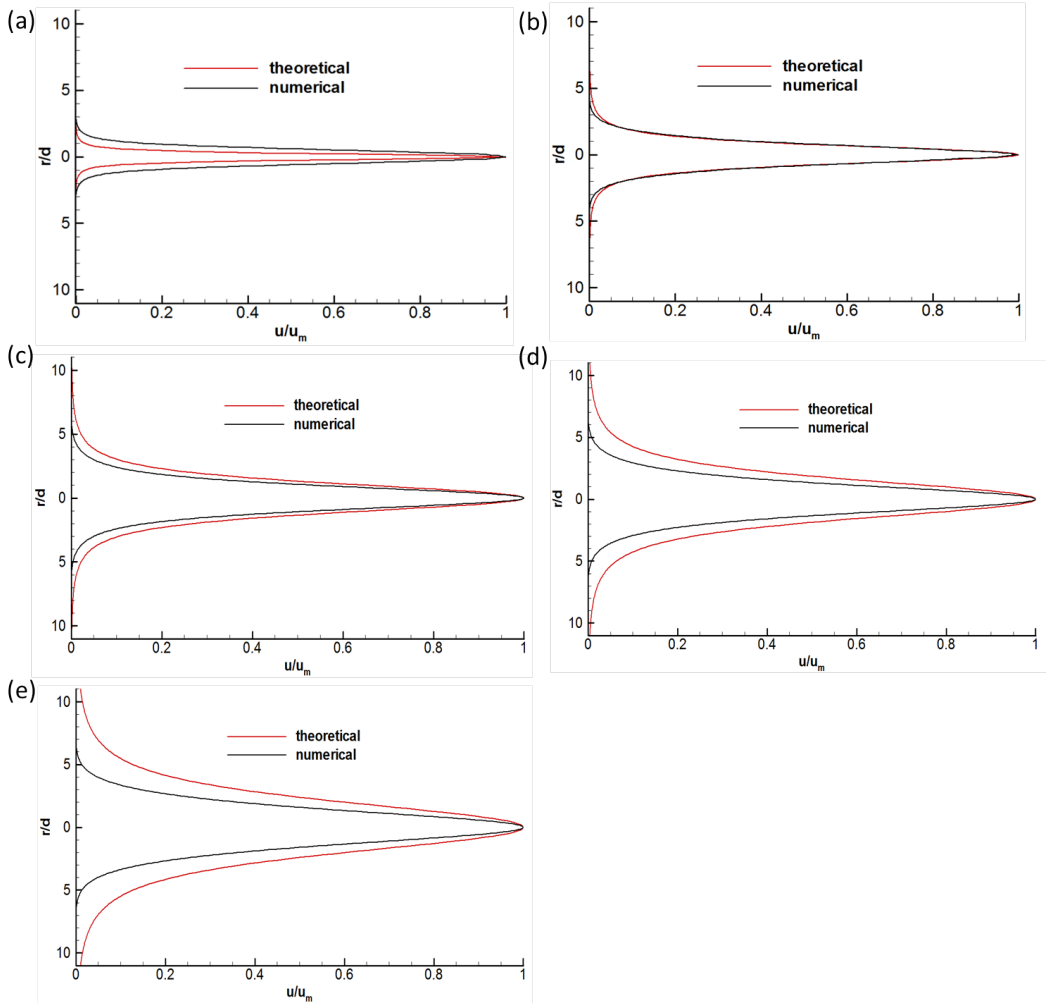

Figure 4.25: Radial distribution of the mean stream velocity of the 2D round jet at (a) $x/d = 10$, (b)$x/d = 30$, (c) $x/d = 50$, (d) $x/d = 70$, and (e) $x/d = 90$. Note that $\overline{u}$ is normalized by $\overline{u}_{\max}$ ($\overline{u}_{\max}$ =max($\overline{u}$)) and radius r by jet inlet diameter d.

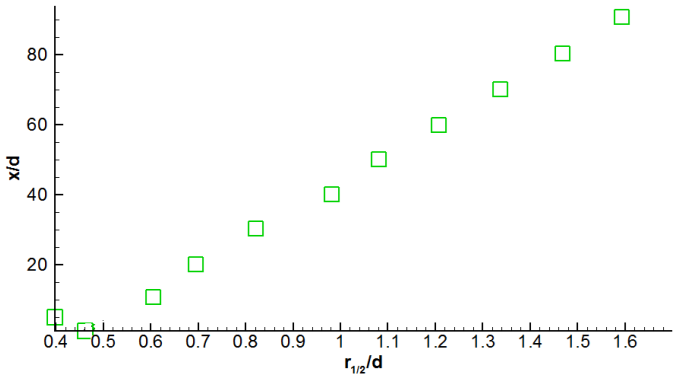

Figure 4.26: Axial distribution of the half-width of 2D round jet. Note that $r_{1/2}$ and distance x are normalized by jet inlet diameter d.

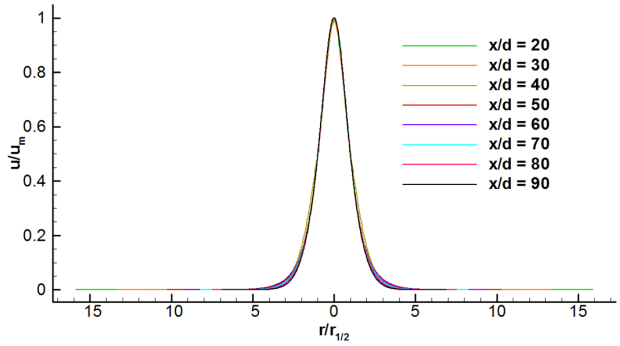

Figure 4.27: 2D round jet self-similarity

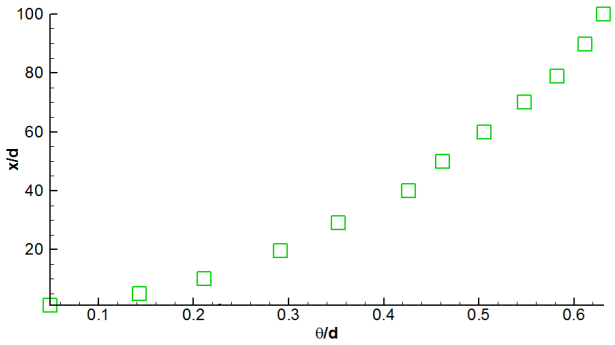

Figure 4.28: The changes in the momentum thickness of 2D round jet with axial distance.

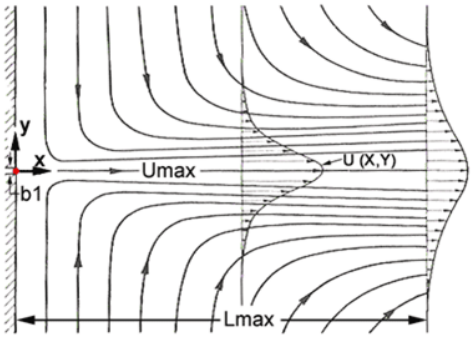

Figure 4.29: Typical 2D laminar plane jet is streamline pattern

The governing equations for the 2D laminar plane jet are

$$\frac{\partial \overline{u}_x}{\partial x} + \frac{\partial \overline{u}_y}{\partial y} = 0 \tag{4.18}$$

$$\overline{u}_x \frac{\partial \overline{u}_x}{\partial x} + \overline{u}_y \frac{\partial \overline{u}_y}{\partial y} \approx \nu \frac{\partial^2 \overline{u}_y}{\partial y^2} \tag{4.19}$$

The analytical solution is

$$\overline{u}_x = (\frac{3J^2}{32\nu x})^{1/3} \sec h^2(\gamma), \tag{4.20}$$

$$\overline{u}_y = (\frac{J\nu}{6x^2})^{1/3} [2\gamma \sec h^2(\gamma) - \tanh(\gamma)], \tag{4.21}$$

where $\gamma \equiv (\frac{J}{48\nu^2})^{1/3} \frac{y}{x^{2/3}}$, and $J = \int_{-\infty}^{\infty} u^2 dy$.

The boundary conditions for the 2D laminar plane jet are shown in Fig. 4.30. Constant axial velocity is assumed at the inlet. The edges at the inlet side are set as non-slip condition. Assuming the symmetry of the jet, symmetry boundary conditions are used at the center line, and only half of the model are simulated. The results of the 2D laminar plane jet simulation are analyzed the same way as those of the 2D laminar round jet. Figure 4.31 shows the distribution of the center line velocity ($\overline{u}_c$) with the distance (x) away from the jet nozzle. $\overline{u}_c$ drops with x roughly following the order $x^{1/3}$. The radial distribution of mean stream velocity ($\overline{u}$) at locations $x = 10d$,$x = 30d$, $x = 50d$, $x = 70d$, and $x = 90d$ are shown in Fig. 4.32. The numerically observed $\overline{u}$ is very close to theoretical $\overline{u}$ at $x = 30d$, but diverges from the analytical solution downstream. The relationship between jet half-width and the distance from the jet nozzle is mostly linear, which can be seen in Fig. 4.33. Self-similarity can be observed in Fig.4.34. Fig. 4.35 shows the changes in momentum thickness at different locations downstream of the jet. The rate of change of momentum thickness reduces downstream of the jet.

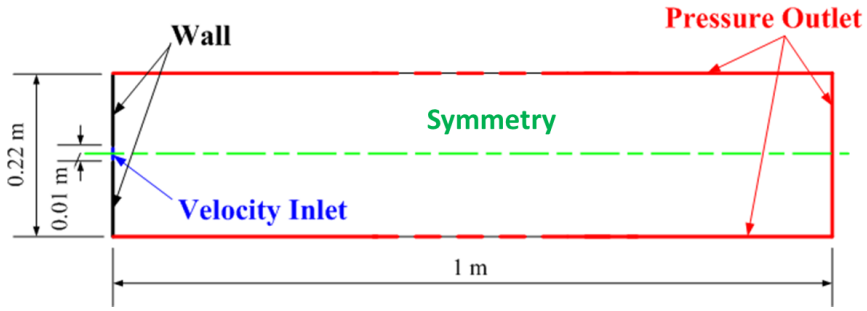

Figure 4.30: Boundary conditions settings for 2D laminar plane jet

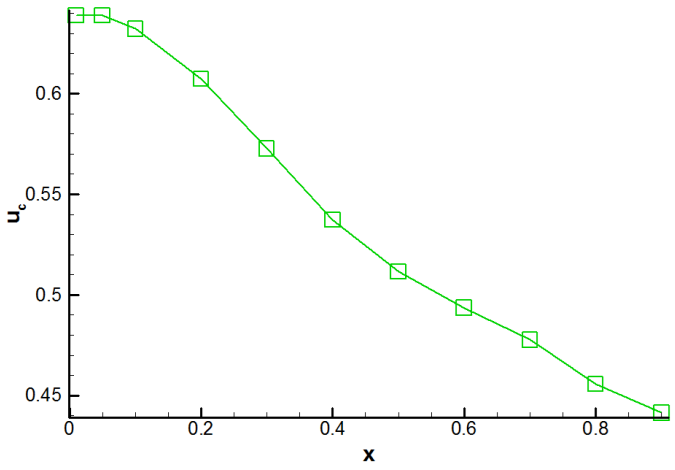

Figure 4.31: Variation of the center line velocity of the 2D plane jet with axial distance

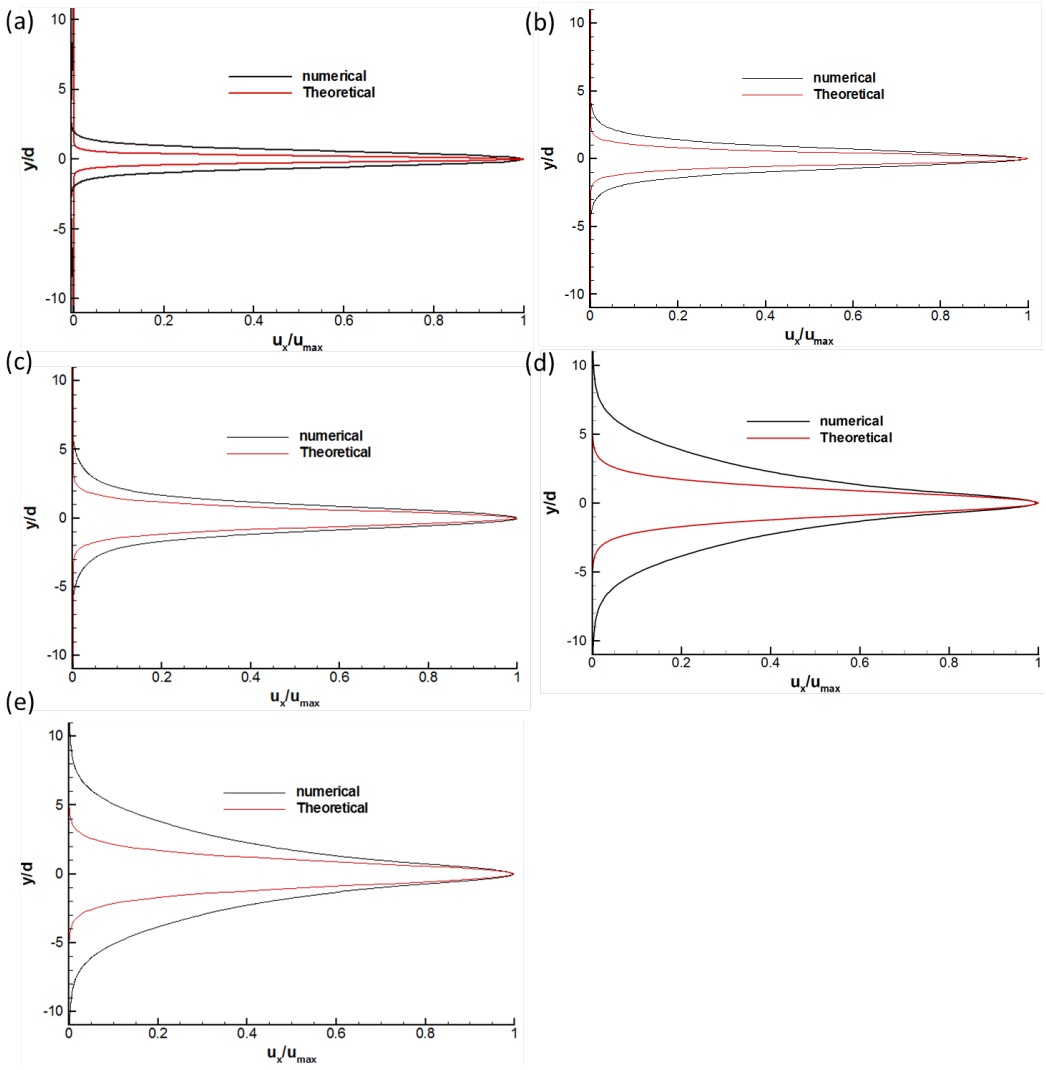

Figure 4.32: Radial distribution of the mean axial velocity in a 2D plane jet at (a) $x/d = 10$, (b)$x/d = 30$, (c) $x/d = 50$, (d) $x/d = 70$, and (e) $x/d = 90$. Note that $\overline{u}$ is normalized by $\overline{u}_{\max}$ ($\overline{u}_{\max}$ =max($\overline{u}$)) and radius r by jet inlet diameter d.

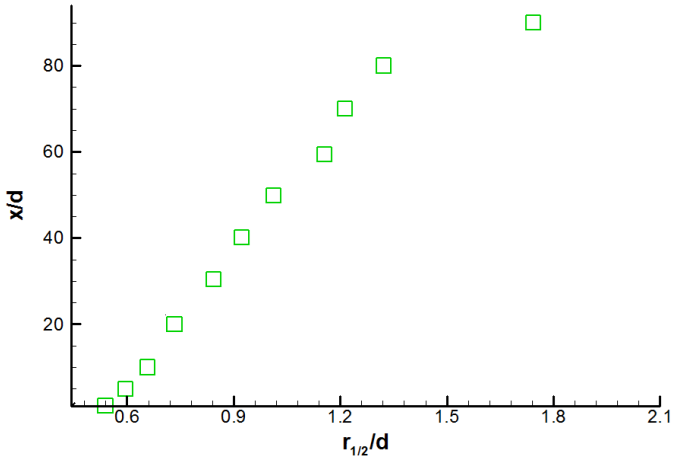

Figure 4.33: Axial distribution of the half-width of 2D plane jet. Note that $r_{1/2}$ and distance x are normalized by jet inlet diameter d.

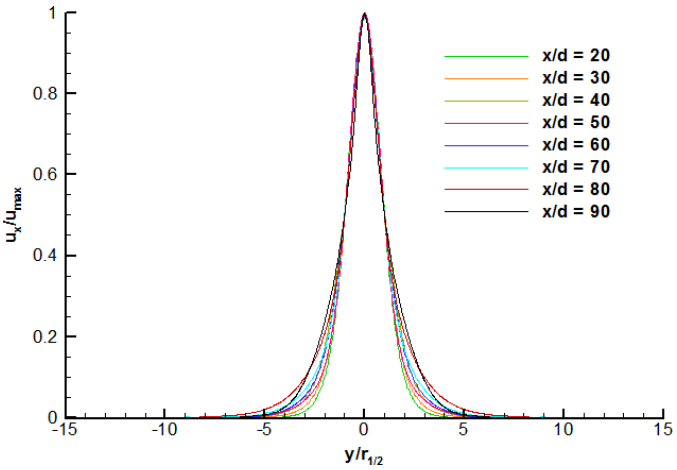

Figure 4.34: 2D plane jet self-similarity

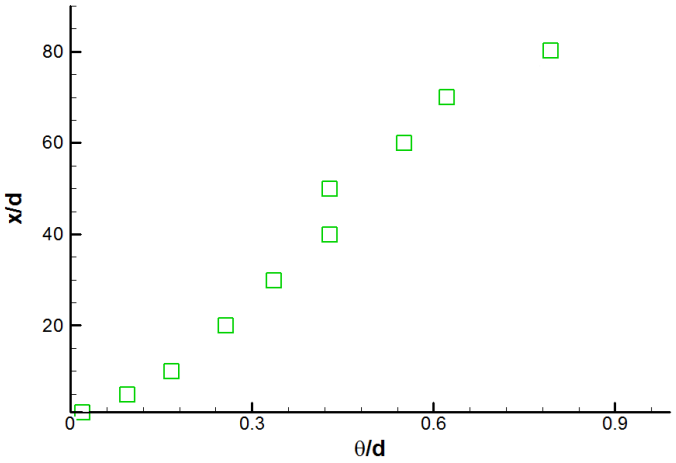

Figure 4.35: The axial distribution of the momentum thickness of 2D plane jet with axial distance.

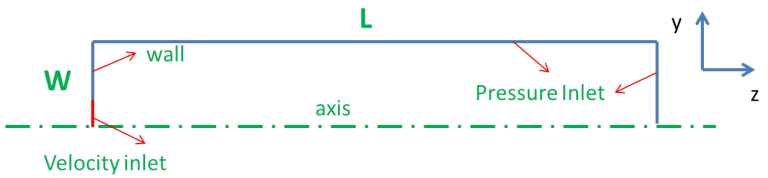

Figure 4.36: The boundary conditions for the 2D turbulent jet simulations

4.4.3 Two Dimensional Turbulent Jet Flow

In this section, the ability of FLUENT code to accurately simulate jet breakup is tested. An axis-symmetric liquid jet flows into still gas with a mean bulk velocity of 100 m/s. The inlet jet diameter is $100\mu m$, and the Reynolds number UD/ν_{liquid} is equal to $5,800$. Figure 4.36 shows the boundary conditions of the problem. The jet inlet uses constant velocity of 100 m/s. The width of the computational domain is chosen $3JD$ or $5JD$, where JD is the jet inlet diameter. The length is $50JD$. The properties of the two phases are shown in table 4.1. To define the mesh size, we assume that only a primary break up occurs for the smallest droplet. This implies that the Weber number is at least smaller that 10 [65], which gives a minimum mesh size of $2.36\mu m$:

$$We \equiv \frac{\rho u^2 \triangle x}{\sigma} = 10 \Rightarrow \triangle x = \frac{We\sigma}{\rho u^2} = \frac{10 * 0.06}{696 * 100 * 100} = 2.36\mu m \tag{4.22}$$

With the grid spacing of $2.36\mu m$, the uniform grid size is 127×2120 for a width of $3JD$ and 212×2120 for $5JD$.

Table 4.1: The properties of two phases in the 2D turbulent jet simulation

phase	Density	Viscosity	Surface Tension
Gas	$25kg/m^3$	$4 \times 10^{-7}m^2/s$	$0.06N/m$
Liquid	$696kg/m^3$	$1.724 \times 10^{-6}m^2/s$	

The VOF method is the standard two-phase method in FLUENT code. However, the new version, current ANSYS FLUENT 14.5, has the capability for the CLSVOF method. Here, we apply both VOF and CLSVOF method in FLUENT to simulate the 2D two-

Table 4.2: The locations of the onset of turbulent breakup for $2JD$ simulations in FLUENT codes

Case	Location of onset of turbulent breakup
3 Jet-Diameter in VOF	$14JD$
3 Jet-Diameter in CLSVOF	$1.6JD$
5 Jet-Diameter in VOF	$11.6JD$
5 Jet-Diameter in CLSVOF	$0.4JD$

phase jet flow. Large-eddy simulations (LES) has been widely used to simulate turbulent jet flow and it seems to be a feasible candidate to obtain the necessary unsteady date for the jet [110, 111, 112, 113, 114, 115, 116, 117, 118, 119, 120, 121]. In LES, the scales of turbulent eddies larger than the computational mesh spacing are computed directly. Eddies smaller than the grid spacing (subgrid scale eddies) are modeled. Therefore, more scales of the turbulent eddies can be resolved directly when the mesh is finer, as in the direct numerical simulation (DNS) approach. Here, an implicit large eddy simulation method, which is called monotone integrated large-eddy simulation, or MILES, has been used. Navier-Stokes equations (NSE) are discretized through finite volumes on a fine mesh of the problem, which is finer than that of LES but coarser than that of DNS. Discretization error appears in the division term. There is no explicit filtering in MILES, but the discretization provides top-hat-shaped-kernel implicit filtering [122] ($\frac{1}{\delta V_p}\int_{\Omega_P} f dV$, where δV_p is volume of the mesh unit, Ω_P is the domain of the mesh unit). MILES resolves large eddies and uses physics-capturing numerics.

Figures 4.37, 4.38, and 4.39 are the results of $3JD$ jet case using VOF method, while Figs. 4.40, 4.41 and 4.42 are the results using CLSVOF method. The CLSVOF results show more jet breakups and the location of breakup is closer to the jet inlet. So is the $5JD$ CLSVOF simulation, as shown in Figs. 4.43 through 4.48. Table 4.2 gives the locations of the onset of turbulent breakup for $2D$ turbulent jet simulation with FLUENT.

When $100 < We_l < 1.1 \times 10^6$, $3400 < Re_l < 8.5 \times 10^5$, and $0.001 < OH_l < 0.017$, P.K Wu developed out a surface breakup regime map for turbulent liquid jets in still gases, seen in Fig. 4.49 [123], where We is Weber number, $We = \frac{\rho D U^2}{\sigma}$ and OH is Ohnesorge number,

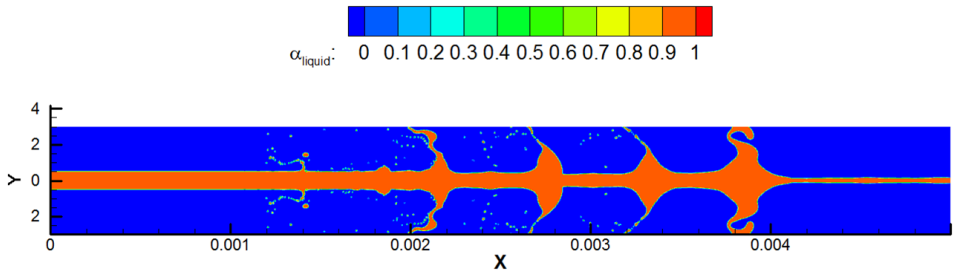

Figure 4.37: The contour of volume of fraction of liquid for the $3JD$ simulation using the VOF method in FLUENT code.

$OH = \frac{\mu}{\sqrt{\rho D \sigma}}$. Also, the equations for the location of the onset/end of turbulent breakup are given in Fig. 4.49. The We_l, Re_l, and OH_l for the studied jet problem are

$$We_l = \frac{\rho_l D U^2}{\sigma} = \frac{696 \times 0.0001 \times 100^2}{0.06} = 11600, \tag{4.23}$$

$$OH_l = \frac{\mu_l}{\sqrt{\rho D \sigma}} = \frac{\sqrt{We_l}}{Re_l} = \frac{\sqrt{11600}}{5800} = 0.01857, \tag{4.24}$$

which are within the considered range in Wu's work. Therefore, the location of onset/end of turbulent breakup for the studied problem is

$$x_i = 2000 We_l^{-0.67} JD = 3.783 JD \tag{4.25}$$

$$x_e = 1.58 \times 10^{-5} We_l^{1.68} JD = 106.4 JD, \tag{4.26}$$

where x_i is the location of the onset and x_e is the location of the end of breakup. Since the computational domain only has a length of $50JD$, the end location of breakup can not be obtained in the present simulations. Thus, only the location of the onset of breakup can be compared between the calculation (Eq. (4.26)) and the simulation (4.2). Although both the VOF and CLSVOF results for the onset location are not $3.783JD$ as in Eq. (4.26), the CLSVOF results leads to a smaller value of $x - i$, which is much better than that from VOF. In subsequent simulations, the CLSVOF model will be used to model the two-phase flow problem.

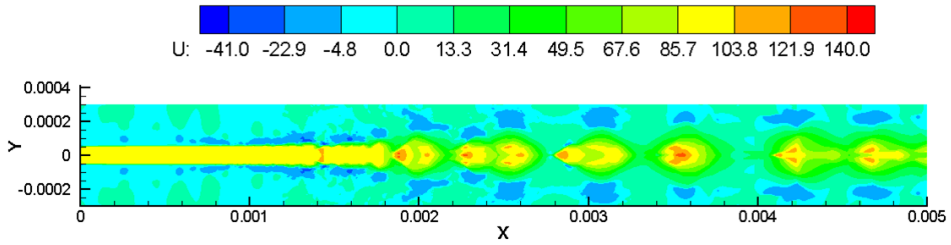

Figure 4.38: The contour of axial velocity for the $3JD$ simulation in VOF method of FLUENT code.

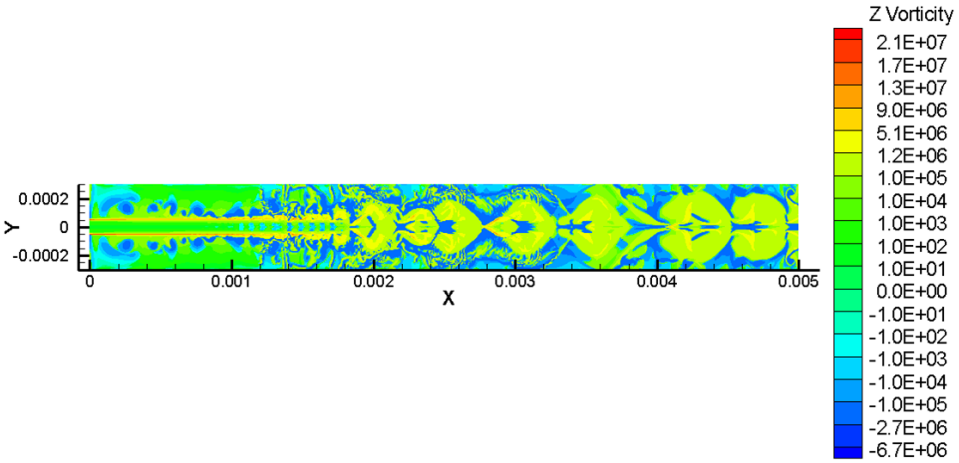

Figure 4.39: The contour of Z vorticity for the MILES $3JD$ simulation using VOF multiphase model.

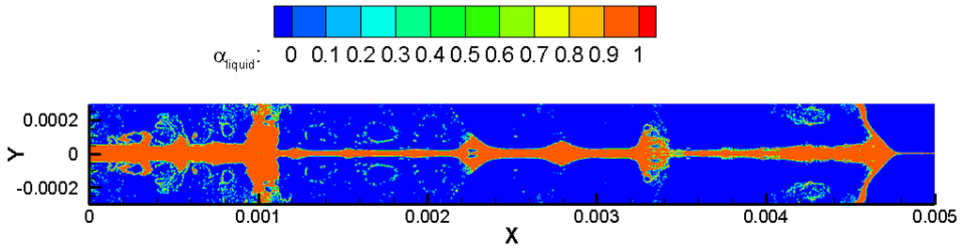

Figure 4.40: The contour of volume of fraction of liquid for the MILES $3JD$ simulation using CLSVOF multiphase model.

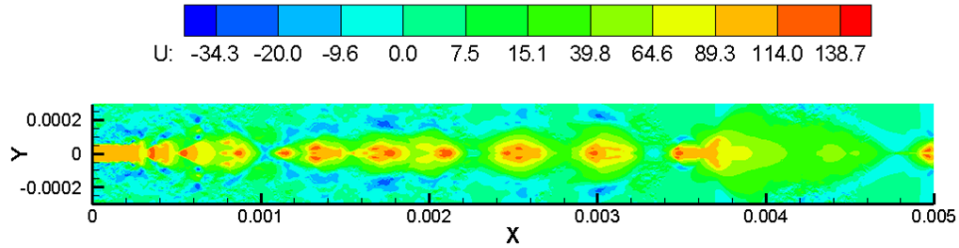

Figure 4.41: The contour of axial velocity for the MILES $3JD$ simulation using CLSVOF multiphase model.

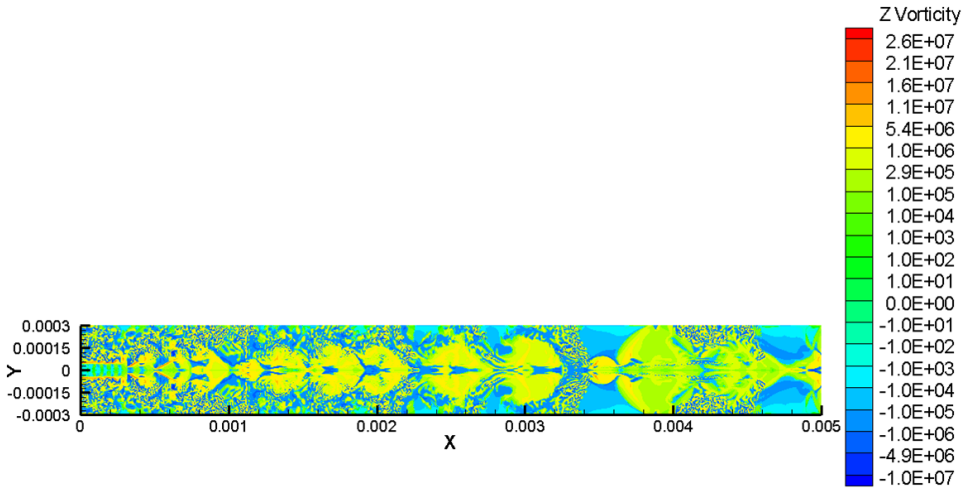

Figure 4.42: The contour of Z vorticity for the MILES $3JD$ simulation using CLSVOF multiphase model.

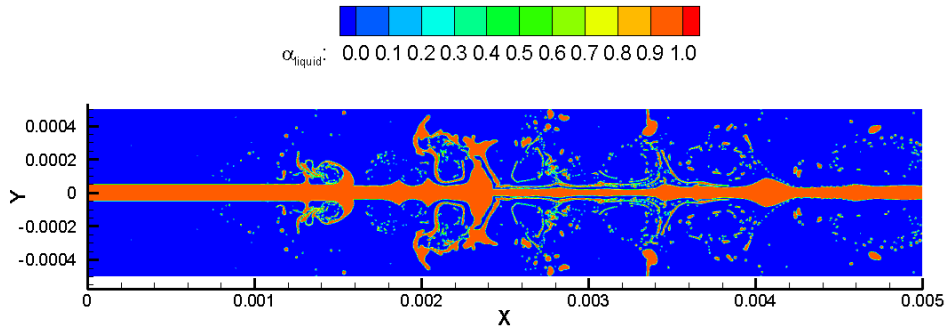

Figure 4.43: The contour of volume of fraction of liquid for the MILES $5JD$ simulation using VOF multiphase model.

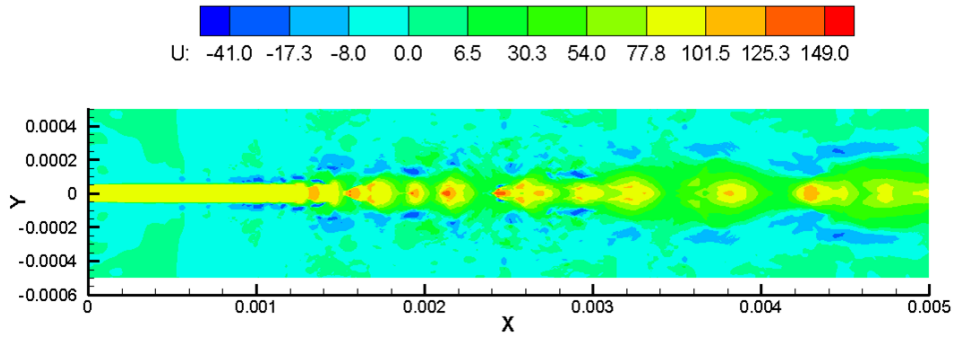

Figure 4.44: The contour of axial velocity for MILES $5JD$ simulation using VOF multiphase model.

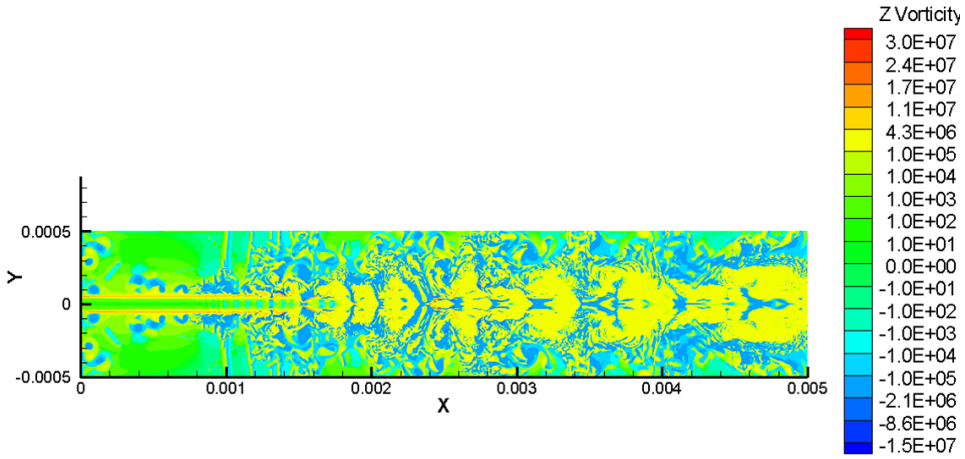

Figure 4.45: The contour of Z vorticity for the MILES $5JD$ simulation using VOF multiphase model.

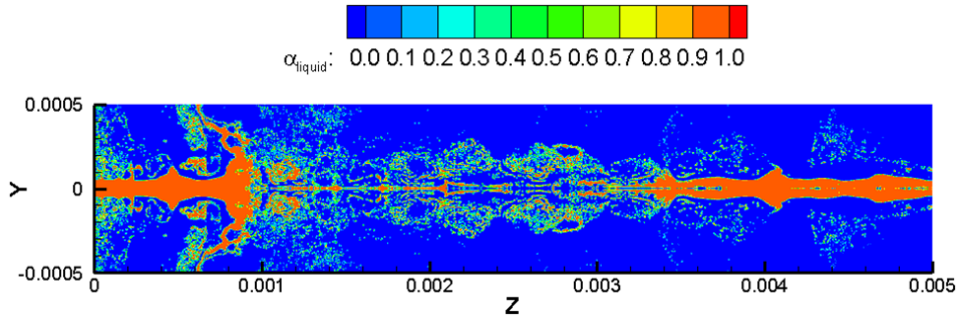

Figure 4.46: The contour of volume of fraction of liquid for the MILES $5JD$ simulation using CLSVOF multiphase model.

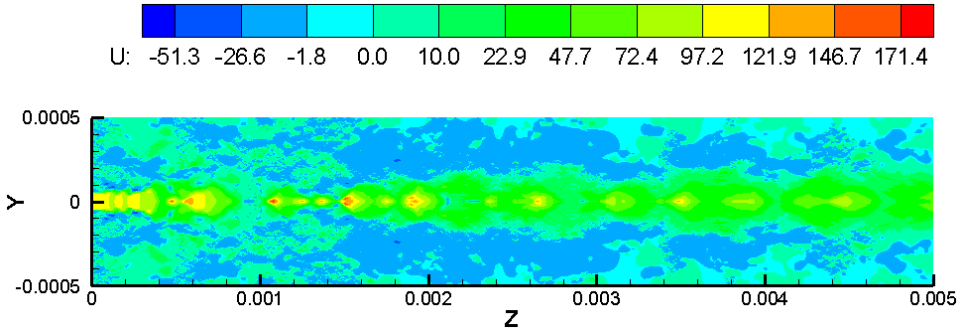

Figure 4.47: The contour of axial velocity for the MILES $5JD$ simulation using CLSVOF multiphase model.

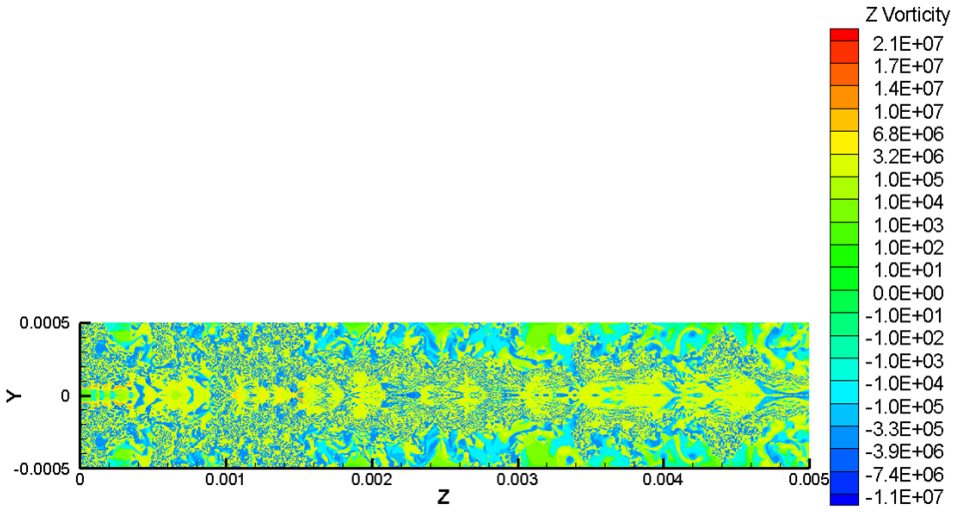

Figure 4.48: The contour of Z vorticity for the MILES $5JD$ simulation using CLSVOF multiphase model.

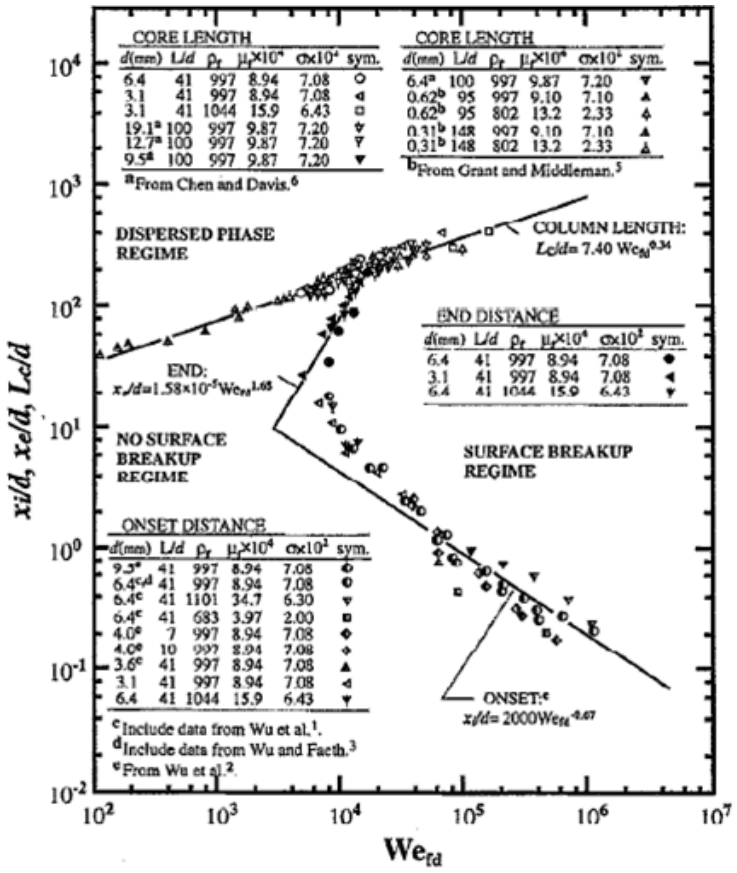

Figure 4.49: Surface breakup regime map for turbulent liquid jets in still gases when aerodynamic effects are small (liquid/gas density ratios are larger than 500)

Chapter 5

Results

5.1 Mercury Internal Flow in A Curved Pipe without A Weld

5.1.1 Problem Description

Since mercury flow becomes fully-developed long before approaching the first 90° half-bend angle, this geometry has been simplified by shortening the inflow section. The eight geometries investigated (Fig. 1.3) have length dimensions that are the same as in the MERIT experiment: the pipe radius is a, curvature radius $R, = 2.33a$, and the inflow and outflow lengths of straight pipe are matched, with or without a nozzle at the exit region. The half-bend angles φ_1/φ_2 investigated are 0°/0°, 30°/30°, 60°/60°, and 90°/90°. The Reynolds number based on the bulk velocity and pipe diameter is approximately equal to 8.244×10^5 and the Dean number is 5.401×10^5.

A full model is tested for the pipe without a weld, whereas symmetry conditions are used for the pipe without or with a nozzle, allowing the use of half of the model, to save on computational cost. The computational grid points are $3.7\times10^6-5\times10^6$ and $3.9\times10^6-6\times10^6$ for pipes of various turning angles without and with nozzles, respectively. There are 48 grid

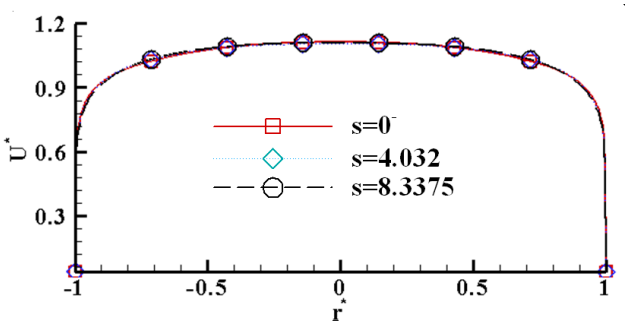

Figure 5.1: Radial distribution of U^* as a function of location along the 0°/0° pipe

points in the circumferential direction and the grid density is 1.8°/ node for the half-bend angle. The distance of the first grid point adjacent to the wall is decided by $y^+ \approx 1$, where $y^+ \equiv u_\tau y/\nu$, u_τ is the friction velocity at the wall, y is the distance to the wall and ν is the local kinematic viscosity of the fluid. Approximately 15 grid points are within the inner layer. The boundary conditions have been described in Chapter 2 of this paper.

5.1.2 Axial Velocity Distribution

As stated earlier, the pseudo coordinate distance, s, is used to describe the locations of points in the straight portions of the pipe, while the bend angles, φ_1 and φ_2, are used for the curved portions. These coordinates are depicted in Figure 1.2. The upstream tangents of all the curved pipes investigated in this paper are of the same length ($-5.17 \leq s \leq 0^-$). So are the downstream tangents ($0^+ \leq s \leq 8.3375$). Figures 5.1 through 5.4 show the radial (r^*) axial-velocity (U^*) distribution for pipes without a nozzle. The effects of the bend angle on flow in the curved pipes are presented only for the cases without nozzles in order to isolate the complication of the nozzles.

In Fig. 5.1, the velocity distribution is identical for the three values of distance s examined, since there is no bend and the flow has already reached the fully developed profile by the inlet of the pipe. The 30°/30°, 60°/60°, and 90°/90° pipes are also imposed the fully developed flow at the inlet, which is a similar, symmetrical, radial distribution of U^*, shown in Fig. 5.1. At the start of the first half-bend ("Bend Starts" for 30°/30° (Fig. 5.2), "Bend Starts" for

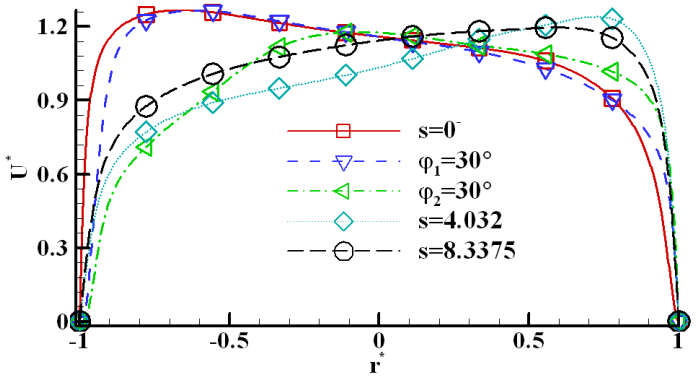

Figure 5.2: Radial distribution of U^* as a function of location along the 30°/30° pipe

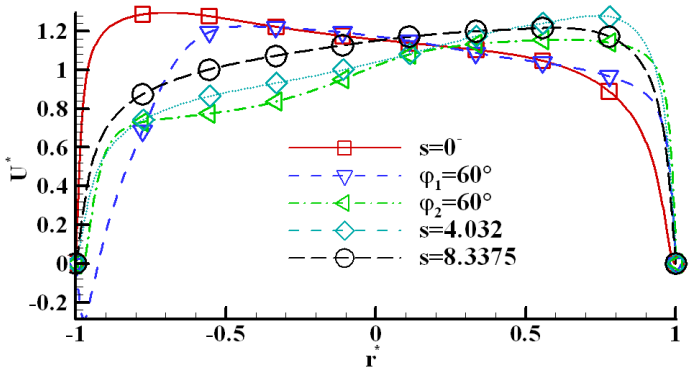

Figure 5.3: Radial distribution of U^* as a function of location along the 60°/60° pipe

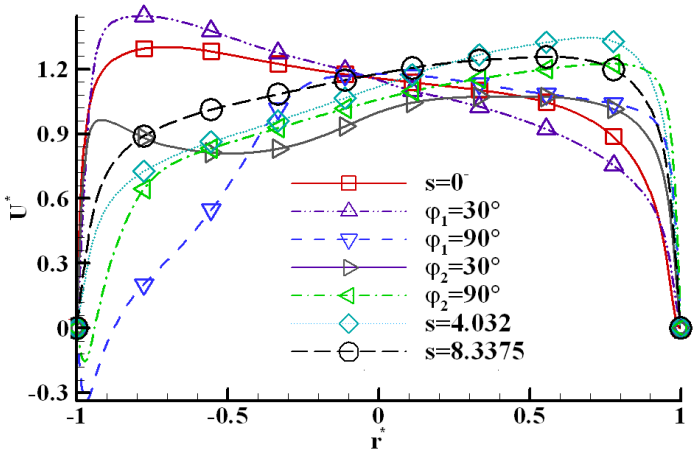

Figure 5.4: Radial distribution of U^* as a function of location along the 90°/90° pipe

60°/60°(Fig. 5.3), and "Bend Starts" for 90°/90° (Fig. 5.4)), the convex (inner) side of the pipe (near $r^* = -1$) shows higher magnitudes of U^*. At the end of the first half-bend ($\varphi_1 = 30°$ for 30°/30° (Fig. 5.2), $\varphi_1 = 60°$ for 60°/60°(Fig. 5.3) maintains its direction at the start of the bend, but with reduced magnitude. That is, at "Bend Starts" and at $\varphi_1 = 30°$ for the 30°/30° pipe (Fig. 5.2), $\partial U^*/\partial r^*$ is negative with a magnitude that is smaller for $\varphi_1 = 30°$ relative to "Bend Starts". Similarly, for the 60°/60° (Fig. 5.3) pipe, $\partial U^*/\partial r^*$ is negative with a reduced magnitude at $\varphi_1 = 60°$. However, for the 90°/90° (Fig. 5.4) pipe, $\partial U^*/\partial r^*$ changes its direction at $\varphi_1 = 90°$. That is $\partial U^*/\partial r^*$ is positive with high velocity region at the center of pipe. For all curved pipes, $\partial U^*/\partial r^*$ is negative, and the high velocity region is located near the concave side ($r^* = 1$) as the flow leaves the second half bend. Actually, for the 90°/90° pipe, the high velocity region moves to the concave side ($r^* = 1$) before the flow leaves out of the second half bend (Fig. 5.4)).

In Fig. 5.5 - Fig. 5.9, the effects of having a nozzle at the exit are shown. For the straight pipe, the nozzle causes a symmetric velocity profile respect to the radial direction, as we move downstream through the pipe (Fig. 5.5). The flow develops complicated patterns (back flow) near the inner side of the half-bend, with one turning point in the velocity profile for both curved pipe with and without a nozzle. The back flow is stronger in the pipe of larger half bend angle. However, the existence of the second half-bend recovers the oscillation (in $r^* = -1$) for all curved pipes. That is to say back flow is weaker at the same relative locations after the second half-bend as those after the first half-bend. Take the 90°/90° pipe as an example, the back flow near the convex side ($r^* = -1$) is stronger in $\varphi_1 = 90°$ (Fig. 5.8(d)) than in $\varphi_2 = 90°$ (Fig. 5.9(g)). At the exit plane ($s = 8.3375$), the flow in the pipes with nozzles tend to have higher velocities in the $-0.9 < r^* < 1$ region, the velocity profile is uniform radially, and the wall boundary layer is much thinner, when compared with those without a nozzle (Fig. 5.5(c), Fig. 5.6(e), Fig. 5.7(e), and Fig. 5.9(g)). The results show that the effect of the nozzle on the upstream flow is extremely weak. The nozzle only comes into effect on the flow at the beginning of the nozzle ($s = 4.032$). The decreasing cross-

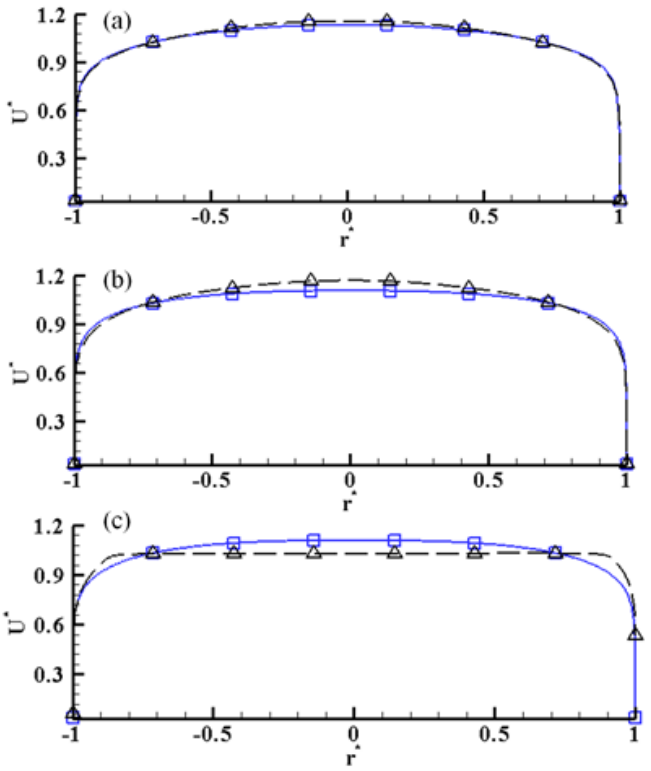

Figure 5.5: Comparison of radial distribution of U^* at the same location along the 0°/0° pipe without (square symbols) and with (delta symbols) a nozzle: (a)$s = 0^-$ (b)$s = 4.032$ (c)$s = 8.3375$

sectional area of the nozzle along the flow path leads to a decrease in the static pressure. The flow being subsonic, the velocity profile becomes steeper at the beginning of the nozzle ($s = 4.032$). The 90°/90° pipes are further investigated in Fig. 5.10 and 5.11 because of the current application in the MERIT experiment (90°/90°). The velocity distribution is similar for these two cases until the nozzle appears ($s = 4.032$). At the end of the first bend, the axial velocity magnitude increases near the concave side while decreasing near the convex side. This pattern is caused by the cross-stream pressure gradient. Once the high velocity fluid encounters the adverse pressure gradient on the convex side, it starts to move towards the concave side (The abbreviations "CC" and "CV" are used in these figures to denote the concave and convex sides, respectively.) . The flow becomes more and more stratified toward the exit ($s = 8.3375$) when the effect of the bend becomes insignificant.

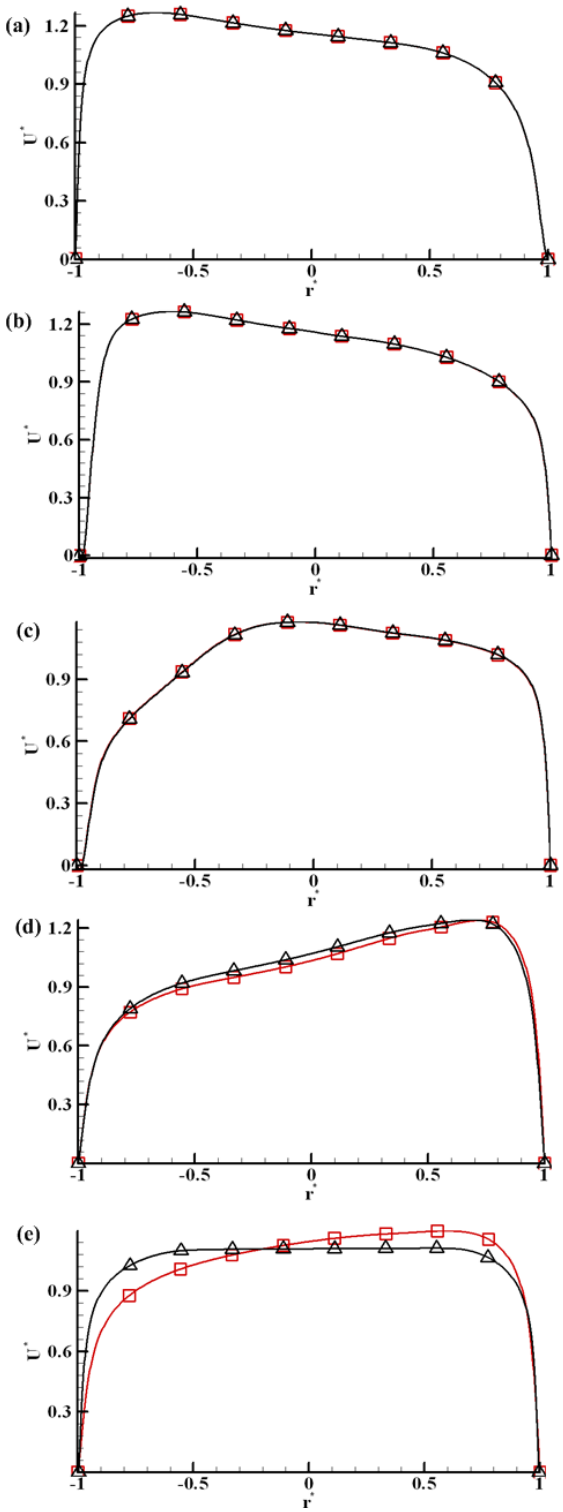

Figure 5.6: Comparison of radial distribution of U^* at the same location along the 30°/30° pipe without (square symbols) and with (delta symbols) a nozzle: (a)$s = 0^-$ (b)$\varphi_1 = 30°$ (c)$\varphi_2 = 30°$ (d)$s = 4.032$ (e)$s = 8.3375$

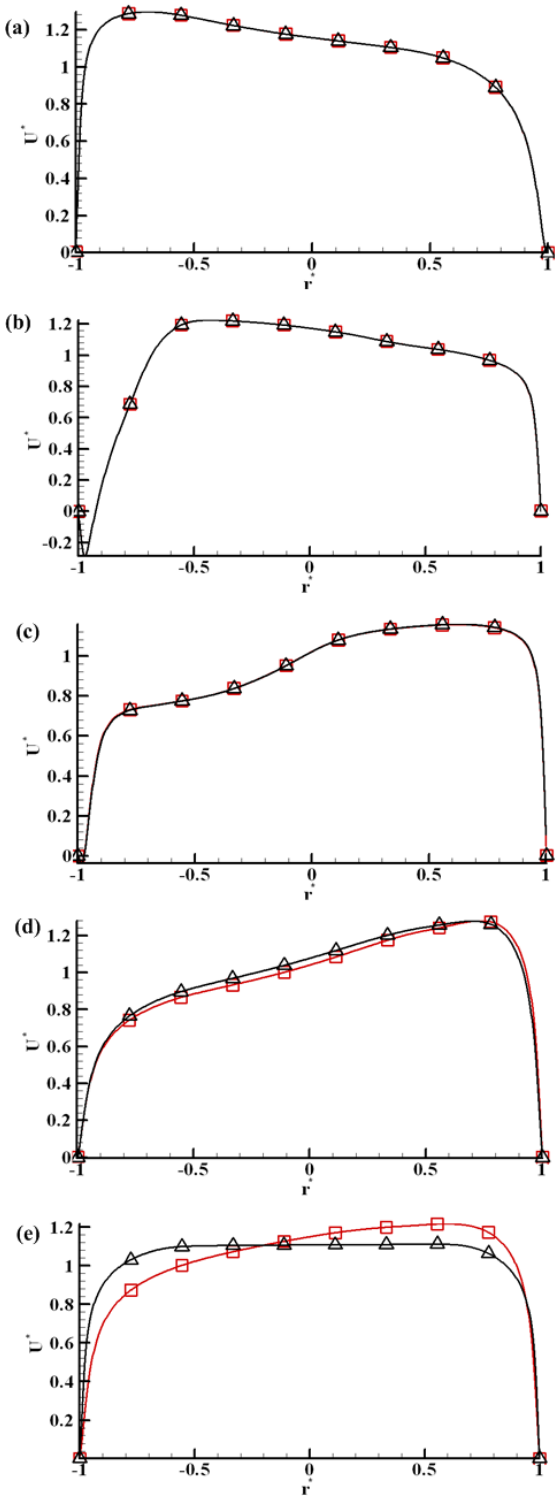

Figure 5.7: Comparison of radial distribution of U^* at the same location along the 60°/60° pipe without (square symbols) and with (delta symbols) a nozzle: (a)$s = 0^-$ (b)$\varphi_1 = 60°$ (c)$\varphi_2 = 60°$ (d)$s = 4.032$ (e)$s = 8.3375$

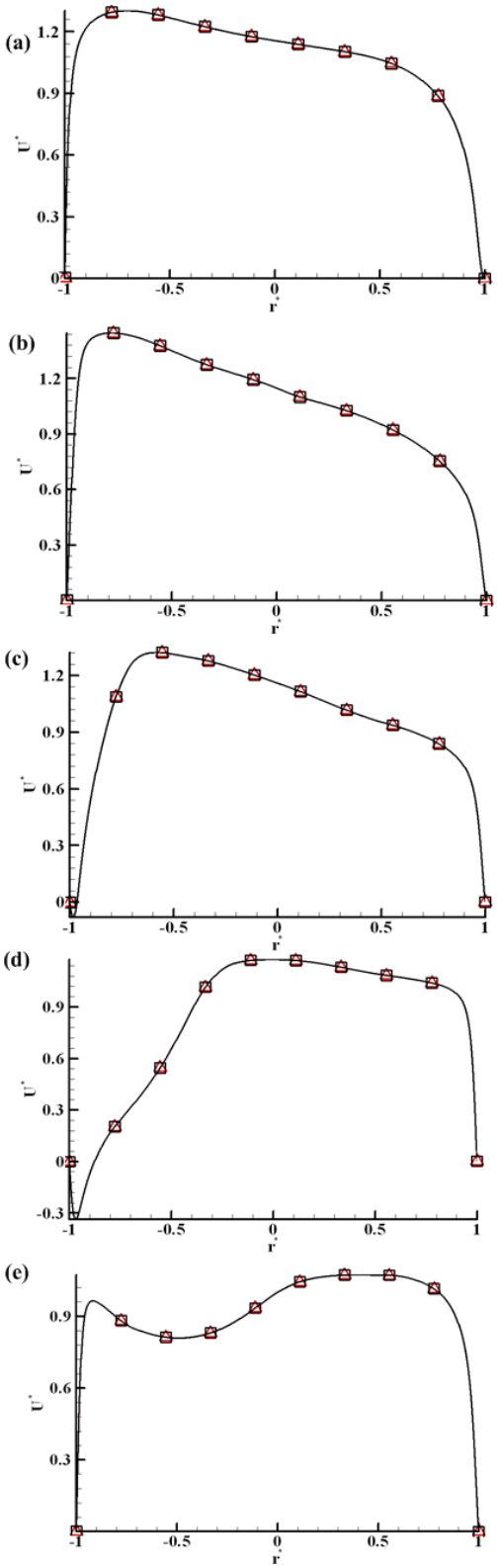

Figure 5.8: Comparison of radial distribution of U^* at the same location along the 90°/90° pipe without (square symbols) and with (delta symbols) a nozzle: (a)$s = 0^-$ (b)$\varphi_1 = 30°$ (c)$\varphi_1 = 60°$ (d)$\varphi_1 = 90°$ (e)$\varphi_2 = 30°$

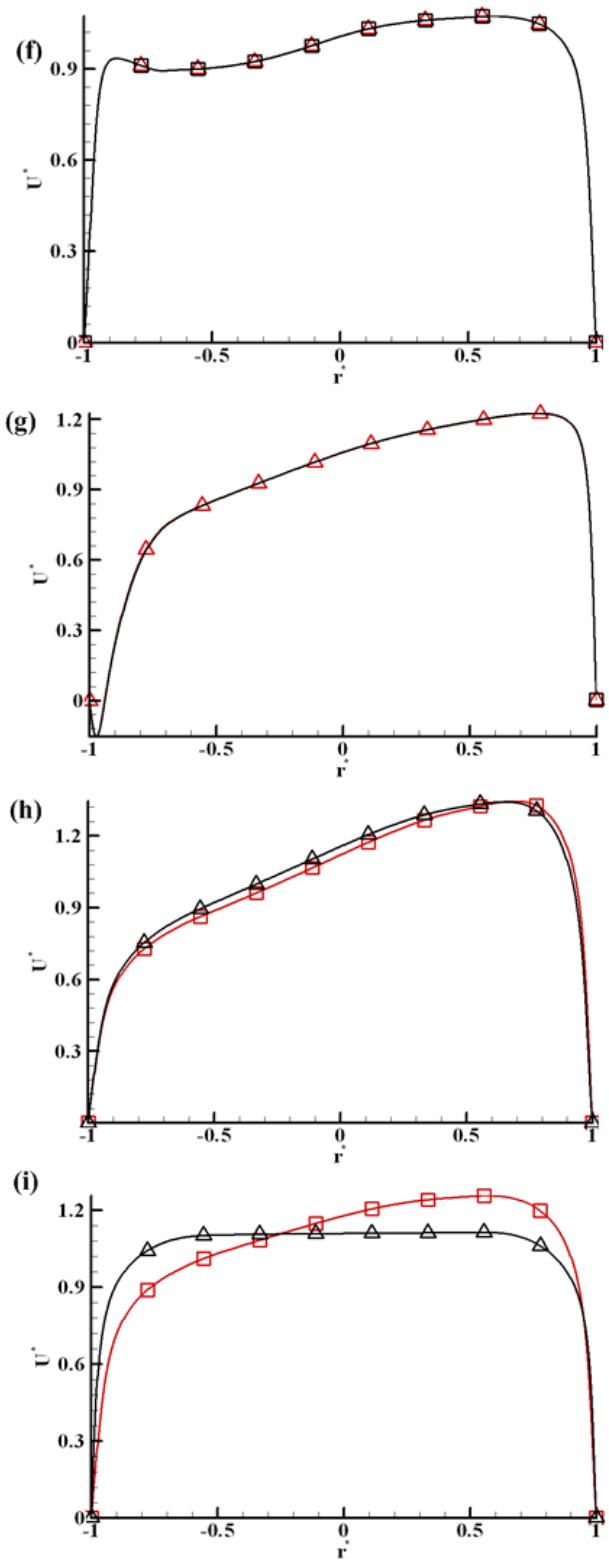

Figure 5.9: Comparison of radial distribution of U^* at the same location along the 90°/90° pipe without (rectangular symbols) and with (delta symbols) a nozzle: (f)$\varphi_2 = 60°$ (g)$\varphi_2 = 90°$ (h)$s = 4.032$ (i)$s = 8.3375$

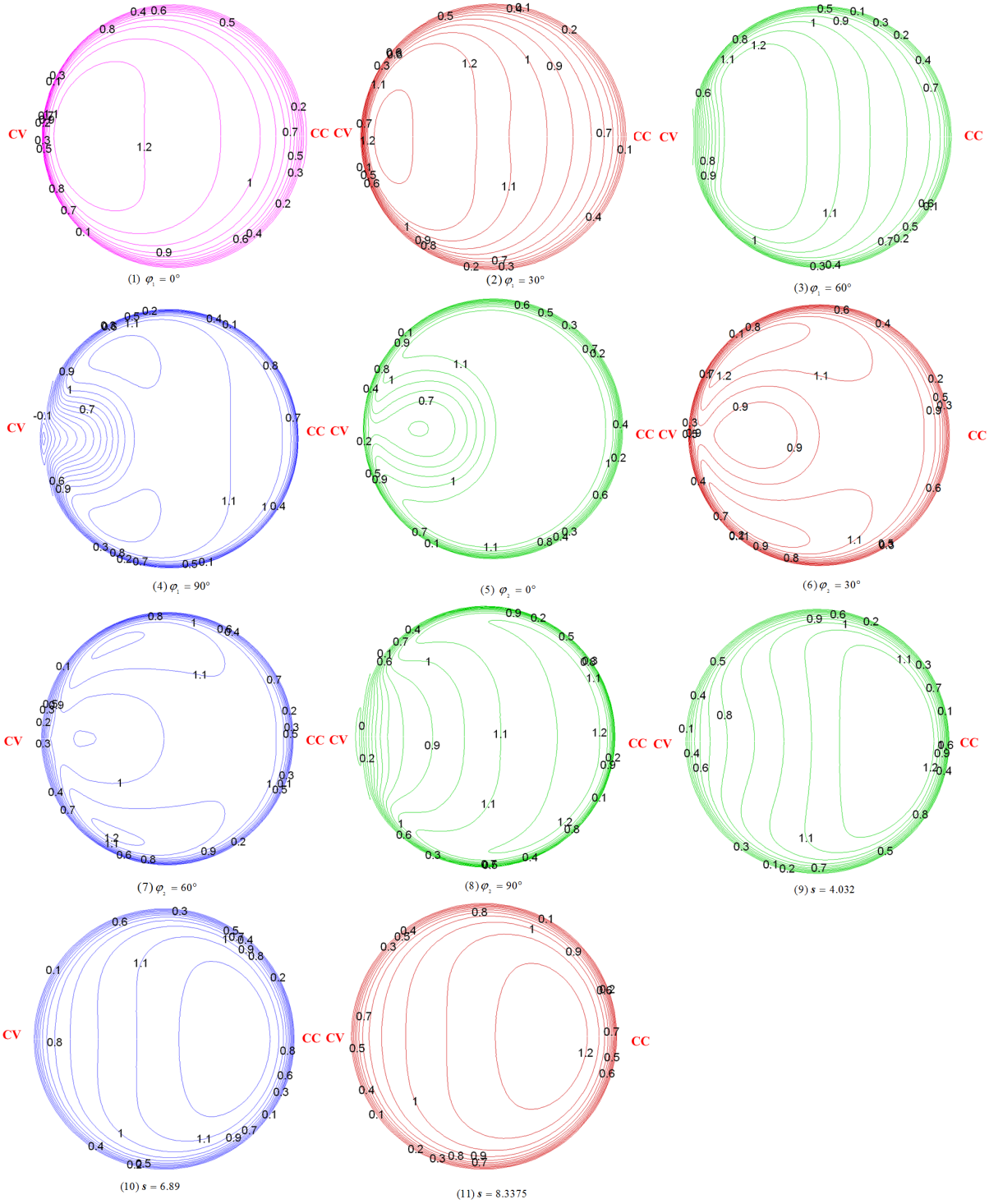

Figure 5.10: The contour of U^* as function of location along the 90°/90° without a nozzle

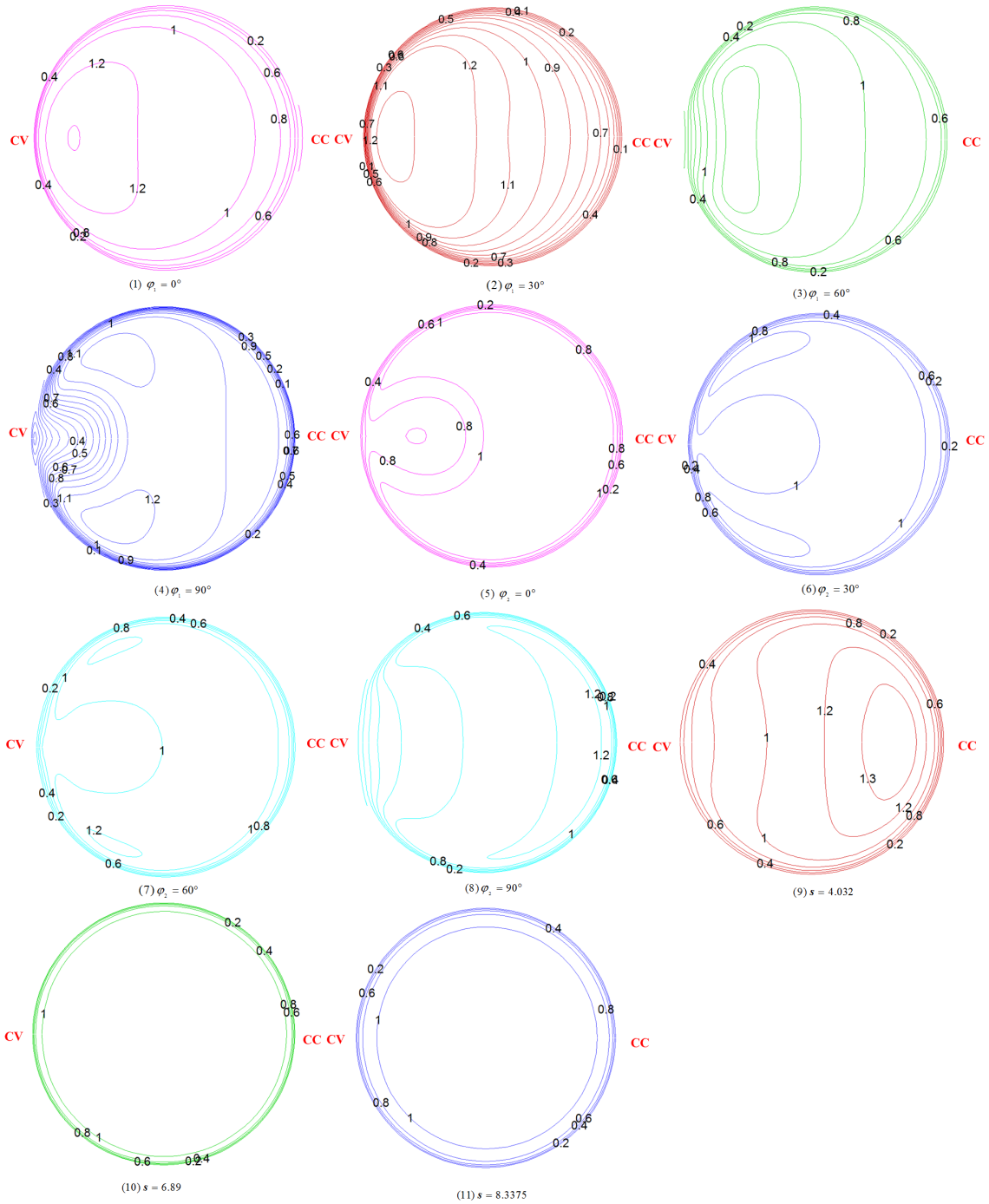

Figure 5.11: The contour of U^* as function of location along the 90°/90° with a nozzle

5.1.3 Momentum Thickness

One goal of the present study is to determine the pipe configuration that has the potential to give the least disturbance in the circular jet shear layer that eventually issues from the nozzle. Therefore, some knowledge of the distribution of the momentum thickness δ_θ at the nozzle exit becomes important. For example, linear stability analysis of Michalke [126] and Plaschko [127] and the experimental work of Cohen and Wygnanski, [128] Corke *et al.*, [129] and Corke and Kusek [130] showed that for large $2a/\delta_\theta$ ($2a/\delta_\theta \gg 1$), both axisymmetric ($m = 0$) and the first spinning or helical instability modes ($m = \pm 1$ or -1) are unstable in the initial jet shear layer.

The polar distribution of δ_θ is shown in Fig. 5.12 and Fig. 5.13 for pipes without and with a nozzle, respectively. The number "0" in the polar plots refers to the wall, while the numbers "1", "2", and "3" respectively refer to the distances $0.1a$, $0.2a$, and $0.3a$ measured from the wall. Momentum thickness decreases with decreasing radius. For pipes without a nozzle (Fig. 5.12), the distribution of δ_θ is non-uniform at the exit but similar. The azimuthal variation of δ_θ becomes stronger as the half-bend angle increases. Thus $90°/90°$ shows the strongest azimuthal variation of δ_θ compared to other pipes. At the exit plane, δ_θ attains its minimum value at $\theta = 0°$ and its maximum value at $\theta = 180°$. Note that the straight pipe does not show an azimuthal variation of δ_θ. Figure 5.13 shows a fairly uniform δ_θ distribution for all pipes, when nozzles are present at the exit.

The differences in the azimuthal variation of δ_θ can be explained by the relationship between momentum thickness and axial velocity, where the latter, at pipe exit, is shown in Figs. 5.2-5.4 for the various pipe configurations. Note that the $90°/90°$ pipe shows the most asymmetry in the distribution of the axial velocity (Fig. 5.4), and hence in the azimuthal distribution of δ_θ. For pipes with nozzles, the axial velocity profile is fairly uniform in the azimuth, which explains the uniform azimuthal distribution of δ_θ.

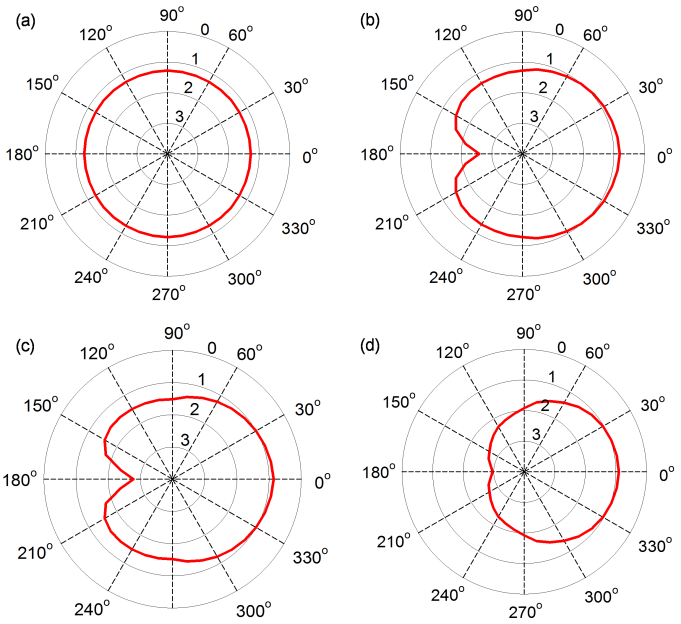

Figure 5.12: Momentum thickness distribution at the exit plane of pipes for turning angles of: (a)0°/0° (b)30°/30° (c)60°/60° (d)90°/90°. These pipes do not have nozzles and $\theta = 180°$, 0° correspond to the convex and concave sides of the pipes, respectively

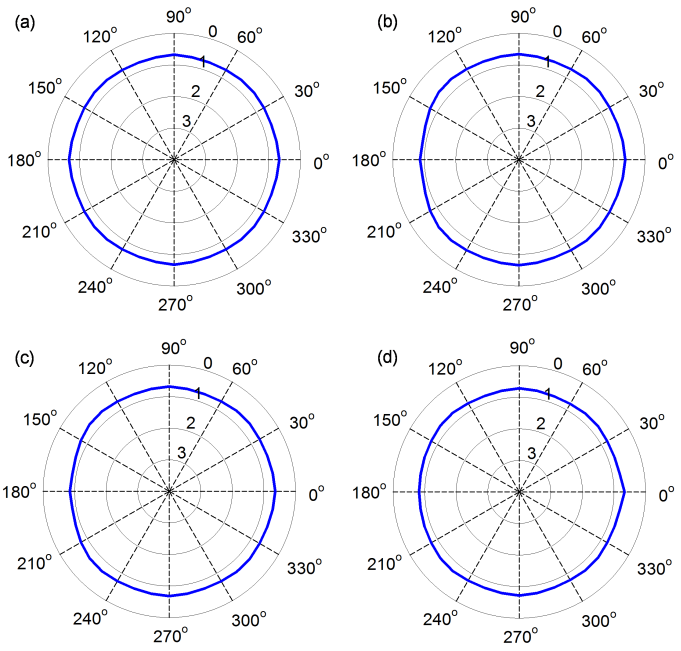

Figure 5.13: Momentum thickness distribution at the exit plane of pipes for turning angles of: (a)0°/0° (b)30°/30° (c)60°/60° (d)90°/90°. These pipes have nozzles and $\theta = 180°$, 0° correspond to the convex and concave sides of the pipes, respectively

5.1.4 Turbulence Intensity

The turbulence intensity at the exit of pipe is of interest, as it determines the turbulence level in the jet. This quantity is defined in this dissertation as

$$I = \sqrt{\frac{2}{3}(\frac{k}{U_b^2})}, \tag{5.1}$$

where k is the turbulence kinetic energy per unit mass and U_b has been used as a scale for u'_{rms}, the root-mean-squared fluctuating velocity. The radial distribution of I at the exit plane along the horizontal direction is presented in Fig. 5.14. I is found to have high values near the walls, with a large gradient for all pipes. It is clear to see that I is reduced when having a nozzle. For the pipe without a nozzle, I increases as the half-bend angle increases. For example, the 90°/90° pipe has the strongest turbulence intensity. The radial distribution of I is symmetrical for the straight pipe (0°/0°), with a flat interior, as expected. The profile of I with r^* along the horizontal direction for the 30°/30°, 60°/60°, and the 90°/90° pipes without nozzles, shows higher values near $r^* = -1$ (concave side) compared to $r^* = 1$ (convex side). The higher values of I on the convex side for the 60°/60° pipe without a nozzle are related to the instabilities associated with adverse pressure gradient. With nozzles, there is a steeper radial gradient of I near wall in the 0°/0°, 30°/30°, 60°/60°, and 90°/90° pipes compared to those without nozzles. I is nearly flat in the interior region ($-0.6 < r^* < 0.6$). In the region of $-1 < r^* < -0.6$, I has relatively higher values as the half-bend angle decreases from nonzero value. Generally speaking, the straight pipe with a nozzle is the pipe with least turbulence intensity among all eight pipes.

5.1.5 Discussions

The objective of this study is to comparatively evaluate various pipe configurations that have been proposed for liquid target delivery in the Muon Collider project. The desirable configurations are those that lead to the weakest turbulence intensity levels and the smallest

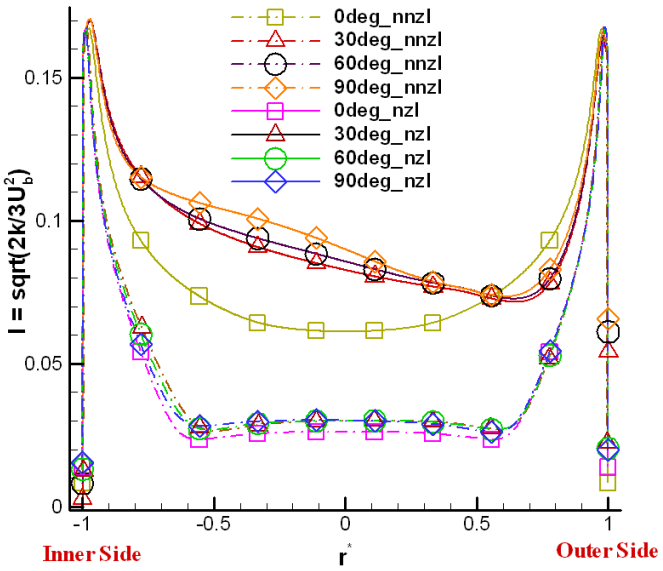

Figure 5.14: The horizontal distribution of turbulence intensity at the exit plane. Subscripts "with" and "without" denote presence or absence of a nozzle at pipe exit

momentum thickness at the exit plane. Eight pipe configurations with different turning angles are studied, without and with a nozzle at the exit region of the pipe. A simple analytical study is performed to describe the laminar flow in curved pipes, in relation to the terms representing curvature effects. The realizable $k-\varepsilon$ (RKE) RANS model has been applied to simulate turbulent flows in the pipes. At the exit plane of the pipe without a nozzle, δ_θ is smaller at $\theta = 0^\circ$ relative to the value at $\theta = 180^\circ$ (Figure 5.12), where a lower level of turbulence intensity occurs. The effects of nozzle include the azimuthal homogenization of the flow, and hence a uniform velocity, as well as a uniform azimuthal distribution of δ_θ. The nozzle also significantly reduces the turbulence intensity at the pipe exit. However, the straight pipe has the least turbulence intensity, because of the absence of secondary flows. From the effects of bend and nozzle shown in this study, a straight pipe with a convergent nozzle was found to have the weakest turbulence intensity level at the exit plane.

5.2 Mercury Internal Flow in A Curved Pipe with A Weld

5.2.1 Problem Description

From the borescope video of the interior of the titanium nozzle for the Muon Collider project, ominous weld beads are visible. It seems like these "turbulators" are responsible for much of the poor performance of the jet. The key issue is the azimuthal-symmetry of the bead. As a start, an azimuthally symmetric bead is modeled for the 90°/90° pipe. Then a nozzle with beads more closer to reality is modeled, which is azimuthally-asymmetric, for example, a 30° azimuthal bead with its center transverse to the bend plane. Both the azimuthally-symmetric and the asymmetric beads are located close to the beginning of the nozzle taper and have a semicircular cross-section, as illustrated in Figures 5.15 (a) and (b), respectively. We can see that the inner radius of the semicircular bead is 1/16 inches.

5.2.2 Computation of the Pipe Simulation with An Azimuthally Complete Weld

In order to determine the proper mesh density for the pipe simulation with a weld, a mesh independence study has been carried out on the 90°/90° pipe with an azimuthally symmetric bead, as shown in Fig. 5.16. The values of turbulent intensity, I, at the pipe exit are comparable for the cases in which grid numbers are 2.5 million and 3.2 million, respectively. When the grid number is 2.5 million, the pipe simulation is independent of mesh.

The effects of the azimuthal symmetric semicircle bead/weld are studied by comparing the I (turbulence intensity) at the exits of pipes with/without a weld. The comparison can be found in Fig. 5.17. It is clear that the turbulence level is higher at the center region of the pipe in the case of the pipe with a weld, which implies that a weld enhances turbulence.

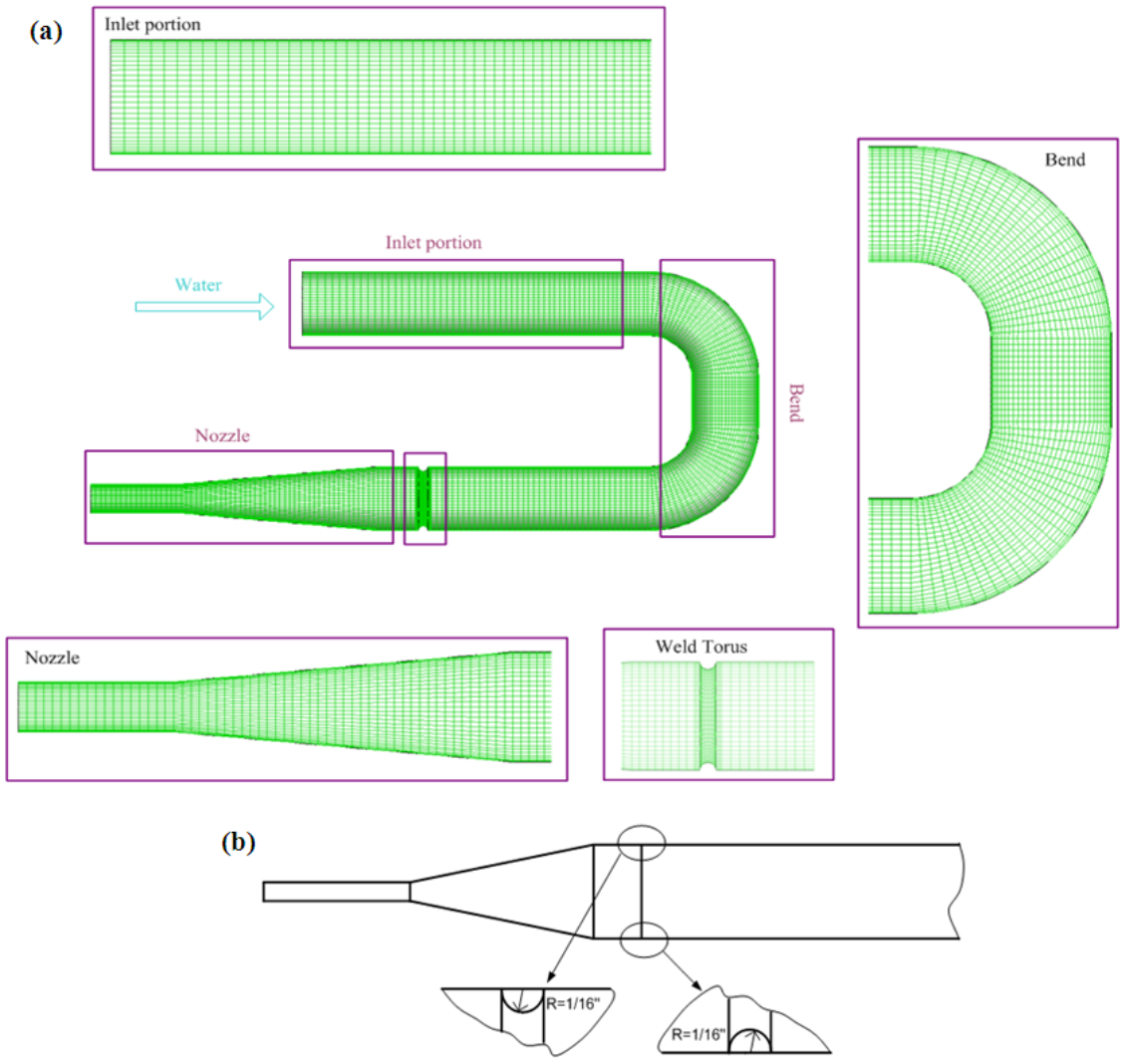

Figure 5.15: (a) Location of the bead in the 90°/90° pipe (b) Dimensions of the semi-circular bead

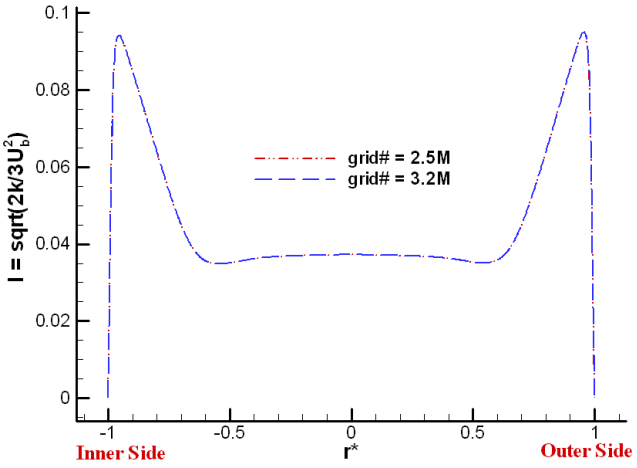

Figure 5.16: Mesh independence check for the pipe with an azimuthally-symmetric bead

The effects of a bend are negligible at the pipe exit, as evidenced by the less asymmetric distribution of I in the direction of r^* (Fig. 5.16).

5.2.3 Computation of the Pipe Simulation with An Azimuthally Incomplete Weld

The geometry of the 90°/90° pipe with an azimuthally-asymmetric 30° weld is shown in figure 5.18. The 30° bead is located along the flow direction as does the 360° bead. The inner diameter as well as the geometry of the bead are otherwise the same as those for the 360° bead. The only difference is the azimuthal angle 30° versus 360°.

Four different meshes are used in the simulations when the pipe has a 30° weld. The total mesh points vary from the relatively coarse 0.7 million to the relatively fine 16 million. The later simulations are carried out for all four different mesh grids. For the 30° weld case, mesh independence was observed at 5 million grid points. The analyses of asymmetric weld calculations are carried out for the following quantities:

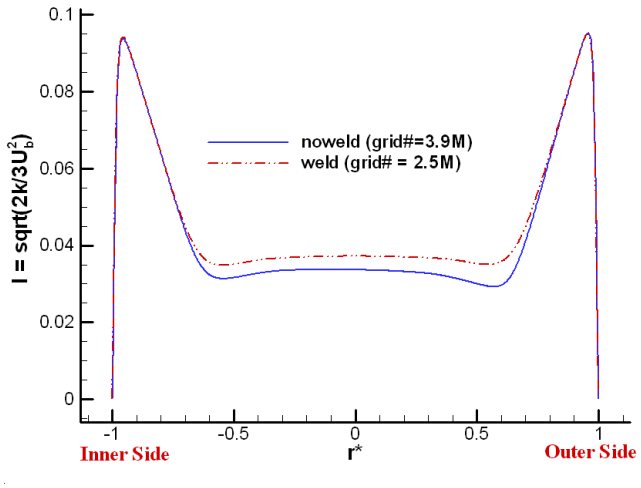

Figure 5.17: Comparison of turbulence intensity between the pipe without a weld and the pipe with an azimuthally-symmetric weld

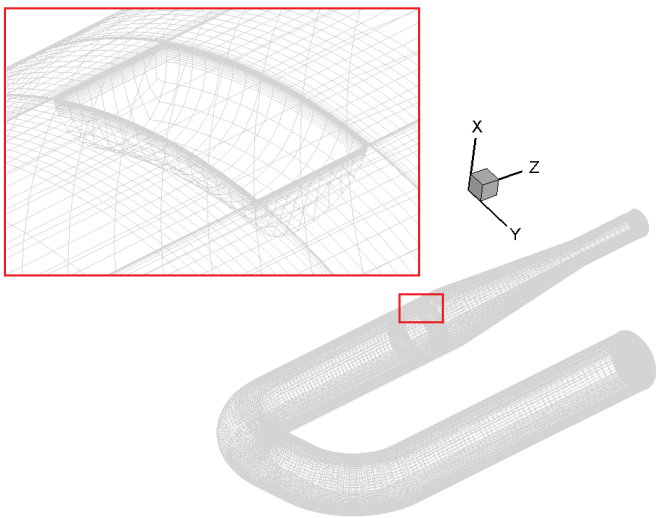

Figure 5.18: The 90°/90° pipe with an azimuthally-asymmetric 30° bead/weld

(1) Wall shear stress, τ_w, is calculated as

$$\tau_w = \mu \frac{\partial U}{\partial n}|_w, \tag{5.2}$$

where $\frac{\partial U}{\partial n}|_w$ is the velocity gradient at the wall. From the wall shear stress, a velocity scale, U_w (friction velocity, also called shear velocity), is introduced:

$$U_w = \sqrt{\frac{\tau_w}{\rho}}. \tag{5.3}$$

The shear velocity characterizes the turbulence strength, u_{rms}, and laminar sub-layer thickness at the boundary, δ_S

$$u_{rms} \sim U_w \tag{5.4}$$

$$\delta_S = 5\nu/U_w. \tag{5.5}$$

(2) Turbulence kinetic energy (TKE), k, is the mean kinetic energy per unit mass associated with eddies in turbulent flow. Generally, the turbulent kinetic energy is calculated by the mean of the turbulence normal stresses:

$$k = \frac{1}{2}(\overline{(u\acute{})^2} + \overline{(v\acute{})^2} + \overline{(w\acute{})^2}). \tag{5.6}$$

(3) Momentum thickness, δ_θ, is the distance by which a surface would have to be moved parallel to itself towards the reference plane in an inviscid fluid stream of velocity $U_{\max}$ to give the same total momentum as exists between the surface and the reference plane in a real fluid.

$$\delta_\theta = \int_0^a \frac{U}{U_{\max}}(1 - \frac{U}{U_{\max}})dr. \tag{5.7}$$

The distributions of the wall shear stress (τ_w), kinetic energy of turbulence (k), kinetic energy dissipation rate (ϵ), the mean velocity (U), and the friction velocity (U_w) from the

beginning to the end of the pipe are shown in Figs. 5.19 and 5.20 along the top and bottom surface of the pipe. The top surface passes through the middle of the weld. The "S" on the x-axis of these figures is defined as the normalized by the pipe diameter at the inlet. The results are compared for the four different mesh densities: 0.7 million, 3 million, 5 million, and 16 million. The results for the cases of 5 million and 16 million show good agreement, indicating that the mesh independence has been achieved at 5 million. The top surface distribution of τ_w, k, ϵ, U, and U_w (Fig. 5.19) shows a local drop at roughly $S = 13$, which coincides with the center of the 30° weld. However, there are no changes to the distribution of k and ϵ at $S = 13$ on the bottom line, as shown in Fig. 5.20, which implies the effect of the 30° weld are too weak to influence the flow on the opposite surface to the weld. Downstream in the 30° weld case, τ_w, k, ϵ, and U_w, but not U, increase rapidly along both the top and bottom surfaces, until $S = 16.62$, where the narrowest straight part of the nozzle starts.

Figs. 5.22 and 5.23 show the detailed distribution of τ_w, k, ϵ, U, and U_w along two orthogonal lines passing through the middle of the weld. The locations of the two orthogonal lines on the weld surface are shown in Fig. 5.24. Mesh independence is observed again by the agreement between the 5 million and 16 million cases. The distribution of τ_w, k, ϵ, U, and U_w along the line of constant Z (Fig. 5.22) is almost symmetric about the Y mid-value shown in the figure. This is not the case near the wall, where the magnitudes of τ_w, k, ϵ, U, and U_w are smaller on the outer side ($Y = -0.0716$) than the inner side ($Y = -0.0664$) of the pipe. However, this difference is very small as can be seen from the Fig. 5.22. Also, for the distribution of τ_w and U_w, the lowest values at the pipe center region ($-0.0706 < Y < -0.0666$) are located to the outer side ($Y = -0.0716$) of the pipe. This implies that the downstream effects of the bends still remain up to the location of the 30° weld but are not significant any more. Along the line of constant Y in the weld region, the magnitudes of τ_w, k, ϵ, U, and U_w are much larger in the upstream than in the downstream of the weld. This can be explained by the flow separation. When pressure in the direction of flow increases (adverse pressure gradient), the boundary layers tend to separate from

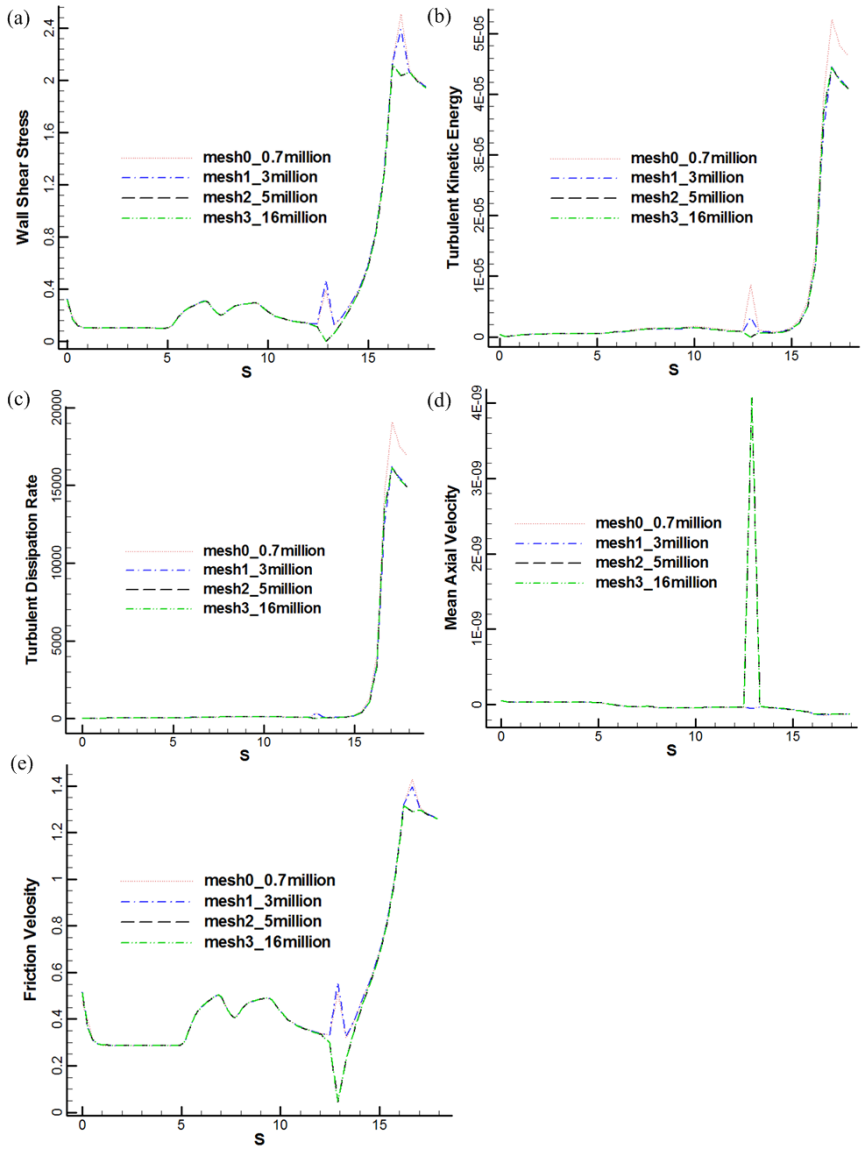

Figure 5.19: The distribution of wall shear stress, turbulence kinetic energy, turbulence kinetic energy dissipation rate, mean axial velocity, and friction velocity along the top line on the pipe wall

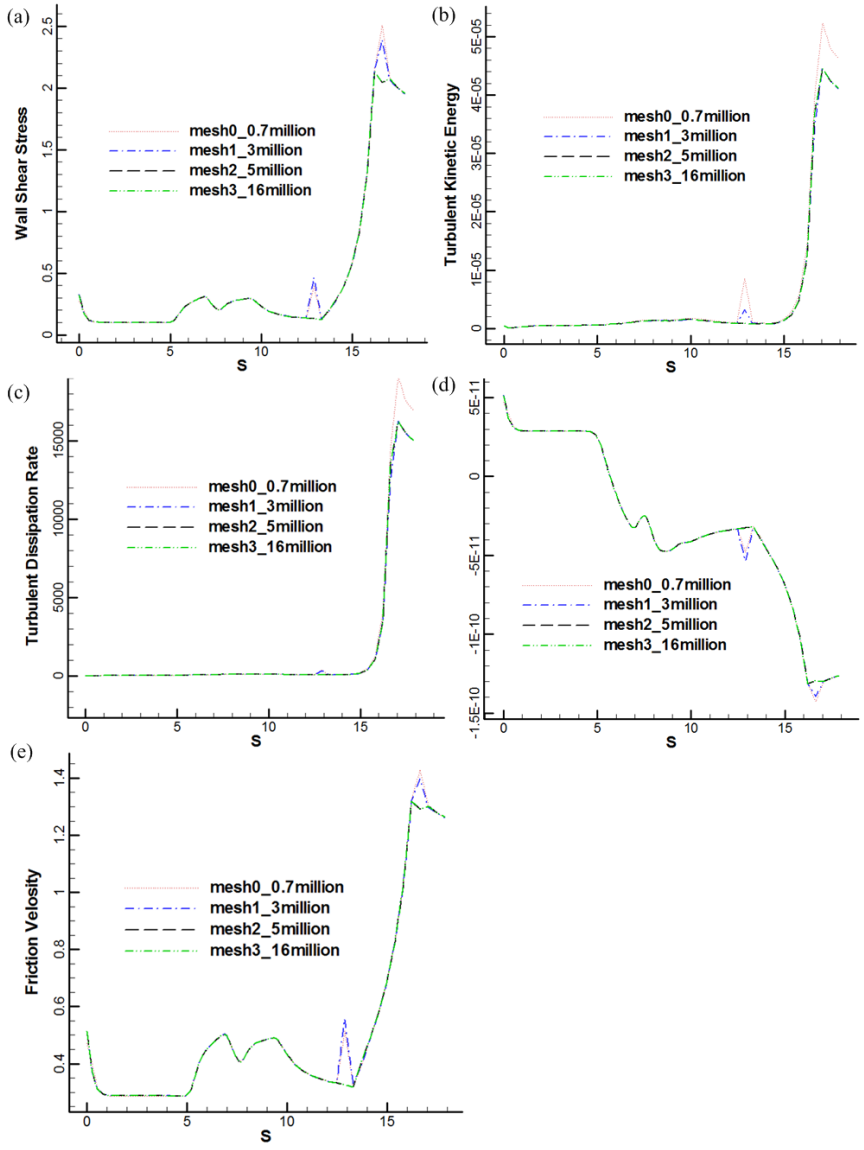

Figure 5.20: The distribution of wall shear stress, turbulent kinetic energy, turbulence kinetic energy dissipation rate, mean axial velocity, and friction velocity along the bottom line on the pipe wall

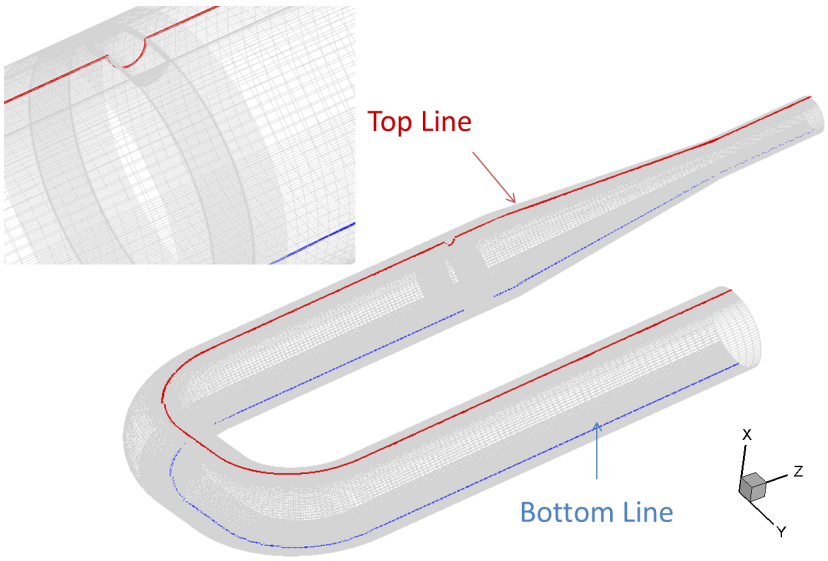

Figure 5.21: The locations of top and bottom surfaces on the pipe wall

the surface. As a result of the increasing fluid pressure, the potential energy of the fluid increases, leading to a decreased kinetic energy. When boundary layer separation happens, the boundary layer thickens, resulting in a reduced wall shear stress.

The exit of the nozzle is akin to the start of the jet flow. Therefore the distribution of k and δ_θ at the pipe exit is used for the subsequent jet flow study as shown in Figs. 5.25 and 5.26 respectively. After the convergent nozzle, the distributions of both k and δ_θ are uniform, although the magnitudes of k and δ_θ differ for different meshes. Also, two planes normal to the pipe axis in the vicinity of the weld, as shown in Figs. 5.27, have been chosen to investigate the distribution of k and δ_θ in the vicinity of the weld. The plane of $z = 0.0430405$ is upstream compared to the plane of $z = 0.0380405$. Compared with the high k magnitude region at the weld location on the plane of $z = 0.0430405$ (Fig. 5.28), the magnitude of k increases by up to 200% on the plane of $z = 0.00380405$ (Fig. 5.29) at the same weld location. Neither magnitude nor the position of its biggest magnitude of k at the pipe center change. δ_θ increases locally in the vicinity of the 30° weld (90° location in Fig. 5.30), which is caused by the thickened boundary layer when flow separation happens. Also, δ_θ increases smoothly and is locally symmetric at the 180° location (Fig. 5.31). Other than at these locations, δ_θ

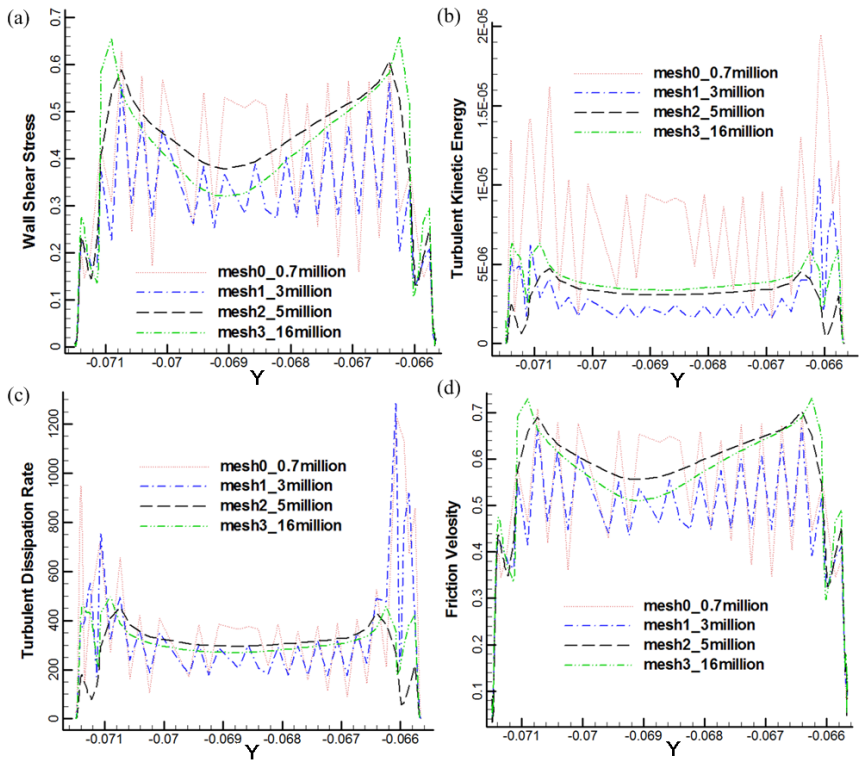

Figure 5.22: The distribution of wall shear stress, turbulent kinetic energy, turbulent dissipation rate, and friction velocity along the constant Z line across the weld center

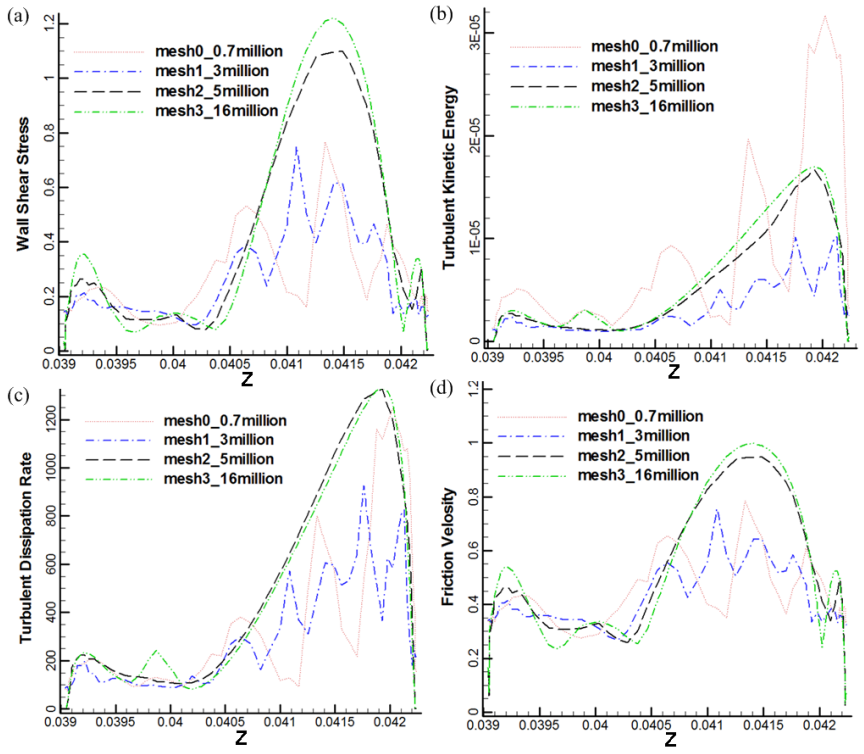

Figure 5.23: The distribution of wall shear stress, turbulence kinetic energy, turbulence kinetic energy dissipation rate, and friction velocity along the constant Y line across the weld center

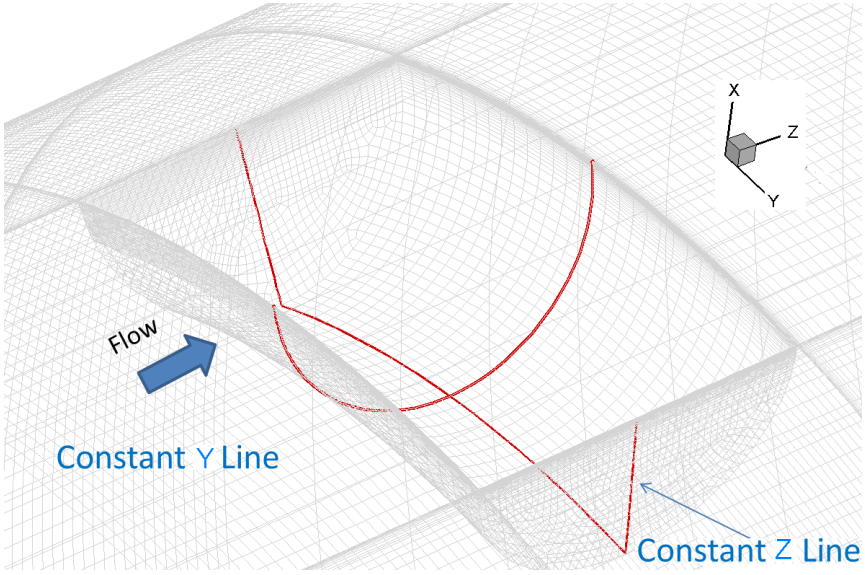

Figure 5.24: The locations of top and bottom surfaces on the pipe wall crossing the weld center

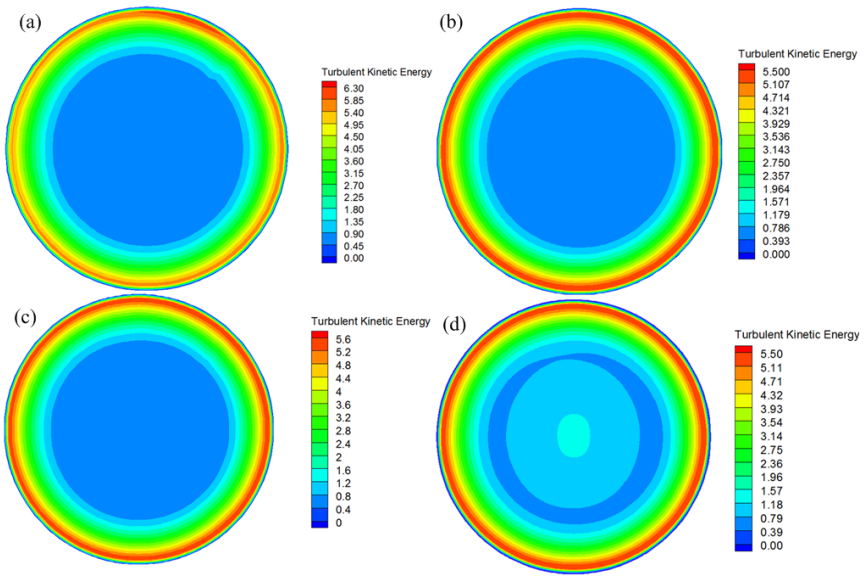

Figure 5.25: Distribution of k at the pipe exit when grid number is (a) 0.7 million (b) 3 million (c) 5 million (d)16 million

maintains the same values before and after the weld.

5.2.4 The Effects of A Bend and A Weld

In order to study the effects of bend and weld on the internal pipe flow, three configurations have been chosen: straight pipe without a weld, 90°/90° pipe without a weld, and 90°/90° pipe with a 30° weld. Static pressure, wall shear stress, axial velocity, momentum thickness, turbulence intensity, and turbulence kinetic energy dissipation rate are analyzed for the flows in these three pipes.

Static Pressure Develops From the Inlet to the Outlet of the Pipe

The static pressure difference between the inlet and the outlet of the pipe is almost the same for all three cases. The pressure loss is 297 Pa for the straight pipe without a weld, 301 Pa for the 90°/90° pipe without a weld, and 301 Pa for the 90°/90° pipe with a 30° weld. This shows little effects of bend and weld on the change in static pressure.

In a more detailed study, static pressure from inlet to outlet of the pipe are analyzed

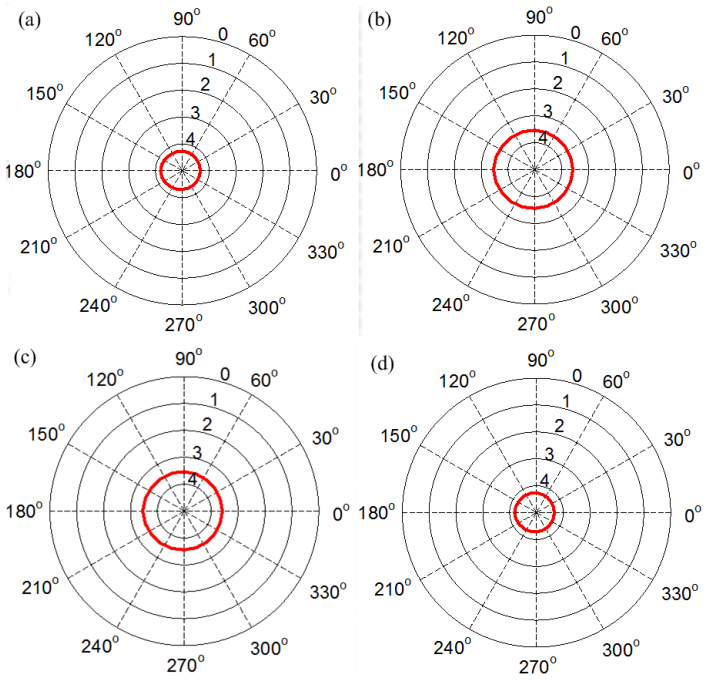

Figure 5.26: Distribution of δ_θ at the pipe exit when the number of grid points is: (a) 0.7 million (b) 3 million (c) 5 million (d)16 million

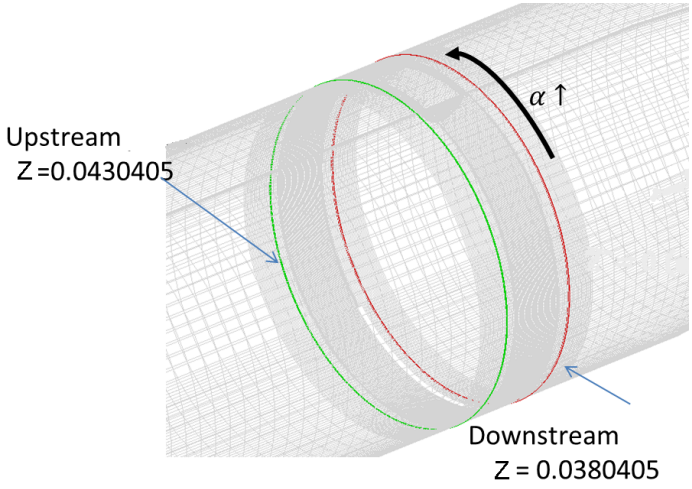

Figure 5.27: Locations of two constant Z planes in the vicinity of the 30° weld

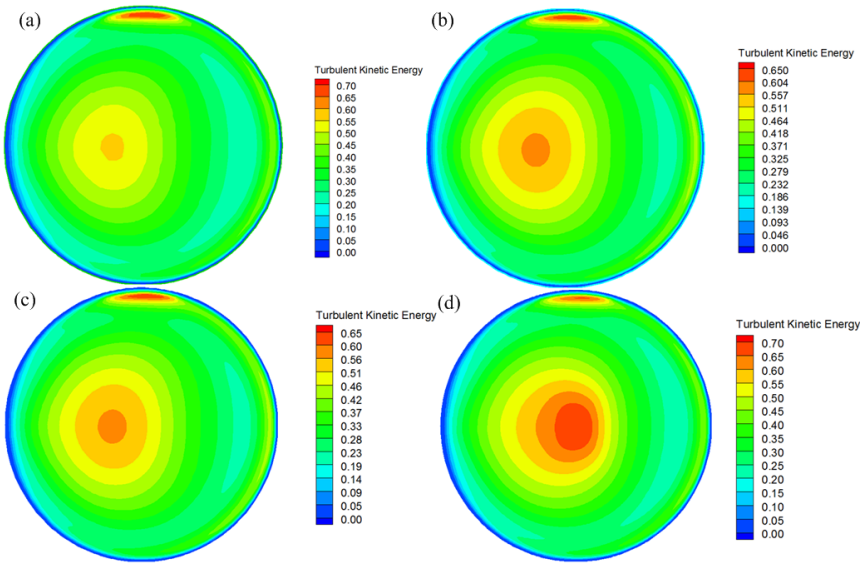

Figure 5.28: Distribution of k on the plane at $z = 0.0430405$, when the number of grid points is: (a) 0.7 million (b) 3 million (c) 5 million (d)16 million

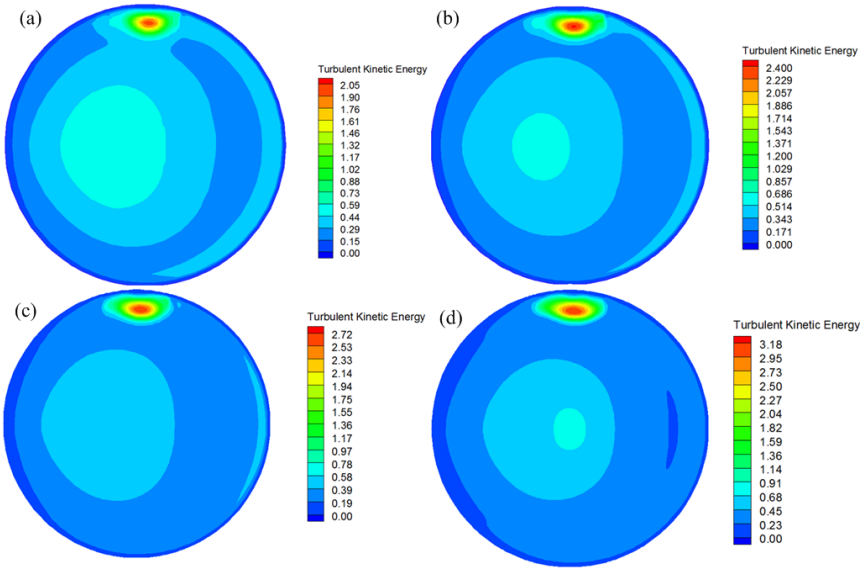

Figure 5.29: Distribution of k on the plane at $z = 0.0380405$, when the number of grid points is: (a) 0.7 million (b) 3 million (c) 5 million (d)16 million

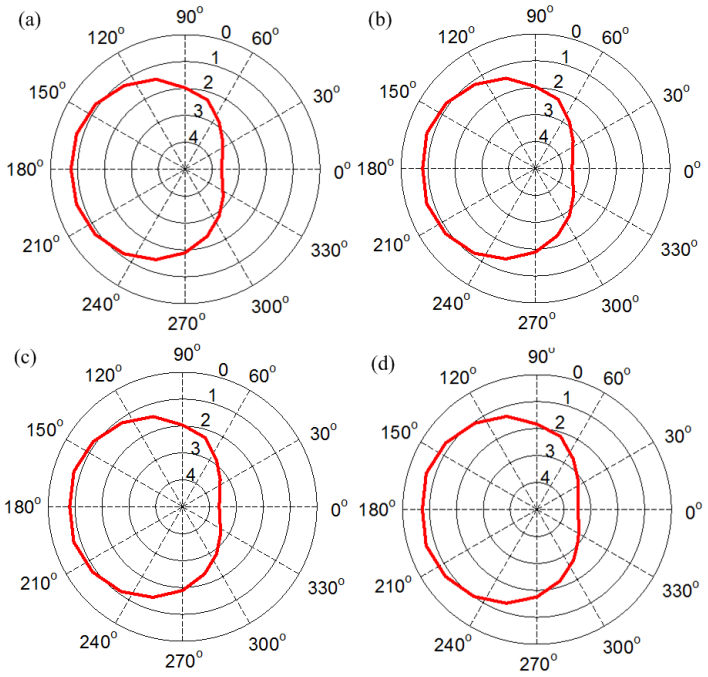

Figure 5.30: Distribution of δ_θ on the plane at $z = 0.0430405$, when the number of grid points is: (a) 0.7 million (b) 3 million (c) 5 million (d)16 million

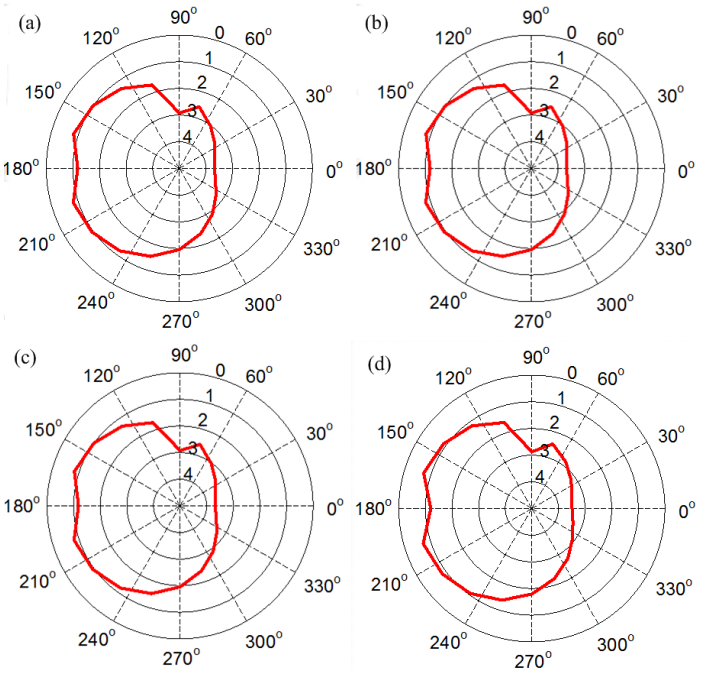

Figure 5.31: Distribution of δ_θ on the plane at $z = 0.0380405$, when the number of grid points is: (a) 0.7 million (b) 3 million (c) 5 million (d)16 million

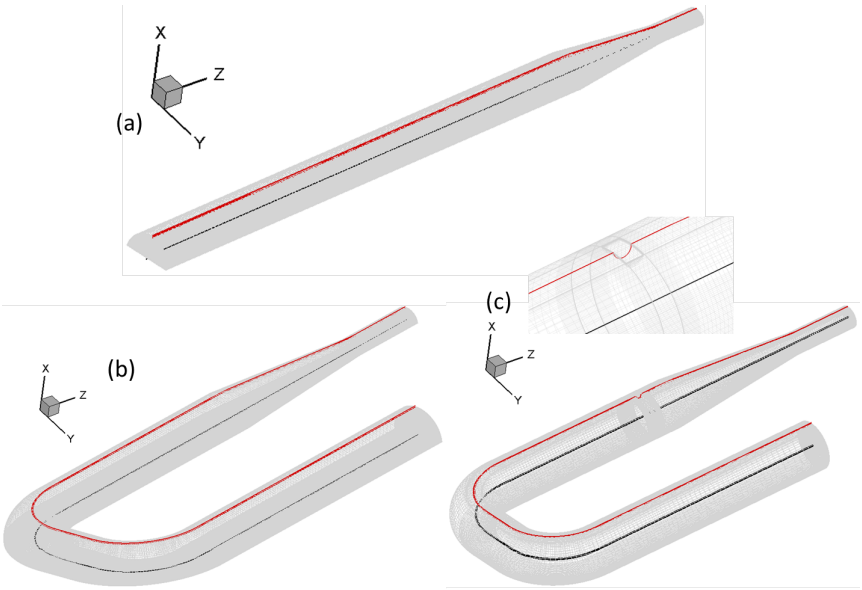

Figure 5.32: Center line and line along the wall (over the weld): (a) straight pipe without a weld, (b) 90°/90° pipe without a weld, and (c) 90°/90° pipe with a 30° weld

along the centerline of the pipe as well as along a line on the wall that passes over the weld, whose locations are shown in Fig. 5.32. Fig. 5.33 shows the static pressure change along the center line as well as an enlarged plot near the weld location. Fig. 5.34 is the plot along the line on the wall over the weld and a close-up of the weld region. In general, the distribution of static pressure doesn't vary much between the three pipes, with only a minor difference near the weld location: for the bent pipe with/without a weld, the static pressure only differs along the wall, while the static pressure in a straight pipe differs from that of bend pipes along both the center line and the line on the wall.

Wall Shear Stress Changes From the Inlet to the Outlet of the Pipe

Figure 5.35 shows the changes in the wall shear stress from the inlet to the outlet of the pipe along the wall. The wall shear stress of the straight pipe without a weld behaves differently from that of the other two cases involving pipes, starting bent from $s = 5.17$ (the location of the first bend) to $s = 15$ (after the weld). The difference in wall shear stress only exists near the location of weld for the two bent pipes.

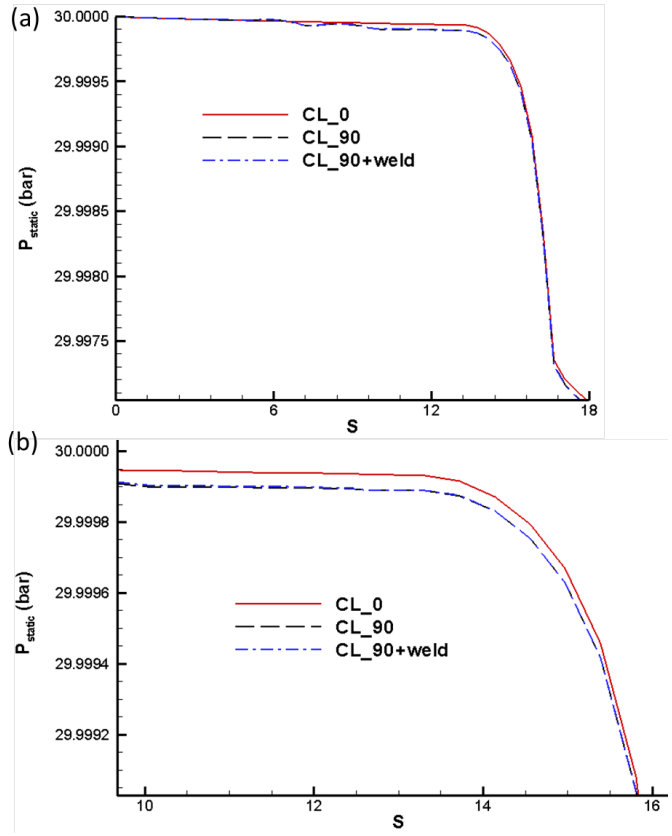

Figure 5.33: Static pressure changes along the center line: (a) From inlet to outlet of the three studied pipes and (b) enlarged plot near the weld location (weld centers at $s = 12.482$). "CL_ 0" is the center line along the straight pipe without a weld, "CL_ 90" is the center line along the 90°/90° pipe without a weld, and "CL_ 90+weld" is the center line along the 90°/90° pipe with a 30° weld

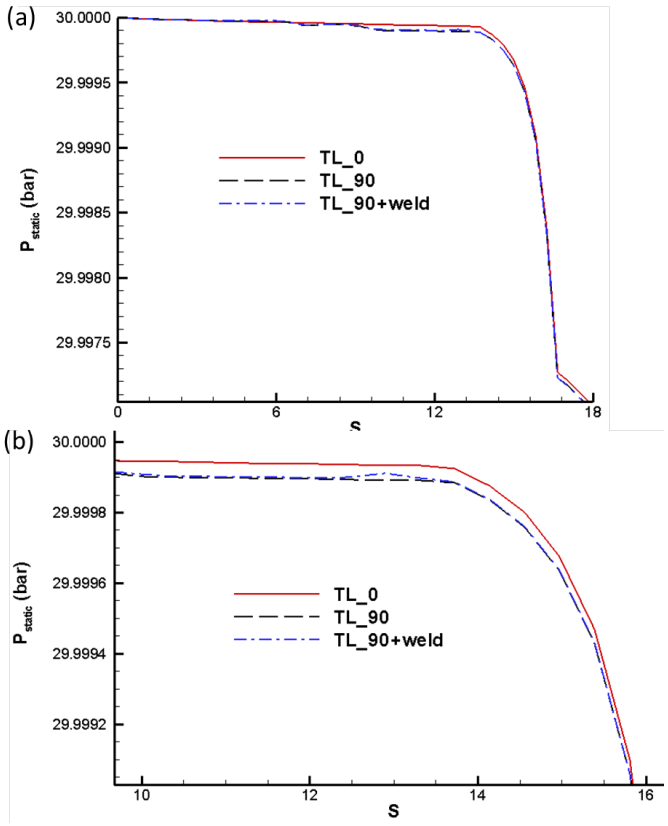

Figure 5.34: Static pressure changes along the wall: (a) From inlet to outlet of of the three studied pipes and (b) enlarged plot near the weld location (weld centers at $s = 12.482$). "TL_ 0" is the line along the wall of the straight pipe without a weld, "TL_ 90" is the line along the wall of the 90°/90° pipe without a weld, and "TL_ 90+weld" is the line along wall of the 90°/90° pipe with a 30° weld

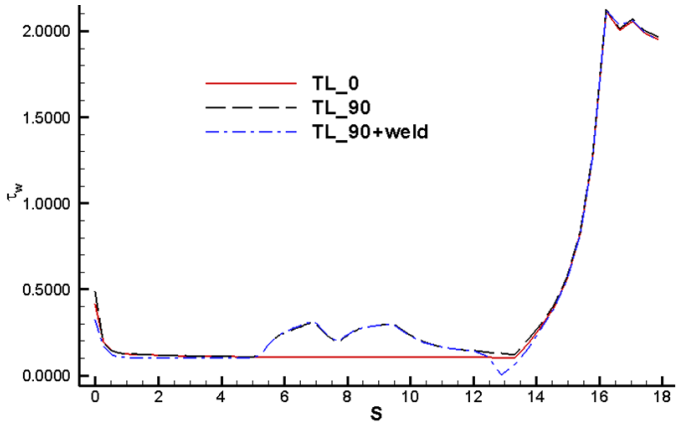

Figure 5.35: Wall shear stress changes along the wall from inlet to outlet of the three studied pipes. "TL_ 0" is the line along the wall of the straight pipe without a weld, "TL_ 90" is the line along the wall of the 90°/90° pipe without a weld, and "TL_9 0+weld" is the line along wall of the 90°/90° pipe with a 30° weld

Plots Near the Vicinity of the Weld Location

The axial velocity, momentum thickness, turbulence intensity, and turbulence kinetic energy dissipation rate are plotted at four s locations for the three studied pipes. Figure 5.36 gives the locations of planes at four s locations: $s = 12.478$ (before the weld), $s = 12.482$ (middle of the weld), $s = 12.601$ (after the weld), and $s = 17.892$ (pipe exit). Figures 5.37, 5.38, and 5.39 are the contour maps of the axial velocity in the straight pipe without a weld, the 90°/90° pipe without a weld, and the 90°/90° pipe with a 30° weld, respectively. The bent pipes show asymmetric axial velocity distributions when flow passes through the bends. Furthermore, flow reversal occurs before the weld and more significant after the weld for the bent pipe with a weld. Flow becomes uniformly distributed after the nozzle for all the three pipes. Figures 5.40, 5.41, and 5.42 are plots of the momentum thickness for the three pipes. The figures show a consistently uniform distribution of momentum thickness at all four s locations for the three pipes. The plots of turbulence intensity for the three pipes are shown in Figs. 5.43, 5.44, and 5.45. The turbulence intensity at the exit of the pipes without welds decreased compared to the values at other s locations. However, the turbulence intensity increases at the exit of the pipe with a weld. Note that all the three pipes have nozzles. It seems that a nozzle reduces the turbulence intensity of the flow, while the weld makes the flow more turbulent. Turbulence kinetic energy dissipation rate increases at the exits of all the three pipes, as shown in Figs. 5.46, 5.47, and 5.48.

5.3 Mercury Turbulent Jet Flow

Mercury flows out of the target delivery pipe to form a free jet. The sketch of the free mercury jet with MHD (magnetohydrodynamic) and energy deposition for the MERIT experiment is shown in Fig. 5.49. The mercury jet study in this paper doesn't consider MHD and energy deposition, but only mercury-air two-phase jet flow, which is the base line of the complicated, real-jet problem in MERIT experiment.

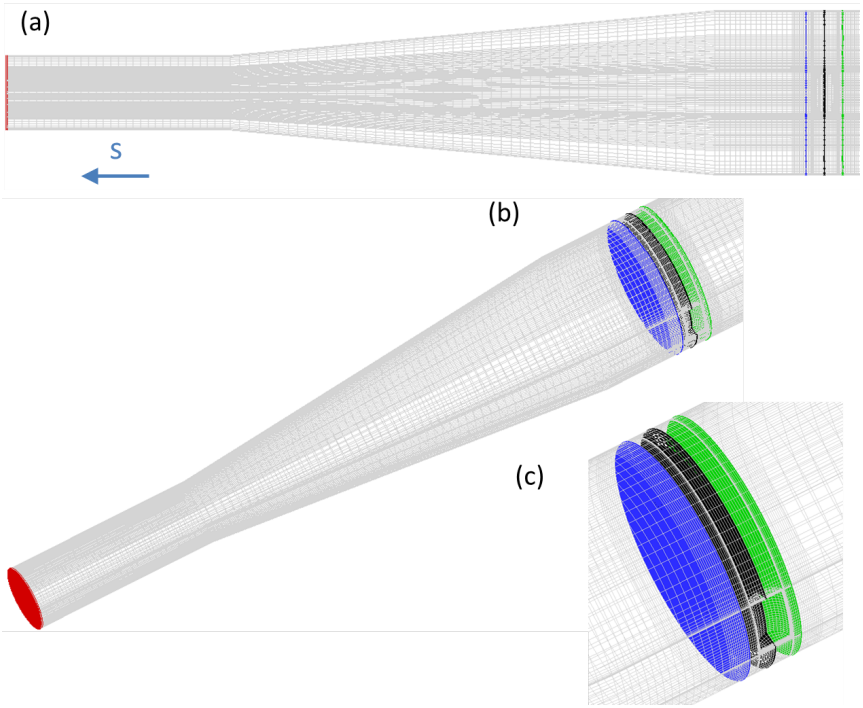

Figure 5.36: Planes at $s = 12.478$, $s = 12.482$, $s = 12.601$, and the exit ($s = 17.892$). (a) $y - z$ view of the plane locations, (b) default view of the plane locations, and (c) enlarged view of the plane locations in the vicinity of a weld

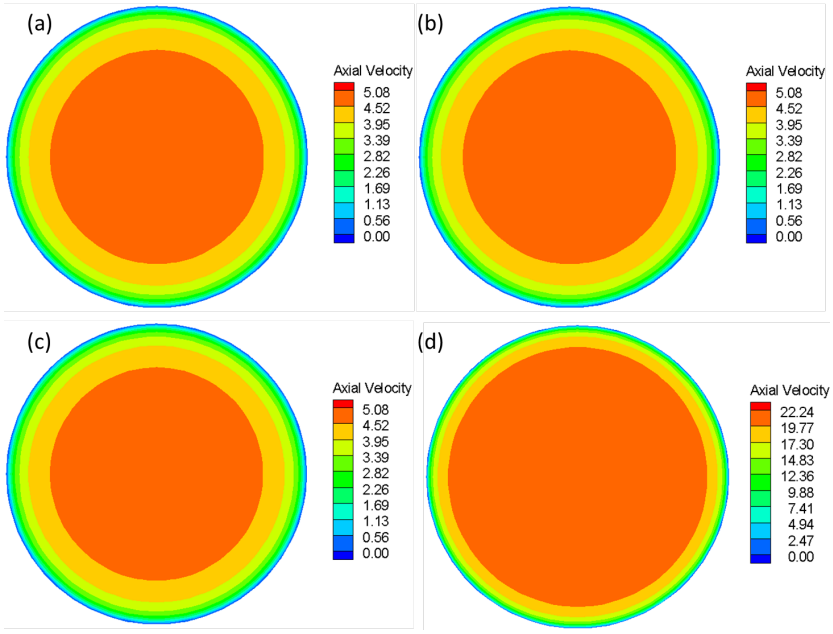

Figure 5.37: Contour maps of the axial velocity for the straight pipe without a weld: (a)$s = 12.478$, (b) $s = 12.482$, (c) $s = 12.601$, and (d) exit

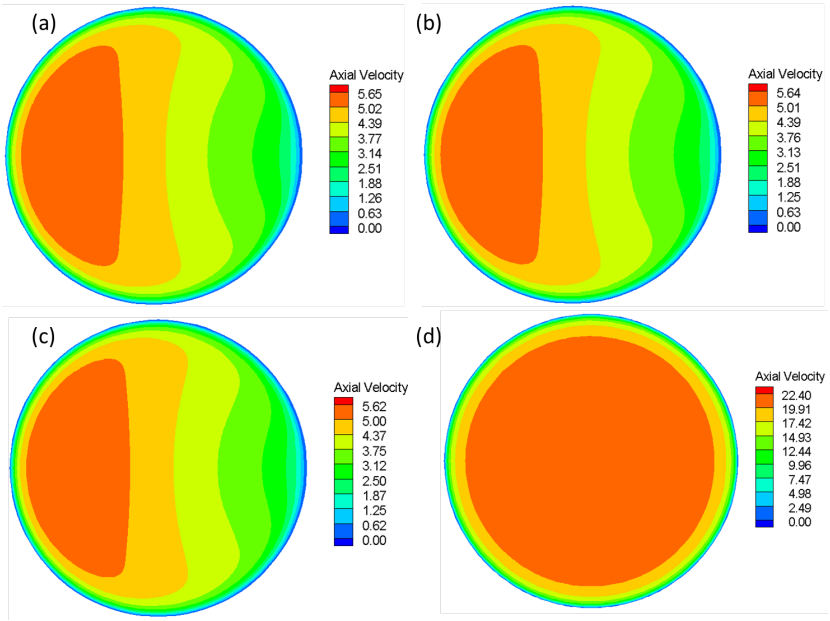

Figure 5.38: Contour maps of axial velocity for the 90°/90° pipe without a weld: (a)s = 12.478, (b) $s = 12.482$, (c) $s = 12.601$, and (d) exit

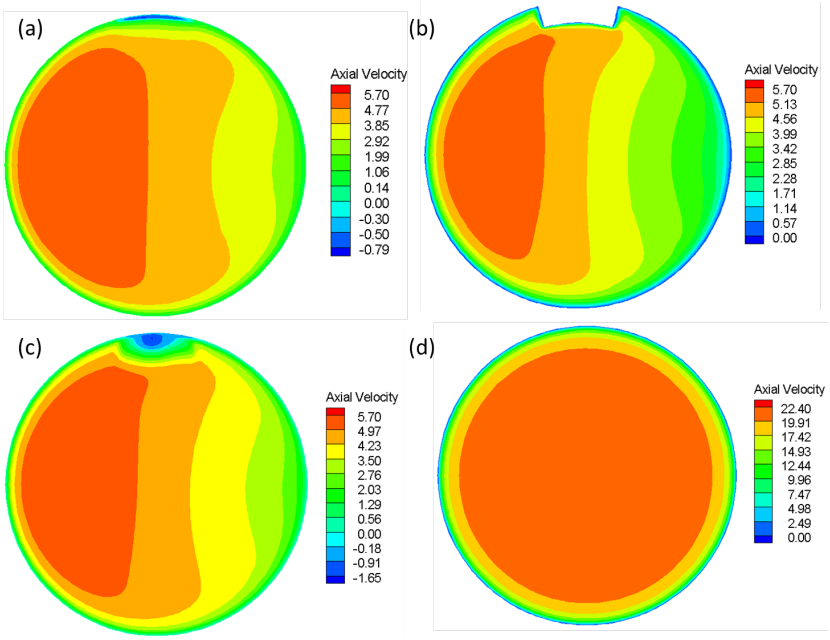

Figure 5.39: Contour maps of axial velocity for the 90°/90° pipe with a 30° weld: (a)s = 12.478, (b) $s = 12.482$, (c) $s = 12.601$, and (d) exit

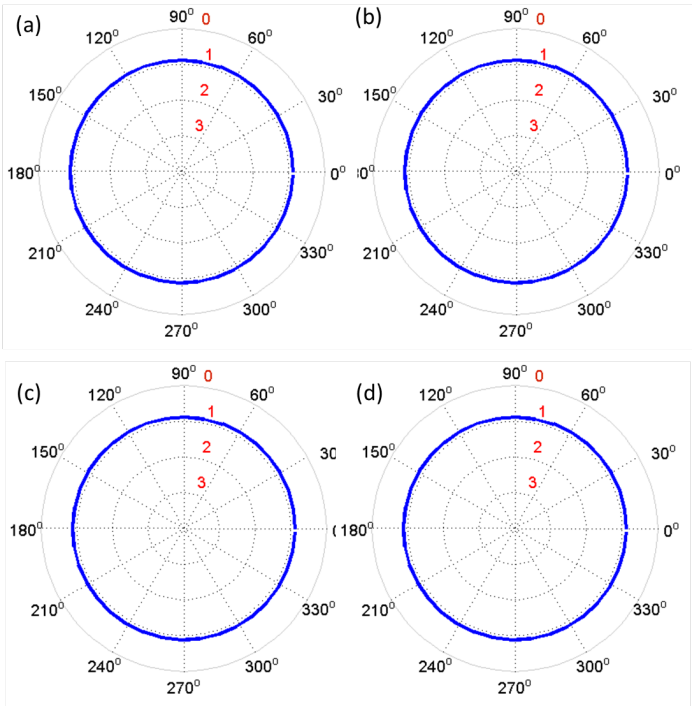

Figure 5.40: Plot of momentum thickness for the straight pipe without a weld: (a)$s = 12.478$, (b) $s = 12.482$, (c) $s = 12.601$, and (d) exit

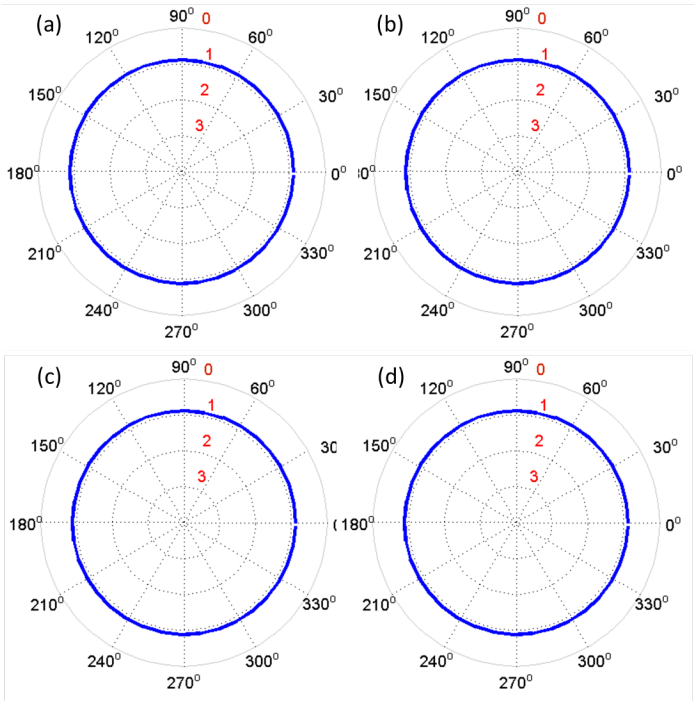

Figure 5.41: Plot of momentum thickness for the 90°/90° pipe without a weld: (a)$s = 12.478$, (b) $s = 12.482$, (c) $s = 12.601$, and (d) exit

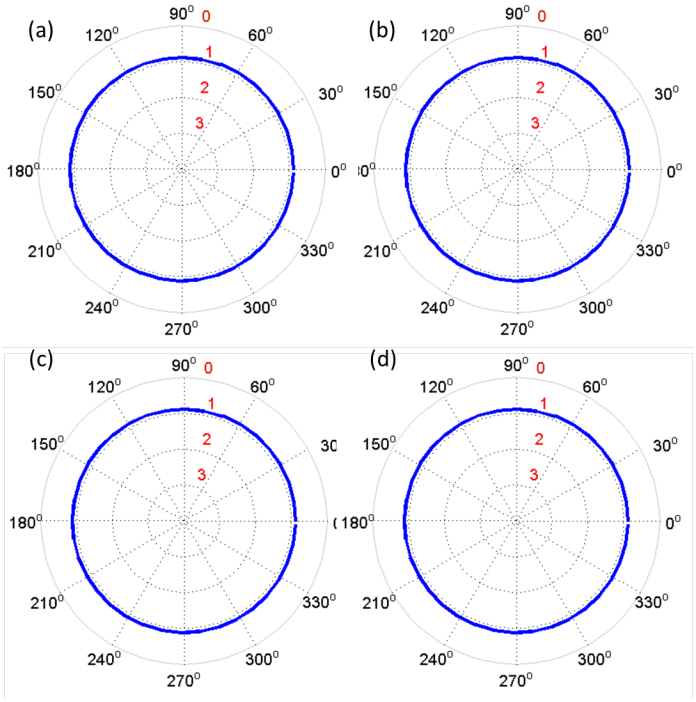

Figure 5.42: Plot of momentum thickness for the 90°/90° pipe with a 30° weld at (a)s = 12.478, (b) $s = 12.482$, (c) $s = 12.601$, and (d) exit

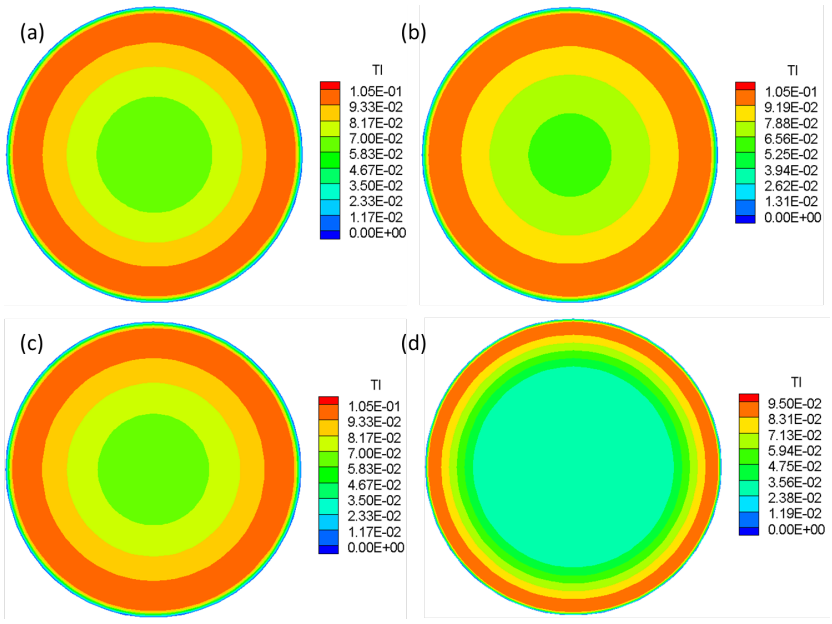

Figure 5.43: Contour of turbulence intensity for the straight pipe without a weld: (a)s = 12.478, (b) $s = 12.482$, (c) $s = 12.601$, and (d) exit

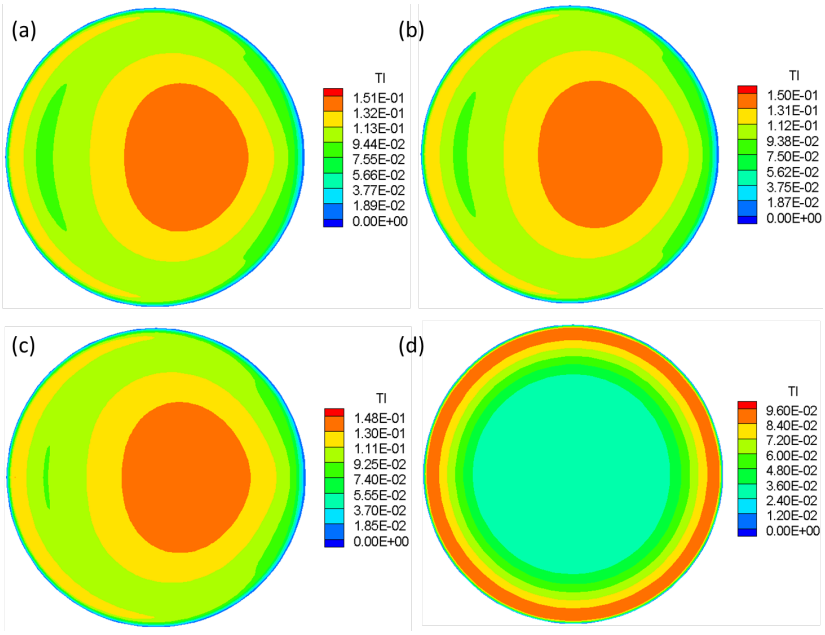

Figure 5.44: Contour maps of turbulence intensity for the 90°/90° pipe without a weld: (a)$s = 12.478$, (b) $s = 12.482$, (c) $s = 12.601$, and (d) exit

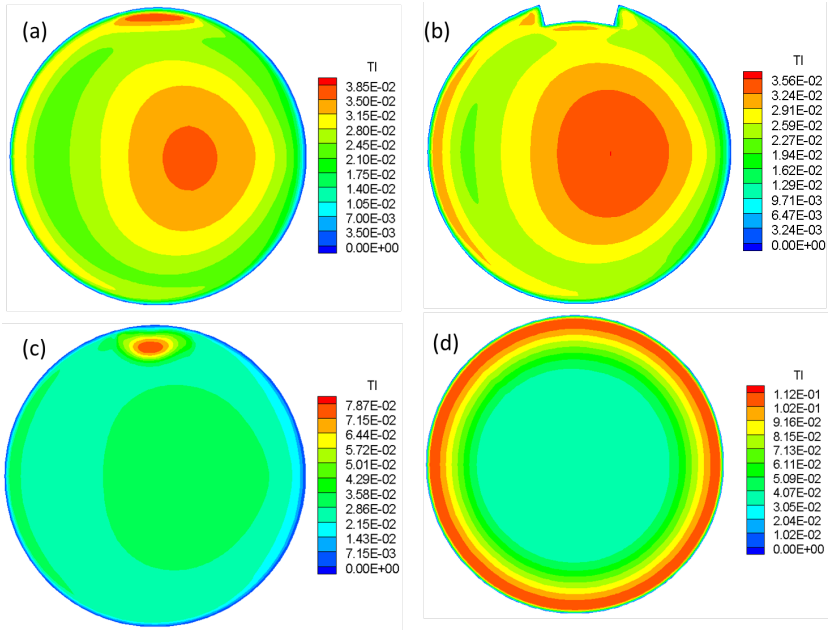

Figure 5.45: Contour maps of turbulence intensity for the 90°/90° pipe with a 30° weld: (a)$s = 12.478$, (b) $s = 12.482$, (c) $s = 12.601$, and (d) exit

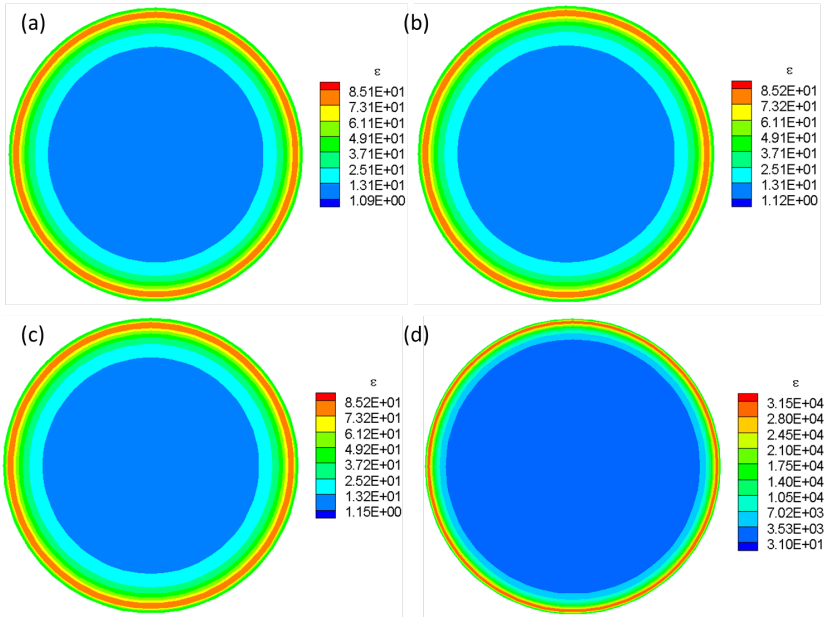

Figure 5.46: Contour of turbulent kinetic energy dissipation rate for the straight pipe without a weld at (a)$s = 12.478$, (b) $s = 12.482$, (c) $s = 12.601$, and (d) exit

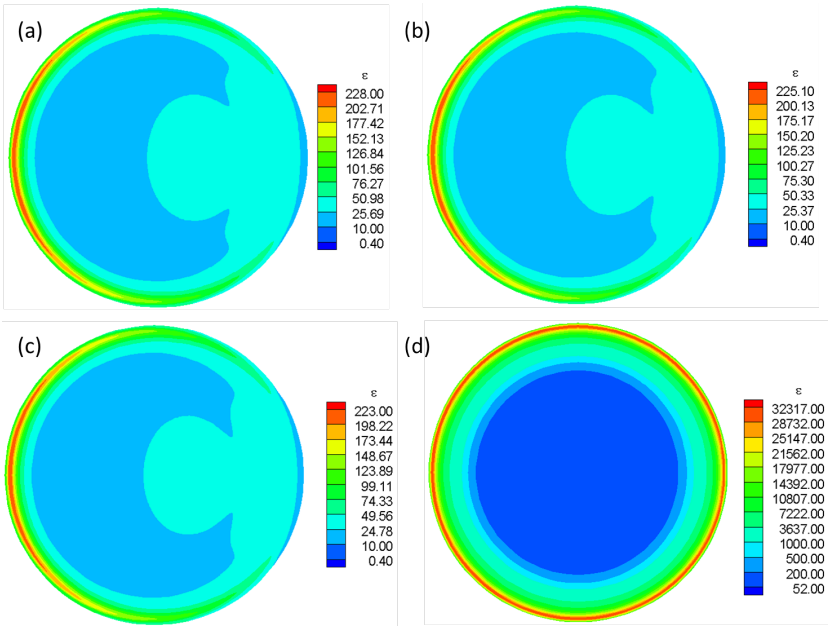

Figure 5.47: Contour maps of turbulent kinetic energy dissipation rate for the 90°/90° pipe without a weld: (a)$s = 12.478$, (b) $s = 12.482$, (c) $s = 12.601$, and (d) exit

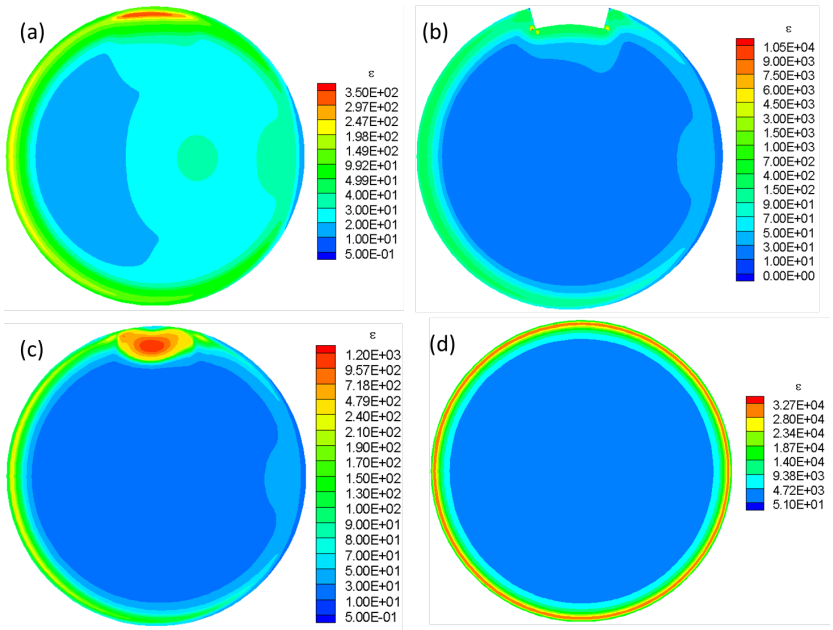

Figure 5.48: Contour maps of turbulent kinetic energy dissipation rate for the 90°/90° pipe with a 30° weld: (a)$s = 12.478$, (b) $s = 12.482$, (c) $s = 12.601$, and (d) exit

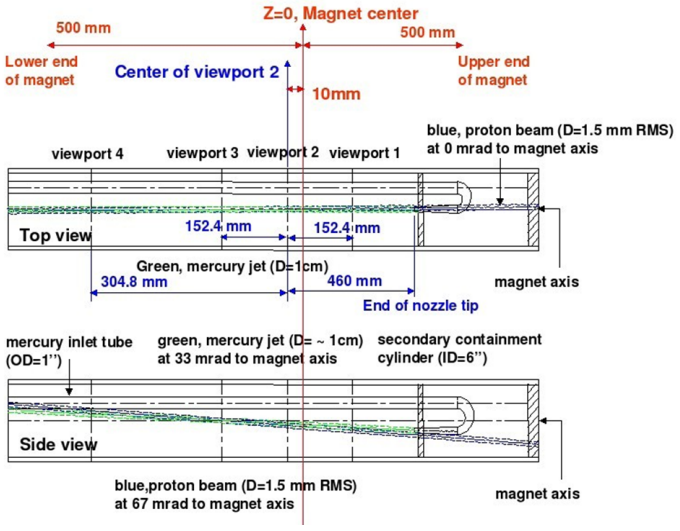

Figure 5.49: Sketch of the mercury free jet with MHD and energy deposition for the MERIT experiment

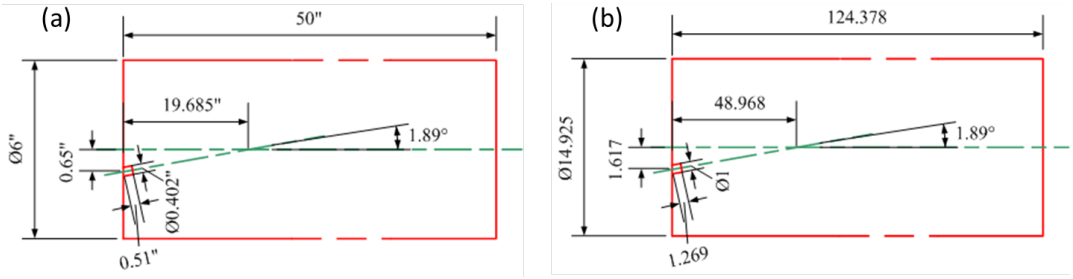

Figure 5.50: The Side view of mercury jet flow (a) in dimensional spatial units (b) normalized spatals units, with jet inlet diameter as the scale

5.3.1 Two Dimensional Turbulent Mercury Jet Flow

A two-dimensional mercury jet flows into air is studied first. When only assume the primary breakup, the critical liquid Weber number is less than 10 [65]. In this case, we can show that the smallest mesh size required to capture jet break up is approximately $0.9\mu m$:

$$We \equiv \frac{\rho u^2 \triangle x}{\sigma} = 10 \Rightarrow \triangle x = \frac{we\sigma}{\rho u^2} = \frac{10 * 0.4855}{13456 * 20 * 20} = 0.9\mu m \approx 8.86 * 10^{-5} D, \qquad (5.8)$$

where D is the jet diameter.

From the mercury jet sketch in the MERIT experiment (Fig. 5.49), we can obtain the side view of mercury jet flow on the $y - z$ plane in both dimensional (Fig. 5.50(a)) and non-dimensional (Fig. 5.50(b)). The real mercury jet problem has a computational domain with a width of $15D$ and a length of $124.4D$. For the mesh size requirement (Eq. 5.8), we would need a mesh with $2.44 * 10^{11}$ grid points when the mesh is uniform. Therefore, we reduced the lengths of the computational domain with the (supposedly) least influence on the jet flow. Also, a halved model is used when considering axisymmetric boundary condition at the centerline. Also, the computational domain is reduced in length, width, and height, (Fig. 5.51). Figure. 5.52 shows the boundary conditions for the 2D mercury jet simulation. The velocity profile at the outlet of a straight nozzle pipe is assumed (Fig. 5.53) at the inlet of the jet flow. The result of α_{Hg} is shown in Fig. 5.54, which shows a very rich jet breakup phenomenon.

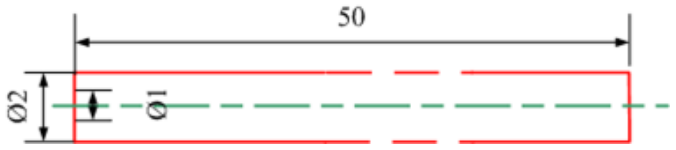

Figure 5.51: Simplified two-dimensional mercury jet model with reduced length, width, and height

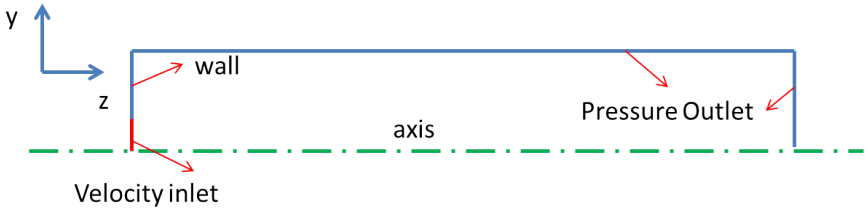

Figure 5.52: The boundary conditions for the two dimensional mercury jet simulation

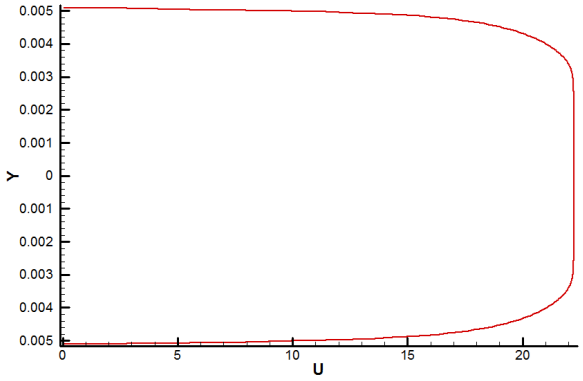

Figure 5.53: The velocity profile at the inlet of the two dimensional mercury jet simulation

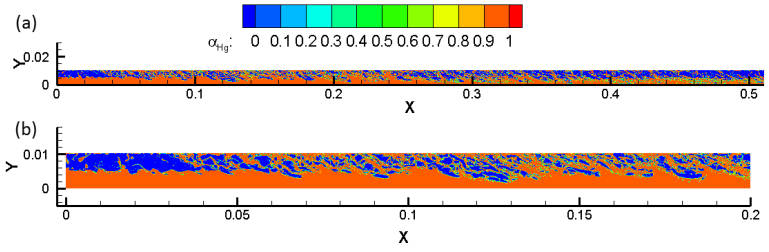

Figure 5.54: Contour map of the volume fraction of mercury for the two-dimensional mercury jet simulation over: (a) the whole computational domain (b) $0 < x < 0.2$ for enlarged view

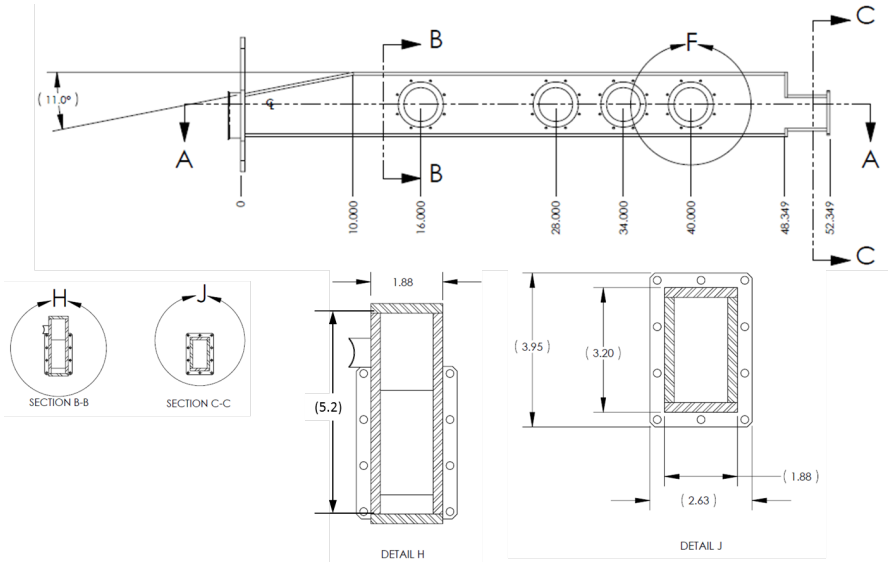

Figure 5.55: Schematics of target delivery system by V. Graves

5.3.2 Three Dimensional Mercury Turbulent Jet Flow

Figure 5.55 is the schematic of the target delivery system in the MERIT experiment. The simulation of a three dimensional mercury jet using the length, width, and height in Fig. 5.55 would lead to a total of 6.8×10^{15} grid points, assuming a uniform mesh spacing $0.9\mu m$ (Eq. (5.8)). Therefore, it is necessary to reduce the lengths of the computational model. Figure 5.56 shows the simplification of the computational model to a parallelepiped of sides $3D \times 3D \times 50D$. Moreover, MILES requires a big number of mesh points for the three-dimensional simulation. With the limited computational resources, we have used time-averaged RANS method for the simulation. Therefore, the turbulent model of RKE has been used here, instead of MILES. Although the complicated unsteady structure on free interface may be time-averaged, it is still possible to analyze the deformation of the jet under different inputs conditions.

The outlet conditions of pipe simulation is assumed at the inlet of the domain used for the mercury jet simulation. In order to determine the effects of having a bend and a weld on the mercury jet interface deformation, the outlet conditions from a straight nozzle pipe without a weld, a 90°/90° pipe without a weld, and a 90°/90° pipe with a 30° off bend plane

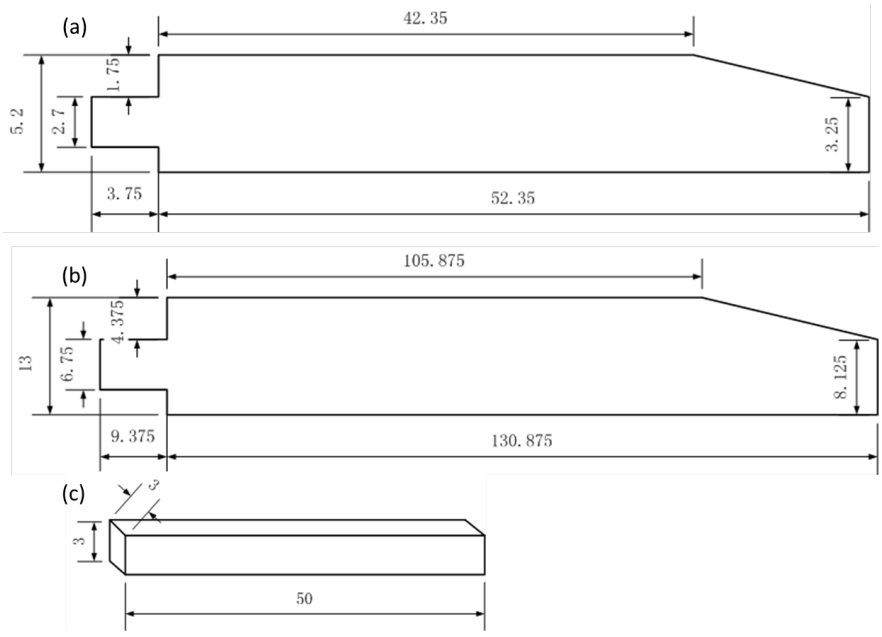

Figure 5.56: Simplification of the three-dimensional mercury jet model:(a) in dimensional spatial units, (b) normalized spatial units, with jet inlet diameter as the scale, (c) simplified model with reduced length, width, and height (normalized by jet inlet diameter, D)

weld, are used in the domain for mercury jet simulation. Therefore, we classify the three dimensional mercury jet simulation into three cases: Case 1 uses the pipe axial conditions of a straight nozzle pipe flow without a weld, Case 2 uses the pipe axial conditions of a 90°/90° pipe flow without a weld, and Case 3 uses the pipe axial conditions of a 90°/90° pipe flow with a 30° off bend plane weld.

Because of the symmetry of the axial flow from a straight pipe without a weld, a half nozzle is used in Case 1 with a symmetry boundary condition. Figure 5.57 describes the boundary conditions for the Case 1. Velocity profile from the outlet of the straight pipe without a weld (Fig. 5.58) is assumed at the jet inlet. The results of α_{Hg} and U_z are shown in Figs. 5.59 and 5.60. The axial flow from the 90°/90° pipe without a weld is also symmetric.

Case 2 has the same boundary conditions as Case 1 (Fig. 5.57). The velocity profile at the inlet of Case 2 jet is shown in Fig. 5.61. The Case 2 jet simulation results are shown in Figs. 5.62 and 5.63. The axial flow from the 90°/90° pipe with a 30° weld is asymmetric. Therefore a complete model needs to be used for Case 3, (Fig. 5.64). The velocity profile at

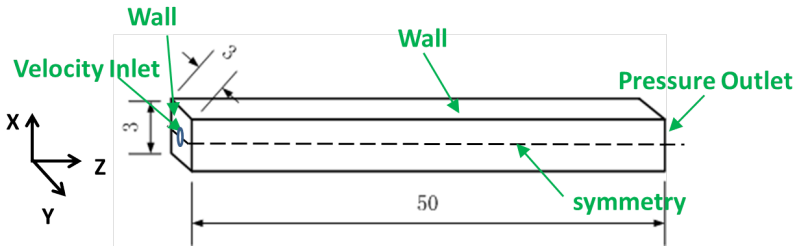

Figure 5.57: The boundary conditions for the three-dimensional mercury jet simulation case 1. The dimension shown in the sketch is normalized by jet inlet diameter, which is 0.01m. No gravity effects are included in the model. Case1: The jet inlet conditions use outputs of straight nozzle pipe without a weld

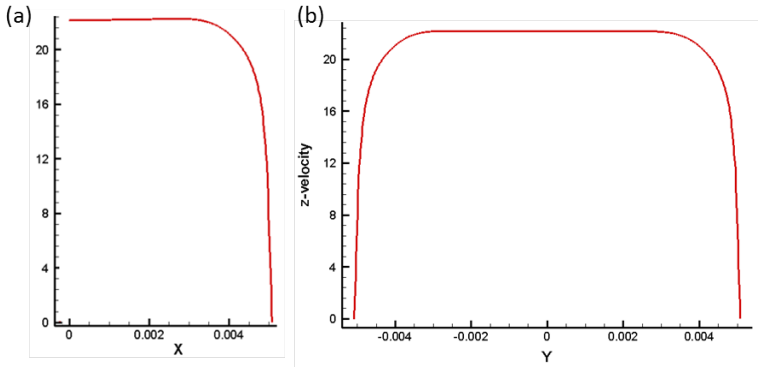

Figure 5.58: The axial velocity profile imposed at the inlet of the three dimensional mercury jet simulation Case 1 (a) x line plot (b) y line plot

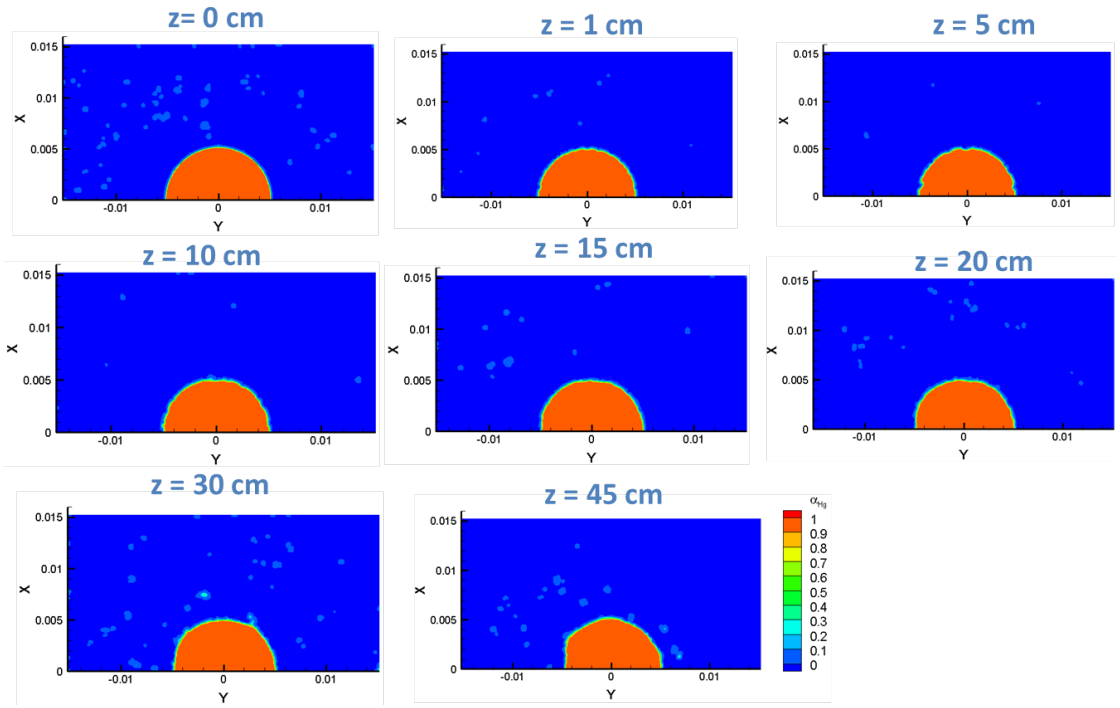

Figure 5.59: Contour maps of the volume fraction of mercury, α_{Hg}, for three-dimensional mercury jet simulation Case 1

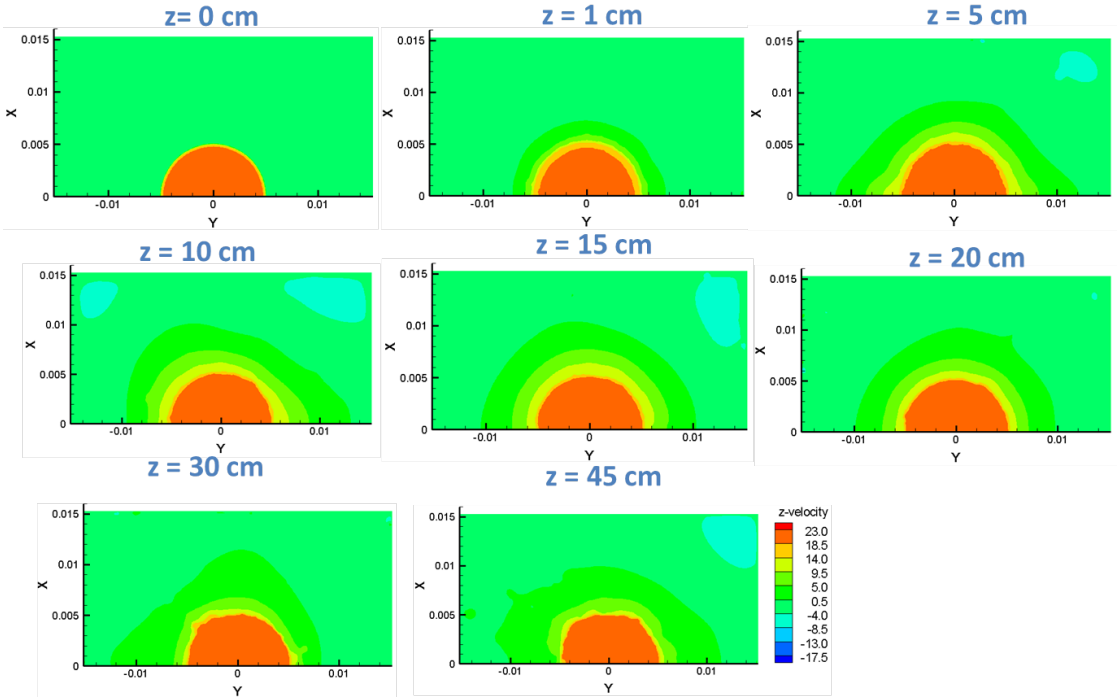

Figure 5.60: Contour maps of the axial velocity, U_z, for three-dimensional mercury jet simulation Case 1

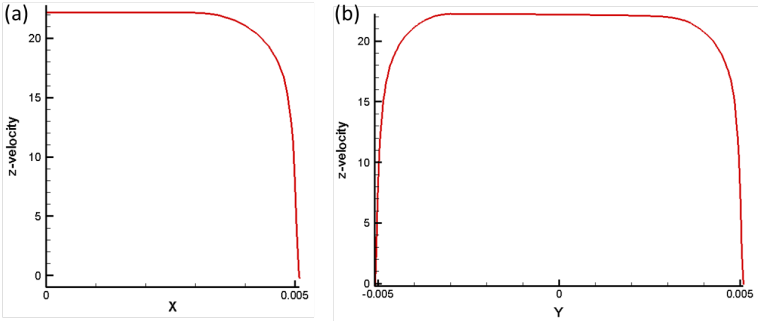

Figure 5.61: The axial velocity profile imposed at the inlet of the three dimensional mercury jet simulation case 2 (a) x line plot (b) y line plot

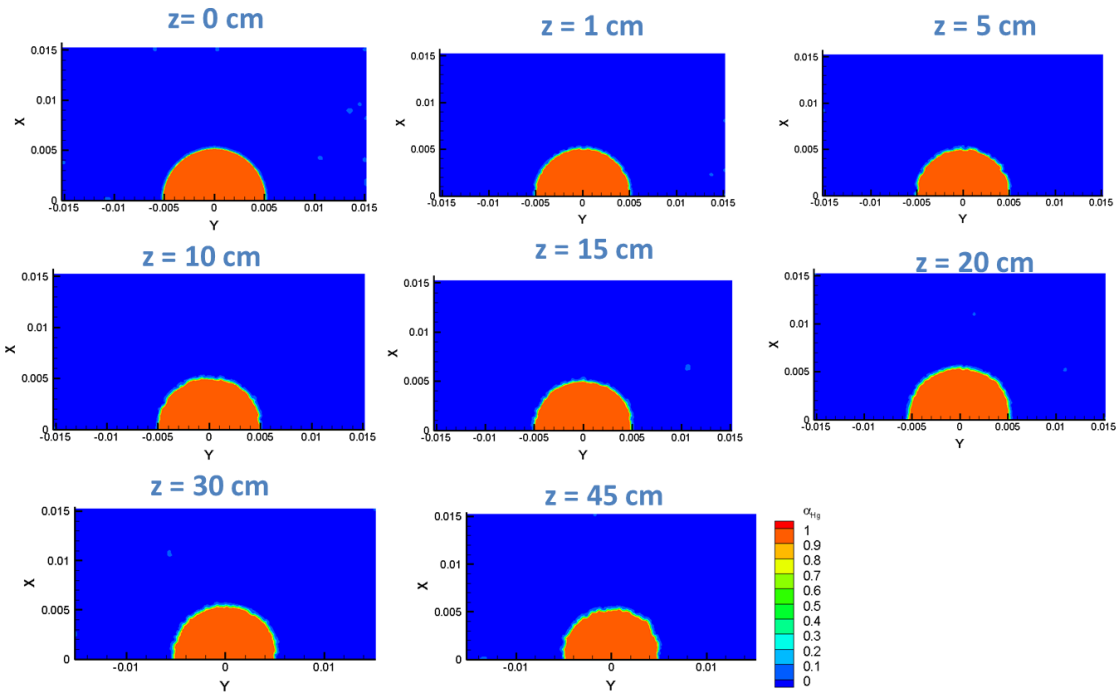

Figure 5.62: Contour maps of the volume fraction of mercury, α_{Hg}, for three-dimensional mercury jet simulation Case 2

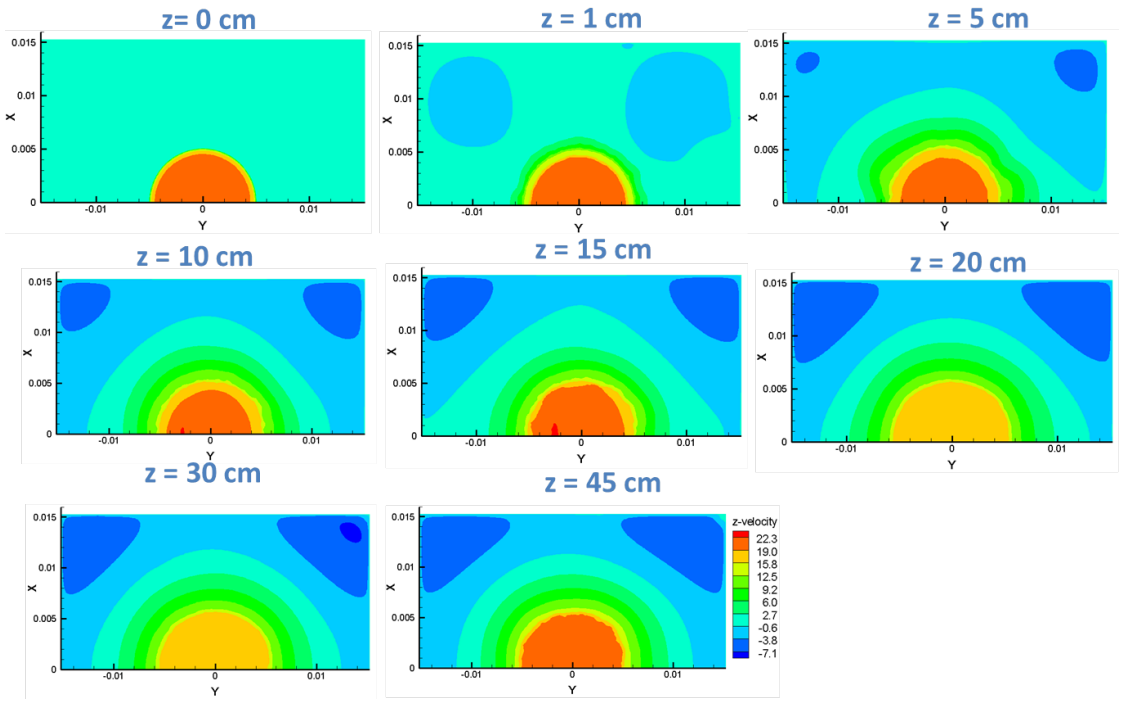

Figure 5.63: Contour maps of the axial velocity, U_z, for three-dimensional mercury jet simulation Case 2

the jet inlet is shown in Fig. 5.65, and results are shown in Figs. 5.66 and 5.67.

Case 1 is the baseline case, without a bend or weld on jet flow, while Case 3 is the most complicated case of the three. The comparative jet deformation between these two cases is of interest. Figure 5.68 is the difference in α_{Hg} between Case 1 and Case 3 at different z locations. The larger values in Fig. 5.68 indicates bigger differences in jet shape. The difference becomes more pronounced downstream of the jet. At $z = 45\,cm$, the bigger difference occurs at the positive x (line $y = 0$), the first quadrant, and the second quadrant. It seems to indicate some effects or combined effects of the bend and weld on the jet deformation. In order to obtain a more quantitative insight on the observed jet deformation, we calculate the ellipticity of the deformed jet.

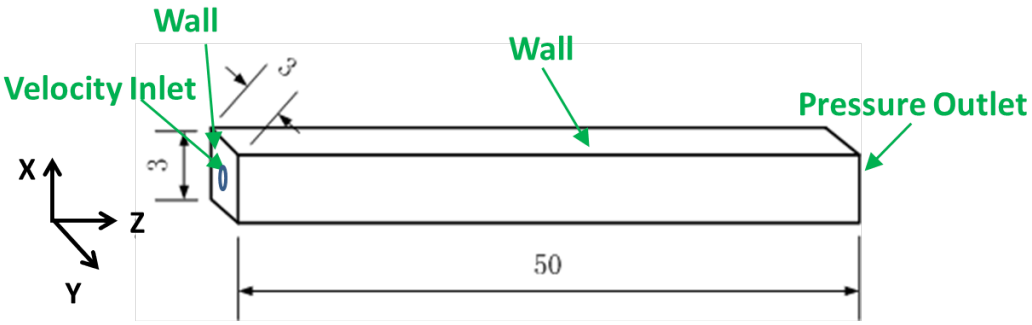

Figure 5.64: The boundary conditions for the three-dimensional mercury jet simulation Case 3. The dimensions shown in the sketch are normalized by the jet inlet diameter, which is 0.01m. No gravity effects are included in the model. Case 3: The jet inlet conditions use outputs of 90°/90° pipe with a 30° weld

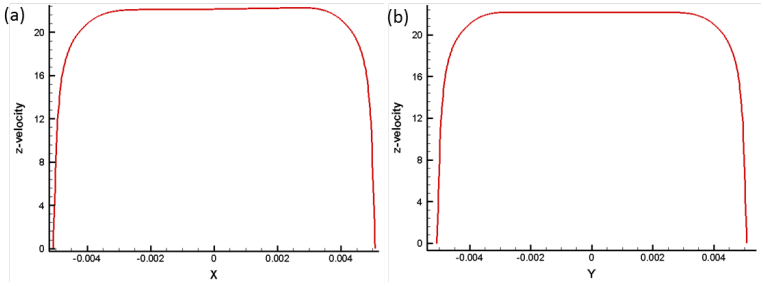

Figure 5.65: The axial velocity profile imposed at the inlet of the three-dimensional mercury jet simulation, Case 3 (a) x line plot (b) y line plot

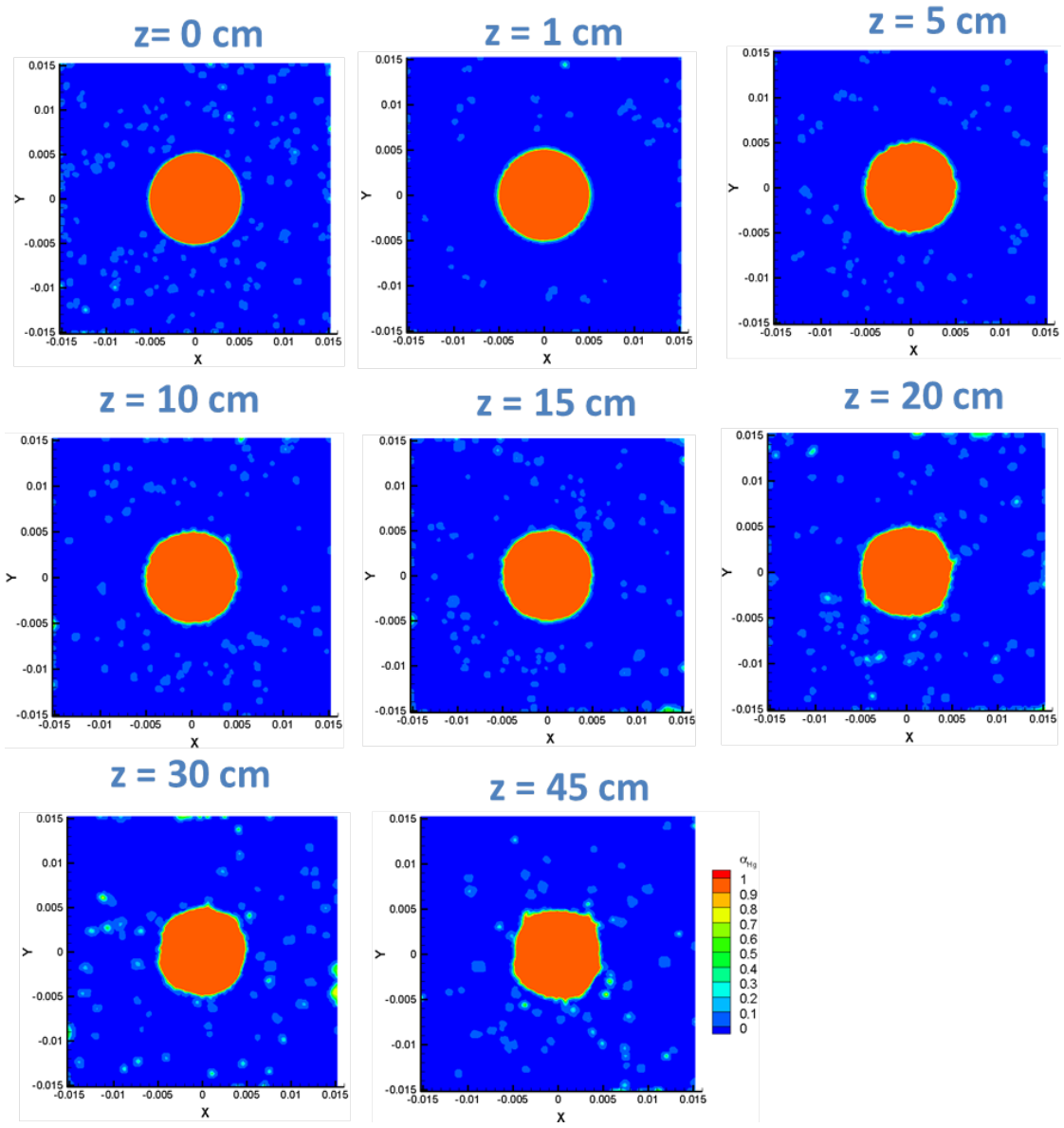

Figure 5.66: Contour maps of the volume fraction of mercury, α_{Hg}, for three-dimensional mercury jet simulation Case 3

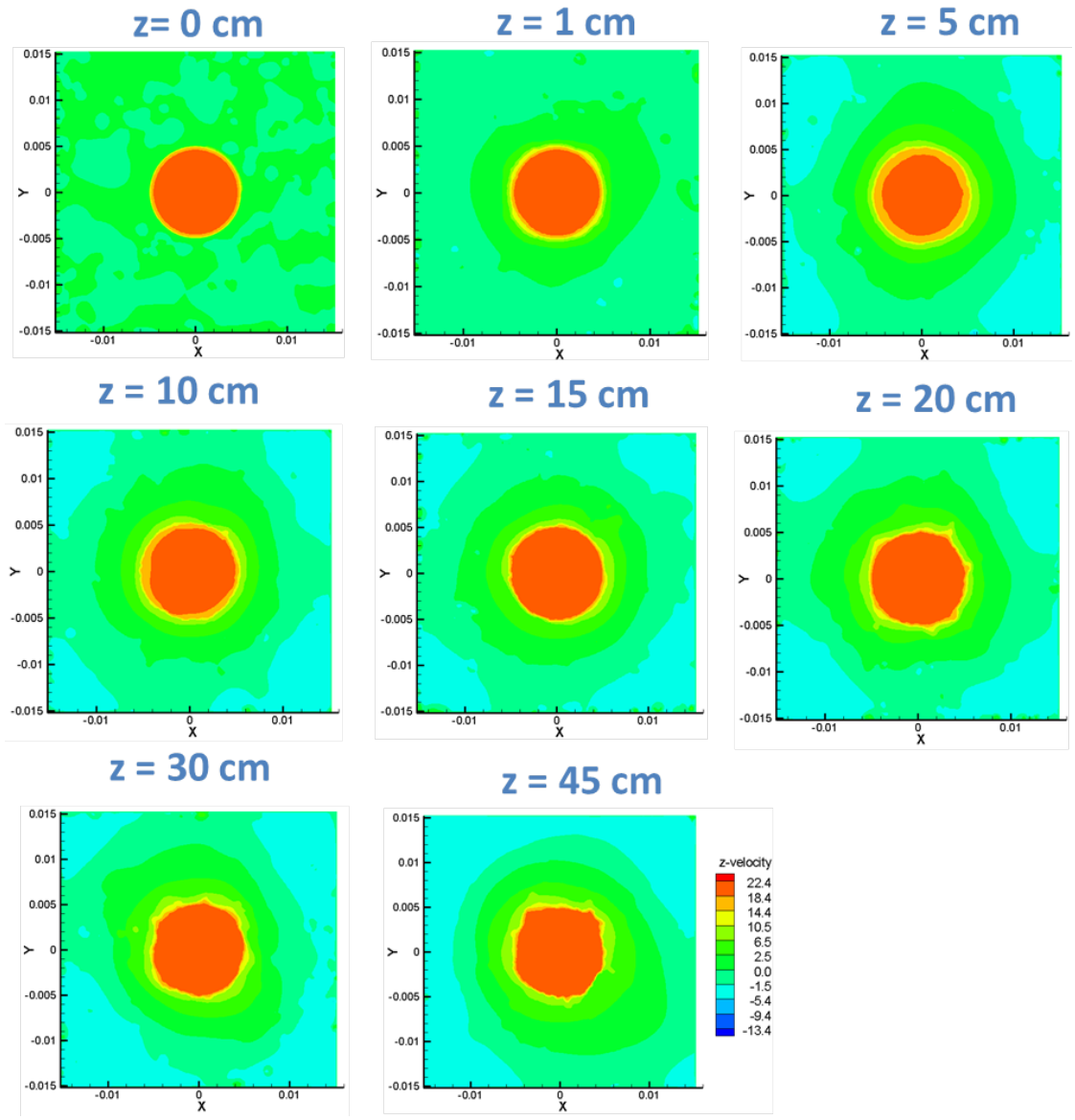

Figure 5.67: Contour maps of the axial velocity, U_z, for three-dimensional mercury jet simulation Case 3

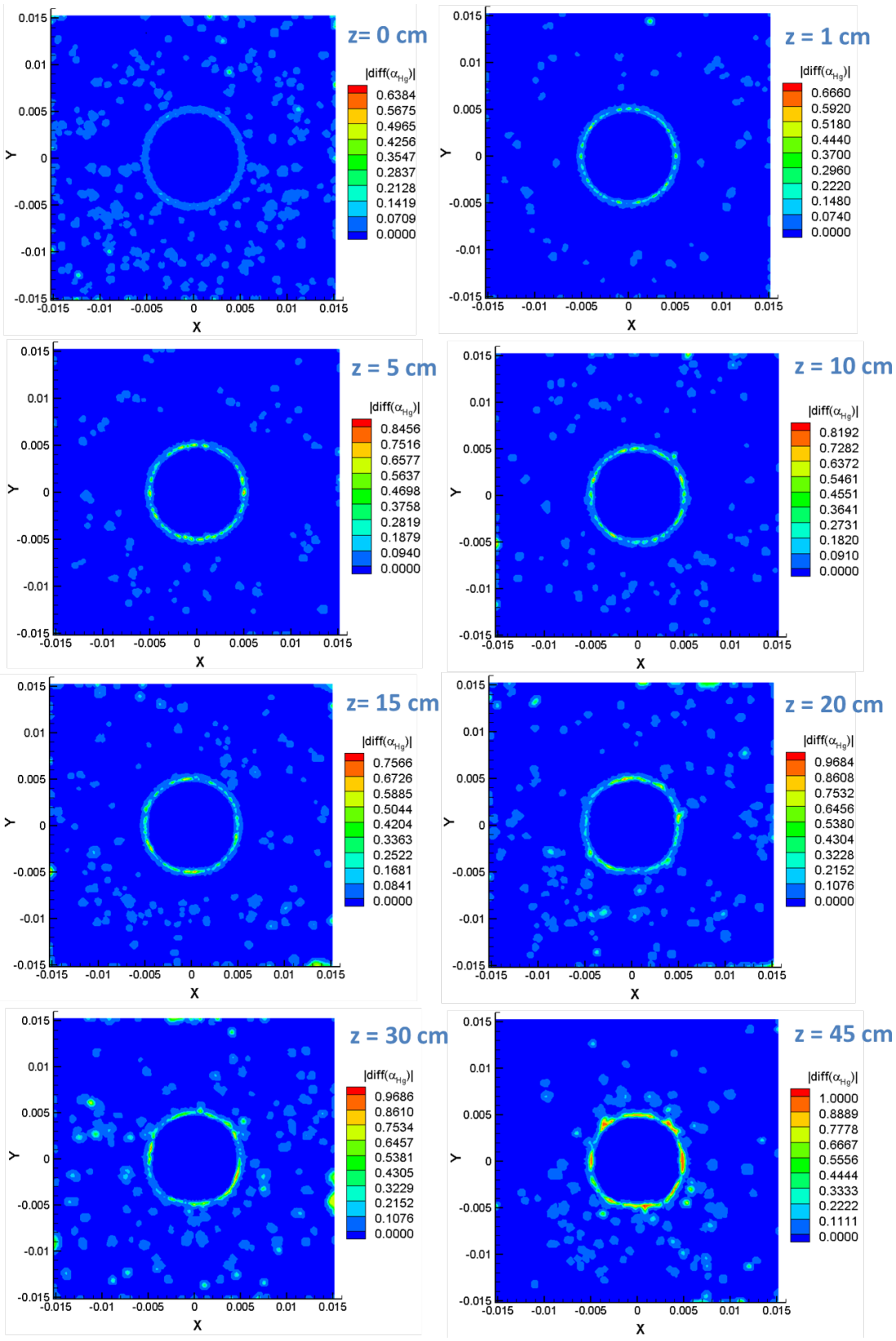

Figure 5.68: Difference of α_{Hg} between three-dimensional mercury jet simulation, Case 1 and Case 3

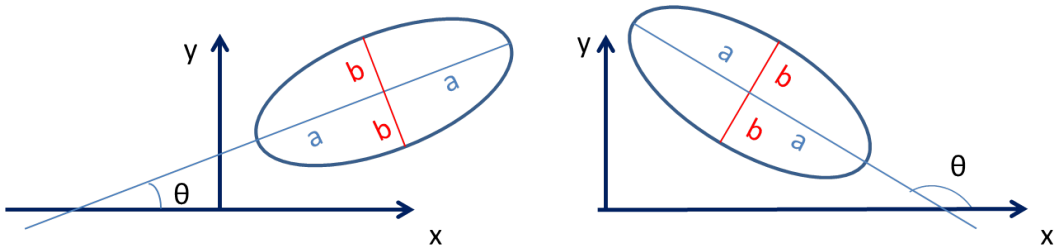

Figure 5.69: Draft of ellipse fitting: a is the major axis, b is the minor axis, and θ is the rotational angle

5.3.3 Least Squares Fitting of Ellipses

In this section, we will detail the least squares method used to fit an ellipse to given points in the plane, as the draft shown in Fig. (5.69).

In analytic geometry, the ellipse is defined as a collection of points (x, y) satisfying the following implicit equation [132]:

$$\tilde{a_1}x^2 + \tilde{a_2}xy + \tilde{a_3}y^2 + \tilde{a_4}x + \tilde{a_5}y = \tilde{a_6}, \tag{5.9}$$

where $\tilde{a_6} \neq 0$ and $\tilde{a_2}^2 - 4\tilde{a_1}\tilde{a_3} < 0$.

To simplify the following analysis, we normalize the above implicit form by dividing $\tilde{a_6}$ an both sides of the equality sign, which reduces to

$$a_1x^2 + a_2xy + a_3y^2 + a_4x + a_5y = 1. \tag{5.10}$$

Several new notations needs to be introduced to ease our discussion. For two vectors $\mathbf{s} = (s_1, s_2, \ldots, s_m)^{\mathrm{T}}$ and $\mathbf{t} = (t_1, t_2, \ldots, t_m)^{\mathrm{T}}$, the tensor product between them are defined as

$$\mathbf{s} \otimes \mathbf{t} = (s_1t_1, s_2t_2, \ldots, s_mt_m)^{\mathrm{T}}. \tag{5.11}$$

Assuming n measurements $((x_1, y_1), (x_2, y_2), ..., (x_n, y_n)$ are given, we define $x = (x_1, x_2, \ldots, x_n)^{\mathrm{T}}$

and $y = (y_1, y_2, \ldots, y_n)^{\mathrm{T}}$, then the following cost function needs to be minimized

$$C(\beta) = (X\beta - \mathbf{1})^{\mathrm{T}} (X\beta - \mathbf{1}), \tag{5.12}$$

where $X = [x \otimes x, x \otimes y, y \otimes y, x, y]$ is a n-by-5 matrix, $\beta = (a_1, a_2, a_3, a_4, a_5)^{\mathrm{T}}$ consists of the parameters to be determined, and $\mathbf{1}$ is a n-dimensional column vector with all 1's. Expand the matrix multiplication, we get

$$C(\beta) = \beta^{\mathrm{T}} X^{\mathrm{T}} X\beta - 2\mathbf{1}^{\mathrm{T}} X\beta + n. \tag{5.13}$$

To minimize $C(\beta)$ it is requested that

$$\frac{\partial C(\beta)}{\partial \beta} = 2\beta^{\mathrm{T}} X^{\mathrm{T}} X - 2\mathbf{1}^{\mathrm{T}} X = 0, \tag{5.14}$$

from which we get

$$\beta = \left(X^{\mathrm{T}} X\right)^{-1} X^{\mathrm{T}} \mathbf{1}. \tag{5.15}$$

The next step is to extract geometric parameters of the best-fitting ellipse from the algebraic equation (5.10). We first check the existence of a tilt, which is present only if the coefficient B in (5.10) is non-zero. If that was the case, we first need to eliminate the tilt of the ellipse. Denoting the tilt angle of the ellipse by θ, the following coordinate rotation transformation is employed

$$\begin{cases} x = \cos\theta x' - \sin\theta y' \\ y = \sin\theta x' + \cos\theta y' \end{cases}. \tag{5.16}$$

Substitute the above expressions into Eq. (5.10), we get

$$\begin{aligned} &\left(a_1 c^2 + a_2 cs + a_3 s^2\right) x'^2 + \left(-2a_1 cs + a_2\left(c^2 - s^2\right) + 2a_3 cs\right) x'y' + \\ &\left(a_1 s^2 - a_2 cs + a_3 c^2\right) y'^2 + \left(a_4 c + a_5 s\right) x' + \left(-a_4 s + a_5 c\right) y' + 1 = 0, \end{aligned} \tag{5.17}$$

where $c = \cos\theta$ and $s = \sin\theta$. Let the term before $x'y'$ to be zero, the following equation for θ is achieved

$$-2a_1 \cos\theta \sin\theta + a_2 \left(\cos\theta^2 - \sin\theta^2\right) + 2a_3 \cos\theta \sin\theta = 0, \tag{5.18}$$

from which we know $\theta = \frac{1}{2}\arctan\left(\frac{a_2}{a_1 - a_3}\right)$. Now the constants c and s are known, Eq. (5.17) is reduced to

$$a'_1 x'^2 + a'_3 y'^2 + a'_4 x' + a'_5 y' = 1, \tag{5.19}$$

where a'_1, a'_3, a'_4 and a'_5 are all known constants. The only remaining step for the ellipse fitting is to transform Eq. (5.19) into the following canonical form

$$\frac{(x' - x'_0)^2}{b^2} + \frac{(y' - y'_0)^2}{a^2} = 1, \tag{5.20}$$

in which (x'_0, y'_0) is the center of the ellipse in the rotated coordinate system, and a and b are the lengths of the semi-axes. Applying a square completion method to Eq. (5.17), we get

$$\frac{\left(x' + a'_4/\left(2a'_1\right)\right)^2}{\left(a'_6/a'_1\right)} + \frac{\left(x' + a'_5/\left(2a'_3\right)\right)^2}{\left(a'_6/a'_1\right)} = 1, \tag{5.21}$$

where $a'_6 = 1 + (a'^2_4)/(4a'_1) + (a'^2_5)/(4a'_3)$. Compare Eqs. (5.20) and (5.21), it easy to notice

$$x'_0 = \frac{-a'_4}{2a'_1}, y'_0 = \frac{-a'_5}{2a'_3}, a = \sqrt{\frac{a'_6}{a'_1}}, b = \sqrt{\frac{a'_6}{a'_3}}. \tag{5.22}$$

Substitute the above expressions of x'_0 and y'_0 into Eq. (5.16), we get the coordinate of the ellipse center in the original coordinate system

$$\begin{cases} x_0 = -\cos\theta \frac{a'_4}{2a'_1} + \sin\theta \frac{a'_5}{2a'_3} \\ y_0 = -\sin\theta \frac{a'_4}{2a'_1} - \cos\theta \frac{a'_5}{2a'_3} \end{cases}. \tag{5.23}$$

The mercury jet was considered at $z = 30$ cm and $z = 45$ cm, which are the locations of view port 1 and view port 2, respectively. 40 points were digitized in mercury jet simulations

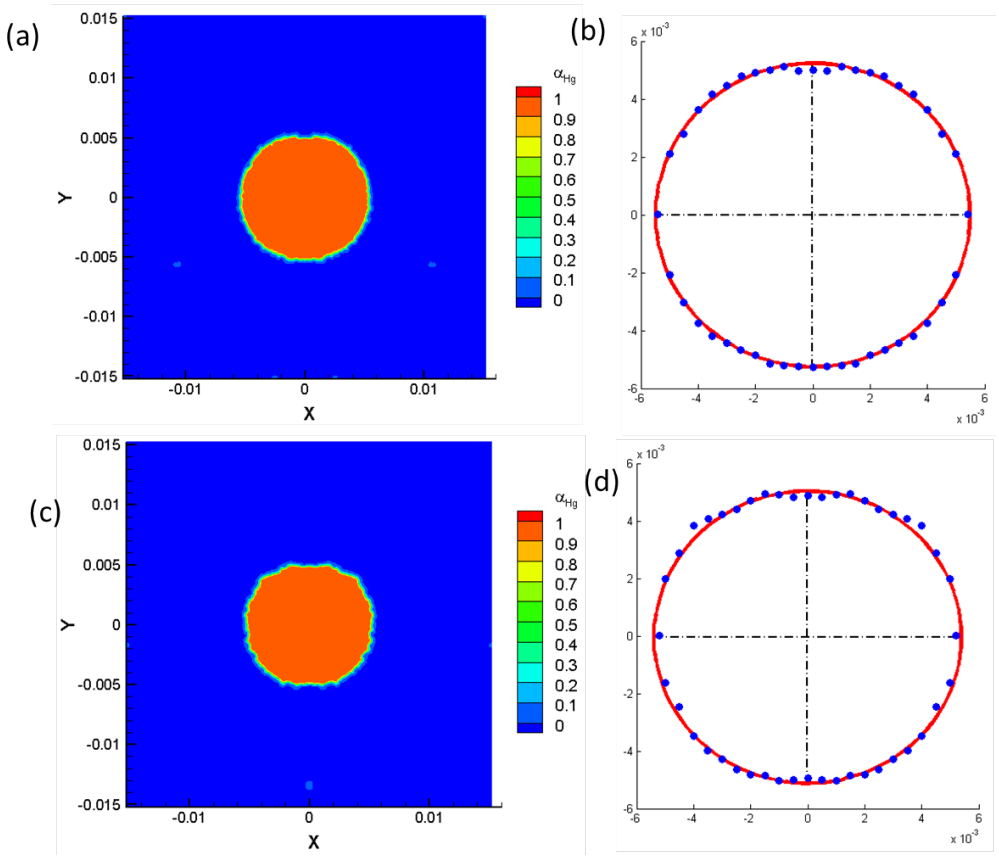

Figure 5.70: Least square fitting of ellipses for 3D mercury jet simulations using as input the output from a straight pipe without a weld: (a) contour of volume fraction of mercury at $z = 30$ cm, (b) ellipse fitting at $z = 30$ cm, (c) contour of volume fraction of mercury at $z = 45$ cm, (b) ellipse fitting at $z = 45$ cm.

at these z values, shown in Figs. (5.59),(5.62), and (5.66). The results of fitting ellipse to these digitzed points are shown in Figs. (5.70), (5.71), and (5.72).

In the results of ellipse fitting, no big significant differences are found among different cases. To quantify this, uncertainties in the fitting should be estimated. Here we apply an error analysis formulated by Prof. McDonald [133]. It gives a prescription for fitting a set of m points, $\{x_j, y_j\}$, (perhaps from digitization of an image) to an ellipse, with the general form (with 5 parameters a_i),

$$a_1 x^2 + a_2 xy + a_3 y^2 + a_4 x + a_5 y - 1 = 0. \tag{5.24}$$

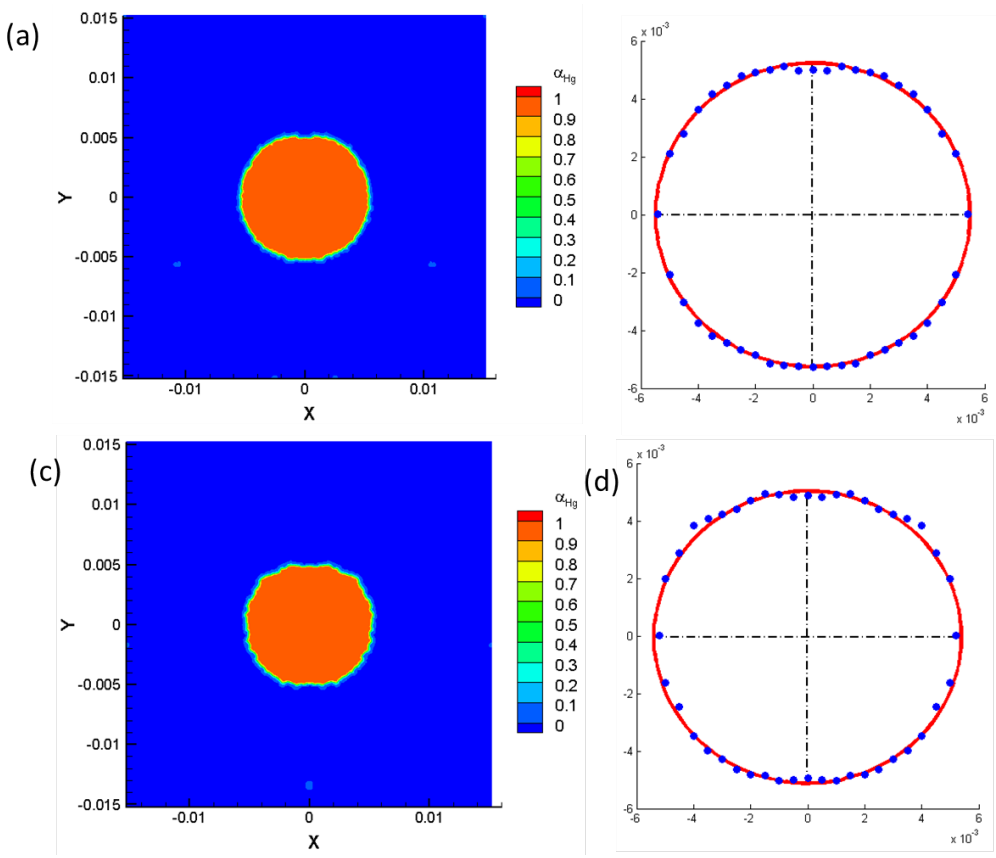

Figure 5.71: Least square fitting of ellipses for 3D mercury jet simulations using as input the output from a 90°/90° pipe without a weld: (a) contour of volume fraction of mercury at $z = 30$ cm, (b) ellipse fitting at $z = 30$ cm, (c) contour of volume fraction of mercury at $z = 45$ cm, (b) ellipse fitting at $z = 45$ cm

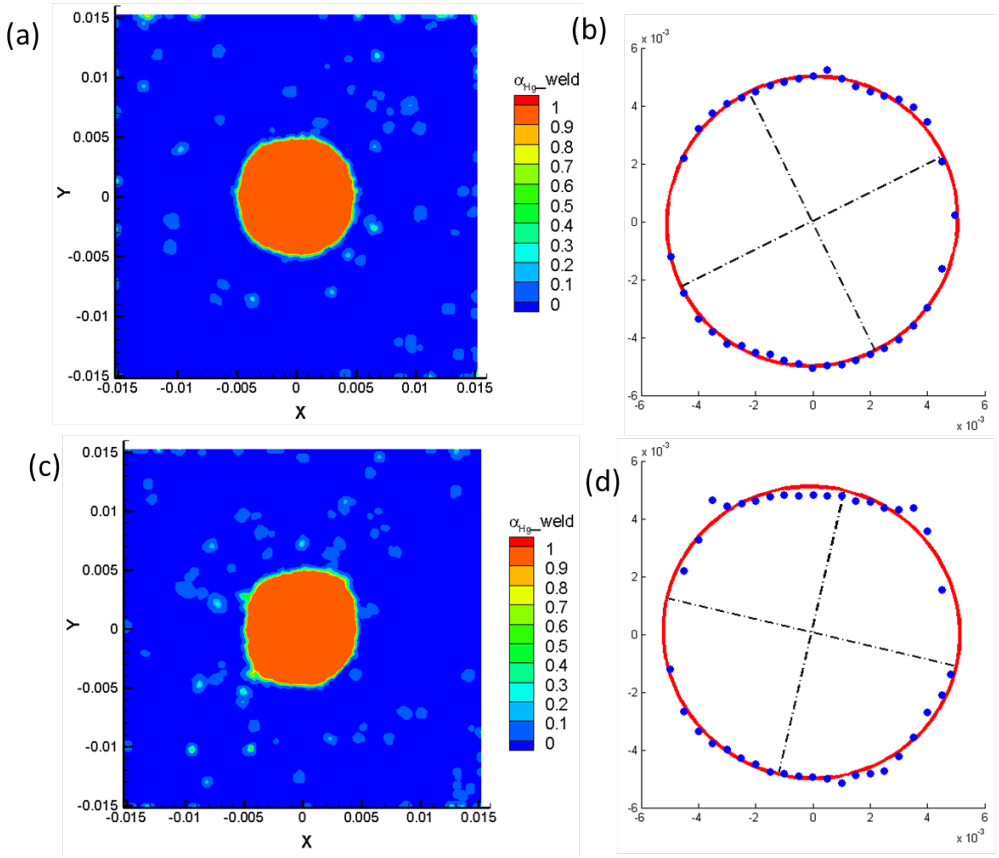

Figure 5.72: Least square fitting of ellipses for 3D mercury jet simulations using as input the output from a 90°/90° pipe with a 30° weld: (a) contour of volume fraction of mercury at $z = 30$ cm, (b) ellipse fitting at $z = 30$ cm, (c) contour of volume fraction of mercury at $z = 45$ cm, (b) ellipse fitting at $z = 45$ cm

In addition, we give an estimate of the errors on the best-fit values of the parameters a_i.

(1) Errors on the Parameters of the Quadratic Form (Eq. 5.24). We first define the auxiliary data set $\{z_{ij}\}$, $(i = 1, 5, j = 1, m)$,

$$z_{i,j} = (x_j^2, x_j y_j, y_j^2, x_j, y_j). \tag{5.25}$$

Among many possible measures of the goodness of fit,[1] we adopt the simplest, writing

$$\chi^2 = \sum_{j=1}^{m} \frac{(\sum_{i=1}^{5} a_i z_{ij} - 1)^2}{\sigma_j^2}\,, \tag{5.26}$$

where σ_j is the measurement uncertainty associated with the data point (x_j, y_j). The best-fit parameters $\hat{a}_i$ are those that minimize the function χ^2 for a set of measurements $\{z_{ij}\}$.

We consider the case that the σ_j are not known, but assumed to have the common value σ. Then, by supposing that the function χ^2 is actually a chi-square [137, 138, 139, 140, 141, 142] with $m - 5$ degrees of freedom, the best-fit (minimum) χ^2 has most probable value $m - 5$. Assuming that the best-fit χ^2 has this value, the unknown σ is determined, and error estimates for the best-fit parameters $_i$ follow via standard procedures.[2]

A great insight is that $\exp(-\chi^2/2)$ can be thought of another way. It is also the (unnormalized) probability distribution that the polynomial coefficients have values a_i when their best-fit values are $\hat{a}_i$ with uncertainties due to the measurements $\{x_j, y_j\}$. Expressing this in symbols,

$$\exp(-\chi^2/2) = \text{const} \times \exp\left(-\sum_{k=1}^{5}\sum_{l=1}^{5} \frac{(a_k - \hat{a}_k)(a_l - \hat{a}_l)}{2\sigma_{kl}^2}\right), \tag{5.27}$$

or equivalently

$$\chi^2/2 = \text{const} + \sum_{k=1}^{5}\sum_{l=1}^{5} \frac{(a_k - \hat{a}_k)(a_l - \hat{a}_l)}{2\sigma_{kl}^2}. \tag{5.28}$$

[1] For a survey of 13 measures, see [134],[135].

[2] For a discussion of this approach for polynomial fitting, see the lab manual of Prof. McDonald [143].

The uncertainty on $\hat{a}_k$ is σ_{kk} in this notation. In Eqs. (5.27) and (5.28) we have introduced the important concept that the uncertainties in the coefficients $\hat{a}_k$ are correlated. That is, the quantity σ_{kl}^2 is a measure of the probability that the values of $\hat{a}_k$ and $\hat{a}_l$ both have positive fluctuations at the same time. In fact, σ_{kl}^2 can be negative indicating that when $\hat{a}_k$ has a positive fluctuation then $\hat{a}_l$ has a correlated negative one.

One way to see the merit of minimizing the χ^2 is as follows. According to Eq. (5.28) the derivative of χ^2 with respect to a_k is

$$\frac{\partial \chi^2}{\partial a_k} = \sum_{l=1}^{5} \frac{a_l - \hat{a}_l}{\sigma_{kl}^2}, \tag{5.29}$$

so that all first derivatives of χ^2 vanish when all $a_l = \hat{a}_l$. That is, χ^2 is a minimum when the coefficients a_i take on their best-fit values $\hat{a}_i$. A further benefit is obtained from the second derivatives:

$$\frac{\partial^2 \chi^2}{\partial a_k \partial a_l} = \frac{1}{\sigma_{kl}^2}. \tag{5.30}$$

For our particular χ^2 (5.26), with $\sigma_j = \sigma$, the first derivatives are

$$\frac{\partial \chi^2}{\partial a_k} = \sum_{j=1}^{m} \frac{z_{kj}(\sum_{i=1}^{5} a_i z_{ij} - 1)}{\sigma^2} = \frac{1}{\sigma^2} \sum_{i=1}^{5} \sum_{j=1}^{m} a_i z_{ij} z_{kj} - \frac{1}{\sigma^2} \sum_{j=1}^{m} z_{kj}, \tag{5.31}$$

and the second derivatives are

$$\frac{\partial^2 \chi^2/2}{\partial a_k \partial a_l} = \frac{1}{\sigma^2} \sum_{j=1}^{m} z_{kj} z_{lj} \equiv \frac{M_{kl}}{\sigma^2}. \tag{5.32}$$

Using the matrix M_{kl} introduced in Eq. (5.32), the condition that the first derivatives (5.31) vanish at the best-fit coefficients $\hat{a}_k$ can be written as

$$\sum_{i=5}^{5} M_{ik} \hat{a}_i = \sum_{j=1}^{m} z_{kj} \equiv V_k. \tag{5.33}$$

We then calculate the inverse matrix M^{-1} and apply it to find the best-fit coefficients $\hat{a}_k$

(which do not depend on the as-yet-unknown value of σ),

$$_k = \sum_{l=1}^{5} M_{kl}^{-1} V_l. \tag{5.34}$$

Comparing eqs. (5.30) and (5.32) we have

$$\frac{1}{\sigma_{kl}^2} = \frac{M_{kl}}{\sigma^2}\,. \tag{5.35}$$

The uncertainty in best-fit coefficient $\hat{a}_i$ is then reported as

$$\sigma_{_i} = \sigma_{ii} = \frac{\sigma}{\sqrt{M_{ii}}}. \tag{5.36}$$

All that remains is to find the value of the unknown uncertainty $\sigma = \sigma_j$ on the measurements. For this, we set the χ^2 for the best-fit parameters $_i$ equal to the number of degrees of freedom, $m - 5$,

$$\chi^2(\hat{a}_i) = m - 5 = \sum_{j=1}^{m} \frac{(\sum_{i=1}^{5} \hat{a}_i z_{ij} - 1)^2}{\sigma^2}\,, \tag{5.37}$$

such that σ is determined to be

$$\sigma = \sqrt{\frac{\sum_{j=1}^{m}(\sum_{i=1}^{5} \hat{a}_i z_{ij} - 1)^2}{m-5}}\,, \qquad \text{and} \qquad \sigma_{_i} = \sigma_{ii} = \sqrt{\frac{\sum_{j=1}^{m}(\sum_{k=1}^{5} \hat{a}_k z_{kj} - 1)^2}{(m-5)\sum_{j=1}^{m} z_{ij}^2}}\,. \tag{5.38}$$

(2) Errors on the Conventional Ellipse Parameters An alternative description of the ellipse of Eq. (5.24) is that it has semimajor axis of length a which makes angle θ to the x-axis, semiminor axis of length b, and center at (x_0, y_0). The shape parameters a, b and θ depend only on a_1, a_2 and a_3, while the center of the ellipse depends on all five of the a_i. We now deduce the alternative parameters, and their fit errors, in terms of the a_i and the errors on the latter as found in sec. 1.

We first translate the coordinates according to $x' = x - x_0$ and $y' = y - y_0$ such that the

resulting parameters a'_i of the quadratic form have

$$a'_1 = a_1, \quad a'_2 = a_2, \quad a'_3 = a_3, \quad a'_4 = 2a_1x_0 + a_2y_0 + a_4, \quad a'_5 = a_2x_0 + 2a_3y_0 + a_5. \quad (5.39)$$

For the ellipse to be centered at $x' = 0 = y'$ we need $a'_4 = 0 = a'_5$, which leads to

$$x_0 = \frac{a_2a_5 - 2a_3a_4}{4a_1a_3 - a_2^2}\,, \qquad y_0 = \frac{a_2a_4 - 2a_1a_5}{4a_1a_3 - a_2^2}\,. \quad (5.40)$$

As a check, we note that if $a_4 = 0 = a_5$ then the original ellipse was centered on the origin, and indeed eq. (5.40) implies that $x_0 = 0 = y_0$.

To deduce the error on, say, x_0 we first consider the differential,

$$dx_0 = \frac{a_5da_2 + a_2da_5 - 2a_4da_3 - 2a_3da_4 - x_0(4a_3da_1 + 4a_ada_3 - 2a_2da_2)}{4a_1a_3 - a_2^2}\,. \quad (5.41)$$

Then, on squaring this we can identify $(dx_0)^2$ with the squared error $\sigma^2_{x_0}$ when we identify the products $da_i\,da_j$ with the σ^2_{ij} found in Eq. (5.35).

The determine the shape parameters a, b and θ we perform a coordinate rotation by angle θ with respect to the x'-axis[3] (which is parallel to the x-axis),

$$x'' = x'\cos\theta + y'\sin\theta, \qquad x' = x''\cos\theta - y''\sin\theta, \quad (5.42)$$

$$y'' = -x'\sin\theta + y'\cos\theta, \qquad y' = x''\sin\theta + y''\cos\theta, \quad (5.43)$$

and require that $a''_2 = 0$, in which case $a''_1 = 1/a^2$ and $a''_3 = 1/b^2$. This leads to

$$\tan 2\theta = \frac{a_2}{a_1 - a_3}\,, \quad \cos 2\theta = \frac{a_1 - a_3}{\sqrt{a_2^2 + (a_1 - a_3)^2}}\,, \quad \sin 2\theta = \frac{a_2}{\sqrt{a_2^2 + (a_1 - a_3)^2}}\,, \quad (5.44)$$

$$\sigma_\theta = \frac{\cos^2 2\theta}{2a_1 - a_3}\sqrt{\tan^2 2\theta(\sigma^2_{11} + \sigma^2_{33} - 2\sigma^2_{13}) + \sigma^2_{22} - 2\tan 2\theta(\sigma^2_{12} - \sigma^2_{23})}, \quad (5.45)$$

[3]We could also make the rotation directly from the (x, y) coordinates, with no affect on the shape parameters, as these don't depend on a_4 and a_5. However, if parameters x_0 and y_0 are deduced only after this rotation, they appear to depend on θ, which complicates the expressions for their errors.

and

$$\frac{1}{a^2} = a_1\cos^2\theta + a_2\sin\theta\cos\theta + a_3\sin^2\theta = \frac{a_1+a_3+(a_1-a_3)\cos 2\theta + a_2\sin 2\theta}{2}$$
$$= \frac{a_1+a_3+\sqrt{a_2^2+(a_1-a_3)^2}}{2}\,, \tag{5.46}$$
$$\frac{1}{b^2} = a_1\sin^2\theta - a_2\sin\theta\cos\theta + a_3\cos^2\theta = \frac{a_1+a_3-(a_1-a_3)\cos 2\theta - a_2\sin 2\theta}{2}$$
$$= \frac{a_1+a_3-\sqrt{a_2^2+(a_1-a_3)^2}}{2}\,. \tag{5.47}$$

Note that $1/b^2 \le 1/a^2$, which means that b is the semimajor axis, and a is the semiminor axis. Note also that $\tan 2\theta = \tan 2(\theta - \pi/2)$, so there is an ambiguity in Eq. (5.44) as to whether θ is the angle to the semimajor or the semiminor axis.

As a measure of the departure of the ellipse from a circle we introduce the ellipticity (flattening) ϱ,[4]

$$\varrho \equiv \frac{b}{a} \ge 1\,, \qquad \varrho^2 = \frac{a_1+a_3+\sqrt{a_2^2+(a_1-a_3)^2}}{a_1+a_3-\sqrt{a_2^2+(a_1-a_3)^2}} \equiv \frac{C_+}{C_-}\,. \tag{5.48}$$

Taking the differential, we have

$$2\varrho\, d\vartheta = \frac{dC_+ - \varrho^2\, dC_-}{C_-} \equiv \frac{C_1\, da_1 + C_2\, da_2 + C_3\, da_3}{C_-}\,, \tag{5.49}$$

where

$$C_\pm = a_1+a_3 \pm \sqrt{a_2^2+(a_1-a_3)^2} = a_1+a_3 \pm S, \qquad S \equiv \sqrt{a_2^2+(a_1-a_3)^2}, \tag{5.50}$$
$$C_1 = 1-\varrho^2+\frac{a_1-a_3}{S}(1+\varrho^2) = -\frac{2[a_2^2-2a_3(a_1-a_3)]}{SC_-} \equiv -2\frac{D_1}{SC_-}\,, \tag{5.51}$$
$$C_2 = \frac{a_2}{S}(1+\varrho^2) = \frac{2a_2(a_1+a_3)}{SC_-} \equiv 2\frac{D_2}{SC_-}\,, \tag{5.52}$$
$$C_3 = 1-\varrho^2-\frac{a_1-a_3}{S}(1+\varrho^2) = -\frac{2[a_2^2+2a_1(a_1-a_3)]}{SC_-} \equiv -2\frac{D_3}{SC_-}\,. \tag{5.53}$$

[4]If we define $\varrho' = (b-a)/a = \varrho - 1$, so that $\varrho' = 0$ for a circle, then $\sigma_{\varrho'} = \sigma_\varrho$.

Then, the error σ_ϱ on the ellipticity ϱ is given by

$$\sigma_\varrho = \frac{1}{\varrho S C_-^2} \sqrt{D_1^2\sigma_{11}^2 + D_2^2\sigma_{22}^2 + D_3^2\sigma_{33}^2 - 2D_1D_2\sigma_{12}^2 - 2D_2D_3\sigma_{23}^2 + 2D_1D_3\sigma_{13}^2}\,. \qquad (5.54)$$

Of course, the "error" computed this way assumes that the fit is "good", which might not be the case. A separate judgment should be made as to whether the fit is indeed "good" before taking seriously the error estimates presented here.

The calculations of theta and ellipticity, and their errors, for the six cases are shown in Table 5.1. The ellipticity is not significantly different in any of these cases. However, in some cases the estimated errors are extremely large, which may be a hint that the error-estimation procedure is itself not very accurate.

Table 5.1: Ellipticity and fitting errors

	θ	ϱ	σ_θ	σ_ϱ
Case 1 ($z = 30$cm)	0.00	1.04	6.52×10^{-2}	5.96×10^{-3}
Case 1 ($z = 45$cm)	0.00	1.03	1.52×10^{0}	8.18×10^{-2}
Case 2 ($z = 30$cm)	0.00	1.04	4.24×10^{2}	3.97×10^{1}
Case 2 ($z = 45$cm)	0.00	1.06	1.91×10^{3}	2.46×10^{2}
Case 3 ($z = 30$cm)	0.46	1.03	4.09×10^{-1}	1.80×10^{-2}
Case 3 ($z = 45$cm)	-0.23	1.03	3.85×10^{0}	2.31×10^{-1}

Chapter 6

Concluding Remarks

The intensity of turbulence in mercury target flow has a significant influence on the particle produced. This work studies the flow in several pipe geometries, with and without weld, with the purpose of identifying the configuration that gives the least turbulence.

A theoretical analysis of the simpler laminar flows in the curved pipes has been undertaken for some basic knowledge of the system, followed by numerical modeling of the turbulent counterpart of the flow. A realizable $k-\varepsilon$ model has been chosen for this purpose, and used as implemented in the FLUENT commercial CFD code. The results show that the straight pipe (zero half-bend angle) with a nozzle gives the flow with the least turbulence intensity. A weld causes the fluid to flow backwards and increases the turbulence intensity of the flow. On the other hand, the presence of a nozzle causes a reduction in the turbulence intensity.

Due to time constraint, the built-in CLSVOF method in FLUENT has been used to simulate the two-phase jet flows in this project, as opposed to the procedure that we developed, even though the latter had also been validated. Rich jet breakups are observed in the two dimensional mercury jet simulation using the MILES method. For 3D mercury jet simulation, it requires a big number of grid points using MILES. In this case, the RKE turbulent model is applied instead. Although unsteady structures on the jet interface is smoothed in the results of the RKE model, it is still useful in analyzing the deformation of the jet. Jet

experiences larger deformations from a pipe with a weld compared to that without a weld.

Least square ellipse fitting is used to quantitatively analyze the jet deformation. The magnitude of ellipticity is very close to each jet simulation, which uses three outputs of pipe simulations as jet inputs. From ellipticity fitting error, we can clearly see that the jet simulation based on the outputs of a 90°/90° pipe with a 30° weld has the largest error. It indicates the biggest influences on jet flow from a bend pipe with a weld.

The developed CLSVOF method has just been worked through. Successful preliminary tests proves its ability in capturing sharp filaments. However, it needs to be tested more rigorously. e.g. for the Rayleigh-Taylor instability problem. The CLSVOF that we developed, unlike the one in FLUENT, is based on a curvilinear coordinate system, which means that it can be used for complex geometries. This capability needs to be further tested for accuracy. A parallel implementation of the developed CLSVOF method should be carried out, since only the serial implementation has been done in the thesis work.

For the three-dimensional mercury jet simulation, one more case is suggested in which the inlet conditions use the the outputs from the 90°/90° pipe with a 30° weld on the bend plane (note: case 3 uses the outputs from the 90°/90° pipe with a 30° weld off the bend plane). Further, the error of the fitting analysis needs to be improved.

Bibliography

[1] V. Graves, A. Carroll, P. Spampinato, H. Kirk, A. Fabich, I. Efthymiopoulos, J. Lettry, K.McDonald, 2009, "Operation of a free Hg jet delivery system in a high-power target experiment," Proc. PAC09, Vancouver, BC, Canada.

[2] H. J. Park, 2009, "Experimental Investigation of Magnetohydrodynamics Flow for A Intense Proton Target", Stony Brook University Ph.D thesis.

[3] J. Eustice, 1910, "Flow of water in curved pipes," Proc. Roy. Soc. Lond. Ser. A, 84, pp. 107-118.

[4] J. Eustice, J. 1911 "Experiments of streamline motion in curved pipes," Proc. Roy. Soc. Lond. A, 85, pp. 119-131.

[5] W.R. Dean, 1927, "Note on the motion of fluid in a curved pipe," Phil. Mag. 4, p. 208.

[6] W.R. Dean, 1928, "Note on the motion of fluid in .a sinuous channel," Phil. Mag., 5, p. 673.

[7] M. Adler, 1934, "Stromung in gekrummten," Rohren Z. angew. Math. Mech.,14, p. 125.

[8] M. Rowe, 1970, "Measurements and computations of flow in pipe bends," J. Fluid Mech., 43, p. 771.

[9] M.M. Enayat, M.M. Gibson, A.M.K.P. Taylor and M. Yianneskis, 1982, "Laser-Doppler measurements of laminar and turbulent flow in pipe bend," Int. J. Heat and Fluid Flow, 3, p. 213.

[10] J. Azzola, JAC, Humphrey, H. Iacovides, and B.E. Launder, 1986, "Developing turbulent flow in a U-bend of circular cross-section: measurement and computation," J. Fluids. Eng.,108, pp. 214-221.

[11] M. Anwer, R.M.C. So, and Y.G. Lai, 1986, "Perturbation by and recovery from bend curvature of a fully developed turbulent pipe flow," Phys. Fluids A, 1, p. 1387.

[12] K. Sudo, M. Sumida, and H. Hibara, 1998, "Experimental investigation on turbulent flow in a circular-sectioned 90-degrees bend," Exp. in Fluids, 25, p. 51.

[13] K. Sudo, M. Sumida, and H. Hibara, 2000, "Experimental investigation on turbulent flow in a circular-sectioned 180-degrees bend," Exp. in Fluids, 28, p. 42.

[14] T.J. Hüttl and R. Friedrich, 2000, "Influence of curvature and torsion on turbulent flow in helically coiled pipes," Int. J. Heat and Fluid Flow 21, p. 345.

[15] P. Rudolf and M. Desova, 2007, "Flow characteristics of curved ducts," Appl. Comp. Mech., 1, p. 255.

[16] Nuri Yucel and Nureddin Dinler, Numerical study of laminar and turbulent flow through a pipe with fins attached. Numerical Heat Transfer, Part A, 49: 195–214, 2006.

[17] S. Garimella and R. N. istensen, Heat Transfer and Pressure Drop Characteristics of Spirally Fluted Annuli: Part I—Hydrodynamics, J. Heat Transfer, vol. 117, pp. 54–60, 1995.

[18] S. Garimella and R. N. Christensen, Heat Transfer and Pressure Drop Characteristics of Spirally Fluted Annuli: Part II—Heat Transfer, J. Heat Transfer, vol. 117, pp. 61–68, 1995.

[19] G. Russ and H. r, Heat Transfer and Fluid Flow in a Pipe with Sinusoidal Wavy Surface—I. Numerical Investigation, Int. J. Heat Mass Transfer, vol. 40, pp. 1061–1070, 1997.

[20] Paul MC, la MM, Roditi G. Large-eddy simulation of pulsatile blood flow. Med Eng Phys 2009;31:153–9.

[21] Molla MM, l MC, Roditi G. LES of additive and non-additive pulsatile flows in a model arterial stenosis. Comput Methods Biomech Biomed Eng 2010;13(1):105–20.

[22] M.M. Molla, M.C. Paul, LES of non-Newtonian physiological blood flow in a model of arterial stenosis.Medical Engineering & Physics 34 (2012) 1079–1087.

[23] E.H. Jones Jr. and R.A. ura, A numerical analysis of pulsating laminar flow through a pipe orifice, J. Fluids Eng., 113, 199 – 205 (1991).

[24] T.S. Lee and Z.D. Shi. Numerical study of effects of pulsatile amplitude for transitional turbulent pulsatile flow in pipes with ring-type constrictions. Int. J. Numer. Meth. Fluids 30: 813 – 830 (1999).

[25] Perry, A. E., Schofield, W. H., and Joubert, P. N., 1969, Rough Wall Turbulent Boundary Layers, J. Fluid Mech., 37, pp. 383–413.

[26] Djenidi, L., Anselmet, F., and Antonia, R. A., 1994, LDA Measurements in a Turbulent Boundary Layer Over a d-Type Rough Wall, Exp. Fluids, 16, pp. 323–329.

[27] Djenidi, L., Elavarasan, R., and Antonia, R. A., 1999, The Turbulent Bound- ary Layer Over Transverse Square Cavities, J. Fluid Mech., 395(4), 271-294.

[28] Eiamsa-ard, S., and Promvonge, P., 2008, Numerical Study on Heat Transfer of Turbulent Channel Flow Over Periodic Grooves, Int. Commun. Heat Mass Transfer, 35, pp. 844–852.

[29] Henrique Stel, Rigoberto E. M. Morales, Admilson T. Franco, Silvio L. M. Junqueira, Raul H. Erthal and Marcelo A. L. GonÃ§alves. Numerical and Experimental Analysis of Turbulent Flow in Corrugated Pipes. J. Fluids Eng. 132(7), 071203 (Jul 22, 2010).

[30] J.S. Lee and Y.F. Fung, 'Flow in non-uniform small blood vessels', J. Micro6asc. Res., 3, 272 – 287 (1971).

[31] J.C. Bentz and N.A. Evans, 'Hemodynamic flow in the region of a simulated stenosis', American Society of Mechanical Engineers, Winter Annual Meeting, Houston, November 30 – December 4, ASME Paper No. 75 -WA/BA10 -10, 1975.

[32] Nash DH, Abid M. Surface sensitivity study of non-gasketed flange joint. J Process Mech Eng; Part-E 2004;E4:218.

[33] M. Abida, M. Siddique. Numerical simulation to study the effect of tack welds and root gap on welding deformations and residual stresses of a pipe-flange joint. International Journal of Pressure Vessels and Piping 82 (2005) 860–871.

[34] Chang, K., Constantinescu, G., and Park, S. O., 2006, Analysis of the Flow and Mass Transfer Processes for the Incompressible Flow Past an Open Cavity With a Laminar and a Fully Turbulent Incoming Boundary Layer, J. Fluid Mech., 561(4), 113-145.

[35] Sutardi, and Ching, C. Y., 2003, The Response of a Turbulent Boundary Layer to Different Shaped Transverse Grooves, Exp. Fluids, 35, pp. 325–337.

[36] D.D. Luo, C.W. Leung, T.L. Chan, W.O. Wong. Flow and forced-convection characteristics of turbulent flow through parallel plates with periodic transverse ribs, Numerical Heat Transfer, Part A: Applications, 48 (1) (2005), pp. 43–58.

[37] K.S. Yang, Large eddy simulation of turbulent flows in periodically grooved channel, Journal of Wind Engineering and Industrial Aerodynamics, 84 (2000), pp. 47–64.

[38] S. Vijiapurapu, J. Cui, Simulation of turbulent flow in a ribbed pipe using large eddy simulation, Numerical Heat Transfer, Part A: Applications, 51 (12) (2007), pp. 1137–1165.

[39] Promvonge, P., and Thianpong, C., 2008, Thermal Performance Assessment of Turbulent Channel Flows Over Different Shaped Ribs, Int. Commun. Heat Mass Transfer, 35, pp. 1327–1334.

[40] Dong, Y., Huixiong, L., and Tingkuan, C., 2001, "Pressure Drop, Heat Transfer and Performance of Single-Phase Turbulent Flow in Spirally Corrugated Tubes," Exp. Therm. Fluid Sci., 24, pp. 131–138.

[41] Ku, David N., 1997, Blood Flow in Arteries, Annu. Rev. Fluid Mech., 29, pp. 399– 434.

[42] Bluestein, D., Gutierrez, C., Londono, M., and Schoephoerster, R. T., 1999, ‘‘Vortex Shedding in Steady Flow Through a Model of an Arterial Stenosis and Its Relevance to Mural Platelet Deposition,’’ Ann. Biomed. Eng., 27, pp. 763– 773.

[43] Stroud, J. S., Berger, S. A., and Saloner, D., 2000, ‘‘Influence of Stenosis Morphology on Flow Through Severely Stenotic Vessels: Implications for Plaque Rupture,’’ J. Biomech., 33, pp. 443– 455.

[44] Fung, Y. C., 1993, Biomechanics: Mechanical Properties of Living Tissues, Springer-Verlag, New York.

[45] Ojha, M., Cobbold, C., Johnston, K. W., and Hummel, R. L., 1989, ‘‘Pulsatile Flow Through Constricted Tubes: An Experimental Investigation Using Photo- chromic Tracer Methods,’’ J. Fluid Mech., 203, pp. 173–197.

[46] Mallingen, F., and Drikakis, D., 2002, Instability in Three-Dimensional Un- steady Stenotic Flows, Intl. J. Heat Fluid Flow, 23, pp. 657– 663.

[47] Mittal, R., Simmons, S. P., and Udaykumar, H. S., 2001, Application of Large Eddy Simulation to the Study of Pulsatile Flow in a Modeled Arterial Stenosis, J. Biomech. Eng., 123, pp. 325–332.

[48] Frankel, S. H., Sherwin, S. J., and Varghese, S. S., 2002, Numerical Simula- tion of Pulsatile Flow Through Stenotic Vessels of Different Local Morpholo- gies, in Proceedings of the Second Joint EMBS-BMES Meeting, Houston, TX, October 23rd–26th.

[49] B. A. Nichita, 2010, "An improved CFD tool to simulate adiabatic and diabatic two-phase flows," Ph.D. thesis.

[50] F. Harlow, and J. Welch, 1965, "Numerical calculation of time-dependent viscous incompressible flow of fluid with free surface," J. Phys. Fluids, 8, pp. 2182-2189.

[51] J. Donea, 1983, "Arbitrary Lagrangian-Eulerian finite element methods," Computational Methods for Transient Analysis, 1, pp. 473-516.

[52] W. Rider and D. Kothe, 1998, "Reconstructing Volume Tracking," Journal of Computational Physics, 141(2), pp. 112-152.

[53] C. Hirt, A. Amsden, and J. Cook, 1997, "An arbitrary Lagrangian-Eulerian computing method for all flow speeds," J. Comput. Phys., 135, pp. 203-216.

[54] T. Hughes, W. Liu, and T. Zimmermann, 1981, "Lagrangian Eulerican finite element formulation for incompressible viscous flow," Comput. Methods Appl. Mesh. Eng., 29, pp. 329-349.

[55] G. Tryggvason, B. Bunner, A. Esmaeeli, D. Juric,, N. Al-Rawahi, W. Tauber, J. Han, S. Nas, and Y.-J. Jan, 2001, "A front tracking method for the computations of multiphase flow," J. Comput. Phys., 169, pp. 708-759.

[56] S.O. Unverdi, and G. Tryggvanson, 1992, "A front tracking method for viscous, incompressible, multi-fluid flows," J. Comput. Phys., 100, pp. 25-37.

[57] Mark Sussman, Peter Smereka, and Stanley Osher, 1994, "A level set approach for computing solutions to incompressible two-phase flow," J. Comput. Phys., 114, pp. 146-159.

[58] Mark Sussman, Emad Fatemi, Peter Smereka, and Stanley Osher, 1998, "An improved level set method for incompressible two-phase flows," Computers & Fluids, 27, pp. 663-680.

[59] Mark Sussman, Ann S. Almgren, John B. Bell, Philip Colella, Louis H. Howell, and Michael L. Welcome, 1994, "A adaptive level set approach for incompressible phase flows," J. Comput. Phys., 148, pp. 81-124.

[60] Mark Sussman and Emad Fatemi, 1999, "An effective interface-preserving level set redistancing algorithm and its application to interfacial incompressible fluid flow," Journal on Scientific Computing, 20, pp. 1165-1191.

[61] C.W. Hirt and B.D. Nichols, 1981, "Volume of fluid (VOF) method for the dynmanics of free boundaries," J. Comput. Phys., 39, pp. 201-225.

[62] D.L. Youngs et al., 1982, "Time dependent multimaterial flow with large fluid distortion," Numerical Methods for Fluid Dynamics, Academic Press, New York, pp. 273-285.

[63] Jie Li, 1995, "Piecewise linear interface calculation," Comptes Rendus de l' Academie des Sciences Series II. Fascicule B - Mecanique, 320, pp. 391-396.

[64] M Sussman, EG Puckett, A coupled level set and volume-of-fluid method for computing 3D and axisymmetric incompressible two-phase flows, Journal of Computational Physics 162 (2), 301-337 (2000).

[65] T. Menard, S. Tanguy, A. Berlemont, Coupling level set/VOF/ghost fluid methods: Validation and application to 3D simulation of the primary break-up of a liquid jet, International Journal of Multiphase Flow 33, 510-524 (2007).

[66] William H. Press, Saul A. Teukolsky, William T. Vetterling, Brian P. Flannery, Numerical Recipes: The Art of Scientific Computing, Cambridge University Press, 3rd edition, 2007.

[67] J. Brackbill, D. Kothe, and C. Zemach, 1992, "A continuum method for modeling surface tension," J. Comput. Phys., 100, pp. 335-354.

[68] ANSYS FLUENT 14.0 Theory Guide.

[69] M. Rhiec and W.L. Chow, 1983, "Numerical Study of the Turbulent Flow Past an Airfoil with Trailing Edge Separation," AIAA Journal, 21, pp. 1525-1532.

[70] J. Choriona, 1968, "Numerical solution of navier-stokes equations," Mathematics of Computation, 22, pp. 745-762.

[71] Ruben Scardoveli and Stephane Zaleski, 1999, "Direct numberical simulation of free surface and interfacial flow," Annual Review of Fluid Mechanics, 31, pp. 603-657.

[72] S.V. Shepel, B.L. Smith, and S. Paolucci, 2005, "Implementation of a level set interface tracking method in FIDAP and CFX-4 codes," J. Fluids Eng., 127, pp. 674-686.

[73] S.V. Shepel, and B.L. Smith, 2006, "New finite-element/finite-volume level set formulation for modeling two-phase incompressible flows," J. Comput. Phys., 218, pp. 479-492.

[74] G. Son and N. Hur, 2002, "A coupled level set and volume-of-fluid method for buoyancy-driven motion of fluid particles," Numer. Heat Transfer, Part B, 42, pp. 523-542.

[75] G. Son, 2003, "Efficient implementation of a coupled level-set and volume of fluid method for three dimensional incompressible two-phase flow," Numer. Heat Transder, Part B, 43, pp. 549-565.

[76] X. Yang, A.J. James, J. Lowengrub, X. Zheng, and V. Cristini, 2006, "An adaptive coupled level-set/volume-of-fluid interface capturing method for unstructured triangular grids," J. Comput. Phys., 217, pp. 364-394.

[77] M. Sussman, K. Smith, M. Hussaini, M. Ohta, and R. Zhi-Wei, 2007, "A sharp interface method for incompressible two-phase flows," J. Comput. Phys., 221, pp. 469-505.

[78] M. Sussman *et al.*, 2003, "A second order coupled level set and volume-of-fluid method for computing growth and collapse of vapor bubbles," J. Comput. Phys., 187, pp. 110-136.

[79] M. Sussman *et al.*, 2000, ″A coupled level set and volume-of-fluid method for computing 3D and axisymmetric incompressible two-phase flows," J. Comput. Phys., 162, pp. 301-337.

[80] A.Y. Tong and Z. Wang, 2007, "A numerical method for capillarity-dominant free surface flows," J. Comput. Phys., 221, pp. 506-523.

[81] N. Rajaratnam, S.A.H. Rizvi, P.M. Steffler, and P.R. Smy, 1994, "An experimental study of very high velocity circular water jets in air," J. Hydraul. Eng., 32, pp. 461-470.

[82] Rajaratnam and Albers, 1998, "Water distribution in very high velocity water jets in air," J. Hydraul. Eng., 124, pp. 647-650.

[83] S.J. Leach, G.L. Walker, A.V. Smith, I.W. Farmer, and G. Taylor, 1966, "Some aspects of rock cutting by high speed water jets," Philosophical Transactions of the Royal Society of London, 260, pp. 295-310.

[84] G.K. Batchelor, 1967, "An introduction to fluid dynamics," Cambridge University Press, Cambridge.

[85] S. Murata, Y. Miyake, and T. Inaba, 1976, "Laminar flow in a curved pipe with varying curvature," J. Fluid Mech., 73, p. 735.

[86] B.E. Launder, G. J. Reece, and W. Rodi, 1975, "Modeling the pressure-strain correlation of turbulence: an invariant dynamical systems approach," J. Fluid Mech., 68, p. 537.

[87] P. R. Spalart and S. R. Allmaras, 1992, "A one equation turbulence model for aerodynamic flows," AIAA92-0439 , p. 439.

[88] F.H. Harlow and P.I. Nakayama, 1968, "Transport of turbulence energy decay rate," Los Alamos Scientific Laboratory Report, LA3854.

[89] T.H. Shih, W.W. Liou, A. Shabbir, Z. Yang, and J. Zhu, 1995, "A new $k-\varepsilon$ eddy viscosity model for high reynolds number turbulent flows - model development and validation," J. Comp. Fluids, 24, p. 227.

[90] S.B. Pope, 1978, "An explanation of the turbulent round-jet/plane jet anomaly," J. of AIAA, 16, p. 279.

[91] K. Hanjalic, and B.E. Launder, 1980, "Sensitizing of the dissipation equation to irrotational strains," Transaction of ASME, 102, p. 34.

[92] H. Haj-Harir, Q. Shi, and A. Borhan, 1997, "Thermocapilary motion of deformable drops at finite reynolds and marangoni numbers," Phys. Fluids, 9, p. 845.

[93] S. Osher and J. A. Sethian, 1988, "Fronts propagating with curvature-dependent speed: Algorithms based on hamilton-jacobi formulations," J. comput. Phys., 79, p. 12.

[94] M. Sussman and P. Smereka, 1997, "Axisymmetric free boundary problems," J. Fluid Mech., 341, p. 269.

[95] Mark Sussman, 1994, "A Level Set Approach for Computing Solutions to Incompressible Two-Phase Flow," UCLA Ph.D. thesis.

[96] N. Peter, 1992, "A spectral closture for premixed turbulent combustion in the flamelet," J. Fluid Mech., 242, pp. 611-629.

[97] P. Nilsson and X.S. Bai, 2000, "Level-set flamelet library approach for premixed turbulent combution," Experimental Thermal and Fluid Sciences, 21, pp. 87-98.

[98] M. Sussman, A.S. Almgren, J.B. Bell, P. Colella, L.H. Howell, and M.L. Welcome, 1994, "A adaptive level set approach for incompressible phase flows," J. Comput. Phys., 148, pp. 81-124.

[99] G. Russo and P. Smereka, 2000, "A remark on computing distance functions," J. Comput. Phys., 163, pp. 51-67.

[100] W.F. Noh and Paul Woodward, 1976, SLIC (Simple Line Interface Calculation). In Proceeding of the Fifth International Conference on Numerical Methods on Fluid Dynamics, 59, pp. 330-340.

[101] ANSYS FLUENT UDF Manual, Release 13.0, 2010.

[102] S.V. Patankar, 1980, "Numerical heat transfer and fluid flow," McGraw Hill Book Company.

[103] H.K. Versteeg and W. Malalasekera, 1995, "An introduction to computational fluid dynamics," Pearson.

[104] Guang-Shan Jiang and Danping. Peng, 2000, "Weighted ENO schemes for Hamilton-Jacobi equations," Journal on Scientific Computing, 21, pp. 2126-2143.

[105] Visbal and Gaitonde, 2002, "On the Use of Higher-Order Finite-Difference Schemes on Curvilinear and Deforming Meshes," J. Comput. Phys., 181, pp. 155-185.

[106] S.A. Berger, L. TALBOT, and L.S. YAO, 1983, "Flow in curved pipes," Ann. Rev. Fluid Mechanics,15, pp. 461-512.

[107] D.R. Webster and J.A.C. Humphrey, 1997, "Traveling wave instability in helical coil flow," J. Phys. Fluids, 9, p. 407.

[108] F. Ladeinde and K.E. Torrance, 1991, "Convection in a rotating, horizontal cylinder with radial and normal gravity forces," J. Fluid Mech., 228, p. 361.

[109] H. Schlichting, "Boundary Layer Theory," 6th ed., McGraw-Hill, New York.

[110] D. Choi, T. J. Barber, and L.M. Chiappetta, 1999, "Large eddy simulation of High-Reynolds number jet flows," AIAA paper, 99, p. 0230.

[111] B.J. Boersma and S.K. Lele, 1999, "Large eddy simulation of compressible turbulent jets," Center for Turbulence Research Annual Research Briefs.

[112] B.J. Boersma and S.K. Lele, 1999, "Large eddy simulation of Mach 0.9 compressible jet," AIAA paper, 99, p. 1874.

[113] B. Vreman, 1996, "Direct and large-eddy simulation of the compressible mixing layer," PhD Thesis, University of Twente, The Netherlands.

[114] M.R. Visbal, D.P. Rizzetta, 2002, "Large-eddy simulation on curvilinear grids using compact differencing and filtering schemes," J. Fluids Eng., 124, 836â847.

[115] D.P. Rizzetta, M.R. Visbal, G.A. Blaisdell, 2003, "A time-implicit high order compact differencing and filtering scheme for large-eddy simulation," Int. J. Numer. Meth. Fluids, 42, 665-693.

[116] J. Mathew, R. Lechner, H. Foysi, J. Sesterhenn, R. Friedrich, 2003, "An explicit filtering method for large eddy simulation of compressible flows," Phys. Fluids 15, 2279-2289.

[117] C. Bogey and C. Bailly, 2004. "A family of low dispersive and low dissipative explicit schemes for flow and noise computations," J. Comput. Phys., 194, 194-214.

[118] C. Bogey and C. Bailly, 2006, "Computation of a high Reynolds number jet and its radiated noise using LES based on explicit filtering," Comput.Fluids, 35, 1344â1358.

[119] C. Bogey and C. Bailly, 2006, "Investigation of downstream and sideline subsonic jet noise using large eddy simulation," Theoret. Comput. Fluid Dynamics, 20, 23-40.

[120] C. Bogey and C. Bailly, 2006, "Large eddy simulations of round free jets using explicit filtering with/without dynamic Smagorinsky model," International Journal of Heat and Fluid Flow, 27, 603â610.

[121] N. Andersson, L.E. Eriksson, L. Davidson, 2005, "Large-eddy simulation of subsonic turbulent jets and their radiated sound," AIAA J. 43, 1899-1912.

[122] F.F. Grinstein, "Computing turbulent flow dynamics with Implicit LES", report.

[123] P.K. Wu and G.M. Faeth, 1995, "Onset and end of drop formation along the surface of turbulent liquid jets in still gases," Phys. Fluids, 7.

[124] A. Guha, R.M. Barron, and R. Balachandar, 2010, "Numerical simulation of high speed turbulent water jets in air," J. Hydraul. Eng., 48, pp. 119-124.

[125] L. Schiller and A. Naumann, 1933, "A drag coefficient correlation," VDI Zeits, 77, p.318.

[126] A. Michalke, 1965, "On spatially growing disturbances in an inviscid shear layer," J. Fluid Mech., 23, p. 521.

[127] P. Plaschko, 1979, "Helical instabilities of slowly divergent jets," J. Fluid Mech., 92, p. 209.

[128] J. Cohen and I. Wygnanski, 1987, "The evolution of instabilities on the axisymmetric jet. part1. the linear growth of disturbances near the nozzle," J. Fluid Mech., 176, p. 191.

[129] T.C. Corke, F. Shakib, and H. Nagib, 1991, "Mode selection and resonant phase locking in unstable axisymmetric jets," J. Fluid Mech., 223, p. 253.

[130] T.C. Corke and S.M. Kusek, 1993, "Resonance in axisymmetric jets with controlled helical mode input," J. Fluid Mech., 249, p. 307.

[131] R.D. Moin and P. Moin, 1987, "The effects of curvature in wall-bounded turbulent flows," J. Fluid Mech. 175, p. 479.

[132] Cynthia Y. Young, Precalculus, John Wiley & Sons, 2010.

[133] K.T. McDonald, 2014, "Error Estimation in Fitting of Ellipses," Lab note.

[134] P.L. Rosin,1996, "Analysing error of fit functions for ellipses," Patt. Rec. Lett., 17, 1461.

[135] P.L. Rosin,1996, "Assessing Error of Fit Functions for Ellipses," Comp. Graph. Info. Proc., 58, 494.

[136] A. Albano, 1974, "Representation of Digitized Contours in Terms of Conic Arcs and Straight-Line Segments," Comp. Graph. Info. Proc., 3, 23

[137] K. Pearson, 1900, "On the Criterion that a given System of Deviations from the Probable in the case of a Correlated System of Variables is such that it can be reasonably supposed to have arisen from random sampling," Phil. Mag., 1, 157.

[138] R.A. Fisher, 1922, "On the Interpretation of χ^2 from Contingency Tables, and the Calculation of P," J. Roy. Stat. Soc., 85, 87.

[139] R.A. Fisher, 1924, "The Conditions under which χ^2 Measures the Discrepancy between Observation and Hypothesis," J. Roy. Stat. Soc., 87, 422.

[140] W.G. Cochran, 1952, "The χ^2 Test of Goodness of Fit," Ann. Math. Soc., 23, 315.

[141] R.L. Plackett, 1983, "Karl Pearson and the Chi-squared Test," Intl. Stat. Rev., 51, 59.

[142] S.D. Bolboacă , 2011,"Pearson-Fisher Chi-Square Statistic Revisited," Information, 2, 528.

[143] K.T. McDonald, 2013, "Princeton Physics 101 Lab Manual."

Appendix A

Properties of Mercury

Table A.1: The properties of mercury

Temperature (K)	Density (kg/m^3)	Specific Heat Capacity ($10^3 J/kgK$)	Thermal Conductivity (W/mK)	Kinematic Viscosity ($10^{-7} m^2/s$)
300	13546	0.139	8.34	1.1257